Technische Universität München

Department Chemie

Fachgebiet Theoretische Chemie

Self-Interaction, Delocalization, and Static Correlation Artifacts in Density Functional Theory: Studies with the Program ParaGauss

Thomas Martin Soini

Vollständiger Abdruck der von der Fakultät für Chemie der Technischen Universität München zur Erlangung des akademischen Grades eines

Doktors der Naturwissenschaften (Dr. rer. nat.)

genehmigten Dissertation.

Vorsitzender:		Univ.-Prof. Dr. Ville R. I. Kaila
Prüfer der Dissertation:	1.	Univ.-Prof. Dr. Dr. h.c. Notker Rösch (i.R.)
	2.	Univ.-Prof. Dr. Andreas Görling (Friedrich-Alexander Universität Erlangen-Nürnberg)

Die Dissertation wurde am 08.01.2015 bei der Technischen Universität München eingereicht und durch die Fakultät für Chemie am 18.02.2015 angenommen.

Acknowledgements

The scientific work of this thesis was carried out at the Fachgebiet für Theoretische Chemie of the Technische Universität München under the guidance of Prof. Dr. Dr. h.c. Notker Rösch. To him I want to express my gratitude for providing me with the opportunity to study this interesting topic in his group as well as for his supervision and his interest in my projects.

I am also very indebted to Dr. Sven Krüger for numerous scientific discussions as well as for his continuous support over the last years, especially in the last phase of this thesis. My special thanks also go to Dr. Alexei Matveev for his help in improving my programming skills as well as to Dr. Alexander Genest for many valuable suggestions and discussions.

I especially want to thank my colleague and friend Cheng-chau Chiu for his help in various aspects of my live. I also thank Dr. Astrid Nikodem for the good collaboration during the completion of the parallelized exact-exchange implementation.

I further want to thank all my past and present colleagues Dr. Duygu Başaran, Dr. Ion Chiorescu, Dr. Konstantina Damianos, Dr. Wilhelm Eger, Ralph Koitz, Dr. Alena Kremleva, Bo Li, Dr. Remi Marchal, Dr. Raghunathan Ramakrishnan, Dr. Yin Wu and Dr. Zhijian Zhao for providing a friendly working atmosphere.

I thank the International Graduate School of Science and Engineering at the Technische Universität München for the generous scholarship and the Leibniz-Rechenzentrum of the Bayerische Akademie der Wissenschaften for providing the computing resources used to complete my scientific work.

Last but not least I thank my family for their love, support, and encouragement, which enabled me to complete this work.

Content

List of Abbreviations

ACE	Accompanying Coordinate Expansion (method)
ACM3, ACM1, …	Adiabatic Connection Method (different variants)
AO	Atomic Orbital
B88, B3, B97, …	Becke Functionals (different variants)
CAS	Complete Active Space (method)
CC	Coupled Cluster
CGTO	Contracted Gaussian Type Orbital
CPU	Central Processing Unit
DFT	Density Functional Theory
DLB	Dynamic Load Balancing (library)
FCI	Full Configuration Interaction (method)
ERI	Electron-Repulsion Integral
EXX	Exact-Exchange
FDO	Functional Derivative with respect to Orbitals
FEN	Fractional Electron Number
FLL	Fully Localized Limit
FLOP	Floating Point Operation
FMO	Fragment Molecular Orbital
FON	Fractional Occupation Number (technique)
GGA	Generalized Gradient Approximation
GKS	Generalized Kohn–Sham (formalism)
HEG	Homogeneous Electron Gas
HF	Hartree–Fock (method)
HFS	Hartree–Fock–Slater (model)
HK	Hohenberg–Kohn
HLG	HOMO-LUMO gap
HOMO	Highest Occupied Molecular Orbital
HRR	Horizontal Recursion Relation
KED	Kinetic Energy Density
KS	Kohn–Sham (formalism)
LDA	Local Density Approximation (method)
LSDA	Local Spin Density Approximation (method)
LUMO	Lowest Unoccupied Molecular Orbital
LYP	Lee–Yang–Parr
M06, M06L, …	Minnesota Functionals (different variants)
MBPT	Many-Body Perturbation Theory
MCSCF	Multi-Configuration Self-Consistent-Field (method)

MD	McMurchie–Davidson
MGGA	Meta Generalized Gradient Approximation
MO	Molecular Orbital
MP	Møller–Plesset (method)
MPI	Message Passing Interface (library)
MSIE	Many-electron Self-Interaction Error
NCIE	Non Covalent Interaction Error
NGA	Non-Separable Gradient Approximation
OEP	Optimized Effective Potential (method)
OER	One-Electron Region
OPTX	Optimized LDA Exchange Functionals (different variants)
OS	Obara–Saika
PBE	Perdew–Burke–Ernzerhof
PGTO	Primitive Gaussian Type Orbital
PH	Pople–Hehre
PKZB	Perdew–Kurth–Zupan–Blaha
PW	Perdew–Wang GGA
PWLDA	Perdew–Wang LDA
PZ	Perdew–Zunger
RKS	Restricted Kohn–Sham (formalism)
SCE	Static Correlation Error
SCF	Self-Consistent-Field (method)
SE	Schrödinger Equation
SIC	Self-Interaction Correction
SIE	Self-Interaction Error
TPSS	Tao–Perdew–Staroverov–Scuseria
UKS	Unrestricted Kohn–Sham (formalism)
vdW	van der Waals
VRR	Vertical Recursion Relation
VSXC	van Voorhis–Scuseria Functional
VWN	Vosko–Wilk–Nusair
WFT	Wave Function Theory
XC	Exchange-Correlation

1. Introduction

1.1. Quantum Chemistry

Electronic structure theory[1-7] of materials and molecules aims to obtain accurate computational descriptions of such systems at an atomic length scale. Predictions of physical observables of such quantum mechanical systems can then be computed from this description. The fields of quantum chemistry and computational chemistry apply electronic structure theory to chemical problems.[8-10] The studied chemical entities range from individual atoms over common molecules to larger biomolecules, nanoparticles and extended systems, like solids and their surfaces.

The electronic structure description of such systems is determined by the underlying Schrödinger equation[11] (SE) which can be solved analytically only for a few one-electron cases.[12,13] Thus, quantum chemistry needs to rely on approximate solution techniques for the many-electron SE. To obtain useful predictions it is desirable to compute for example reaction energies with a precision of ~2 kcal/mol (~8 kJ/mol, chemical precision). These results are usually obtained from total energies of much larger values which therefore need to be computed with a high relative accuracy. Except for high level quantum chemical approximations, most methods do not reliably deliver chemical precision and their accuracy usually varies depending on the type of systems at hand. While in the case of main group compounds an accuracy of a few kcal/mol is feasible, a precision of 10 kcal/mol or more may still be reasonable for reaction energies involving systems with transition metal elements.

The Hartree–Fock (HF) method[2,14-16] is one of the earliest electronic structure approximations and the simplest meaningful approach based on wave function theory (WFT). The HF ansatz for the many-electron wave function as Slater-determinant fulfills the requirements of electronic non-distinguishability and the antisymmetry principle, which provides an “ab-initio” electronic structure description of chemical systems. However, being an effective mean-field theory, HF neglects important aspects of the many-particle nature of the electron-electron interactions and therefore most of the resulting correlation effects. Within a finite basis set approximation introduced to represent the wave functions all correlation effects are recovered by the full configuration interaction (FCI) method,[4,17-20] which represents the exact solution in this case. FCI employs a many-electron basis set in the form of determinants which is usually constructed from the corresponding HF solutions. As this basis set grows exponentially with the system size, FCI is computationally intractable for all but the smallest systems.[4,17-20] These extreme computational requirements motivated a large variety of approximations to FCI.[21-26] All of these so-called post-HF methods aim to

reduce the computational complexity of the calculation of the correlation energy while still retaining all relevant physical effects.[26]

Density functional theory[27-33] (DFT) of the electronic structure stands in some sense opposed to these methods as it is based on the idea to employ the electron density instead of the many-body wave function as fundamental quantum mechanical variable. The theorems of Hohenberg and Kohn (HK) show DFT to be an exact reformulation of many-body quantum mechanics.[27] Furthermore, the HK theorems justify the total energy density functional for any quantum chemical system, which is minimized by the electronic ground state density.[27] Kohn and Sham (KS) subsequently proposed another important contribution which removed many obstacles for the practical applicability of DFT.[28] Within the KS formalism only the non-classical parts of the electron-electron interaction remain unknown and require to be approximated. The earliest and simplest of such exchange-correlation (XC) approximations were based on the homogeneous electron gas model (HEG).[28] Already these local density approximations (LDA) often supersede the accuracy of lower-level post-HF methods, especially in the case of systems involving transition metal elements.[34] Compared to the HF method LDA approaches exhibit far lower computational requirements, when combined with density fitting techniques.[35-43] Thus, the efficiency of LDA gave access to a theoretical description of much larger systems and significantly extended the applicability of quantum chemistry.

Further improved XC approximations beyond LDA, are based on adding a functional dependence on the gradient of the electron density.[44] This approach led to the so-called generalized gradient approximation (GGA).[45] A large variety of such semi-local XC functionals were proposed in the following.[46-50] For many physical properties GGA methods were found to provide a consistently improved accuracy over LDA.[51-57]

Despite their success, LDA and GGA density functionals still rely on several approximations that eventually break down in some situations, which can lead to significant failures. The most prominent examples of such a failure are the so-called self-interaction error (SIE) and the closely connected delocalization error, for which a number of corrections have been suggested.[58] The approach of Perdew and Zunger[59] (PZ) and the DFT+U method[60-69] are probably the most widely applied self-interaction corrections (SIC).[58] In the context of the present thesis, a generalization of the DFT+U method to molecular fragment orbitals (DFT+Umol) has been implemented as part of the density functional program package ParaGauss.[70] Furthermore, several classes of XC functionals have been proposed that go beyond GGA and aim for being at least partially free of self-interaction artifacts. Most of these methods do not only depend on the electron density and its gradient but also include additional functional dependencies on the KS orbitals. In the case of the meta generalized gradient approximation[71-78] (MGGA) the kinetic energy density is used as additional, orbital-dependent variable.[79,80] As this quantity is computed from the local gradient of the

KS orbitals only, MGGA approximations are semi-local XC functionals as well and exhibit computational costs which are comparable to those of GGA methods. This is different in the case of hybrid DFT functionals where a part of the semi-local (GGA or MGGA) exchange term is replaced by the exact-exchange (EXX) energy.[71,81-83] Being computed in the same fashion as the HF exchange part, this latter term significantly increases the computational costs of hybrid DFT methods compared to local or semi-local XC approximations. Several hybrid DFT approximations have been implemented in the context of this thesis. Furthermore, these functionals were assessed with regard to their accuracy for the description of transition metal clusters. Also these performance studies are part of this thesis. Aside from the commonly employed hybrid functionals,[50,75,81,82,84-90] also variations like range-separated hybrid DFT[91-97] and screened exact-exchange DFT methods[98,99] exist. Even more elaborate concepts like local hybrid functionals employ a locally varying exact-exchange energy density and allow the design of hyper GGA functionals, which are exact for arbitrary one-electron densities and thus, potentially more accurate for many-electron systems too.[100-103]

Like local and semi-local XC functionals also hybrid DFT methods do not account for nonlocal correlation effects. Thus, all of these approximations are unable to describe van der Waals (vdW) type interactions, which, among other consequences, leads to the non-covalent interaction error (NCIE).[104] To improve the descriptions of such effects, empirical corrections like DFT-D have been suggested.[95,105-107] Such correction terms represent an efficient alternative to more advanced but significantly more expensive approaches like the random phase approximation (RPA) or double hybrid DFT which have nonlocal dependencies on the unoccupied KS orbitals as well.[108-114] Furthermore, the purely density-dependent vdW-DFT approaches[115-119] were developed to describe the nonlocal correlation interactions that cause the vdW interactions as well and thus essentially remove the NCIE.

Static correlation effects arise in situations where the ground state cannot be properly approximated by a mean-field description. These effects represent another source of error in DFT approximations. The lack of a proper, explicit description of static correlation and the resulting static correlation error (SCE) become apparent mostly for systems with significant multi-reference character like radical species or transition metal compounds. This type of correlation is, however, implicitly included in local exchange functionals which leads to the unfortunate situation that most modifications of these terms, e.g. by a SIE correction, deteriorate the description with regard to static correlation aspects. The interplay between SIE and SCE is examined and discussed for the employed hybrid DFT functionals and the DFT+Umol method in the context of several applications which are part of this thesis. The development of XC approximations that avoid self-interaction while simultaneously including nonlocal and static correlation effects, hence tackle all three issues – SIE, SCE, and NCIE, has begun only very recently.[97,102,120]

1.2. Thesis Outline

The present thesis is dedicated to the development, implementation, and assessment of hybrid DFT functionals as well as the DFT+Umol method. The subsequent application of these methods primarily aims at cases related to computational catalysis for which semi-local DFT methods are unable to provide qualitatively correct results due to spurious self-interaction and delocalization errors.

DFT and especially its more advanced XC approximations rely heavily on theoretical concepts originating from WFT. While a detailed coverage of WFT is beyond the scope of this thesis, some topics that are important for later discussions will be briefly highlighted in the Chapter 2 which deals with theoretical concepts. The rest of that chapter addresses DFT. Thereby, the most fundamental approaches and approximations to DFT are presented first. Subsequently, the self-interaction and delocalization effects as well as the closely connected implicit description of static correlation are introduced, which both arise in local and semi-local DFT approximations. Chapter 2 concludes with a discussion of the theoretical aspects of hybrid DFT and DFT+U methods in the context of the self-interaction error.

Chapter 3 is dedicated to algorithmic details and implementation aspects of the DFT methods added to the parallel density functional program package PARAGAUSS[70] in the context of this thesis. The first section covers exact-exchange and includes discussions about the calculation of four-center electron-repulsion integrals, their contraction with the density matrix, as well as serial and parallel efficiency aspects. The second part of this chapter deals with the implementation of the DFT+Umol method which represents an extension of conventional DFT+U approaches to linear combinations of orbitals.

Finally, Chapter 4 presents various applications of the methods implemented in the framework of this thesis. First, the effects and origins of self-interaction artifacts are examined by means of hybrid DFT and DFT+Umol calculations of metal-CO dissociation energies of nickel (sub-) carbonyls. The trend of these dissociation energies represents an example for a qualitative failure of GGA methods due to the self-interaction error. Second, in a transition metal cluster scaling approach the performance of several hybrid DFT approximations and the impact of the static correlation error is assessed. The same XC functionals are subsequently applied to study the adsorption of CO molecules on the facets of platinum clusters. The correct description of CO adsorption site preferences represents a situation where the prediction of physical quantities by GGA methods is known to suffer considerably from self-interaction artifacts. Simultaneously the description of the metallic moiety requires including, at least implicitly, static correlation effects. This problem is addressed with hybrid DFT methods as well as with the DFT+Umol correction, which allows for a more detailed analysis of the general adsorption site behavior on the employed model clusters.

2. Theory

2.1. Aspects of Wave Function Theory

2.1.1. Exact-Exchange and Hartree–Fock Theory

The Schrödinger Equation[11] (SE) provides the fundamental quantum mechanical description of molecular systems, solids and surfaces on an atomic scale. Within the Born–Oppenheimer approximation[121] the electronic and nuclear degrees of freedom are separated so that the SE for the electronic components of the wave function reads as

$$\hat{H}_{el} \,|\, \Psi_{el} \rangle = E_{el} \,|\, \Psi_{el} \rangle \,. \qquad 2.1.1$$

The electronic wave functions are denoted as $\left|\Psi_{el}\right\rangle$ and the standard *n*-electron Hamiltonian for molecular systems

$$\hat{H}_{el} = \sum_{a} \left(-\tfrac{1}{2} \nabla_a^2 + \hat{V}_{\text{ext}}(\mathbf{r}_a) + \sum_{b>a} \hat{W}(\mathbf{r}_a, \mathbf{r}_b) \right) \qquad 2.1.2$$

is expressed in terms of spatial electronic coordinates $\mathbf{r}_a = (x_a, y_a, z_a)$, the external potential[1] V_{ext} which arises from the atomic nuclei, as well as the pairwise electron-electron interaction $\hat{W}(\mathbf{r}_a, \mathbf{r}_b) = 1/\left|\mathbf{r}_a - \mathbf{r}_b\right|$. Of special interest is the ground state $\left|\Psi_0\right\rangle$ and the corresponding ground state energy E_0. As Eq. 2.1.1 represents a generally unsolvable many-body problem, the search for accurate approximations to $\left|\Psi_{el}\right\rangle$ is central to WFT.[2,4,6]

The approximate solution of the many-body SE remains a high-dimensional problem though, which demands for reliable and efficient numerical techniques. The Hartree–Fock method[2,14-16] uses a Slater-determinant[122]

$$\Phi\left(\mathbf{x}_1, \mathbf{x}_2, \ldots, \mathbf{x}_n\right) = \sqrt{\frac{1}{n!}} \begin{vmatrix} \phi_1(\mathbf{x}_1) & \phi_1(\mathbf{x}_2) & \cdots & \phi_1(\mathbf{x}_n) \\ \phi_2(\mathbf{x}_1) & \phi_2(\mathbf{x}_2) & \cdots & \phi_2(\mathbf{x}_n) \\ \vdots & \vdots & \ddots & \vdots \\ \phi_n(\mathbf{x}_1) & \phi_n(\mathbf{x}_2) & \cdots & \phi_n(\mathbf{x}_n) \end{vmatrix} \qquad 2.1.3$$

as ansatz for $\left|\Psi_{el}\right\rangle$, which fulfills the requirements of electronic non-distinguishability and the Pauli antisymmetry principle.[123] The single-electron orbitals $\{\phi_a(\mathbf{x}_b)\}$ depend on combined electronic spatial $\mathbf{r}_a$ and spin σ_a coordinates, $\mathbf{x}_a = \left(\mathbf{r}_a, \sigma_a\right)$, and can be interpreted as wave functions of single electrons. Compared to the *n*-dimensional many-body wave function these orbitals are much simpler and allow one to approximate efficiently the SE in actual computations. After expressing $\left\langle \Phi \middle| \hat{H}_{el} \middle| \Phi \right\rangle$ in terms of the orbitals $\{\phi_a(\mathbf{x}_b)\}$, most terms vanish as the latter are defined to be pairwise orthogonal. For the spin-restricted case,

[1] The external potential includes the interaction between nuclei and electrons as well as the nuclear-nuclear repulsion term. As the latter term is independent of the electronic degrees of freedom it enters the many-body Hamiltonian only in form of a constant energetic shift.

$\phi_a(\mathbf{r},\uparrow) = \phi_a(\mathbf{r},\downarrow) = \phi_a(\mathbf{r})$, the resulting total energy expression of the single-determinant ansatz, E^{SD}, reads as follows

$$\begin{aligned} E^{\mathrm{SD}} &= \sum_a^{n/2}\left(2\langle\phi_a \mid -\tfrac{1}{2}\nabla^2 + \hat{V}_{\mathrm{ext}} \mid \phi_a\rangle + \sum_b^{n/2}\left(2\langle\phi_a\phi_b \mid \hat{W} \mid \phi_a\phi_b\rangle - \langle\phi_a\phi_b \mid \hat{W} \mid \phi_b\phi_a\rangle\right)\right) \\ &= T + E_{\mathrm{ext}} + E_{\mathrm{Coul}} + E_{\mathrm{X}} \end{aligned} \qquad 2.1.4$$

with *T* and *V* denoting the one-electron terms for the kinetic energy and the external potential, respectively. Note, that the electron-electron interaction ($\hat{W} = 1/|\mathbf{r} - \mathbf{r}'|$) is described by an electrostatic Coulomb part E_{Coul} (Hartree term) as well as by E_{X}, the non-classical exchange term. This latter term is a direct consequence of the determinant ansatz for $|\Psi_{el}\rangle$ and is central for hybrid DFT methods as well (see Section 2.3).[81,82]

The HF energy E^{HF} is obtained as the energetically lowest stationary point of E^{SD} with respect to variations of the arguments $\{\phi_a\}$ while imposing pairwise orthonormality conditions on them. The canonical spin-restricted Hartree–Fock equations

$$\left(-\tfrac{1}{2}\nabla^2 + \hat{V}_{\mathrm{ext}}\right)|\phi_a\rangle + \sum_b\left(2\langle\phi_b \mid \hat{W} \mid \phi_b\rangle|\phi_a\rangle - \langle\phi_b \mid \hat{W} \mid \phi_a\rangle|\phi_b\rangle\right) = \hat{f}_{\mathrm{HF}}|\phi_a\rangle = \varepsilon_a|\phi_a\rangle \qquad 2.1.5$$

result from this variation. Each of these equations in Eq. 2.1.5 describes an individual electron as a particle that moves within the electrostatic field created by the atomic nuclei as well as the Coulomb and exchange potentials arising from all other electrons of the system. This makes HF an effective mean-field theory. The orbitals $\{\phi_a\}$ and orbital energies $\{\varepsilon_a\}$ emerge as solutions of the HF equations and represent the eigenfunctions and eigenvalues of the corresponding single-particle Hamiltonian $\hat{f}_{\mathrm{HF}}$ (Fock operator), respectively. In the context of an approximated ground state $|\Psi_0\rangle$ the *n* solutions that lead to the energetically lowest total energy E^{SD} are occupied by electrons and included in the determinant $|\Phi_0\rangle$, Eq. 2.1.3. The remaining unoccupied (virtual) orbitals do not affect the HF ground state and the corresponding HF ground state energy E^{HF}.

A finite set of *N* functions $\{\varphi_i\}$ is commonly employed to represent the HF orbitals according to

$$\phi_a(\mathbf{r}) = \sum_i \varphi_i(\mathbf{r})\, C_{ia}\,, \qquad 2.1.6$$

whereas $N \geq n$ to account for the presence of all electrons in the system. Left-multiplication of Eq. 2.1.5 by $\langle\varphi_j|$ (and integration) yields a single matrix equation[124,125]

$$\mathbf{fC} = \mathbf{SC}\boldsymbol{\varepsilon} \qquad 2.1.7$$

in terms of the Fock matrix

$$\begin{aligned} f_{ij} &= \langle\varphi_i \mid \hat{h}_{\mathrm{HF}} \mid \varphi_j\rangle = T_{ij} + V_{ij} + 2J_{ij} + K_{ij} \\ &= \langle\varphi_i \mid -\tfrac{1}{2}\nabla^2 + \hat{V}_{\mathrm{ext}} \mid \varphi_j\rangle + \sum_a\sum_{kl} C_{ka}^* C_{la}\left(2\langle\varphi_i\varphi_k \mid \hat{W} \mid \varphi_j\varphi_l\rangle - \langle\varphi_i\varphi_k \mid \hat{W} \mid \varphi_l\varphi_j\rangle\right) \end{aligned} \qquad 2.1.8$$

and the overlap matrix $S_{ij} = \langle\varphi_i \mid \varphi_j\rangle$, whose non-diagonal elements arise in the case of non-orthogonal basis functions. Thus, the integro-differential equations from HF theory are

reduced to the computation of the matrix elements in Eq. 2.1.8 and the solution of the generalized eigenvalue problem in Eq. 2.1.7. Well-established algorithms exist for both of these steps. However, Eq. 2.1.5 is non-linear in the HF orbitals $\{\phi_a\}$ due to the electron-electron interactions. In consequence, also the Fock matrix **f** depends on its own eigenvectors. Because of these dependencies the correct solution of Eq. 2.1.7 can only be obtained iteratively, which is commonly achieved with the self-consistent-field (SCF)[2] iteration.[2] The density matrix $\mathbf{P} = \mathbf{C}(\mathbf{C}^{\dagger})$ is obtained as the matrix representation of the density matrix operator

$$\hat{\rho} = \left|\Psi_{el}\right\rangle\left\langle\Psi_{el}\right| \qquad 2.1.9$$

in the case of a single-determinant ansatz. In this context **P** can be interpreted as a projector onto the subspace of occupied HF orbitals.[126] This quantity allows one to avoid the transformation of the electron-repulsion integrals (ERI) into the HF orbital basis in Eq. 2.1.8

$$J_{ij} = \sum_{kl} P_{kl} \langle \varphi_i \varphi_k \,|\hat{W}|\, \varphi_j \varphi_l \rangle = \sum_{kl} P_{kl} (ij \,|\, kl) \,, \qquad 2.1.10a$$

$$K_{ij} = \sum_{kl} P_{kl} \langle \varphi_i \varphi_k \,|\hat{W}|\, \varphi_l \varphi_j \rangle = \sum_{kl} P_{kl} (ik \,|\, lj) \,, \qquad 2.1.10b$$

and simplifies the computation of the HF energy from the corresponding Fock matrix

$$E^{\mathrm{HF}} = \mathrm{Tr}\{\mathbf{f}\,\mathbf{P}\} \,. \qquad 2.1.11$$

The size of the four-center two-electron integral tensor **g**, $\{\mathbf{g}\}_{ijkl} = (ij \,|\, kl)$ in Eqs. 2.1.10 formally scales in forth order $\mathcal{O}(N^4)$ with respect to the number of basis functions *N*. The calculation of **g** and its contraction with **P** to the matrices **J** and **K** generally represent the computationally most demanding steps in Hartree–Fock calculations.

2.1.2. Post-HF Methods and Correlation Effects

Some concepts from WFT beyond HF theory are important in the context of this thesis as well. This holds especially for the correlation energy, which is commonly subdivided into its dynamic and static correlation components. The most important WFT approximations for the correlation energy as well as the origin of dynamic and static correlation terms shall be discussed in the following.

Each Hartree–Fock equation describes only an individual electron while treating all other particles in terms of their quantum mechanical distributions. Thus, the HF equations neglect the particle nature of the electron-electron interaction, which essentially prevents the electrons from correlating their motions beyond effects arising from spin interactions (Fermi correlation). However, the mean-field description arises naturally from the ansatz of single-

[2] SCF is often used synonymously for the HF method. However, the term HF itself denotes the analytical theory in Eqs. 2.1.5 while SCF stands for the procedure used to converge the non-linear equations arising from single-determinant theories. As such the term SCF will also appear in the context of KS-DFT.

determinant approximation for $|\Psi_{el}\rangle$ in Eq. 2.1.3. This implies that the single-particle basis is unable to describe correlation effects and that the missing correlation energy is recovered only within a true many-electron basis.[127]

The Slater-determinant in Eq. 2.1.3 was chosen for its non-distinguishability and antisymmetry properties but any linear combination of Slater-determinants

$$|\Psi_{el}\rangle \approx \sum_{i}^{M} c_i |\Phi_i\rangle \qquad 2.1.12$$

meets these requirement as well.[4] Post-HF theories usually generate the elements of such a basis of Slater-determinants by substituting occupied and virtual orbitals from a previously obtained HF ground state solution.[4,17-26] The FCI method thereby employs a basis of all possible determinants that can be generated with this approach and thus yields, within the employed finite basis set, the exact solution of the *n*-electron SE, Eq. 2.1.1.[2] However, FCI accounts for a very large number of determinants which exponentially grows with respect to the basis set size *N*.[7] These unfavorable computational requirements essentially restrict FCI to very small systems.[7] All other post-HF methods reduce the degrees of freedom of the many-electron basis while aiming to retain most correlation effects covered by FCI.[4,17-20] Like FCI, these methods always introduce the unoccupied orbitals[3] of the HF ground state solution into the expression of the correlation energy. The second-order many-body perturbation theory[21] (MBPT2 or MP2) and coupled cluster (CC) approaches,[22] mostly in form of its CCSD(T) variant,[23] are nowadays the most popular approaches of this type. The former directly provides an estimate for the correlation energy

$$E_{\mathrm{C}}^{\mathrm{MP2}} = \tfrac{1}{4} \sum_{ab} \sum_{uv} \frac{|\langle \phi_a \phi_b | \hat{W} | \phi_u \phi_v \rangle - \langle \phi_a \phi_b | \hat{W} | \phi_v \phi_u \rangle|^2}{\varepsilon_a + \varepsilon_b - \varepsilon_u - \varepsilon_v} \,, \qquad 2.1.13$$

from many-body perturbation theory.[21] In contrast to that, CC approaches employ an exponential ansatz for the many-body wave function

$$|\Psi_{el}\rangle \approx e^{\hat{T}} |\Phi_0\rangle \qquad 2.1.14$$

in terms of a truncated substitution operator $\hat{T}$. Coupled cluster theory formally includes all of the up to *n*-fold substituted determinants in the total energy expressions, although the variation of the determinant coefficients c_i is subject to specific restrictions.[26]

At this point some important considerations need to be made about the correlation interactions that are recovered by MP2 and CCSD(T) approaches. In most cases the electronic correlation is caused by the tendency of the electrons to avoid each other in their dynamic motion due to electrostatic repulsion. The resulting electronic rearrangement is rather limited and reflects itself in rather small correction terms to $|\Phi_0\rangle$ in Eq. 2.1.12. Dynamic correlation effects are mostly localized, except for long-range correlation effects

[3] Denoted by the indices *u* and *v*.

that lead to vdW interactions. Both, short- and long-range dynamic correlation effects are well handled by post-HF methods.[128]

However, in some cases the tendency of the electrons to avoid each other can be large enough to cause dramatic rearrangements.[129-131] These relocations can locate the interaction partners to entirely different spatial regions or even to different atomic centers.[129-131] Compared to dynamic correlation effects such rearrangements are quite nonlocal and of a less instantaneous nature.[129-131] Thus these relocations are denoted as non-dynamic or static correlation effects.[129-131] At the level of wave functions, static correlation expresses itself in the presence of one or more substituted determinants that are (nearly) degenerate to $|\Phi_0\rangle$ in HF theory. These determinants contribute to the eigenfunction of the many-body Hamiltonian, Eq. 2.1.12, with similar prefactors[4] c_i as $|\Phi_0\rangle$.[132] While FCI covers all types of correlation interactions, standard low-order post-HF methods like MP2 or CCSD(T) can exhibit dramatic failures in cases where static correlation prevails.[133] Multi-reference approaches like multi-configuration SCF[134,135] (MCSCF) or complete active space[136] (CAS) methods are more reliable approximations in such cases.[137] However, these methods are computationally far more demanding than MP2 or even CCSD(T).

[4] Although the transition between dynamic and static correlation is smooth and not well defined, c_i values larger than 0.1 or 0.2 are usually considered as strong indicators for the presence of static correlation interactions (T_1 diagnostics).[116]

2.2. Kohn–Sham Density Functional Theory

2.2.1. Fundamental Concepts

The following section briefly presents the fundamentals of density functional theory, namely the Hohenberg–Kohn theorems, the Kohn–Sham formalism and the Kohn–Sham equations which result from the latter.

The many-body SE has $3n$ dimensional solutions and is thus quite difficult to handle. This leads to the high computational requirements (formal scaling of $\mathcal{O}(N^5)$ at least)[5] of WFT methods beyond HF. Density functional theory[27-33] follows a different approach. At its heart lies the electron density

$$\rho(\mathbf{r}) = \sum_{\sigma}\sum_{a}\left\langle \Psi_{el} \middle| \delta(\mathbf{x}-\mathbf{x}_a) \middle| \Psi_{el} \right\rangle = n\sum_{\sigma}\left\langle \Psi_{el} \middle| \delta(\mathbf{x}-\mathbf{x}_1) \middle| \Psi_{el} \right\rangle \ , \qquad 2.2.1$$

and its usage as the fundamental quantity of electronic structure formalisms instead of complicated many-body wave functions.[27,138] While WFT employs a wave function functional for the total energy

$$E_{el} = E_{el}[\Psi_{el}] = \left\langle \Psi_{el} \middle| \hat{H}_{el} \middle| \Psi_{el} \right\rangle \ , \qquad 2.2.2$$

DFT formulates the ground state energy E_0 as a functional of the ground state electron density ρ_0

$$E_0 = E_{el}[\rho_0] \ . \qquad 2.2.3$$

Given the fact that $\rho(\mathbf{r})$ is a three-dimensional function only, such a density based electronic structure theory should be more efficient by orders of magnitude compared to WFT approaches.

Density functional theory is justified by the theorems of Hohenberg and Kohn which prove the uniqueness of the total energy density functional in Eq. 2.2.3.[27] While referring to the original work[27] for the detailed mathematical proof, the essential argumentation of the HK theorems can be outlined as follows: For a given number of electrons n each external potential V_{ext} uniquely defines (up to a constant) a many-body Hamiltonian.[27] The corresponding many-body wave function $\left|\Psi_0\right\rangle$ emerges as a uniquely defined solution of the SE.[11] From the wave function $\left|\Psi_0\right\rangle$ the corresponding ground state electron density ρ_0 is obtained by means of Eq. 2.2.1, which gives rise to the following mapping

$$V_{\text{ext}} \overset{b'}{\mapsto} \left|\Psi_0\right\rangle \overset{a'}{\mapsto} \rho_0 \ . \qquad 2.2.4$$

The first HK theorem (HK1) deals with the reverse mapping,[27] namely that every ground state density ρ_0 uniquely defines a corresponding external potential V_{ext},[138]

$$\rho_0 \overset{a}{\mapsto} \left|\Psi_0\right\rangle \overset{b}{\mapsto} V_{\text{ext}} \ . \qquad 2.2.5$$

[5] The effective cost scaling is reduced by various techniques (integral cutoffs, density fitting, orbital localization etc.). Nevertheless, the formal scaling remains a useful measure to compare the computational efficiency of methods.

Hohenberg and Kohn proved the uniqueness of the mapping *a* and assumed that *b* is unique[6] as well.[27] The so-called strong form of the HK theorem

$$\int \Delta\rho(\mathbf{r}) \cdot \Delta V_{\text{ext}}(\mathbf{r})\, d\mathbf{r} < 0 \ , \qquad 2.2.6$$

represents a more modern alternative that does not rely on this assumption. Eq. 2.2.6 is more general than the HK theorems, which are restricted to non-degenerate ground states.[139,140] Eq. 2.2.6 is proven independently from the HK theorems by means of perturbation theory[141] and predicts for any change ΔV_{ext} in the external potential a corresponding, non-vanishing change $\Delta\rho$ of the electron density. Thus, two different external potentials cannot yield the same ρ_0, which proves the one-to-one mapping $\rho_0 \mapsto V_{\text{ext}}$.

Because of the unique mapping $\rho_0 \mapsto V_{\text{ext}}$ and the fact that ρ_0 integrates to the number of electrons *n* any quantum mechanical system is entirely defined by its ground state density. Consequently, the information about any property of the quantum mechanical system at hand is contained in ρ_0 as well. Thus, ρ_0 indeed qualifies as a substitute for the many-body wave function. This holds especially for the total electronic energy so that the existence of a density functional for the total electronic energy is guaranteed by the HK1 theorem and Eq. 2.2.6.

The second theorem of HK (HK2) formulates a variational principle

$$E_{el}[\rho_0] < E_{el}[\rho'], \qquad 2.2.7$$

which states that the total energy $E_{el}[\rho]$ is a convex functional of the electron density. This functional is minimized by the ground state density ρ_0. The HK2 theorem is proven using the relations established by HK1 as well as the standard variational principle of quantum mechanics. However, it assumes that any trial density ρ' fulfills the requirements (i) to be representable in terms of a many-body wave function as in Eq. 2.2.1 (*n*-representability) and (ii) to be the ground state density of some system with external potential V_{ext}' (*V*-representability). A violation of these conditions implies severe consequences as Eq. 2.2.7 holds for the domain of *V*-representable densities only. The constrained search of Levy and Lieb represents an alternative to the variational principle in Eq. 2.2.7 as well as to the HK1 theorem.[142-145] It relaxes the *V*-representability requirement to the conditions

$$\rho'(\mathbf{r}) \geq 0 \, , \ \int \rho'(\mathbf{r})\, d\mathbf{r} = n \, , \ \int \left| \nabla \sqrt{\rho'(\mathbf{r})} \right|^2 d\mathbf{r} < \infty \, , \qquad 2.2.8$$

which are known to suffice for a trial density $\rho'(\mathbf{r})$ to be *n*-representable.[142-146] These requirements are considerably weaker than the not yet entirely understood *V*-representability conditions.[146,147]

All of the approaches presented above can only be considered as theoretical proofs of concepts and none of them actually provides a viable way to compute any physical quantity.

[6] It can be proven as well that a many-body wave function cannot be simultaneously a ground state of two external (physically meaningful) potentials. However, such a proof involves a much more complicated argumentation in terms of the topology of regions where the wave function vanishes and thus, is omitted in most presentations.

This holds even in cases where the correct ground state density is known. Indeed, the density functionals for kinetic, exchange, and correlation energy terms are unknown and so is the total energy functional in Eq. 2.2.3.

Especially the accurate representation of the kinetic energy density functional is utterly important as the dramatic failures of early DFT approaches[148-150] trace back to poor approximations of this term.[151] Some indications about how to include an accurate formulation of the kinetic energy were provided by the Hartree–Fock–Slater model (HFS), which was developed prior to the work of HK as an approximation to the HF method.[152] The HFS approach employed an averaged exchange potential (Slater potential) which only depends on the electron density while retaining the orbital-dependent kinetic energy term.[152] Surprisingly, the HFS model was often found more accurate than HF itself.[153,154]

Kohn and Sham (KS) introduced an exact DFT formalism which shares many aspects with the HFS model.[28] Their underlying idea was to replace the original many-body problem by a fictitious auxiliary system of n non-interacting, independent particles.[28] As the HK formalism does not depend on the specific type of electron-electron interaction, setting $\hat{W}(\mathbf{r}_a,\mathbf{r}_b)=0$ in Eq. 2.1.2 is a valid choice from the formal viewpoint of HK theory. The Hamiltonian of the KS system

$$\hat{H}^{\mathrm{KS}}=\sum_{a\sigma}\left(-\tfrac{1}{2}\nabla_a^2+V_{\mathrm{KS}}^{\sigma}(\mathbf{r}_a)\right) \qquad 2.2.9$$

includes the usual kinetic energy operator as well as an effective potential V_{KS}, which is multiplicative as the electrons do not interact.[155] However, the electrons within the KS reference system are still supposed to be non-distinguishable and their wave function needs to obey the Pauli antisymmetry principle. Thus, the exact ground state of the KS Hamiltonian in Eq. 2.2.9 is represented by a single Slater-determinant.[28] Just as in Eq. 2.1.3 the KS determinant $\left|\Phi_{\mathrm{KS}}\right\rangle$ is formed by single-particle wave functions. The single-particle wave functions of the KS system differ from the HF orbitals as they include many-body effects beyond HF theory.[28] To distinguish them from the HF orbitals, the KS molecular orbitals (MO) will be denoted as $\{\psi_a\}$ or $\{\psi_a^{\sigma}\}$ in the following.

The original and KS systems are connected by the requirement that they exhibit equal ground state densities ρ_{KS} and ρ_0,[28] hence

$$\rho_0(\mathbf{r})=\rho_{\mathrm{KS}}(\mathbf{r})=\sum_{\sigma}\sum_{a}\left|\psi_a^{\sigma}(\mathbf{r})\right|^2 \quad\text{or}\quad \rho_0(\mathbf{x})=\rho_{\mathrm{KS}}(\mathbf{x})=\sum_{a}\left|\psi_a^{\sigma}(\mathbf{r})\right|^2 \qquad 2.2.10$$

in the case of an unrestricted, spin-resolved treatment.[7] This identity is fulfilled by a suitable choice of V_{KS}^{σ}, which implies ρ_0 to be V-representable in the KS system (non-interacting-V-representable).[28] Figure 2.2.1 depicts the connections between density, potentials, and wave functions in both systems.

[7] A spin-resolved density is obtained likewise from a correspondingly adapted version of Eq. 2.2.1.

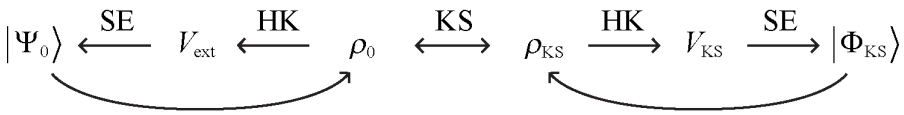

Figure 2.2.1: Relations between ground state density ρ_0, external potential V_{ext}, and ground state $|\Psi_0\rangle$ of the original system as well as ρ_{KS}, effective KS potential V_{KS}, and single-determinant ground state $|\Phi_{\text{KS}}\rangle$ of the KS reference system.

The idea to express the numerically largest interactions in the original system (with $\hat{W} = 1/|\mathbf{r} - \mathbf{r}'|$) by the corresponding terms of the reference system turns KS-DFT into a working theory.[28] This is not possible for all energy terms of the original system. However, the unknown terms are assumed to be small and are left to be approximated.[28] To this end, the KS formalism defines the following partition of the kinetic energy[28]

$$T = T_{\text{S}} + T_{\text{C}} \ . \qquad 2.2.11$$

Thereby, T_{S} denotes the kinetic energy of the reference interacting system and $T_{\text{C}} = T - T_{\text{S}}$ the difference to the kinetic energy of the interacting system.[8] While T_{C} remains unknown, T_{S} is given in terms of the MOs as[28]

$$T_{\text{S}} = \sum_{a\sigma} \left\langle \psi_a^\sigma \left| -\tfrac{1}{2}\nabla^2 \right| \psi_a^\sigma \right\rangle . \qquad 2.2.12$$

The term T_{S} should comprise by far the largest part of T so that T_{C} is expected to be small in most cases.[28] The total electronic energy is partitioned by the KS formalism as

$$E^{\text{KS}} = T_{\text{S}}[\{\psi_a^\sigma\}] + E_{\text{ext}}[\rho] + E_{\text{Coul}}[\rho] + E_{\text{XC}}[\rho] \ , \qquad 2.2.13$$

with the kinetic energy term from Eq. 2.2.12 as well as E_{ext} and E_{Coul} arising from the external and classical Coulomb potentials, respectively.[28] The exchange-correlation term E_{XC} is thereby defined as

$$E_{\text{XC}}[\rho] = E_{\text{X}}[\rho] + E_{\text{C}}[\rho] + T_{\text{C}}[\rho] \qquad 2.2.14$$

and includes all unknown terms which require to be approximated.[28] The non-classical electron-electron interaction is usually separated into exchange (E_{X}) and correlation (E_C) parts, mostly to retain the analogy to WFT. For actual DFT approximations this definition is not essential. However, it seems suggestive to construct $E_{\text{X}}[\rho]$ in such a way that the HF energy (and density) is reproduced if the correlation term is neglected.[156] Alternatively, the exchange term E_{X} may be defined in terms of a dimensional analysis as that part of E_{XC} that exhibits the same uniform scaling behavior as the Coulomb repulsion.[157]

For being formulated only in terms of ρ and the single-electron wave functions $\{\psi_a^\sigma\}$, KS-DFT mathematically appears as a mean-field approach, while still being an exact theory. If accurate approximations for E_{XC} are available, actual KS-DFT applications provide a full many-body description at the computational costs of a mean-field approach.

---

[8] The subscripts "S" and "C" in the kinetic energy terms are commonly used in the literature to denote "single-determinant" and "correlation" contributions, respectively.

Just like in HF theory, the variational equations

$$\left(\frac{\delta E^{\mathrm{KS}}}{\delta \psi_a^{\sigma\dagger}}\right)\psi_a^{\sigma} = \hat{f}_{\mathrm{KS}}^{\sigma}\,\psi_a^{\sigma} = \varepsilon_{a\sigma}^{\mathrm{KS}}\psi_a^{\sigma} \qquad 2.2.15$$

for the spin-unrestricted KS orbitals (see below) emerge as stationary points of a Lagrangian, which includes the boundary conditions of normalized and pairwise orthogonal MOs. The eigenvalues of the KS spin-orbitals are thereby denoted as $\{\varepsilon_{a\sigma}^{\mathrm{KS}}\}$. Despite of being a quantity within a fictive system, the highest KS eigenvalue corresponds to the first ionization energy of the system.[158,159] In contrast to the HF energy in Eq. 2.1.4, the last three terms on the right side of Eq. 2.2.13 are defined as density functionals.[28] Thus, the single-particle Kohn–Sham Hamiltonian (KS operator) is derived with the chain rule for functional derivatives[29]

$$\frac{\delta E^{\mathrm{KS}}}{\delta \psi_a^{\sigma\dagger}} = \left[\sum_{b\sigma'}\frac{\delta\left\langle\psi_b^{\sigma'}\left|-\frac{1}{2}\nabla^2\right|\psi_b^{\sigma'}\right\rangle}{\delta\psi_a^{\sigma\dagger}} + \left(\frac{\delta E_{\mathrm{ext}}[\rho]}{\delta\rho_\sigma} + \frac{\delta E_{\mathrm{Coul}}[\rho]}{\delta\rho_\sigma} + \frac{\delta E_{\mathrm{XC}}[\rho_\uparrow,\rho_\downarrow]}{\delta\rho_\sigma}\right)\frac{\delta\rho_\sigma}{\delta\psi_a^{\sigma\dagger}}\right]. \qquad 2.2.16$$

Thereby, $V_{\mathrm{XC}}^{\sigma} = \delta E_{\mathrm{XC}}[\rho_\uparrow,\rho_\downarrow]/\delta\rho_\sigma$ is defined as a local and multiplicative potential[9] arising from the XC term.[28] From Eq. 2.2.16 the KS operator is identified as

$$\hat{f}_{\mathrm{KS}}^{\sigma} = -\tfrac{1}{2}\nabla^2 + V_{\mathrm{ext}} + V_{\mathrm{Coul}} + V_{\mathrm{XC}}^{\sigma} \qquad 2.2.17$$

and a comparison with Eq. 2.2.9 reveals the effective KS potential as

$$V_{\mathrm{KS}}^{\sigma} = V_{\mathrm{ext}} + V_{\mathrm{Coul}} + V_{\mathrm{XC}}^{\sigma}\ . \qquad 2.2.18$$

Just as in Eq. 2.1.7, the introduction of a finite basis set allows one to formulate the KS equations as a generalized eigenvalue problem, which needs to be solved iteratively e.g. by the SCF method. The most striking technical difference to the Fock matrix of HF theory consists in the term

$$V_{ij\sigma}^{\mathrm{XC}} = \left\langle\varphi_i\left|\delta E_{\mathrm{XC}}[\rho_\uparrow,\rho_\downarrow]/\delta\rho_\sigma\right|\varphi_j\right\rangle, \qquad 2.2.19$$

which needs to be computed on numerical grids.[7,31,160-166] A correspondingly adapted variant of Eq. 2.1.11 allows one to compute the estimate of E^{KS} in a finite basis.

Note, that the original DFT treatment was established in terms of the total electronic density, while the above discussion followed an alternative formulation in terms of the spin-resolved density[167] $\rho_\sigma(\mathbf{r}) = \rho_{\mathrm{KS}}(\mathbf{x})$ (spin density) in Eq. 2.2.10. Even more general DFT formulations exist, dealing with time dependent[168] or current densities.[169] However, only the spin-resolved variant is relevant in the context of this thesis and thus, demands further explanation. Without external magnetic field, the exact total density and spin density functional theories[10] always yield the same ground state energy, even for spin-polarized systems.[130] As the total density formulation restricts both spin components of the density to be identical (restricted KS, RKS), it does not provide the correct spin-resolved density for spin polarized systems.[130] Thus, actual spin-restricted KS-DFT approximations yield

[9] As opposed to the nonlocal and non-multiplicative HF exchange potential.

[10] Indeed, in the non-magnetic, non-relativistic, and time independent case the time dependent and current density formulations of DFT yield the same ground state energy as well.

different total energies compared to corresponding spin-unrestricted (UKS) variants.[130] As UKS approximations are formulated in terms of the more flexible variable $\rho(\mathbf{x})$, their ground state energies are likely to be closer to the exact result for spin-polarized systems.[170] Thus, most DFT correlation approximations are specifically constructed as spin resolved density functionals, while the spin scaling relation[171]

$$E_{\mathrm{X}}[\rho_{\uparrow},\rho_{\downarrow}] = \tfrac{1}{2}E_{\mathrm{X}}[\rho_{\uparrow}] + \tfrac{1}{2}E_{\mathrm{X}}[\rho_{\downarrow}] \qquad 2.2.20$$

provides an UKS formulation of the exchange term. Whenever more convenient, the UKS formulation will be used for some expressions in the following sections.

2.2.2. Exchange-Correlation Holes

The exchange and correlation holes are important quantities in density functional theory. Exchange and correlation holes provide useful insights to the properties of the exact XC functional as well as to the behavior of XC approximation with regard to self-interaction and static correlation effects (see Sections 2.2.5 and 2.2.6). Thus, the origin and properties of these quantities will be addressed in the following section.

Approximations to the XC term can be obtained from either an empirical parameter optimization of reasonable functional forms or by considering scaling relations, boundary conditions, and other known properties of the exact E_{XC} functional.[46,47,73,172-176] The XC hole

$$h_{\mathrm{XC}}(\mathbf{x},\mathbf{x}') = h_{\mathrm{X}}(\mathbf{x},\mathbf{x}') + h_{\mathrm{C}}(\mathbf{x},\mathbf{x}') = \theta(\mathbf{x},\mathbf{x}') - \rho(\mathbf{x}') \qquad 2.2.21$$

represents a common starting ground for both, empirical and non-empirical approaches. This quantity derives from the conditional pair density[11]

$$\theta(\mathbf{x},\mathbf{x}') = \frac{n(n-1)}{\rho(\mathbf{x})}\left\langle \Psi_{el} \middle| \delta(\mathbf{x}-\mathbf{x}_1)\delta(\mathbf{x}'-\mathbf{x}_2) \middle| \Psi_{el} \right\rangle . \qquad 2.2.22$$

Thereby, $\theta(\mathbf{x},\mathbf{x}')$ is interpreted as the electron density appearing from the perspective of a single electron, the so-called reference electron.[31] If an electron with spin σ is found at the reference position $\mathbf{r}$, $\theta(\mathbf{x},\mathbf{x}')$ provides the probability for finding another electron of spin σ' at another location $\mathbf{r}'$.[33] In this context the reference electron is described as a particle located at $\mathbf{x}$ so that the pair density is normalized to $n-1$ electrons.[33] These $n-1$ electrons comprise the electron density appearing from the perspective of the reference electron.[33] However, if exchange-correlation effects are neglected, the particle description of the reference electron at $\mathbf{x}$ does not hold any longer. In this case the conditional pair density would equal $\rho(\mathbf{x}')$ and consequently have an unphysical normalization factor of n. The exchange-correlation hole $h_{\mathrm{XC}}(\mathbf{x},\mathbf{x}')$ is introduced as the change of the conditional pair density which arises from non-classical electron-electron interactions.[33] Its further purpose

[11] Noting the analogy between the pair density and the electron density in Eqs. 2.2.1.

is to restore the particle nature[12] of the reference electron at **x** by removing it from the density. Thus the XC hole $h_{\mathrm{XC}}(\mathbf{x},\mathbf{x}')$ is normalized to −1, in accordance with the normalization factors in Eqs. 2.2.1 and 2.2.22.[31,33]

The XC hole is subdivided into exchange (h_{X}) and correlation terms (h_{C}); again to retain the analogy to WFT. While each HF equation treats the residual particles of the system as distributions, the actual electron described by it is considered a particle. Thus, the HF exchange hole

$$h_{\mathrm{X}}^{\mathrm{HF}}(\mathbf{x},\mathbf{x}') = -\frac{\delta_{\sigma\sigma'}}{\rho_\sigma(\mathbf{r})}\left|\sum_a \phi_a^{\sigma*}(\mathbf{r})\phi_a^{\sigma'}(\mathbf{r}')\right|^2 \qquad 2.2.23$$

exhibits already the correct normalization and prevents two electrons with identical spin from being found at the same position (Fermi correlation).[29,31] Due to the nonlocal character of the HF orbitals, the HF exchange hole is delocalized and may extend over many atomic centers.[33,102]

A detailed analysis of Eq. 2.2.23 reveals the following properties

$$\int h_{\mathrm{X}}(\mathbf{x},\mathbf{x}')d\mathbf{x}' = -1 \;, \quad h_{\mathrm{X}}(\mathbf{x},\mathbf{x}') = h_{\mathrm{X}}(\mathbf{r},\mathbf{r}')\delta_{\sigma\sigma'} \le 0 \;, \quad h_{\mathrm{X}}(\mathbf{x},\mathbf{x}) = -\rho(\mathbf{x}) \;, \qquad 2.2.24$$

which are attributed to the KS exchange hole as well. However, compared to the HF exchange hole, h_{X} assumes a less extended shape and is more localized.[33] The correlation hole integrates to zero

$$\int h_{\mathrm{C}}(\mathbf{x},\mathbf{x}')d\mathbf{x}' = 0\,. \qquad 2.2.25$$

This normalization of h_{C} is to be expected as the presence of the electron at **x** arises already from the ansatz of a determinant wave function that leads to the exchange term. The singularity of $\hat{W} = 1/|\mathbf{r}-\mathbf{r}'|$ at $\mathbf{r}=\mathbf{r}'$ causes h_{C} to exhibit distinct cusps whenever two electrons of different spin assume identical positions.[18,31,102] Just as the correlation interaction itself, the correlation hole is localized, apart from exceptions that arise from nonlocal vdW or static correlation interactions. In the latter case, h_{C} is found to be large but mostly independent of the reference point **x** over larger regions that may extend over entire atoms.[177,178] In contrast to that, the hole describing normal, dynamic correlation interactions varies stronger with respect to **x**.[177,178] Compared to the exchange hole which removes an electron from ρ and can assume only negative values, h_{C} rearranges electrons due to their Coulomb repulsion, hence depletes the electron density at **x** and augments it at other locations $\mathbf{x}'$. Thus, both contributions cancel each other partially in the long-range and the extent of the total XC hole is smaller than that of h_{X}. The properties of the XC hole in Eqs. 2.2.24 to 2.2.25, turn it into a useful quantity for the development of approximations to the XC term. Furthermore, the picture of h_{XC} as an incremental density that reduces or modifies $\rho(\mathbf{r})$ will be beneficial in subsequent discussions.

[12] As well as the correct normalization of $\theta(\mathbf{x},\mathbf{x}')$.

2.2.3. Adiabatic Connection

The adiabatic connection formalism provides a continuous link between the KS reference system and the interacting system. This concept is briefly reviewed in the following, mainly because of its importance for the theoretical justification of hybrid DFT methods.

In contrast to $h_{\mathrm{X}}^{\mathrm{HF}}$, the exchange-correlation hole in KS theory is just as unknown as the XC functional itself. This is rationalized by considering the fact that it directly relates to the energy density $\varepsilon_{\mathrm{XC}}(\mathbf{r})$

$$E_{\mathrm{XC}}[\rho] = \int \rho(\mathbf{x}) \cdot \varepsilon_{\mathrm{XC}}[\rho](\mathbf{x})\, d\mathbf{x} = \int \rho(\mathbf{x}) \int \frac{h_{\mathrm{XC}}(\mathbf{x},\mathbf{x}')}{|\mathbf{x}-\mathbf{x}'|}\, d\mathbf{x}'\, d\mathbf{x} \ , \qquad 2.2.26$$

thus to the exact XC energy functional.

The KS reference system is defined to be free of electron-electron interactions so that the XC hole should vanish in this case. However, it is customary to define an XC hole according to the single-determinant description of the KS reference system to restore the normalization of $\theta(\mathbf{x},\mathbf{x}')$ in Eq. 2.2.22, thus the particle picture of a non-interacting reference electron (see Section 2.2.2).[31,33,131,152,179-181] The resulting hole $h_{\mathrm{XC}}^{\lambda=0}$ in the so-called KS exchange only limit has the same form as $h_{\mathrm{X}}^{\mathrm{HF}}$ in Eq. 2.2.23 and differs from it just by its definition in terms of the KS orbitals $\{\psi_a^\sigma\}$ instead of the HF orbitals.[31,33]

The adiabatic connection relates $h_{\mathrm{XC}}^{\lambda=0}$ to the real XC hole of the interacting system.[31,33,131,152,179-181] Thereby, a coupling parameter λ is defined on the interval between 0 and 1, which controls the strength of the electron-electron interaction $\hat{W}$. The resulting λ-dependent many-body Hamiltonian writes as

$$\hat{H}_{el}^{\lambda} = \sum_a \left(-\tfrac{1}{2}\nabla_a^2 + V^{\lambda}(\mathbf{r}_a) + \lambda \cdot \sum_{b>a} \hat{W}(\mathbf{r}_a,\mathbf{r}_b) \right) \qquad 2.2.27$$

with the limiting cases $V^0 = V_{\mathrm{KS}}$ and $V^1 = V_{\mathrm{ext}}$. Furthermore, a λ-dependent XC hole $h_{\mathrm{XC}}^{\lambda}$ can be defined which retains the ground state density for every value of λ in the interval between 0 and 1. The exact XC hole of the interacting system emerges then as the following coupling-strength average[31,33,131]

$$h_{\mathrm{XC}}(\mathbf{x},\mathbf{x}') = \int_0^1 h_{\mathrm{XC}}^{\lambda}(\mathbf{x},\mathbf{x}')\, d\lambda = \int_0^1 \theta^{\lambda}(\mathbf{x},\mathbf{x}')\, d\lambda - \rho(\mathbf{x}') \qquad 2.2.28$$

with a correspondingly defined λ-dependent conditional pair density $\theta^{\lambda}(\mathbf{x},\mathbf{x}')$. Like the XC hole itself, the concept of adiabatic connection is utterly important for the theoretically driven development and analysis of KS-DFT approximations. This is especially true for hybrid DFT methods (Section 2.3).

2.2.4. Local and Semi-Local Density Functional Approximations

While hybrid DFT methods are one of the central topics of the present thesis, these approximations are also compared to several semi-local XC functionals in the applications presented in Sections 4.3 and 4.4. Furthermore, the behavior of hybrid functionals with regard to self-interaction and static correlation effects (see Sections 2.2.5 and 2.2.6) is best understood when considered together with that of semi-local DFT methods. Thus, the following section provides a general discussion of local and semi-local DFT methods.

The exact h_{XC} and E_{XC} represent rather complicated quantities as they comprise a full description of many-body effects. However, significant progress can be made with comparatively simple approximations to them. Indeed, the most basic DFT approximation to E_{X}, hence the Dirac exchange functional and the exchange term resulting from the HFS approximation to the exchange potential, existed already before KS-DFT.[150,152] Both exchange functionals are examples of local density approximations (LDA), hence are local in terms of the electron density. The corresponding exchange potential

$$V_{\mathrm{X}}^{\mathrm{X}\alpha/\mathrm{LDA}}(\mathbf{r}) = -\frac{3}{2}\alpha\left(\frac{3}{\pi}\rho(\mathbf{r})^{1/3}\right) \qquad 2.2.29$$

has the same form for both, the Dirac exchange functional and the exchange term of the HFS model.[28,150,152,182] For the potential of the Dirac exchange functional a value of $\alpha = 2/3$ results, while $\alpha = 1$ is obtained when approximating V_{X} directly by the corresponding expression of the HEG model as in the HFS method. These different prefactors gave rise to more empirical choices of α (Xα method, e.g. $\alpha \approx 0.75$) in the early days of KS-DFT.[37,38,183,184] Despite of being rather old, the idea of a modified α-parameter saw a recent revival in form of the OPTX-type GGA and hybrid GGA functionals.[128] Such methods include a scaled LDA exchange term to improve the implicit description of static correlation (see Section 2.2.6).[128] OPBE and O3LYP are the most common OPTX functionals.[185]

LDA approximations to the correlation term existed before the formulation of KS-DFT too.[186-190] These correlation functionals were later refined by means of the random phase approximation as well as by quantum Monte Carlo simulations.[172-175] The nowadays most widely used LDA correlation approximations are known as VWN[191] and PWLDA.[192] LDA approximations to the XC term often exceed HF and sometimes also MP2 with regard to their accuracy, especially in the case of transition metals.[34] This performance is rationalized by the rather slowly varying density in solid state systems as well as by the behavior of the spherically symmetric and very localized LDA exchange hole

$$h_{\mathrm{X}}^{\mathrm{LDA}}(\mathbf{r},\mathbf{r}') \propto -1\Big/\left(\rho(\mathbf{r})^{1/3}\,|\mathbf{r}-\mathbf{r}'|^4\right) \quad \text{for} \quad |\mathbf{r}-\mathbf{r}'| \to \infty \qquad 2.2.30$$

in molecular systems.[152,193] While $h_{\mathrm{X}}^{\mathrm{LDA}}$ and the exact h_{X} differ considerably, the spherically averaged forms of both holes agree well.[193] As the radial behavior is most important for exchange holes, this agreement rationalizes the accuracy of LDA for molecular systems.[193]

Despite the good performance of LDA, its absolute value of the exchange energy deviates often by about 10% from the HF result, which may lead to errors in some cases as E_X is considerably larger than E_C in most cases.[2,5-7] These problems can be partially resolved by extending LDA to a spin-unrestricted formalism (LSDA).[28] Nevertheless, significant effort was put forward to improve the exchange density functional beyond the LDA level. Such improvements can consist in averaged, nonlocal functionals.[193,194] However, an expansion of E_{XC} in terms of spatial derivatives of the local density, hence of the dimensionless reduced density gradient $s_1 = |\nabla\rho(\mathbf{r})|/[(24\pi^2)^{1/3}\rho(\mathbf{r})^{4/3}]$ and its higher order analogues, represents a far more viable and popular alternative.[28,195-197] The functionals resulting from this approach are denoted as semi-local DFT approximations as they partially address the nonlocal character the XC term while still retaining a mathematically local XC functional.[45] While such an approach is certainly promising, the exact polynomial expansion of the exact exchange hole in terms of s_1 exhibits a divergent behavior for large values of this variable.[195] Therefore, so-called "generalized gradient approximations" (GGA) were introduced, which modify the exact gradient expansion, mostly for large gradients $s_1 > 3$, and exhibit the following general form[45]

$$\begin{aligned} E_X^{GGA}[\rho] &= \int \rho(\mathbf{r})\, \varepsilon_X^{GGA}(\rho(\mathbf{r}), s_1(\mathbf{r}), \dots)\, d\mathbf{r} \\ &= \int \rho(\mathbf{r})\, \varepsilon_X^{LDA}(\rho(\mathbf{r}))\, F_X^{GGA}(\rho(\mathbf{r}), s_1(\mathbf{r}), \dots)\, d\mathbf{r}\ . \end{aligned} \qquad 2.2.31$$

The choice of the gradient exchange enhancement factor F_X^{GGA} adds some degree of empiricism to KS-DFT. In consequence, many GGA variants have been proposed.[46-50] Nevertheless, the enhancement factors of all GGA methods are always larger than one, which yields more negative exchange energies compared to LDA.[31] The reduced density gradient s_1 and thus also the absolute values of F_X^{GGA} and E_X are reduced upon formation of chemical bonds.[198] In consequence, GGA functionals tend to lower reaction energies, which often reduces the overbinding tendency of LDA.[31,198] The most common GGA variants are the B88[46] exchange term and the LYP[47] correlation functional as well as the XC formulations PW91[192] and PBE.[49] Novel, non-separable gradient approximations (NGA) have recently been proposed.[176] These functionals exhibit dependencies on ρ and s_1 as well but, opposed to the canonical separation in Eq. 2.2.14, are formulated as a combined XC term.[176]

When pursuing the argumentation, that led from LDA to GGA methods, one step further, one arrives at XC functionals that also include the Laplacian of the electron density. Indeed, the usage of Laplacian dependent exchange terms has been reported to improve over functional forms purely dependent on the electron density gradient.[199] However, functionals that include higher order density derivatives may tend to a more erratic behavior when integrated numerically.[200,201] The electronic kinetic energy density (KED)[72,80,202,203]

$$\tau(\mathbf{r}) = \sum_\sigma \tau(\mathbf{x}) = \tfrac{1}{2}\sum_\sigma \sum_a \left|\nabla \psi_a(\mathbf{x})\right|^2\ , \qquad 2.2.32$$

is more stable in this regard. As one of the second-order derivative terms of the electron density it includes similar information as the Laplacian of ρ.[72,80,202,203] Despite of being orbital-dependent, τ is well justified by the HK formalism as a density functional variable as the value of each KS orbital at **x** represents a density functional too. The optimized effective potential (OEP, see Section 2.3.2) method allows one to compute $\partial E_{\mathrm{XC}}/\partial\rho$ for orbital-dependent XC functionals, thus to perform self-consistent calculations within the KS-formalism.[204-206] However, this approach introduces very high computational costs, but changes energies only slightly; it is mostly popular for properties like NMR shielding constants.[206,207] The generalized Kohn–Sham formalism (GKS, see Section 2.3.2) provides an alternative justification for orbital-dependent XC approximations.[208] Within the GKS formalism the XC potential can be computed in terms of functional derivatives with respect to the orbitals (FDO) only.[208]

The KED exhibits several additional beneficial properties that go beyond what is provided by derivatives of the density.[202] First, the KS orbitals are solutions of the nonlocal KS equations and thus, represent nonlocal density functionals themselves. This nonlocal character is included in τ as well, although only in an intrinsic fashion and not directly accessible for the construction of XC approximations. Nevertheless, the nonlocal information included in τ has been shown to provide, to some extent, a description of nonlocal properties (see Section 2.2.7).[77] Second, the HEG limit of τ,

$$\lim_{\rho\to\rho^{\mathrm{HEG}}}\left\{\tau(\mathbf{r})\right\}=\tau_{\mathrm{HEG}}(\mathbf{r})=\frac{3}{10}(3\pi^2)^{2/3}\left(\rho(\mathbf{r})\right)^{5/3}\ , \qquad 2.2.33$$

allows detecting spatial regions where the density approaches a HEG-like behavior.[209] By exploiting Eq. 2.2.33 the XC energy density $\varepsilon_{\mathrm{XC}}$ can be constructed to reduce to the corresponding LDA form in these regions.[209,210] In this way, the violation of the HEG limit can be avoided, thus eliminating a source of error in XC approximations.[198,209,210] Furthermore, spatial regions which are dominated by a single KS spin orbital (thus individual electrons), so-called one-electron regions[79] (OER, see Section 2.2.5), can be identified by comparing the KED with the von Weizsäcker kinetic energy density τ_{W},

$$\lim_{\rho\to\psi_a}\left\{\tau(\mathbf{x})\right\}=\tau_{\mathrm{W}}(\mathbf{x})=\frac{1}{8}\frac{|\nabla\rho(\mathbf{x})|^2}{\rho(\mathbf{x})}\ . \qquad 2.2.34$$

As discussed in the next section, OERs are often responsible for the self-interaction error. It is therefore beneficial to identify locally OERs and to adapt $\varepsilon_{\mathrm{XC}}$ to such situations.[72,74]

Functionals which depend on τ (besides depending on ρ and s_1) are referred to as meta-generalized gradient approximations (MGGA).[71,211] As expected from the aforementioned properties of the KED, MGGA functionals provide improvements over GGA methods although the additional gain in accuracy is usually not as large as when going from LDA to GGA.[77,212,213] The functionals TPSS[75,76,212] and M06L[77] are the most common MGGA methods; they are based on the earlier MGGA variants PKZB[74] and VSXC,[73] respectively.

2.2.5. Self-Interaction Error

The self-interaction error (SIE) is the most common artifact arising to some extent in all current approximations to KS-DFT. This error and its consequences will be first explained on the examples of single-electron systems and one-electron regions (OER). In the following the many-electron self-interaction or delocalization error will be discussed. Although this latter artifact has been recognized long time ago, the detailed study of its effects and implications has begun only recently. In consequence the available literature on this topic is somewhat sparse and ambiguous with regard to some details. While occasionally referring to the results and explanations of Mori-Sánchez–Cohen–Yang,[101,120,214-217] the subsequent presentation mainly follows the work of Perdew *et al.*[130,158,218-220] and employs the concept of fractional electron numbers (FEN) for many explanations.

Despite the remarkable success of LDA, GGA, and MGGA KS-DFT methods one has to consider that these methods are still far from being close to the exact XC functional. Indeed, the local form of these methods represents the most striking difference to the exact XC term. The implications of this difference become apparent when one considers the very simple example of a system that includes a single electron only.[13] Within such a system all electron-electron interactions terms are supposed to vanish due to the lack of interaction partners. Within HF theory this is always accomplished as the exchange and Coulomb terms cancel in the case of a single occupied spin-orbital. Retaining the analogy of the exchange interaction between HF and KS-DFT, the exact functional $E_{\mathrm{X}}[\rho]$ should behave likewise. This implies

$$E_{\mathrm{X}}[\rho] = -E_{\mathrm{Coul}}[\rho] = -\int\int \frac{\rho(\mathbf{r})\rho(\mathbf{r}')}{|\mathbf{r}-\mathbf{r}'|}\, d\mathbf{r}'\, d\mathbf{r} \qquad 2.2.35$$

for all densities that originate from a single occupied KS orbital, $\rho(\mathbf{r}) = |\psi_1(\mathbf{r})|^2$. As visible for example from Eq. 2.1.13 the correlation term in post-HF theories vanishes by a similar cancellation mechanism. Therefore,

$$E_{\mathrm{C}}[\rho] = 0 \qquad 2.2.36$$

must hold for single electron densities as well.

Thus, Eq. 2.2.35 clearly reflects the nonlocal character of the exact KS-DFT exchange. However, for arbitrary single-electron densities local (LDA) or semi-local (GGA, MGGA) exchange approximations can never completely cancel with the Coulomb term.[101,214,215,217,218,220] In single-electron systems the latter term is generally found to prevail over the exchange energy provided by local and semi-local exchange approximations.[101] This excessive Coulomb interaction leads to an unphysical, residual self-repulsion, which is known as the self-interaction error.[101]

[13] The hydrogen atom and the H_2^+ ion are thereby the most prominent examples and the most frequently studied model systems in this context.

The occurrence of self-interaction artifacts as introduced by the local ansatz for the XC energy density represents a significant limitation already for one-electron systems alone. However, the SIE is not limited to one-electron densities. Indeed, this artifact becomes notable also in the aforementioned one-electron regions (OER) of many-electron systems. Within an OER, a single electron can be found for each spin value at most. This electron interacts with the electrons outside of the OER as well as with its eventual counterpart of opposite spin via the Coulomb and correlation terms. As depicted in Figure 2.2.2, the interactions between parallel spin components of the density are subject to analogous conditions as in Eqs. 2.2.35 and 2.2.36.

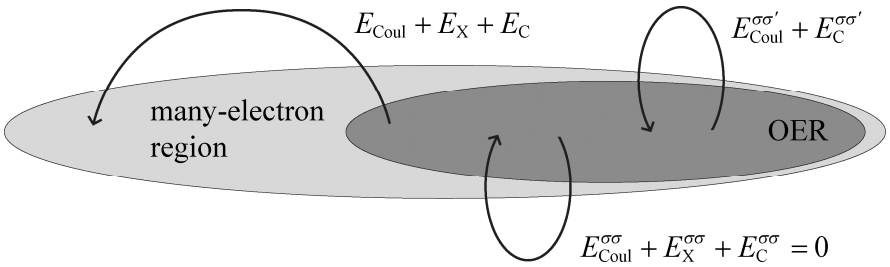

Figure 2.2.2: Sketch of the electron-electron interactions within one-electron regions as well as between one-electron regions and other many-electron regions of the system.

Knowledge about OERs within a chemical system is thus helpful to construct KS-DFT approximations with reduced self-interaction. As stated by the HK1 theorem, the information about single-electron regions is included in the electron density. While this information is contained in the ρ in an implicit and hardly accessible way, the comparison of the density with quantities relating from the KS orbitals as in Eq. 2.2.34 provides a relatively straight-forward approach to identify a local OER. Indeed, most MGGA functionals employ Eq. 2.2.34 to remove locally the correlation energy density as in Eq. 2.2.36. The residual self-repulsion due to the violation of the condition for the exchange term, Eq. 2.2.35, remains, however, as a nonlocal exchange term is needed to correct it.

The PZ self-interaction correction represents a similar approach, which, in contrast to the local correlation corrections provided by MGGA functionals, aims to remove the SIE at the level of the XC and Coulomb energy terms.[59] This method introduces an additional term which individually subtracts the self-repulsion from the XC part for each occupied KS orbital

$$E_{\mathrm{XC}}^{\mathrm{PZ}}[\rho,\{\psi_a^\sigma\}] = E_{\mathrm{XC}}[\rho] - \sum_{b\sigma}\left(E_{\mathrm{Coul}}[|\psi_b^\sigma|^2] + E_{\mathrm{XC}}[|\psi_b^\sigma|^2]\right) . \qquad 2.2.37$$

While the PZ correction is not restricted to specific types of XC functionals, it introduces an explicit dependency on the KS orbitals, similar to that of MGGA methods. This approach is

less popular nowadays as it does not always lead to consistent improvements due to its missing invariance with respect to unitary transformations of the KS orbitals.[58,221]

One-electron regions of many-electron systems are usually found distant from the atomic nuclei, where the exact XC potential behaves as

$$V_{\mathrm{XC}}(\mathbf{r}) = -1/|\mathbf{r}| \quad \text{for} \quad |\mathbf{r}| \to \infty \tag{2.2.38}$$

for electrically neutral, finite systems. In contrast, approximated local and semi-local XC potentials decay exponentially at large distances.[33] This behavior originates from the exponential decay of the density in this limit.[33] The incorrect form of the XC potentials of LDA, GGA, and MGGA functionals has a significant effect on the $\{\varepsilon_a^{\mathrm{KS}}\}$ values. The eigenvalues of KS orbitals partially located in OERs are thereby most affected and raised in energy due to the remaining self-repulsion.[29] Furthermore, the XC potential

$$V_{\mathrm{XC}}(\mathbf{x}) = \varepsilon_{\mathrm{XC}}[\rho](\mathbf{x}) + \rho(\mathbf{x})\frac{\delta\varepsilon_{\mathrm{XC}}[\rho](\mathbf{x})}{\delta\rho(\mathbf{x})} \tag{2.2.39}$$

and thus also the eigenvalues of the KS orbitals are subject to a discontinuous shift at integer values of n or at band gaps in the case of extended systems.[5] The second term on the right-hand side of Eq. 2.2.39 represents the response potential and describes the changes in the XC hole due to variations of the density.[222] For non-metallic systems this term causes the aforementioned discontinuity of V_{XC} whenever a new KS orbital starts to become occupied. This sudden potential change leads then to the corresponding shift of all KS eigenvalues $\{\varepsilon_a^{\mathrm{KS}}\}$.[223-225] Thereby, the derivative discontinuity adjusts the eigenvalue of the highest occupied orbital to the ionization energy of the system.[158,159]

It might appear odd that an infinitesimally small addition of electronic charge to a single KS orbital changes the eigenvalues within the entire system, which may eventually be very extended. Nevertheless, this behavior can be rationalized when considering that the KS reference system and its orbitals do not have to represent physical quantities. Furthermore, as KS-DFT uses an orbital-dependent kinetic energy term, the derivative of the formal functional $T_{\mathrm{S}}[\rho]$ must exhibit discontinuities as well.[5] An analogous argumentation reveals such a behavior also for the effective KS potential.[5] As all terms of the KS potential, Eq. 2.2.18, except for V_{XC} are explicitly known density functionals, only the XC potential can adjust the discontinuous behavior of V_{KS}.[5] Despite of eventual dependencies on the KS orbitals, the behavior of local and semi-local approximations to KS-DFT is still largely governed by the electron density. Therefore, LDA, GGA, and MGGA functionals are generally unable to reproduce properly the discontinuity of the KS potential.[5]

In self-consistent applications of local KS-DFT approximations, the system at hand always tends to lower the destabilizing self-repulsion to some extent. This relaxation can lead to overly delocalized KS orbitals. This delocalization as well as the incorrect behavior of the aforementioned eigenvalue shifts due to the SIE can significantly affect the description of chemical bonds, ionic compounds, and of many electronic properties.[14] Bonding energies are thereby often overestimated, while anionic species can become destabilized.[101,214,215,217,226]

Aside from the well understood self-repulsion artifacts in one-electron situations, self-interaction can affect many-electron regions as well.[214,218] The many-electron self-interaction error[214] (MSIE) recently gained significant attention and was recognized on the examples of improperly charged dissociation fragments,[218,220] spurious maxima in the dissociation curves of small molecules,[220] and an incorrect behavior of the bond lengths in conjugated π-systems.[216,227] These failures were found to be related self-interaction effects as most other sources of errors could be excluded as cause.[214] However, methods like HF or the PZ correction which do not exhibit single-electron self-interaction are unable to provide the correct solutions in these cases as well.[214,220,228] Even functionals like B05[229] or MCY,[230] which remain unchanged by the PZ correction, are affected by the MSIE.[214] While MSIE-free XC approximations are not yet entirely explored,[120] the considerations made in this context provide a generalized perspective on the self-interaction phenomenon itself. As will be discussed in Section 2.2.6 the MSIE of local and semi-local XC approximations is closely connected to their implicit description of static correlation. After this relation was recognized, the term "delocalization error" was put forward by Mori-Sánchez *et al.* to describe both, the MSIE and the implicit description of static correlation.[101,215-217] However, this term will be less frequently used in the following, as both aspects are mostly considered separately in the present discussion.

As mentioned above, the exact XC potential exhibits a discontinuous behavior at integer occupation numbers of the KS orbitals.[158,219] This phenomenon is generalized by the concept of fluctuating electron numbers (FEN), where an open subsystem S is introduced which is well separated from a distant electron reservoir R that comprises the rest of the system.[130,158,219] While S and R are separated, the KS orbitals can still extend over both subsystems.[130,158,219] In consequence, electrons may fluctuate between R and S which in turn leads to fractional electron numbers in the latter.[130,158,219] Nevertheless, the contribution E_{el}^{S} of the subsystem S to the total electronic energy, is well defined for fully separated subsystems S and R.[130,158,219] Although the complete system S+R is still covered by standard KS-DFT, an extension of the formalism to density ensembles[29,231] is necessary to describe

[14] Although not relevant for the present discussion, it is worth mentioning that quantities like electron excitation energies and Rydberg states are even more affected by the SIE. This essentially limits local DFT methods to calculations of ground state properties, even if a proper time-dependent formalism would be employed.

correctly the isolated subsystem *S*.[219,232] Such an ensemble is represented by a generalization of the density matrix operator in Eq. 2.1.9[126]

$$\hat{\rho} = \sum_n \sum_i e_{ni} \left|\Psi_{ni}\right\rangle \left\langle\Psi_{ni}\right| \ , \qquad 2.2.40$$

to include projectors onto different states $\left|\Psi_{ni}\right\rangle$ which can exhibit different numbers of electrons *n*. In finite-temperature grand-canonical-ensemble theory the probabilities $\{e_{ni}\}$ of the ensemble elements optimize the grand potential

$$\begin{aligned} \Omega[\{e_{ni}\},\{\Psi_{ni}\}] &= \mathrm{Tr}\left\{\hat{\rho}\left(k_\mathrm{B}\theta \cdot \ln(\hat{\rho}) + \hat{H}^{\mathrm{KS}} + \mu \cdot \hat{n}\right)\right\} \\ &= \sum_n \sum_i e_{ni}\left(k_\mathrm{B}\theta \cdot \ln(e_{ni}) + \left\langle\Psi_{ni}\right|\hat{H}^{\mathrm{KS}}\left|\Psi_{ni}\right\rangle + \mu \cdot n\right) , \end{aligned} \qquad 2.2.41$$

with the Boltzmann constant k_B, the temperature θ, the chemical potential μ, and the electron number operator $\hat{n}$. Eq. 2.2.41 accounts for the contributions of different orthogonal eigenfunctions of $\hat{H}^{\mathrm{KS}}$ as well as for a varying electron number of electrons *n*. In contrast to this usual application of ensemble DFT, the FEN model employs density ensembles only for the purpose of representing the electronic structure of the subsystem *S*. In this context the probabilities $\{e_{ni}\}$ are defined by the ground state of the system *S*+*R* and do not lead to stationary points of the grand potential in Eq. 2.2.41. The FEN formalism provides a unified approach for non-integer total electron counts as well as for fractional occupation numbers of the KS orbitals.[233] The latter concept is also widely applied in form of the fractional occupation number technique (FON).[234-237]

The exact total energy $E_{el}^S(n)$ of an open subsystem *S* must behave as a linear function in terms of the electron count between integer values of *N*.[158] This behavior is known as the linearity theorem[158] and is closely connected to the Janak theorem[233]

$$\frac{\partial E_{el}^S(f_a^\sigma)}{\partial f_a^\sigma} = \varepsilon_a^{\sigma\mathrm{KS}} \ , \qquad 2.2.42$$

which states a similar behavior for E_{el}^S in terms of individual orbital occupation numbers $\{f_a\}$. Both, the linearity theorem and the Janak theorem extend and quantify the aforementioned discontinuous behavior of the KS potential. Furthermore, these theorems allow one to compare the behavior of the exact KS-DFT with that of DFT approximations, especially with regard to the self-interaction error.

Fractional occupation numbers of KS orbitals and fractional electron counts of isolated subsystems occur only in specific cases like transition metals treated with the FON technique or ionic dissociation fragments (see above), respectively. However, the fact that the linearity theorem is formulated in terms of an open subsystem does not imply that its violation affects only such model systems. As will be discussed in the following, convex and concave deviations from the linearity theorem reflect tendencies for localization or delocalization of KS orbitals, respectively. Thus, any violations of the linearity theorem are likely to affect the general description of chemical bonds in systems with integer occupation numbers as well. In

this context the FEN model can be considered as a formal approach to examine the many-electron self-interaction and delocalization errors isolated from other interactions.

Figure 2.2.3 provides a graphical representation of the exact total electronic energy $E_{el}^{S}(n)$ and of the eigenvalue of the highest occupied KS orbital $\varepsilon_{\mathrm{HOMO}}^{\mathrm{GKS}}(n)$ between integer values of the number of electrons in *S*. This comparison can even be extended to the HF method, which qualifies as a density functional within the generalized Kohn–Sham formalism (GKS, see Section 2.3.2).[208] Note that in this context both, local DFT and HF, are assumed to provide exact total energies at integer electron counts.

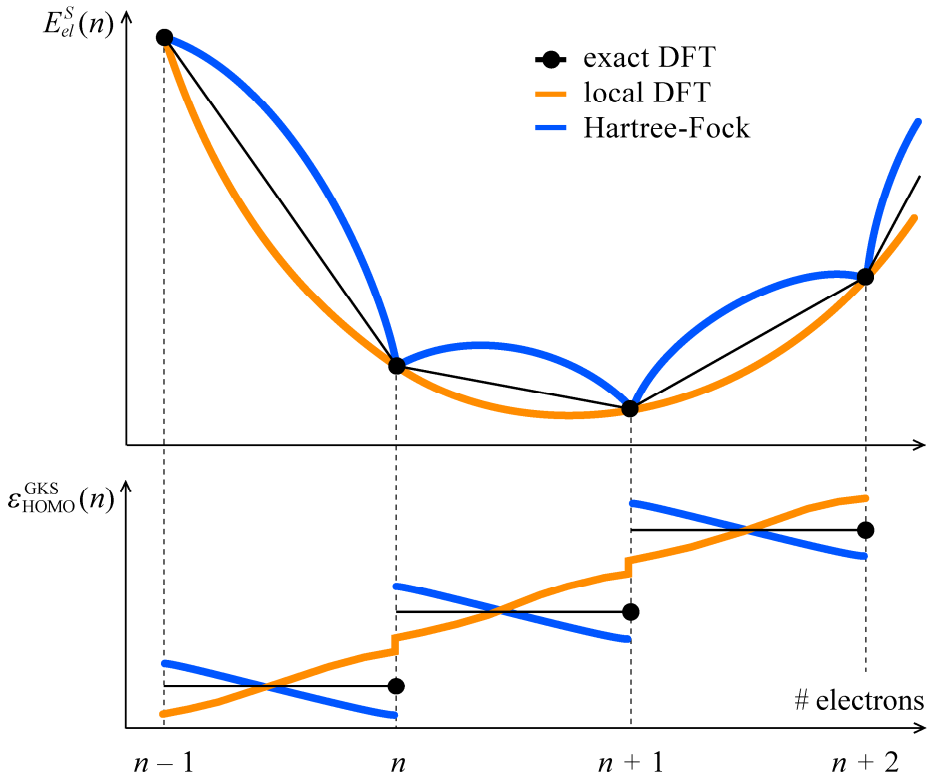

Figure 2.2.3: Qualitative comparison between exact DFT, local DFT, and HF results for the total electronic energy $E_{el}^{S}(n)$ and the eigenvalue $\varepsilon_{\mathrm{HOMO}}^{\mathrm{GKS}}(n)$ of the highest molecular orbital with varying electron count under the assumption that all methods yield the correct $E_{el}^{S}(n)$ values at integer *n*. Figure adapted from Ref. [219].

Figure 2.2.3 shows that, compared to the exact $E_{el}^{S}(n)$ function, local and semi-local DFT methods yield more negative total electronic energies between integer values of *n*.[101,214,215,217-220,238] This deviation from the exact energy $E_{el}^{S}(n)$ agrees with the aforementioned tendency of LDA, GGA, and MGGA for an overly large electronic delocalization due to self-repulsion. Accordingly, these functionals also underestimate the discontinuous shift of the eigenvalue $\varepsilon_{\mathrm{HOMO}}^{\mathrm{GKS}}(n)$ and thus the HOMO-LUMO gap (HLG) or band gap of the system. The convex behavior of local DFT methods can be rationalized with

the normalization of the XC hole in the fictitious KS exchange only limit.[219] The exchange hole has the same form as $h_{\mathrm{X}}^{\mathrm{HF}}$ in Eq. 2.2.23 (see Section 2.2.2), as the KS system is described by a single Slater-determinant.[181] For fractional occupation numbers f_a^σ the KS exchange hole integrates[59,219] to

$$\int h_{\mathrm{XC}}^{\lambda=0}(\mathbf{x},\mathbf{x}')d\mathbf{x}' = -1 + \sum_{a\sigma} f_a^\sigma (f_a^\sigma - 1)\frac{\left|\psi_a^\sigma(\mathbf{r})\right|^2}{\rho_\sigma(\mathbf{r})}. \qquad 2.2.43$$

As the exchange hole partially resides in *R*, this integral differs from the expected value of –1 unless all KS spin-orbitals exhibit integer occupations.[219] The normalization of the exact XC hole behaves likewise.[239] However, the actual LDA exchange hole, Eq. 2.2.30, is more localized than $h_{\mathrm{XC}}^{\lambda=0}$ and h_{X}.[178,219] Thus, the exchange hole obtained with LDA remains entirely located in *S* and still normalized to –1.[178] In consequence, this hole yields a higher exchange energy density than the exact hole.[219] As a result also the corresponding exchange energy will be more negative than in the exact case.[219] As nearly all semi-local DFT approximations are based upon LDA exchange, such methods tend to favor fractional electron counts as well.[49,75,219]

The behavior of $E_{el}^S(n)$ found in the case of the Hartree–Fock method contrasts with that of local DFT approximations. Compared to the exact results, HF yields less negative total electronic energies for the subsystem *S* at non-integer electron counts. Furthermore, the discontinuous shift of the frontier orbital eigenvalue $\varepsilon_{\mathrm{HOMO}}^{\mathrm{GKS}}(n)$ is overestimated at integer values of *n*, which causes the HF method to overestimate the HLG.[101,215,217,219] HF delivers a concave shaped function $E_{el}^S(n)$ which can be interpreted as a tendency for an overly large orbital localization (Figure 2.2.3). In the case of HF the higher $E_{el}^S(n)$ values at non-integer electron counts can be rationalized by considering that the open subsystem *S* is described by an ensemble of states.[219] Recall, that the probabilities $\{e_{ni}\}$ for the ensemble elements in Eq. 2.2.40 are determined to represent the electronic structure of the subsystem *S* within the whole system *S*+*R* but not by a minimization of the grand potential of *S*.[219] In consequence, $E_{el}^S(n)$ will be lower at integer electron counts where the corresponding electronic structures can be described by pure states.[219]

Following the argumentation discussed above, DFT approximations are only considered free of the MSIE when they are able to provide the correct linear variation of the total electronic energy between integer electron counts for arbitrary systems.[101,215,217,230]

2.2.6. Static Correlation Error

Static correlation effects were defined in Section 2.1.2 as large reorganizations in the electronic structure. These rearrangements arise from interactions between the HF ground state and one or more other single-determinant states nearly degenerate to it. In contrast to multi-reference approaches, KS-DFT relies on a purely single-determinant description of the non-interacting reference system.[28] This situation leads to the question whether static correlation can be reliably captured within the KS formalism.[130] Furthermore, the model of fractional spins[215,217] will be discussed in this section, which allows one to examine the description of static correlation by different methods isolated from self-interaction effects.

While KS-DFT is based on a single-determinant description, physically meaningful densities exist which are not *V*-representable within the KS system in terms of a pure, single-determinant state.[143,144,240-242] Such a missing *V*-representability indicates a strong influence of static correlation effects. It is nevertheless always possible to restore this representability in terms of the ensemble DFT approach (see Eqs. 2.2.40 and 2.2.41). In this context it is not surprising, that FON techniques can be used to describe static correlation effects.[243]

HF and even low level post-HF methods (see Section 2.1.2) can exhibit an erratic behavior for systems dominated by static correlation interactions.[133] Opposed to that, local and semi-local KS-DFT approximations are often found to provide a reasonable accuracy, despite the fact that they are based on a single-determinant approach.[129,177] This accuracy is especially pronounced for transition metal compounds whose exact ground state wave functions include many nearly degenerate single-determinant terms.[129,177] However, for systems like radicals or atoms severe failures are known semi-local DFT approximations.[31,240,244] In such cases broken symmetry treatments may yield more reliable results.[31,240,244]

Nevertheless, the reasonable description of transition metals provided by local and semi-local KS-DFT approximations strongly indicates that these methods are, to some extent, able to account implicitly for static correlation.[129,177] This description of static correlation was traced back to the LDA exchange functional.[129,177] As GGA and MGGA exchange functionals always include an LDA exchange energy density factor, these methods behave likewise.[129,177] Nevertheless, the description of static correlation is most pronounced in LDA.[129,177]

The finding that LDA can account for static correlation effects is again rationalized by referring to its exchange hole.[129,177] Recall that static correlation locates electrons to different regions in space (see Section 2.1.2) and thus, suppresses electron fluctuations between these locations.[130] In theories like HF where this suppression is missing, the exchange hole h_X^{HF}, Eq. 2.2.23, tends to be overly delocalized.[129,130,177] As the KS XC hole in the exchange only limit

$$h_{\mathrm{XC}}^{\lambda=0}(\mathbf{x},\mathbf{x}') = -\frac{\delta_{\sigma\sigma'}}{\rho_\sigma(\mathbf{r})}\left|\sum_a \psi_a^{\sigma*}(\mathbf{r})\ \psi_a^{\sigma'}(\mathbf{r}')\right|^2, \qquad 2.2.44$$

has the same form as $h_{\mathrm{X}}^{\mathrm{HF}}$, it is delocalized as well.[31,33] While the exact exchange hole h_{X} is delocalized to a similar extent as $h_{\mathrm{X}}^{\mathrm{HF}}$, the total exact XC hole is more compact (see Section 2.2.2).[31,33,129,130,177] This implies a partial cancellation between the long-range parts of h_{X} and h_{C}.[130] Such a cancellation can often only be provided from the static correlation part of h_{C}, as dynamic correlation is a mostly small and very localized effect.[129,130,177]

While the static correlation hole and h_{X} cancel, the LDA exchange hole is already far more compact than $h_{\mathrm{XC}}^{\lambda=0}$ or $h_{\mathrm{X}}^{\mathrm{HF}}$.[178] With LDA correlation being an even more local functional, the total LDA hole $h_{\mathrm{XC}}^{\mathrm{LDA}}$ appears more similar to the exact h_{XC} than $h_{\mathrm{XC}}^{\lambda=0}$ or $h_{\mathrm{X}}^{\mathrm{HF}}$.[129,177] Thus, the overly compact LDA exchange hole can mimic the long-range cancellation between the exact h_{X} and h_{C} holes which occurs in the presence of static correlation effects.[129,177] In exchange approximations that admit the density gradient and/or the kinetic energy density as variables, the corresponding hole becomes somewhat more delocalized compared to the pure LDA case.[178] Compared to LDA the implicit static correlation description can therefore be slightly reduced in GGA and MGGA methods.[178]

The above rationalization also depicts the intrinsic connection between the description of static correlation provided by local DFT methods and the many-electron self-interaction error.[58,129,177] Most corrections for the latter tend to bring the exchange hole of local and semi-local KS-DFT approximations closer to the exact h_{X}, thus to delocalize it in most situations.[58,129,177] This delocalization of the XC hole effectively reduces its capability to mimic static correlation effects.[58,129,177] Indeed, the OPTX-type functionals (see Section 2.2.4) exhibit an increased prefactor of the LDA exchange term to address this problem in parts.[128,185] However, any modification of this numerically largest term of the XC functional is likely to affect the quality of the electronic structure in cases where static correlation is less important. Thus, without a correlation functional E_{C} that can properly account for static correlation, any attempt to reduce the SIE and the delocalization error in local and semi-local functionals will inevitably result in a deteriorated description of static correlation, thus in the so-called static correlation error (SCE).[130,215,217,245,246]

Just as in the case of fractional electron numbers (see Section 2.2.5), special model systems can be defined which allow one to examine specifically the static correlation error.[177] An example for such a static correlation effect, which is not influenced by any self-interaction artifacts, is provided by the fractional spin model.[101,215,217] This model considers a single electron which is distributed over two KS spin orbitals, $\psi_\uparrow$ and $\psi_\downarrow$.[101,215,217] Both orbitals have opposite spin components but the same spatial form.[101,215,217] The spatial component of these orbitals is defined to remain constant and may be even infinitely extended to exclude any eventual self-interaction artifacts.[101,215,217]

Figure 2.2.4 provides a sketch of the behavior of the total energy $E^F(f_\uparrow, f_\downarrow)$ of the fractional spin model system in terms of the occupation numbers of both orbitals, $f_\uparrow$ and $f_\downarrow$.[101,215,217] As neither the spatial components of $\psi_\uparrow$ and $\psi_\downarrow$ nor the total number of electrons can change, the total electron density $\rho(\mathbf{r})$ remains constant. Thus, by virtue of the HK1 theorem (Section 2.2.1), also the exact total energy is constant for any spin value between –1 and +1. This implies the states of the KS reference system to be degenerate for all spin values in this range.[15] However, all commonly employed local KS-DFT approximations are unable to reproduce this degeneracy and yield a higher energy for states with fractional spins.[101,215,217] In the case of LDA this failure can be rationalized by pointing to the fact that

$$E_X^{LDA}[\rho_\uparrow, \rho_\downarrow] \propto \int \left(\rho_\uparrow(\mathbf{r})\right)^{3/4} d\mathbf{r} + \int \left(\rho_\downarrow(\mathbf{r})\right)^{3/4} d\mathbf{r} \qquad 2.2.45$$

is nonlinear in the individual spin components of the density and includes interactions between electrons of parallel spin only.[217] Thus, Eq. 2.2.45 reaches its maxima at integer occupations.[217] For fractional spin values the (negative) exchange energy is reduced and the total electronic energy is increased relative to states with integer occupations. However, the overestimation of $E^F(f_\uparrow, f_\downarrow)$ for fractional spin states is not as large as that of the HF method, which, by definition, does not account for electron correlation.[215,217] This agrees with the aforementioned implicit (partial) static correlation description of local and semi-local XC functionals.[215,217] Note, that the representation of fractional spin states requires the same ensemble formalism as the representation of the subsystem S of the FEN model (see Section 2.2.5). Also in the case of fractional spin states the corresponding probabilities $\{e_{ni}\}$ of the ensemble elements are determined by the fractional spin density and not by a minimization of the grand potential in Eq. 2.2.41. This rationalizes why the HF method largely overestimates $E^F(f_\uparrow, f_\downarrow)$ for fractional spin states.[215,217] Thus, the degeneracy of all possible states with fractional spins is not correctly reproduced in both cases, semi-local DFT approximations and HF.[215,217]

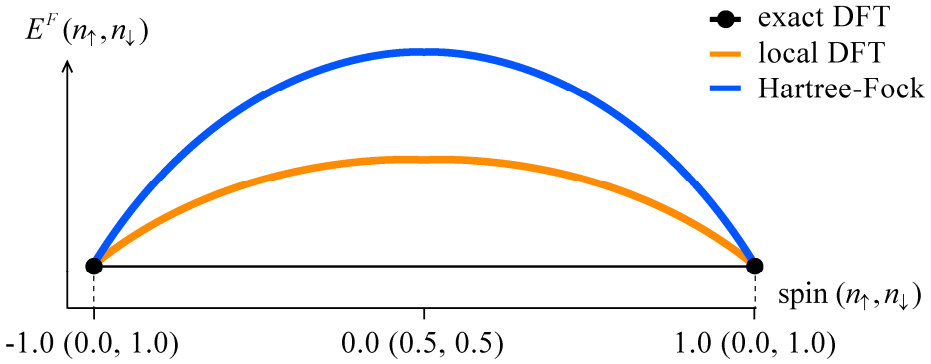

Figure 2.2.4: Sketch of the behavior of the total energy $E^F(f_\uparrow, f_\downarrow)$ of the fractional spin model in terms of the orbital occupations $n_\uparrow$ and $n_\downarrow$. Figure adapted from Ref. [215].

[15] This degeneracy arises from the fact that the electrons of the KS reference system do not interact.

2.2.7. Non-Covalent Interaction Error

The non-covalent interaction error (NCIE) represents the third important aspect that is not accounted for by standard local and semi-local KS-DFT approximations. The non-covalent interaction error recently gained much attention resulting in the development of various classes of approximations and corrections.[77,105-107,111-119,210,247] The NCIE is of a lesser relevance in the context of the present thesis compared to the SIE or the SCE. However, for the sake of completeness, the approaches most commonly used for the description of non-covalent interactions shall be briefly reviewed in the following as well.

The motion of electrons can create dynamic dipoles (or multipoles in general) even in molecules that lack a permanent dipole (or multipole) moment. Such instantaneous dipoles can affect the electronic structure of distant parts of the system and induce dipoles there as well.[248] The attractive interaction between such dynamic dipoles located near different atomic positions **A** and **B** is known as London dispersion energy E_{disp} and is one of several types of non-covalent (van der Waals, vdW) interactions.[248] The dispersion interaction between distant atomic centers of a molecular system exhibits an asymptotic behavior proportional to $-C_6/|\overline{\mathbf{AB}}|^6$, in terms of the interatomic distances $|\overline{\mathbf{AB}}|=|\mathbf{A}-\mathbf{B}|$ and the dispersion coefficients C_6.[248]

Although it originates from instantaneous effects, the dispersion energy still results from the interactions of electrons which can be described by a time independent many-body wave function. Indeed, these effects result from electron correlation as well and the only difference between dispersive interactions and normal dynamic correlation interactions (see Section 2.1.2) consists in their locality. The nonlocal character of dispersive interactions implies that any KS-DFT approximation which can account for such effects has to feature a nonlocal correlation functional.[104] As LDA and GGA methods employ only local correlation terms, these approximations are unable to capture dispersive interactions between distant parts of the system.[104] On the other hand, the nonlocal correlation terms occurring in post-HF methods like MP2 account for dispersion effects.[7] This led to the idea to employ the KS orbitals in an MP2-type correlation term[109] which is then combined with a suitably adapted semi-local correlation functional,[111-114]

$$E_{\mathrm{C}}^{\mathrm{DH}} = \beta_1 E_{\mathrm{C}}^{\mathrm{DHGGA}} + \beta_2 \sum_{ab}\sum_{uv} \frac{|\langle\psi_a\psi_b|\hat{W}|\psi_u\psi_v\rangle - \langle\psi_a\psi_b|\hat{W}|\psi_v\psi_u\rangle|^2}{\varepsilon_a^{\mathrm{KS}} + \varepsilon_b^{\mathrm{KS}} - \varepsilon_u^{\mathrm{KS}} - \varepsilon_v^{\mathrm{KS}}}. \qquad 2.2.46$$

The coefficients β_i and the local $E_{\mathrm{C}}^{\mathrm{DHGGA}}$ term of these so-called double hybrid functionals were thereby fitted to experimental reference data.[111-114] Double hybrid functionals have the same $\mathcal{O}(N^5)$ scaling computational requirements as the MP2 method, as they exhibit a nonlocal dependency on both, occupied and unoccupied, KS orbitals.[109] Furthermore, these methods are limited to non-self-consistent applications only as their XC potentials diverges for many-electron systems.[109] A similar nonlocal dependency on the unoccupied KS orbitals

is found in random phase approximations (RPA), which, however, represent significantly less empirical approaches to a nonlocal correlation functional.[108,110]

To circumvent these high computational requirements, a much simpler empirical expression for the dispersion energy

$$E_{disp}^{\mathrm{D}} = -\tfrac{1}{2}\sum_{AB} f_{damp}(|\overline{\mathbf{AB}}|)\, C_{6,AB} \big/ |\overline{\mathbf{AB}}|^6 \qquad 2.2.47$$

was suggested by Wu and Yang which depends on the atomic positions only.[105] This so-called DFT-D correction employs empirical pairwise dispersion coefficients $C_{6,AB}$ as well as a damping function f_{damp} to reduce the double-counting between dispersion and semi-local correlation terms.[105] The DFT-D method was subsequently refined by Grimme and others.[95,106,249] Approaches to compute the $C_{6,AB}$ coefficients in terms of the actual electron density of the system were proposed as well.[107,247] While being very efficient compared to double hybrid and RPA approaches, the DFT-D corrections in Eq. 2.2.47 are highly empirical and not applicable in all situations. The vdW-driven adsorption of molecular species on extended metal surfaces represents such an example in which DFT-D descriptions break down.[250-252] Thereby the collective polarizability of the metallic moiety causes an asymptotic R^{-3} scaling of vdW interactions which is not accounted for by DFT-D corrections of the general form in Eq. 2.2.47.[250-252]

A different attempt to include vdW interactions into an efficient semi-local DFT approximation has been proposed in form of the M06L MGGA functional.[77] As already mentioned in Section 2.2.4, the value of the kinetic energy density $\tau(\mathbf{r})$ at any point $\mathbf{r}$ represents a nonlocal density functional itself.[202] In this context the usage of τ in MGGA functionals implicitly introduces a small amount of nonlocal information into the semi-local XC term.[202] This fact was exploited in the parametrization of the M06L functional on data sets which emphasize vdW-type interactions.[77,210] Compared to most DFT-D approaches, the M06L functionals describes dispersion interactions in a self-consistent fashion. However, its extensive parametrization can lead to large deviations in the case of systems that are not part of the data set used for the parametrization of M06L (see Sections 4.3 and 4.4).[253]

The so-called vdW functionals represent another approach to the description of non-covalent interactions.[115-119] These methods exhibit the following functional form

$$E_{\mathrm{C}}^{\mathrm{VDW}}[\rho] = \tfrac{1}{2}\iint \rho(\mathbf{r})\cdot\Theta\big(\rho(\mathbf{r}),\rho(\mathbf{r}'),\nabla\rho(\mathbf{r}),\nabla\rho(\mathbf{r}')\big)\cdot\rho(\mathbf{r}')\, d\mathbf{r}' d\mathbf{r} \qquad 2.2.48$$

and employ a complicated integral kernel Θ to describe nonlocal aspects of the correlation between electrons at two distant locations.[115-119] Such functionals are mostly based on non-empirical considerations.[116] In contrast to the aforementioned RPA and double hybrid approaches, vdW DFT methods are formulated only in terms of ρ and $\nabla\rho$, and do not depend on the KS orbitals. Compared to the high computational requirements of RPA and double hybrid terms or the high empiricism of DFT-D corrections and the M06L functional

vdW DFT methods can be considered as a significant breakthrough.[131]. Despite the double integral required in Eq. 2.2.48, vdW functionals can be applied quite efficiently, at least when Fourier transformation techniques are employed.[254] In the case of systems including appreciable vdW interactions, these functionals provide a significant gain in accuracy.[255]

2.3. Hybrid Density Functional Theory

2.3.1. Rationale for Exact-Exchange Mixing

The following discussion deals with the early attempts to include a nonlocal exact-exchange (EXX) term in local KS-DFT approximations. In this context several theoretical justifications for such an approach are presented.

The concept of incorporating an exact-exchange term into DFT is as old as the KS formalism itself. In their seminal paper Kohn and Sham already considered the idea to employ a nonlocal, HF-type exchange expression

$$E_{\mathrm{EXX}} = \tfrac{1}{2}\sum_{ab} f_a f_b \langle \psi_a \psi_b \,|\, \hat{W} \,|\, \psi_b \psi_a \rangle = \tfrac{1}{2}\sum_{ab} f_a f_b \iint \frac{\psi_a^*(\mathbf{r})\psi_b(\mathbf{r})\psi_b^*(\mathbf{r}')\psi_a(\mathbf{r}')}{|\mathbf{r}-\mathbf{r}'|} d\mathbf{r}' d\mathbf{r} \,, \qquad 2.3.1$$

in terms of the KS orbitals.[28] This would imply a reference system of non-correlated particles (instead of non-interacting ones). Furthermore, also the corresponding effective potential V_{KS}^{σ} would not be multiplicative; opposed to the requirements of the KS formalism (see Section 2.2.1). Nevertheless, a multiplicative EXX potential can be obtained by means of the optimized effective potential method (OEP), as discussed in Section 2.3.2.[204-206] However, with regard to energetic properties the resulting functional

$$E_{\mathrm{XC}}[\rho, \{\psi_a\}] = E_{\mathrm{EXX}}[\{\psi_a\}] \qquad 2.3.2$$

will behave very similarly to the HF method. The addition of a local correlation term to Eq. 2.3.2 improves over HF but still yields less accurate atomization energies than LDA or GGA, even in the case of main group compounds.[31,81,256-258]

Nevertheless, good reasons for adding a scaled EXX term to semi-local XC terms exist. One example is the behavior of the electronic energy $E_{el}^{S}(n)$ of the FEN model obtained with HF and semi-local DFT approximations at non-integer electron counts, respectively (see Section 2.2.5). When combining the convex and concave functions of semi-local DFT approximations and HF, respectively, the resulting $E_{el}^{S}(n)$ function should be closer to the exact linear function, as illustrated by Figure 2.3.1.[101] It is emphasized that, although mostly being a fictitious system, the FEN model provides an important reference for the delocalization errors of different DFT approximations (see Section 2.2.5).[101,215,217] Thus, a linear combination between EXX and a local exchange term

$$E_{\mathrm{XC}}[\rho, \{\psi_a\}] = \alpha_1 E_{\mathrm{EXX}}[\{\psi_a\}] + \alpha_2 E_{\mathrm{X}}[\rho] + \alpha_3 E_{\mathrm{C}}[\rho] \,, \qquad 2.3.3$$

in terms of suitable mixing coefficients α_i should provide a beneficial error cancellation with regard to the delocalization error.[101,215,217]

Further justification for such hybrid DFT methods can be obtained when considering the XC holes. As discussed in Sections 2.2.5 and 2.2.6, the exact XC hole is less localized than those resulting from semi-local KS-DFT methods but more compact than the KS hole in the exchange only limit. Thus, from the perspective of XC holes a significant error compensation can be expected from the combination of semi-local and exact-exchange terms.[131]

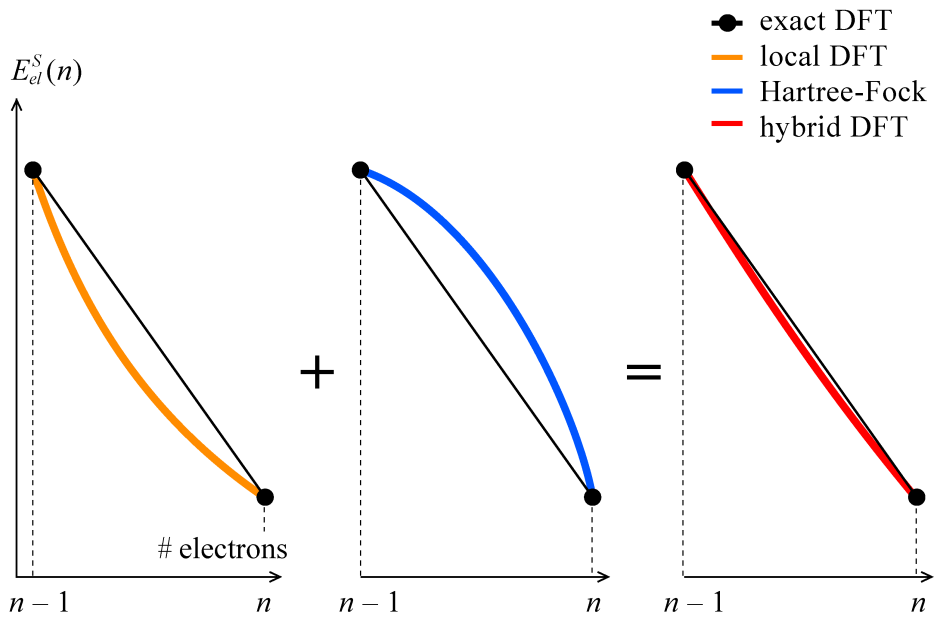

Figure 2.3.1: Schematic representation of the rationale for a linear combination of local and exact-exchange terms to reduce self-interaction effects in the total electronic energy of an open subsystem with non-integer electron counts.

Furthermore, the XC hole in the KS exchange-only limit is required to restore the correct normalization of the conditional pair density (Section 2.2.3).[31,33,131,152,179-181] Thus, a linear combination of exact and semi-local exchange terms is justified also by the adiabatic connection formula, Eq. 2.2.28.[259] The first hybrid functional was obtained from a simple trapezoidal approximation

$$h_{\mathrm{XC}}(\mathbf{x},\mathbf{x}') = \int_0^1 h_{\mathrm{XC}}^{\lambda}(\mathbf{x},\mathbf{x}')\, d\lambda \approx \frac{h_{\mathrm{XC}}^{\lambda=1}(\mathbf{x},\mathbf{x}') + h_{\mathrm{XC}}^{\lambda=0}(\mathbf{x},\mathbf{x}')}{2} \qquad 2.3.4$$

for the coupling-strength average (see Section 2.2.3).[81] While $h_{\mathrm{XC}}^{\lambda=0}$ is the XC hole in the KS exchange-only limit, Eq. 2.2.44, the hole $h_{\mathrm{XC}}^{\lambda=1}$ was approximated by the XC hole of the PWLDA functional.[81,192] Given its simplicity, the resulting "half-and-half" functional

$$E_{\mathrm{XC}}[\rho,\{\psi_a\}] = \tfrac{1}{2} E_{\mathrm{EXX}}[\{\psi_a\}] + \tfrac{1}{2} E_{\mathrm{XC}}^{\mathrm{PWLDA}}[\rho]\ , \qquad 2.3.5$$

was found to yield surprisingly accurate thermochemical results of main group compounds.[81] However, the form in Eq. 2.3.5 is not ideal as the correlation term is scaled by a factor of $1/2$ as well. Nevertheless, the half-and-half functional represented a significant step towards a reasonable linear combination of local KS-DFT approximations and the HF method. However, it has to be emphasized that, despite the theoretical justifications given above, the first hybrid DFT methods mostly became popular due to their improved accuracy for thermochemical results.[81]

2.3.2. Exact-Exchange Potential

Before presenting the various functionals that followed the half-and-half formula, two approaches for the self-consistent application of orbital-dependent XC approximations shall be briefly discussed; the optimized effective potential (OEP) and the method of functional derivatives with respect to KS orbitals (FDO).

The KS formalism requires the XC potential to be local, thus multiplicative. Opposed to that, the potential resulting from the EXX term is entirely nonlocal. The question how to obtain a local (multiplicative) potential from an orbital-dependent XC functional is rather involved. The HF equations are obtained from a variation of the orbitals $\{\phi_a\}$ leading to the non-multiplicative HF exchange potential whereas the KS formalism requires a local potential defined as $V_{\mathrm{XC}} = \delta E_{\mathrm{XC}}[\rho]/\delta\rho$. The optimized effective potential method can provide such a multiplicative EXX potential.[204-206] Thereby, the chain rule for functional derivatives[16]

$$V_{\mathrm{EXX}}^{\mathrm{OEP}}(\mathbf{r}) = \iint \sum_a \left(\frac{\delta E_{\mathrm{EXX}}}{\delta\psi_a(\mathbf{r}'')} \cdot \frac{\delta\psi_a(\mathbf{r}'')}{\delta V_{\mathrm{KS}}(\mathbf{r}')} \right) \frac{\delta V_{\mathrm{KS}}(\mathbf{r}')}{\delta\rho(\mathbf{r})} d\mathbf{r}'' d\mathbf{r}' \,, \qquad 2.3.6$$

is applied to obtain V_{EXX}, whereas the individual partial derivatives can be expressed in terms of a perturbative ansatz and response functions.[204-206] The double integral in Eq. 2.3.6 required to evaluate $V_{\mathrm{EXX}}^{\mathrm{OEP}}$ at a single location **r** clearly illustrates the complexity of the OEP method and the effort required to obtain $\delta E_{\mathrm{EXX}}[\rho]/\delta\rho$. Even in the form of the more efficient Krieger–Li–Iafrate approximation, this approach remains far more expensive than the computation of the EXX term itself.[206] Furthermore, while providing energetic results similar to HF, the values HOMO-LUMO gaps obtained with the OEP treatment of the EXX term are often closer to those of local KS-DFT methods.[223,260,261]

Self-consistent hybrid DFT calculations are mostly conducted in terms of the generalized Kohn–Sham (GKS) FDO-type approach.[96,208,262] The GKS formalism extends the orbital dependent kinetic energy operator of the KS system (see Eq. 2.2.9) by all other orbital dependent terms of the KS potential.[208] The resulting operator ($\hat{O}_{\mathrm{S}} = -\frac{1}{2}\nabla^2 + \alpha_1 \hat{V}_{\mathrm{EXX}}^{\sigma}$ in the case of hybrid DFT) is then used in the Levy–Lieb constrained search approach,[142-145] which provides another formal justification for orbital dependent XC approximations like hybrid DFT methods.[208] In a similar fashion the GKS single-particle equations

$$\hat{f}_{\mathrm{GKS}}^{\sigma}\psi_a(\mathbf{x}) = \left(-\tfrac{1}{2}\nabla^2 + \hat{V}_{\mathrm{EXX}}^{\sigma} + V_{\mathrm{ext}} + V_{\mathrm{Coul}} + V_{\mathrm{XC}}^{\sigma}\right)\psi_a(\mathbf{x}) = \varepsilon_a^{\mathrm{GKS}}\psi_a(\mathbf{x}) \qquad 2.3.7$$

can be derived. Opposed to the EXX potential resulting from the OEP method, $\hat{V}_{\mathrm{EXX}}^{\sigma}$ in Eq. 2.3.7 is different for each individual KS orbital. Like the HF exchange potential in Eq. 2.1.5, $\hat{V}_{\mathrm{EXX}}^{\sigma}$ is defined in terms of its effect on ψ_a

[16] In this notation, $\delta a(x)/\delta b(x')$ denotes the derivative of the functional $a(x)[b]$ with respect to b evaluated at x', hence $\{\delta a[b](x)/\delta b\}(x')$ in a more explicit notation.

$$\hat{V}_{\mathrm{EXX}}^{\sigma}\,\psi_a(\mathbf{x}) = -\sum_b \langle \psi_b \,|\, \hat{W} \,|\, \psi_a \rangle \;\; \psi_b(\mathbf{x})\,. \qquad 2.3.8$$

The local potential terms in Eq. 2.3.7 are again expressed as functional derivatives with respect to the electron density (Eq. 2.2.16). It needs to be emphasized that the GKS formalism mostly represents a theoretical justification. Apart from the computation of the EXX term, the algorithms required for hybrid DFT methods are identical to those of standard local and semi-local KS-DFT approximations.

2.3.3. Hybrid Density Functionals

The concepts upon which the most important hybrid DFT methods are based shall be discussed in the following. In this context also the more advanced concepts of range-separated hybrid and local hybrid DFT approximations are briefly presented.

Starting from the half-and-half functional in Eq. 2.3.5, the hybrid DFT approach was refined further. The mixing coefficients α_i were defined more flexibly and GGA correction terms were added.[82] Initially these latter corrections were not directly applied to the semi-local XC terms but merely at the level of the whole hybrid functional.[82] This approach led to Becke's B3 formula[82]

$$E_{\mathrm{XC}}^{\mathrm{B3PW91}} = \alpha_1 E_{\mathrm{EXX}} + (1-\alpha_1) E_{\mathrm{X}}^{\mathrm{LDA}} + \alpha_2 (E_{\mathrm{X}}^{\mathrm{B88}} - E_{\mathrm{X}}^{\mathrm{LDA}}) + E_{\mathrm{C}}^{\mathrm{PWLDA}} + \alpha_2 (E_{\mathrm{C}}^{\mathrm{PW91}} - E_{\mathrm{C}}^{\mathrm{PWLDA}}) \qquad 2.3.9$$

which is also known as 3-parameter adiabatic connection method (ACM3). The coefficients in Eq. 2.3.9 were determined from a least-squares fit to experimental data as $\alpha_1 = 0.20$, $\alpha_2 = 0.72$, and $\alpha_3 = 0.81$.[82] In this way, the ACM3 method acquires an empirical character. Eq. 2.3.9 was modified by Stephens *et al.* who substituted the correlation terms in Eq. 2.3.9 by a linear combination of the VWN[17] LDA and the LYP GGA functional[47,84,191]

$$E_{\mathrm{XC}}^{\mathrm{B3LYP}} = \alpha_1 E_{\mathrm{EXX}} + (1-\alpha_1) E_{\mathrm{X}}^{\mathrm{LDA}} + \alpha_2 (E_{\mathrm{X}}^{\mathrm{B88}} - E_{\mathrm{X}}^{\mathrm{LDA}}) + E_{\mathrm{C}}^{\mathrm{VWN}} + \alpha_3 (E_{\mathrm{C}}^{\mathrm{LYP}} - E_{\mathrm{C}}^{\mathrm{VWN}})\,. \qquad 2.3.10$$

With the mixing coefficients from Eq. 2.3.9, this represents the B3LYP[84] functional which is the most widely applied DFT method.[263] The popularity of B3LYP originated mostly from its success when modeling main group compounds.[8,31] On the other hand, significant failures with regard to transition metals are well known for B3LYP.[198,264] Also in the case of large organic molecules the performance of the original B3PW91 variant in Eq. 2.3.9 is found to perform consistently better.[212,265] These failures of B3LYP can be traced back to its LYP correlation part, which does not exhibit the proper HEG limit.[198,266-270]

The local terms of hybrid DFT variants based on the ACM3 formula originate from linear combinations of already existing local KS-DFT approximations. Therefore, such terms likely are not optimal for being employed in nonlocal hybrid DFT expressions. In consequence,

[17] A specific parametrization to RPA data was used, which is denoted as VWN3 and different from the more common VWN5 variant.

subsequent developments focused on local XC terms that are specifically designed to be used in combination with the EXX term.[85] The hybrid GGA B97

$$E_{\mathrm{XC}}^{\mathrm{B97}} = \alpha_1 E_{\mathrm{EXX}} + (1-\alpha_1) E_{\mathrm{X}}^{\mathrm{B97}} + E_{\mathrm{C}}^{\mathrm{B97}} \qquad 2.3.11$$

was one of the first hybrid DFT methods based on this concept.[85] Due to the specific adaption of its local terms, B97 allowed one to substitute the ACM3 formula by the simpler single-parameter mixing scheme, ACM1. Thereby, B97 is used with an EXX mixing factor of ~0.19, while the semi-local terms $E_{\mathrm{X}}^{\mathrm{B97}}$ and $E_{\mathrm{C}}^{\mathrm{B97}}$ include nine empirical parameters in total, which were again adapted to experimental reference data. Other well-known examples of ACM1 hybrid DFT approximations are the methods M05 und M06 whose semi-local terms feature even more parameters.[77,89,90,210] M06 and its variants M06-2X and M06-HF include the parameters $\alpha_1 = 0.27,\ 0.54$, and 1, respectively; they are based on the same construction principles as the MGGA functional M06L (Sections 2.2.4 and 2.2.7). Indeed, in this context M06L appears as a local re-parametrization of M06 under the constraint $\alpha_1 = 0$.[77]

Nevertheless, ACM1-type functionals were proposed from existing semi-local XC terms as well. While the adaption of the semi-local XC term to the EXX part is neglected, such approaches can significantly reduce the empiricism of hybrid DFT if based on non-empirical DFT approximations. Indeed, the hybrid DFT variants of PBE and TPSS, PBEh, $\alpha_1 =$ 0.32,[261] and TPSSh, $\alpha_1 =$ 0.10,[212], include the EXX mixing factor as the only empirical parameter.

It is not possible to construct a hybrid DFT functional without an empirically determined EXX parameter.[271] However, Perdew *et al.*[83,259] rationalized a specific value for α_1 with the following ansatz for the coupling-strength dependence of the XC energy

$$\begin{aligned} E_{\mathrm{XC}}^{\mathrm{HYB}} &= \int_0^1 E_{\mathrm{XC}}^{\mathrm{HYB},\lambda} d\lambda = \int_0^1 \left[E_{\mathrm{XC}}^{\mathrm{GGA},\lambda} + \left(E_{\mathrm{EXX}} - E_{\mathrm{X}}^{\mathrm{GGA}} \right) (1-\lambda)^{\mu-1} \right] d\lambda \\ &= E_{\mathrm{XC}}^{\mathrm{GGA}} + \frac{1}{\mu} \left(E_{\mathrm{EXX}} - E_{\mathrm{X}}^{\mathrm{GGA}} \right) , \end{aligned} \qquad 2.3.12$$

where

$$E_{\mathrm{XC}}^{\mathrm{GGA},\lambda}[\rho] = \frac{\partial}{\partial \lambda} \left(\lambda^2 E_{\mathrm{XC}}^{\mathrm{GGA}}[\rho/\lambda] \right). \qquad 2.3.13$$

This was compared with the polynomial λ-dependence of the XC energy from many-body perturbation theory (MBPT) of order μ

$$E_{\mathrm{XC}}^{\mathrm{MP}\mu,\lambda} \approx E_0 + \lambda E_1 + \ldots + \lambda^{\mu-1} E_{\mu-1} \ . \qquad 2.3.14$$

With increasing value of μ the EXX term in Eq. 2.3.12 is reduced in favor of the GGA term. The order of MBPT which is used as reference for Eq. 2.3.12 has therefore to be as low as possible to still include a numerically significant EXX term,. On the other hand the MBPT method itself should still qualify as accurate reference. On the example of the atomization energies of small main group compounds, Perdew *et al.* concluded that MP4, hence $\mu = 4$, represents the lowest MBPT order able to provide an acceptable description of the XC energy

as a function of λ. Thus, $\mu = 4$ was considered a suitable order for the polynomial coupling strength dependency in Eq. 2.3.12. In this context $\alpha_1 = \frac{1}{4}$ can be viewed as slightly less empirical value for the EXX mixing factor compared in the ACM1 form. In this way, Perdew *et al.* were led to suggest[83,259] the ACM0 hybrid DFT variant which was subsequently employed in form of the PBE0[87] functional

$$E_{\mathrm{XC}}^{\mathrm{PBE0}} = \tfrac{1}{4} E_{\mathrm{EXX}} + \tfrac{3}{4} E_{\mathrm{X}}^{\mathrm{PBE}} + E_{\mathrm{C}}^{\mathrm{PBE}} . \qquad 2.3.15$$

Nevertheless, the optimum value for α_1 still depends on the specific type of the system. Thus, other strategies are required to obtain further improvements. Range-separated hybrid DFT (RSH) represents such a mixing strategy.[91-97] RSH approaches are based on the linear combination of EXX and local DFT at the level of XC holes instead of exchange energy terms.[91-97] The ratio of local and nonlocal exchange holes thereby depends on the electron-electron distance $|\mathbf{r} - \mathbf{r}'|$. A second alternative consists in a linear combination of exchange energy densities.[100,102,103,244,272] This leads to a position dependent admixture of EXX to a semi-local MGGA exchange term, which potentially allows one to satisfy more properties of the exact XC energy density.[100,271] Both of these alternative hybrid DFT approaches are not entirely explored yet and combinations in form of a position dependent range separation have been considered as well.[96,273,274]

2.4. The DFT+U Method

In the following the origins of the DFT+U method from the Hubbard model Hamiltonian are presented. The DFT+U self-interaction correction term is then reformulated to be invariant under unitary transformations of the KS orbitals. This reformulation is thereby based on occupation matrices of specific target orbitals onto which the DFT+U self-interaction correction is applied. The occupation matrices of localized target orbitals are then generalized to linear combinations of atomic orbitals. This generalization leads to the DFT+Umol method which was developed and applied in the context of this thesis.

As discussed in Section 2.3.1, hybrid DFT methods are expected to be less affected by the SIE due to the error cancellation between convex and concave terms of the total energy at fractional electron numbers (see Figure 2.3.1). Indeed, the nonlocal exchange term of standard hybrid DFT methods can be considered as a global self-interaction and delocalization correction which is applied to the entire system. While the SIE often manifests itself only in specific parts of a system, e.g. an open atomic subshell, hybrid DFT methods may not provide an optimal description for the other moieties of the system. Thus, the EXX term may lead to an undesired deterioration of other aspects (see Section 2.2.6).[245]

In contrast, the DFT+U method[60-64,66-69,275] represents a locally confined correction for the SIE.[65,67,276] The DFT+U framework has its roots in the field of theoretical solid state physics and was proposed to correct the electronic structure description (and especially the band gaps) of antiferromagnetic transition metal oxide insulators.[60,277] Prior to DFT+U, these systems were often described by the empirical Hubbard model Hamiltonian.[278-280] While the DFT results of such systems are heavily plagued by the delocalization of electrons within partially filled bands,[60,277] the much simpler Hubbard model was often found to provide a qualitatively correct description.[278-280] Apart from kinetic energy terms the Hubbard model only accounts for the Coulomb repulsion between the N_I different orbitals χ_t and χ_u which both belong to the same atomic subshell I,[278-280]

$$E_{\mathrm{Coul}}^{\mathrm{Hub}}[\{n_{tt\sigma}\}] = \sum_I \frac{J_I}{2}\left(\sum_t n_{tt\uparrow} n_{uu\downarrow} + \sum_\sigma \sum_{t\neq u} n_{tt\sigma} n_{uu\sigma} \right). \qquad 2.4.1$$

Thereby, the Coulomb integrals are simplified to only depend on the corresponding orbital occupation numbers $\{n_{tt\sigma}\}$ and a spherically averaged, subshell specific Coulomb interaction parameter[60,277,281]

$$J_I = \frac{1}{N_I^2} \sum_{t,u\in I} \iint \chi_t^*(\mathbf{r})\,\chi_t(\mathbf{r}) W(\mathbf{r},\mathbf{r}')\,\chi_u^*(\mathbf{r}')\,\chi_u(\mathbf{r}')\,d\mathbf{r}'d\mathbf{r}\,. \qquad 2.4.2$$

The Hubbard model can be generalized to include also exchange interactions,[60,277] which are given analogously to the Coulomb interactions in terms of the occupation numbers and a spherically averaged exchange interaction parameter K_I. The total Hubbard electron-electron interaction term reads then as

$$E_{\mathrm{ee}}^{\mathrm{Hub}}[\{n_{tt\sigma}\}] = \sum_I \left(\frac{J_I}{2} \sum_t n_{tt\uparrow} n_{uu\downarrow} + \frac{J_I - K_I}{2} \sum_\sigma \sum_{t \neq u} n_{tt\sigma} n_{uu\sigma} \right). \qquad 2.4.3$$

Note that the symbols J_I and K_I were chosen here to keep the notation consistent with that of the discussions in the previous sections. Within the DFT+U community the Coulomb and exchange parameters are usually denoted as U_I and J_I, respectively.[60-69]

The DFT+U method originated from the idea to describe the band structure by a KS-DFT approximation while using the Hubbard model to approximate the electron-electron interactions missing in this description.[60,61,275,280] In the context of a DFT+U self-interaction correction the additional Hubbard terms are only applied to specific orthonormal target orbitals $\{\chi_t\}$ which are most affected by the SIE.[60,61,275] Furthermore, the resulting DFT+U functional

$$E^{\mathrm{DFT+U}}[\rho, \{n_{tt\sigma}\}] = E^{\mathrm{LDA}}[\rho] + E_{\mathrm{ee}}^{\mathrm{Hub}}[\{n_{tt\sigma}\}] - E^{\mathrm{DC}}[\{n_{tt\sigma}\}] \qquad 2.4.4$$

includes an additional term E^{DC} to prevent an eventual double counting of the on-site interactions described by both, E^{LDA} and E^{Hub}. While several approximations have been proposed for E^{DC},[68] its so-called fully localized limit (FLL) form represents its most widely applied variant.[63] The FLL approximation assumes that $E_{\mathrm{ee}}^{\mathrm{Hub}}$ becomes identical to the electron-electron interactions of the KS-DFT approximation in the case of fully localized electrons, hence when all occupation numbers assume values of either 0 or 1.[63] With this assumption Eq. 2.4.3 is used to express E^{DC} after some manipulations as[281]

$$E_{\mathrm{FLL}}^{\mathrm{DC}}[\{n_{tt\sigma}\}] = \sum_I \left(\frac{J_I}{2} \sum_t n_{tt\uparrow} n_{uu\downarrow} + \frac{J_I - K_I}{2} \left(\sum_\sigma \sum_{tu} n_{tt\sigma} n_{uu\sigma} - \sum_\sigma \sum_t n_{uu\sigma} \right) \right). \qquad 2.4.5$$

When subtracting Eq. 2.4.5 from Eq. 2.4.3 the opposite-spin terms cancel and the factor $J_I - K_I$ can be summarized to a single parameter U_I. The residual term

$$E^{\mathrm{U}p}[\{n_{tt\sigma}\}] = E_{\mathrm{ee}}^{\mathrm{Hub}}[\{n_{tt\sigma}\}] - E^{\mathrm{DC}}[\{n_{tt\sigma}\}] = \sum_I \frac{U_I}{2} \sum_{t\sigma} \left(n_{tt\sigma} - n_{tt\sigma} n_{tt\sigma} \right) \qquad 2.4.6$$

represents the DFT+U correction which is added to the total electronic energy from the employed KS-DFT approximation (LDA in most early applications)[60,61,275]

$$E^{\mathrm{DFT+U}}[\rho, \{n_{tt\sigma}\}] = E^{\mathrm{LDA}}[\rho] + E^{\mathrm{U}p}[\{n_{tt\sigma}\}]. \qquad 2.4.7$$

Thus, the DFT+U energy is a functional in terms of the electron density and the occupation numbers of the target orbitals

$$n_{tt\sigma} = \langle \chi_t \sigma \,|\, \hat{\rho} \,|\, \chi_t \sigma \rangle = \sum_a f_a \langle \chi_t \sigma \,|\, \psi_a \rangle \langle \psi_a \,|\, \chi_t \sigma \rangle \ , \qquad 2.4.8$$

which are obtained as expectation values of the density matrix operator[126]

$$\hat{\rho} = \sum_a f_a \left| \psi_a \right\rangle \left\langle \psi_a \right| . \qquad 2.4.9$$

The effective on-site parameter U_I can thereby be interpreted as the strength with which the DFT+U term is applied to the individual corrected subshells *I*.[60]

When individual KS orbitals $\{\psi_a\}$ are chosen as target orbitals, the terms in Eq. 2.4.6 are proportional to the corresponding summation terms of the integrated $h_{\mathrm{XC}}^{\lambda=0}$ hole in Eq. 2.2.43. Indeed, $E^{\mathrm{Up}}[\{n_{tt\sigma}\}]$ represents a penalty functional which is nonzero for fractional target orbital occupations and increases (penalizes) the total energy for fluctuating electron configurations. Thus, it can be considered as a self-interaction correction. The underlying concept of this correction is depicted in Figure 2.4.1; again based on the discussion in Section 2.2.5.[282] However, in contrast to what is often asserted, the DFT+U term does not describe "strong correlation" phenomena which can cause electron localization as well.[219]

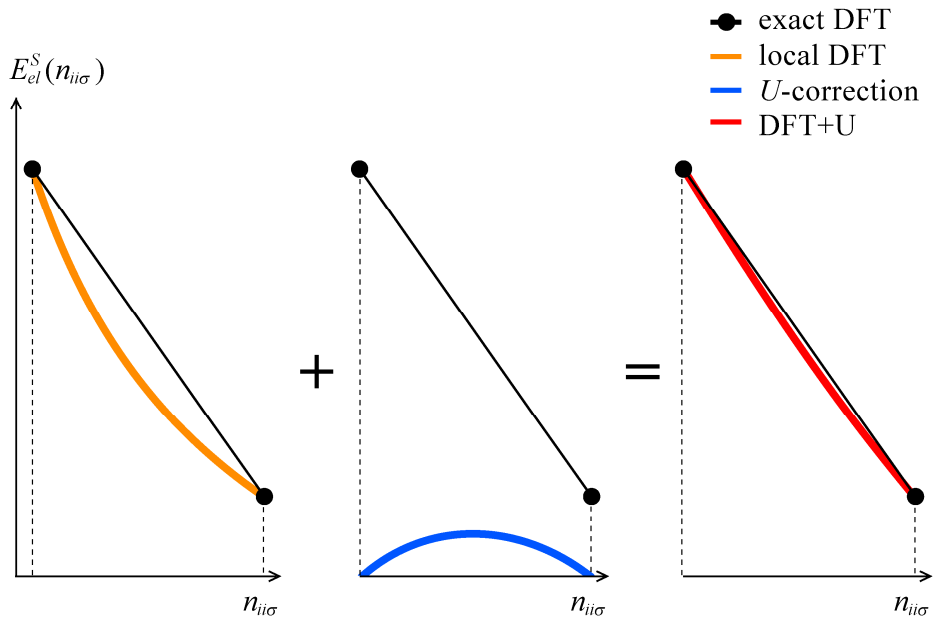

Figure 2.4.1: Scheme of the self-interaction reduction provided by the *U*-correction term on the example of the total electronic energy of an open subsystem with non-integer occupation numbers. Figure adapted from Ref. [282].

The self-interaction correction provided by Eq. 2.4.6 acts at the level of orbital specific energy contributions, just like the PZ correction in Eq. 2.2.37. Thus, Eq. 2.4.6 is not invariant with respect to unitary transformations of the KS orbitals. In contrast to the PZ method this problem can, however, be resolved for the DFT+U approach. To this end, the orbital occupation numbers $\{n_{tt\sigma}\}$ are considered as eigenvalues of a more general subshell occupation matrix $\mathbf{n}_I^\sigma$. Opposed to the assumption of fully localized orbitals that lead to Eq. 2.4.6 this generalization allows a mixing among the orbitals of the subshell *I* due to unitary transformations.[275] According to that, Eq. 2.4.6 can be reformulated to the following form

$$E^{\mathrm{U}} = \tfrac{1}{2}\sum_{I\sigma} U_I \left(\mathrm{Tr}\{\mathbf{n}_I^\sigma\} - \mathrm{Tr}\{\mathbf{n}_I^\sigma \mathbf{n}_I^\sigma\}\right), \qquad 2.4.10$$

in terms of traces over occupation matrices

$$\{\mathbf{n}_I^\sigma\}_{tu} = n_{tu\sigma} = \langle \chi_t\sigma \,|\, \hat{\rho} \,|\, \chi_u\sigma\rangle = \sum_a f_a \langle \chi_t\sigma \,|\, \psi_a\rangle\langle \psi_a \,|\, \chi_u\sigma\rangle \quad \text{with} \quad t,u \in I \;, \qquad 2.4.11$$

for individual subshells of target orbitals. This formulation exhibits the desired invariance property while still retaining the purpose of the DFT+U term as an energy penalty functional for fractional occupations. Thus, it can be used as correction term to local KS-DFT functionals as well,

$$E^{\text{DFT+U}} = E^{\text{KS-DFT}} + E^{\text{U}} . \qquad 2.4.12$$

To apply the DFT+U method in actual calculations the elements of the occupation matrices in Eq. 2.4.11 need to be expressed in terms of basis functions $\{\varphi_i\}$. After the corresponding expansion of $\{\psi_a\}$ and $\{\chi_t\}$,

$$\psi_a(\mathbf{x}) = \sum_i \varphi_i(\mathbf{r})\, C_{ia}^{\sigma} \quad \text{and} \quad \chi_t(\mathbf{r}) = \sum_i \varphi_i(\mathbf{r})\, v_{it} \ , \qquad 2.4.13$$

Eq. 2.4.11 reads as

$$n_{tu\sigma} = \sum_{ijkl} v_{it}^{*} \langle \varphi_i \,|\, \varphi_j \rangle \sum_a f_a C_{ja}^{\sigma} C_{ka}^{\sigma *} \langle \varphi_k \,|\, \varphi_l \rangle v_{lu} \ . \qquad 2.4.14$$

The overlap and density matrices can be identified in Eq. 2.4.14 as

$$S_{ij} = \langle \varphi_i \,|\, \varphi_j \rangle \quad \text{and} \quad P_{ij\sigma} = \sum_a f_a C_{ia}^{\sigma} C_{ja}^{\sigma *} \ , \qquad 2.4.15$$

so that the target orbital occupation matrices result to

$$\mathbf{n}_I^{\sigma} = \mathbf{v}_I \mathbf{S} \mathbf{P}^{\sigma} \mathbf{S} \mathbf{v}_I^{\dagger} \ . \qquad 2.4.16$$

Apart from this canonical definition of target orbital occupation matrices alternative variants like

$$\mathbf{n}_I^{\sigma} = \tfrac{1}{2} \mathbf{v}_I (\mathbf{S}\mathbf{P}^{\sigma} + \mathbf{P}^{\sigma}\mathbf{S}) \mathbf{v}_I \ , \qquad 2.4.17a$$

$$\mathbf{n}_I^{\sigma} = \mathbf{v}_I \mathbf{S}^{1/2} \mathbf{P}^{\sigma} \mathbf{S}^{1/2} \mathbf{v}_I \ , \text{ and} \qquad 2.4.17b$$

$$\mathbf{n}_I^{\sigma} = \mathbf{v}_I \mathbf{P}^{\sigma} \mathbf{v}_I \qquad 2.4.17c$$

have been rationalized, which resemble the common definitions of orbital occupation numbers.[66,281]

It needs to be emphasized that in practical applications of the DFT+U method the orbitals $\{\chi_t\}$ do not exactly correspond to KS orbitals of the system. In fact projectors are used to apply the self-interaction correction to the individual target orbitals.[60-64,66-69,275] While the details of these projectors will be discussed in Section 3.2.1, several comments are appropriate at this point. Selecting $v_{it} = \delta_{it}$, hence projecting onto individual basis functions, reduces Eq. 2.4.16 to the conventional atomic formulation of DFT+U.[281,283-285] However, the formulation in Eq. 2.4.16 allows for projectors onto general linear combinations of basis functions. This formulation provides some further flexibility which is exploited by the DFT+Umol method to apply the DFT+U correction to fragment molecular orbitals (FMO).[286,287]

Finally, different options for determining the effective on-site parameter U_I shall be discussed. While Eq. 2.4.2 and the analogous expression for K_I are rarely used to compute $U_I = J_I - K_I$, this latter parameter is often determined empirically, by adjusting it to

spectroscopic quantities.[288] This strategy makes DFT+U a highly system specific approach.[288] Alternatively, U_I can be defined also in terms of the curvature of $E^{\text{KS-DFT}}$ with respect to fractional occupation numbers, e.g.:

$$U_I = \sum_{\sigma} \frac{1}{N_I^2} \sum_{t,u \in I} \frac{\partial^2 E^{\text{KS-DFT}}(\mathbf{n}_I^{\sigma})}{\partial n_{tu\sigma} \partial n_{ut\sigma}} \qquad 2.4.18$$

The second derivative in Eq. 2.4.18 can be interpreted as the curvature that is required for the DFT+U correction to restore the linear behavior of the total electronic energy between integer values of n (Figure 2.4.1). Following this approach, U_I can be obtained either in terms of response properties or from numerical differentiation.[65,275] In any case, the DFT+U method represents a viable option for studying solid state systems that are heavily affected by the SIE.[275,277] In recent years, the DFT+U method has been applied to molecular systems as well.[67,281,283-287]

3. Algorithms and Implementation

3.1. Exact-Exchange

3.1.1. Electron-Repulsion Integrals

The following section starts with a brief presentation of density fitting methods that allow one to avoid the calculation of the four-center electron-repulsion integrals (ERI). As these integrals cannot be avoided in most applications of hybrid DFT methods, the rest of this section is dedicated to a detailed discussion of the most important concepts and algorithms for the calculation of ERIs. This discussion of ERI algorithms is followed by a presentation of the implementations in PARAGAUSS[70] which were carried out in the context of this thesis.

Within local and semi-local DFT approximations (Section2.2.4), the evaluation of the XC term requires a computational effort of $\mathcal{O}(N_g)$ on a numerical grid of size N_g and of $\mathcal{O}(N^2 N_g)$ to obtain the XC potential, Eq. 2.2.19. Thus, the evaluation of the Coulomb term (Eq. 2.1.10) would dominate such calculations as its computational requirements formally scale as $\mathcal{O}(N^4)$. However, the Coulomb energy and potential (Eqs. 2.2.13 and 2.2.16) are explicitly known functionals of the density. The density in turn can be approximated with an auxiliary basis set $\{\zeta_m\}$ of the size[18] N_a as $\rho(\mathbf{r}) \approx \sum_m d_m \zeta_m(\mathbf{r})$.[35-43] In terms of the approximated electron density the Coulomb potential from Eq. 2.1.10a reads then as[35-43]

$$J_{ij} = \sum_{kl} P_{kl} g_{ijkl} \approx \sum_m d_m \int\int \frac{\varphi_i(\mathbf{r})\,\varphi_j(\mathbf{r})\,\zeta_m(\mathbf{r}')}{|\mathbf{r}-\mathbf{r}'|} d\mathbf{r}' d\mathbf{r} = \sum_m d_m\, \tilde{g}_{ijm} . \qquad 3.1.1$$

Thus, the original formal $\mathcal{O}(N^4)$ scaling of the computational effort required for the Coulomb term is reduced to $\mathcal{O}(N^2 N_a)$.[35-43] This density fitting technique entails a considerable reduction of the computational costs of local and semi-local DFT calculations.[264,289] In consequence, this approximation significantly contributed to the success of local and semi-local KS-DFT approximations.[264] The coefficients $\{d_m\}$ in Eq. 3.1.1 may be obtained by minimizing the difference between the original and the approximated density in either an overlap or a Coulomb metric.[35-43] The former approach is known as "resolution of the identity" technique (RI).[35,36,41] Compared to that, the usage of a Coulomb metric is more accurate for a given auxiliary basis as it directly minimizes the error of the Coulomb self-energy of the charge density.[37-39,42,43] In the following this latter technique will be denoted as fitting-function approach (FF or DF-FF).

[18] The size N_a of the auxiliary basis set usually needs to be larger than that of the orbitals basis *N*. This can be understood by considering that the auxiliary basis $\{\zeta_k\}$ is required to cover the two-center contributions that appear when expressing Eq. 2.2.10 in terms of orbital basis functions.

On the other hand, the EXX term as it appears in HF theory and hybrid DFT methods can not be expressed as a simple density functional. Nevertheless, RI approaches to the exact-exchange term have been suggested as well.[290] In contrast to the DF-FF representation of the Coulomb potential, these approaches do not reduce the formal $\mathcal{O}(N^4)$ scaling of the EXX term.[290] Furthermore, such methods mostly provide efficiency gains when systems of moderate sizes are to be treated with a large basis set.[290]

Thus, the calculation of four-center electron-repulsion integrals[19]

$$g_{ijkl} = (ij\,|\,kl) = \langle \varphi_i \varphi_k \,|\, \hat{W} \,|\, \varphi_j \varphi_l \rangle = \iint \frac{\varphi_i(\mathbf{r})\varphi_j(\mathbf{r})\varphi_k(\mathbf{r}')\varphi_l(\mathbf{r}')}{|\,\mathbf{r}-\mathbf{r}'\,|}\, d\mathbf{r}' d\mathbf{r} \;, \qquad 3.1.2$$

cannot be avoided in most applications of HF and hybrid DFT methods. As the computation and processing of ERIs represent the computationally most demanding steps in hybrid DFT and HF calculations, they were extensively studied and influenced also other algorithmic parts of quantum chemical calculations. The introduction of contracted Gaussian-type orbitals (CGTO)

$$\varphi_i(\mathbf{r}) = \sum_{i'}^{\kappa_i} c_{ii'} G_{\ell_i m_i a_{i'}}(\mathbf{r}-\mathbf{A}) \qquad 3.1.3$$

as elements of a single-electron atomic orbital (AO) basis is an example for such an influence of the need for an efficient calculation of ERIs.[291-294] CGTOs are represented as linear combinations of primitive Gaussian orbitals $G_{\ell_i m_i a_{i'}}$ (PGTO) with coefficients $\{c_{ii'}\}$.[291,295-298] PARAGAUSS[70] employs real solid harmonic CGTO functions (SHCGTO) that consist of κ_i different primitive Gaussian functions (PGTO) with various exponents $\{a_{i'}\}$

$$G_{\ell m a_{i'}}(\mathbf{r}_\mathbf{A}) = N_\ell(a_{i'}) S_{\ell m}(\mathbf{r}_\mathbf{A}) \exp\left(-a_{i'} \mathbf{r}_\mathbf{A}^{\,2}\right). \qquad 3.1.4$$

All functions of such a contraction are centered at the same nuclear position[20] $\mathbf{A}$ ($\mathbf{r}_\mathbf{A} = \mathbf{r} - \mathbf{A}$). Every SHCGTO function exhibits a solid harmonic prefactor $S_{\ell m}$ and a normalization factor $N_\ell(a_{i'})$, whereas ℓ denotes the angular momentum and m ($|\,m\,| \le \ell$) the magnetic quantum number.[299-302]

The simplest approach to tackle Eq. 3.1.2 consists in first computing ERIs over PGTO functions.[291] The final integral results then by a subsequent contraction of the primitive indices.[291] Indices and factors related to the first spatial variable $\mathbf{r}$ are commonly designated as bra-side $(ij\,|$, while quantities related to $\mathbf{r}'$ are denoted as ket-side $|\,kl)$. The ERI $(ij\,|\,kl)$ over four CGTOs with angular momenta ℓ_i, ℓ_j, ℓ_k, and ℓ_l, magnetic quantum numbers m_i, m_j, m_k, and m_l, and atomic centers **A**, **B**, **C**, and **D**, respectively, then reads as[21]

---

[19] A real basis set $\{\varphi_i\}$ is thereby assumed throughout the entire presentation. Furthermore, the notation $g_{ijkl} = (ij\,|\,kl)$ will be employed, which is most commonly used in the context of algorithms for ERI calculation.

[20] The center of the PGTO was actually allowed to vary slightly in early formulations to represent of Gaussian lobe functions, which nowadays are of purely historical importance only.

[21] Using $(ij\,|\,k'l')$ and $(i'j'\,|\,kl)$ to denote bra and ket half-contracted integrals and $(i'j'\,|\,k'l')$ for ERIs over PGTOs.

$$(ij\,|\,kl) = \sum_{i'j'} c_{ii'} c_{jj'} \{i'j'\,|\,kl) = \sum_{i'j'} \sum_{k'l'} c_{ii'} c_{jj'} c_{kk'} c_{ll'} \{i'j'\,|\,k'l'\}\,. \qquad 3.1.5$$

Eq. 3.1.5 is thereby formulated in terms of the intermediate integrals

$$\{i'j'\,|\,k'l'\} = \iint \frac{G_{\ell_i m_i a}(\mathbf{r}_\mathbf{A}) G_{\ell_j m_j b}(\mathbf{r}_\mathbf{A}) G_{\ell_k m_k c}(\mathbf{r}'_\mathbf{C}) G_{\ell_l m_l d}(\mathbf{r}'_\mathbf{D})}{|\,\mathbf{r} - \mathbf{r}'\,|}\, d\mathbf{r}' d\mathbf{r}\,, \qquad 3.1.6$$

over PGTO functions. Subsequently, the following abbreviations for the exponents $a = a_{i'}$, $b = a_{j'}$, $c = a_{k'}$, and $d = a_{l'}$ will be used in most expressions.

As indicated by the matrix notation for the contraction coefficients $\{c_{ii'}\}$, multiple CGTOs are often formed from a common set of PGTO functions. Thus, Eq. 3.1.5 illustrates that significant efficiency gains are possible when calculating four-center integrals in batches $(IJ\,|\,KL)$ of quadruples of AO shells *I*, *J*, *K*, and *L*. A shell *I* comprises all AO functions of angular momentum ℓ_i which are centered at the same nuclear position $\mathbf{A}$. Individual shell orbitals $i \in I$ differ from each other by their angular and/or their radial components; hence by the magnetic quantum numbers m_i and/or their linear combinations of PGTOs. In the context of a batch-wise calculation of ERIs one exploits the fact that many integrals of a batch are formed from the same quantities like $\{i'j'\,|\,k'l'\}$ or $\{i'j'\,|\,kl)$, which can be stored as intermediates. The contraction of a fully computed set of $\{i'j'\,|\,k'l'\}$-type integrals over PGTOs in Eq. 3.1.5 is far from being the most efficient approach to ERIs. However, many other algorithmic steps offer similar possibilities to exploit the presence of common intermediates. Thus, literally all modern approaches to the computation of ERIs rely on a batch-wise calculation of ERIs.[303-305]

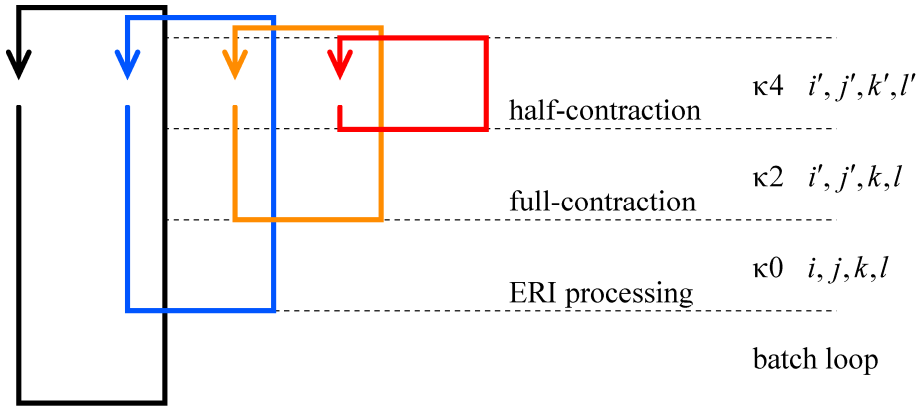

Figure 3.1.1: General outline of ERI algorithms in terms of κ4, κ2, and κ0 steps.

Furthermore, many algorithms share the contraction scheme outlined in Eq. 3.1.5 and depicted in Figure 3.1.1. The $(ij\,|\,kl)$ ERIs are obtained from a batch of (bra or ket) half-contracted intermediates, $(ij\,|\,k'l')$ or $\{i'j'\,|\,kl)$, which result from the first half-contraction step. As the number of PGTOs is generally larger than that of CGTOs, calculations prior to

the first half-contraction step on primitive intermediates are most expensive. These algorithmic parts are denoted as κ4 steps and are followed by the less expensive κ2 operations on half-contracted quantities. Finally, the mostly inexpensive κ0 steps are entirely formulated in terms of fully contracted quantities and only followed by the subsequent processing of four-center integrals. Figure 3.1.1 depicts the general loop structure of these κ4, κ2, and κ0 steps.

ERIs over four *s*-type PGTO functions represent the most simple case of Eq. 3.1.5 and are denoted as $\{ss\,|\,ss\}$. The Gaussian product rule states that the multiplication of two Gaussian functions results in another Gaussian function.[2,4] This product distribution exhibits the exponent $p = a + b$, is centered at the exponent-weighted average position $\mathbf{P} = \big(a\mathbf{A} + b\mathbf{B}\big)\big/ p$ on the line segment connecting the centers of the two initial Gaussians and scaled by the overlap between them,

$$\exp\left(-a\,\mathbf{r}_{\mathrm{A}}^2\right)\exp\left(-b\,\mathbf{r}_{\mathrm{B}}^2\right) = \exp\left(-(ab/p)\overline{\mathbf{AB}}^2\right)\exp\left(-p\,\mathbf{r}_{\mathrm{P}}^2\right). \qquad 3.1.7$$

The uncontracted $\{ss\,|\,ss\}$-type integral results from using Eq. 3.1.4 in Eq. 3.1.6 with $N_0(a)S_{00}(\mathbf{r}_{\mathbf{A}}) = \left(2a/\pi\right)^{3/4}$ and the analogously defined other three PGTO prefactors. Applying the Gaussian product rule of Eq. 3.1.7 as well as the following Laplace-like transformation of the Coulomb operator

$$\frac{1}{|\,\mathbf{r}-\mathbf{r}'\,|} = \frac{2}{\pi}\int_0^\infty \exp\left(-|\,\mathbf{r}-\mathbf{r}'\,|^2\,u^2\right)du \qquad 3.1.8$$

in Eq. 3.1.6 yields after several manipulations[4,291,305]

$$\{G_{00a}G_{00b}\,|\,G_{00c}G_{00d}\} = Z\cdot\exp\left(-(ab/p)\overline{\mathbf{AB}}^2\right)\exp\left(-(cd/q)\overline{\mathbf{CD}}^2\right)\int_0^1 \exp\left(-\gamma\,\overline{\mathbf{PQ}}^2u^2\right)du\,. \qquad 3.1.9$$

The variables q and $\mathbf{Q}$ are defined analogously to p and $\mathbf{P}$, respectively. Furthermore, the intermediates

$$\gamma = \frac{pq}{p+q} \quad \text{and} \quad Z = \frac{16}{\sqrt{\pi}}\frac{(abcd)^{3/4}}{pq\sqrt{p+q}} \qquad 3.1.10$$

are introduced. The integral in Eq. 3.1.9 is an example of the Boys function, which, for reasons discussed below, is generalized to an arbitrary order M (with $M \geq 0$)[4,291]

$$F_M(x) = \int_0^1 u^{2M}\exp\left(-xu^2\right)du\,. \qquad 3.1.11$$

The Mth-order Boys functions $F_M(x)$ are related to the error function, the incomplete gamma function, and other special functions.[4,291,306]

Subsequently, the final batch of $(ss\,|\,ss)$ integrals can be formed according to Eq. 3.1.5 from the $\{i'j'\,|\,k'l'\}$ ERIs for all quadruples of primitive exponents. The ERI in Eq. 3.1.6 has thus been reduced to a much simpler one-dimensional integral over the finite interval $[0,1]$.

Having established a method to obtain ERIs over four *s*-type centers, this algorithm can be generalized to the calculation of integral-classes over AOs of higher angular momenta like

$(ps\,|\,ps)$, $(fd\,|\,dp)$, … . In contrast to $(ss\,|\,ss)$-type integrals, such ERIs include integrands with angular degrees of freedom, hence $\ell > 0$. Using the identity $\mathbf{r_A} = \mathbf{r_P} + \overline{\mathbf{PA}}$ and expanding polynomial products of the form $(r - P_r + \overline{PA}_r)^{i_r}(r - P_r + \overline{PB}_r)^{j_r}$ allows one to obtain the corresponding ERI formulae for general PGTOs from a derivation analogous to that of Eq. 3.1.9.[307] Nevertheless, with growing angular momentum ℓ the resulting expressions quickly become much more involved than Eq. 3.1.9.

PGTOs have the very useful property that their angular prefactors can be obtained from a parameter differentiation with respect to their nuclear centers.[2,4] For a p_z-type primitive AO this concept is illustrated as follows:

$$\begin{aligned} &G_{10a_{i'}}(\mathbf{r_A}) \propto (z - A_z)\exp\left(-a_{i'}(\mathbf{r}-\mathbf{A})^2\right) = \frac{1}{2a_{i'}}\frac{\partial}{\partial A_z}\exp\left(-a_{i'}(\mathbf{r}-\mathbf{A})^2\right) \\ &\Rightarrow \{G_{10a_{i'}}\, j'\,|\,k'l'\} \propto \frac{1}{2a_{i'}}\frac{\partial}{\partial A_z}\{G_{00a_{i'}}\, j'\,|\,k'l'\} \end{aligned} \qquad 3.1.12$$

When applied to Eq. 3.1.9 for general ERI classes of higher angular momenta, a repetitive differentiation of both overlap and integral factors is required. Furthermore, cross-terms arise for $\ell > 1$ or non-zero angular momenta on different centers so an explicit parameter differentiation quickly becomes rather cumbersome that in such cases. General real solid spherical harmonic angular GTO prefactors can be obtained from parameter differentiation as well.[301,302,308-311] Such approaches are based on the application of the spherical harmonic tensor gradient theory, which is formulated in terms polynomial differential operators of the form $S_{\ell_i m_i}(\nabla_\mathbf{A})$.[301,302,308-311] Different rules are known for the coupling of angular momenta and the application of spherical harmonic tensors which can be employed to compute ERIs over SHCGTOs.[301,302,308-314]

However, most ERI algorithms do not directly compute integrals over SHCGTOs, but first evaluate integrals over contracted Gaussian orbitals with Cartesian angular prefactors (CCGTO)

$$\tilde{\varphi}_i(\mathbf{r}) = \sum_{i'}^{\kappa_i} c_{ii'} G_{\mathbf{i}a_{i'}}(\mathbf{r_A}) = \sum_{i'}^{\kappa_i} c_{ii'} N_\mathbf{i}(a_{i'})(x - A_x)^{i_x}(y - A_y)^{i_y}(z - A_z)^{i_z}\exp\left(-a_{i'}\mathbf{r_A}^2\right) \quad 3.1.13$$

with $\mathbf{i} = (i_x, i_y, i_z)$ and $0 \le i_x \le i_y \le i_z$, $i_x + i_y + i_z = \ell_i$. The resulting integrals are subsequently transformed from the CCGTO to the SHCGTO basis.[315] Integrals over Cartesian GTOs will be denoted as $[\mathbf{ij}\,|\,\mathbf{kl}]$ in the following. For a given angular momentum ℓ, the magnetic quantum number m varies from $-\ell$ to ℓ which results in $2\ell+1$ different functions $S_{\ell m}$. In contrast, the corresponding set of Cartesian prefactors includes $(\ell+2)(\ell+1)/2$ elements and thus, is larger than the number of spherical harmonic functions for $\ell > 1$. The additional Cartesian prefactors with $\ell > 1$ result in form of lower angular momentum functions; for example $\mathbf{r_A}^2$ in the case of d-orbitals, $(r - A_r)\mathbf{r_A}^2$ for f-type shells, and so on. Furthermore, the repetitive differentiation of the PGTOs with respect to the nuclear coordinates

$$\begin{aligned}\tilde{G}_{\mathbf{i}a_{i'}}(\mathbf{r}_\mathbf{A}) &= \tilde{N}_\mathbf{i}(a_{i'})\sqrt{a_{i'}}\tilde{h}_\mathbf{i}(\sqrt{a_{i'}}\mathbf{r}_\mathbf{A})\exp\left(-a_{i'}\mathbf{r}_\mathbf{A}{}^2\right) \\ &= \tilde{N}_\mathbf{i}(a_{i'})\left(\frac{\partial}{\partial A_x}\right)^{i_x}\left(\frac{\partial}{\partial A_y}\right)^{i_y}\left(\frac{\partial}{\partial A_z}\right)^{i_z}\exp\left(-a_{i'}\mathbf{r}_\mathbf{A}{}^2\right)\end{aligned} \qquad 3.1.14$$

does not directly generate the Cartesian prefactors but rather yields angular components in terms of Hermite polynomials $\tilde{h}_\mathbf{i}$. Integrals over Hermite polynomials may either be converted to the $[\mathbf{ij}|\mathbf{kl}]$ batch or directly transformed to the SHCGTO basis.[316]

Despite their larger number for $\ell > 1$ and the need to convert the Hermite polynomials, Cartesian prefactors allow for more transparent expressions which resulted in the development of powerful and versatile recursion relations.[303] Corresponding recursion techniques for ERIs over spherical harmonic PGTOs have been suggested as well, but are either far more involved or less well applicable.[317] The recursion relations for ERIs over Cartesian GTOs will be discussed after presenting the techniques for the computation of the Boys functions.

Differentiating the integral factor in Eq. 3.1.9, hence the zero-order Boys function, with respect to $x = \gamma\overline{\mathbf{PQ}}^2$ directly leads to the aforementioned Boys functions of order *M*,

$$\frac{\partial^M F_0(x)}{\partial x^M} = (-1)^M \int_0^1 u^{2M}\exp\left(-xu^2\right)du = (-1)^M F_M(x)\ . \qquad 3.1.15$$

It can be shown that any ERI over PGTOs can be expressed as a linear combination of Boys functions up to order $\ell_{\text{tot}} = \ell_i + \ell_j + \ell_k + \ell_l$,

$$\{i'j'|k'l'\} = Z\sum_{M=0}^{\ell_{\text{tot}}}\Omega_M F_M(\gamma\overline{\mathbf{PQ}}^2), \qquad 3.1.16$$

whereas the coefficients Ω_M denote complicated functions of ℓ, m, $a_{i'}$, and $\mathbf{A}$ of all four PGTOs, respectively.[307,318] Thus, ERIs over GTOs with nonzero angular momenta require the calculation of the entire series of Boys functions from F_0 to $F_{\ell_{\text{tot}}}$.

At $x = 0$ the exponential factor of the integrand in Eq. 3.1.15 equals one. In consequence, the remaining monomial integrates to

$$F_M(0) = \int_0^1 u^{2M}du = 1/(2M+1)\ . \qquad 3.1.17$$

In combination with $\partial F_M(x)/\partial x = -F_{M+1}(x)$ this allows for a Taylor-series expansion

$$F_M(x) = \sum_i^\infty \frac{(-x)^i}{i!\ (2M+2i+1)} \qquad 3.1.18$$

around $x = 0$. While this series is always convergent,[4] several hundred terms may be required to compute $F_M(x)$ from Eq. 3.1.18 with a sufficiently high accuracy.[22] However, the convergence of the series can be significantly improved if pre-tabulated $F_M(x)$ values on a regular grid $x = x_t$ are used,[4,318-320]

[22] For the FORTRAN double precision floating point data type of 64 bit length this implies a relative precision of 10^{-16}.

$$F_M(x) = \sum_{i=0}^{M_t} \frac{F_{M+i}(x_t)(x_t - x)^i}{i!} \quad . \tag{3.1.19}$$

If x lies in between (sufficiently close) grid points, the Taylor expansion from the nearest grid point converges after a few terms only.[4] Having obtained the value of $F_{\ell_{\text{tot}}}(x)$, the Boys functions of lower orders are computed in terms of the following "downward" recursion

$$F_M(x) = \frac{2x \cdot F_{M+1}(x) + \exp(-x)}{2M+1} . \tag{3.1.20}$$

If the Boys functions are tabulated over a sufficiently large interval of x, the expression

$$F_M(x) \approx \frac{(2M-1)!!}{2^{M+1}} \sqrt{\frac{\pi}{x^{2M+1}}} , \qquad x \gg 1 \tag{3.1.21}$$

can be used to compute $F_M(x)$ for x values beyond the extent of the grid. In this case it may be sufficient to use Eq. 3.1.21 to compute $F_0(x)$ only. All other $F_M(x)$ values can then be obtained from the "upward" recursion formula

$$F_{M+1}(x) = \frac{(2M+1) \cdot F_M(x) - \exp(-x)}{2x} , \tag{3.1.22}$$

which becomes stable at sufficiently large values of x. The Boys functions F_M of orders $M = 0, \ldots, \ell_i + \ell_j + \ell_k + \ell_l$ can then be converted into the derivatives of F_0 with respect to the distance between the product centers **P** and **Q**

$$\Gamma_{\mathbf{0}}^{M}(\gamma \overline{\mathbf{PQ}}^2) = Z \left(\frac{\partial}{\partial \overline{\mathbf{PQ}}^2} \right)^M F_0(\gamma \overline{\mathbf{PQ}}^2) = Z(-2\gamma)^2 F_M(\gamma \overline{\mathbf{PQ}}^2) \quad . \tag{3.1.23}$$

The use of recursion relations became popular with the approach of McMurchie and Davidson (MD) to four-center integrals.[319] Indeed, the MD method was the first ERI algorithm which was equally efficient for various ERI classes, over CGTOs with large contraction length κ_i as well as over CGTOs with higher angular momenta.[319] The MD algorithm is based on the idea to generate higher angular momentum functions via derivatives with respect to the centers **P** and **Q**,

$$\begin{aligned} & Z \frac{\partial^{p_x}}{\partial P_x^{p_x}} \frac{\partial^{p_y}}{\partial P_y^{p_y}} \frac{\partial^{p_z}}{\partial P_z^{p_z}} \frac{\partial^{q_x}}{\partial Q_x^{q_x}} \frac{\partial^{q_y}}{\partial Q_y^{q_y}} \frac{\partial^{q_z}}{\partial Q_z^{q_z}} F_0(\gamma \overline{\mathbf{PQ}}^2) \\ & = Z(-1)^{q_x+q_y+q_z} \frac{\partial^{p_x+q_x}}{\partial P_x^{p_x+q_x}} \frac{\partial^{p_y+q_y}}{\partial P_y^{p_y+q_y}} \frac{\partial^{p_z+q_z}}{\partial P_z^{p_z+q_z}} F_0(\gamma \overline{\mathbf{PQ}}^2) = (-1)^{q_x+q_y+q_z} \Gamma_{\mathbf{p}+\mathbf{q}}^{0}(\gamma \overline{\mathbf{PQ}}^2) \quad . \end{aligned} \tag{3.1.24}$$

In this context it is common to define $\mathbf{p} = (p_x, p_y, p_z)$, $\mathbf{q} = (q_x, q_y, q_z)$, $p_x = i_x + j_x$, $q_x = j_x + l_x$, and so on. The first-order derivative with respect to a single Cartesian component $r = x, y, z$ of **P** yields

$$\frac{\partial}{\partial P_r} F_0(\gamma \overline{\mathbf{PQ}}^2) = \left(\frac{\partial \overline{\mathbf{PQ}}^2}{\partial P_r} \right) \left(\frac{\partial F_0}{\partial \overline{\mathbf{PQ}}^2} \right) = \overline{\mathbf{PQ}}(-2\gamma)^2 F_M(\gamma \overline{\mathbf{PQ}}^2) , \tag{3.1.25}$$

whereas the partial derivative on the right hand side of Eq. 3.1.25 is provided by Eq. 3.1.23. From the commutative behavior of the derivative operator

$$\left(\frac{\partial}{\partial P_r}\right)^{p_r} \overline{PQ}_r = p_r \left(\frac{\partial}{\partial P_r}\right)^{p_r-1} + \overline{PQ}_r \left(\frac{\partial}{\partial P_r}\right)^{p_r}, \qquad 3.1.26$$

the intermediates Γ in Eq. 3.1.24 are found to behave according to

$$\Gamma^{M}_{\mathbf{p+q+1}_r}(\gamma\overline{\mathbf{PQ}}^2) = \overline{PQ}_r \cdot \Gamma^{M+1}_{\mathbf{p+q}}(\gamma\overline{\mathbf{PQ}}^2) + p_r \cdot \Gamma^{M+1}_{\mathbf{p+q-1}_z}(\gamma\overline{\mathbf{PQ}}^2) \ . \qquad 3.1.27$$

With $\Gamma^{M}_{\mathbf{0}}(\gamma\overline{\mathbf{PQ}}^2)$ given by Eq. 3.1.23 this defines a recursion relation for Eq. 3.1.24 which relates the order *M* of the Boys function to Hermite polynomials of varying degree. Thus, Eqs. 3.1.24 to 3.1.27 lead to integrals over Gaussian product distributions with Hermite polynomial prefactors, centered at **P** and **Q**, respectively.

These intermediates may be coupled with the Hermite functions that originate from the differentiation of the overlap factors,[23]

$$\begin{aligned} & Z\frac{\partial^{i_r}}{\partial {A_r}^{i_r}} \exp\left(-\frac{ab}{p}\overline{\mathbf{AB}}^2\right) F_0(\gamma\overline{\mathbf{PQ}}^2) \\ & = Z\sum_{t=0}^{i_r}\left(\left(\frac{\partial}{\partial A_r}\right)^{t} \exp\left(-\frac{ab}{p}\overline{\mathbf{AB}}^2\right)\right)\left(\left(\frac{\partial P_r}{\partial A_r}\right)^{i_r-t} \Gamma^{0}_{i_r\mathbf{1}_r-t\mathbf{1}_r}(\gamma\overline{\mathbf{PQ}}^2)\right) . \end{aligned} \qquad 3.1.28$$

The resulting integrals over GTOs with Hermite prefactors $\tilde{h}_{\mathbf{i}}(\mathbf{r}_\mathbf{A})$ can then be converted into integrals over $G_{\mathbf{i}a_{i'}}(\mathbf{r}_\mathbf{A})$. Originally, MD proposed an alternative approach to convert the $\Gamma^{0}_{\mathbf{p+q}}$ intermediates to the final ERIs.[319] Their approach consists in a direct transfer of angular momentum from the Hermite product distributions to the Cartesian AO functions.[319] This approach is understood best in terms of product distributions with combined Cartesian atom-centered and product-centered Hermite angular components,

$$\tilde{P}^{\mathbf{p}}_{\mathbf{ij}} = \exp\left(-(\mathbf{x}-\mathbf{P})^2\right) \prod_{r=x,y,z} (r-A_r)^{i_r} \cdot (r-B_r)^{j_r} \cdot p^{p_r/2} \tilde{h}_{p_r}\left(p^{1/2}(r-P_r)\right) . \qquad 3.1.29$$

The results of the recursion in Eq. 3.1.27, hence the uncontracted ERIs over product distributions with Hermite polynomial prefactors can then be rewritten as follows

$$[\tilde{P}^{\mathbf{p}}_{\mathbf{00}} \mid \tilde{Q}^{\mathbf{q}}_{\mathbf{00}}] = (-1)^{q_x+q_y+q_z} \Gamma^{0}_{\mathbf{p+q}}(\gamma\overline{\mathbf{PQ}}^2) . \qquad 3.1.30$$

After adding and subtracting P_r in one of the $(r-A_r)$ factors in Eq. 3.1.29 according to

$$(r-A_r)^{u_i} = (r-P_r)(r-A_r)^{i_r-1} + (P_r-A_r)(r-A_r)^{i_r-1} \qquad 3.1.31$$

and using the Hermite recursion formula

$$(p^{1/2}r)\cdot p^{p_r/2}\tilde{h}_{p_r}(p^{1/2}r) = p_r \cdot \tilde{h}_{p_r-1}(p^{1/2}r) + \tfrac{1}{2}\tilde{h}_{p_r+1}(p^{1/2}r) \ , \qquad 3.1.32$$

one obtains the recursive MD transfer relation[319]

$$\tilde{P}^{\mathbf{p}}_{\mathbf{ij}} = p_r \cdot \tilde{P}^{\mathbf{p-1}_r}_{\mathbf{i-1}_r,\mathbf{j}} + (P_r-A_r)\tilde{P}^{\mathbf{p}}_{\mathbf{i-1}_r,\mathbf{j}} + \frac{1}{2p}\tilde{P}^{\mathbf{p+1}_r}_{\mathbf{i-1}_r,\mathbf{j}} . \qquad 3.1.33$$

Eq. 3.1.33 and its analogues for the other Cartesian components and product centers include only quantities over which ERIs were established above. Thus, one can equally well write

[23] Note, that upon successive application of $\partial/\partial B_x$ to Eq. 3.1.28 various cross-terms have to be considered and that the factor $(-1)^{u'+v'+w'}$ needs to be included in the derivatives with respect to C_x and D_x.

$$[\tilde{P}^{\mathbf{p}}_{\mathbf{i}+\mathbf{1}_r,\mathbf{j}}\,|\,\tilde{Q}^{\mathbf{q}}_{\mathbf{kl}}] = p_r\cdot[\tilde{P}^{\mathbf{p}-\mathbf{1}_r}_{\mathbf{ij}}\,|\,\tilde{Q}^{\mathbf{q}}_{\mathbf{kl}}] + \overline{PA}_r\cdot[\tilde{P}^{\mathbf{p}}_{\mathbf{ij}}\,|\,\tilde{Q}^{\mathbf{q}}_{\mathbf{kl}}] + \frac{1}{2p}[\tilde{P}^{\mathbf{p}+\mathbf{1}_r}_{\mathbf{ij}}\,|\,\tilde{Q}^{\mathbf{q}}_{\mathbf{kl}}], \qquad 3.1.34a$$

$$[\tilde{P}^{\mathbf{p}}_{\mathbf{ij}}\,|\,\tilde{Q}^{\mathbf{q}}_{\mathbf{k}+\mathbf{1}_r,\mathbf{l}}] = q_r\cdot[\tilde{P}^{\mathbf{p}}_{\mathbf{ij}}\,|\,\tilde{Q}^{\mathbf{q}-\mathbf{1}_r}_{\mathbf{kl}}] + \overline{QC}_r\cdot[\tilde{P}^{\mathbf{p}}_{\mathbf{ij}}\,|\,\tilde{Q}^{\mathbf{q}}_{\mathbf{kl}}] + \frac{1}{2q}[\tilde{P}^{\mathbf{p}}_{\mathbf{ij}}\,|\,\tilde{Q}^{\mathbf{q}+\mathbf{1}_r}_{\mathbf{kl}}], \qquad 3.1.34b$$

and obtain the final uncontracted integrals over Cartesian PGTOs as

$$[\mathbf{ij}\,|\,\mathbf{kl}] = [\tilde{P}^{\mathbf{0}}_{\mathbf{ij}}\,|\,\tilde{Q}^{\mathbf{0}}_{\mathbf{kl}}]\ . \qquad 3.1.35$$

Equivalent MD algorithms result when Eqs. 3.1.34 are reformulated as matrix multiplications or by expanding Eq. 3.1.28 and subsequently transforming the resulting integrals.[4,316]

Recursion relations are not restricted to Hermite functions only. From combining the parameter differentiation with the translational invariance property,

$$\left(\nabla_{\mathbf{A}}+\nabla_{\mathbf{B}}+\nabla_{\mathbf{C}}+\nabla_{\mathbf{D}}\right)[\mathbf{ij}\,|\,\mathbf{kl}] = \mathbf{0}\,, \qquad 3.1.36$$

Obara–Saika[321,322] (OS) and others[323,324] discovered a recursion relation which provides a direct transformation of the $[\mathbf{00}\,|\,\mathbf{00}]^M = \Gamma^M_{\mathbf{0}}(\alpha\overline{\mathbf{PQ}}^2)$ intermediates into $[\mathbf{ij}\,|\,\mathbf{kl}] = [\mathbf{ij}\,|\,\mathbf{kl}]^0$ integrals,[303]

$$\begin{aligned}[\mathbf{i}+\mathbf{1}_r,\mathbf{j}\,|\,\mathbf{kl}]^M &= \overline{PA}_r[\mathbf{ij}\,|\,\mathbf{kl}]^M + \frac{1}{2p}\overline{PQ}_r[\mathbf{ij}\,|\,\mathbf{kl}]^{M+1}\\ &+\frac{i_r}{2p}\left([\mathbf{i}-\mathbf{1}_r,\mathbf{j}\,|\,\mathbf{kl}]^M - \frac{1}{2p}[\mathbf{i}-\mathbf{1}_r,\mathbf{j}\,|\,\mathbf{kl}]^{M+1}\right)\\ &+\frac{j_r}{2p}\left([\mathbf{i},\mathbf{j}-\mathbf{1}_r\,|\,\mathbf{kl}]^M - \frac{1}{2p}[\mathbf{i},\mathbf{j}-\mathbf{1}_r\,|\,\mathbf{kl}]^{M+1}\right)\\ &+\frac{1}{4pq}\left(k_r[\mathbf{ij}\,|\,\mathbf{k}-\mathbf{1}_x,\mathbf{l}]^{M+1} + l_r[\mathbf{ij}\,|\,\mathbf{kl}-\mathbf{1}_x]^{M+1}\right).\end{aligned} \qquad 3.1.37$$

Based on the MD and OS approaches a large number of variations were developed in the following.[303,325-333] From using identities like $(x-B_x) = (x-A_x)+(A_x-B_x)$ inside the electron repulsion integrals, another important connection can be established

$$[\mathbf{i},\mathbf{j}+\mathbf{1}_r\,|\,\mathbf{kl}] = \overline{AB}_r[\mathbf{i},\mathbf{j}\,|\,\mathbf{kl}] + [\mathbf{i}+\mathbf{1}_r,\mathbf{j}\,|\,\mathbf{kl}]\,, \qquad 3.1.38$$

which is known as horizontal recursion relation (HRR).[325] The horizontal recursion relation effectively transfers angular momentum between the two bra-side centers (likewise for the ket side).[325,334,335] Thus, Eq. 3.1.38 allows one to reduce the generation of angular momenta to intermediate $[\mathbf{e0}\,|\,\mathbf{f0}]$-type classes. These intermediate classes include all integrals over Cartesian GTOs with angular momenta ranging from $\ell_e = \ell_i$ to $\ell_i+\ell_j$ and, likewise, $\ell_f = \ell_k,\ldots,\ell_k+\ell_l$. The number N_{ef} of such intermediates is at most equal than the size N_{ijkl} of the final $[\mathbf{ij}\,|\,\mathbf{kl}]$ class, as shown here for the bra side

$$\begin{aligned}&\left((\ell_i+\ell_j+1)(\ell_i+\ell_j+2)(\ell_i+\ell_j+3) - \ell_i(\ell_i+1)(\ell_i+2)\right)/6\\ &\qquad\le (\ell_i+1)(\ell_i+2)(\ell_k+1)(\ell_k+2)/4\ .\end{aligned} \qquad 3.1.39$$

The HRR in Eq. 3.1.38 itself does not provide any significant benefit because a similar number of elements needs to be processed to obtain the final $[\mathbf{ij}\,|\,\mathbf{kl}]$ class of integrals as during a direct generation of ERIs. The great advantage of the horizontal recursion relation

derives from the fact that Eq. 3.1.38 does not comprise any primitive-related quantities (like exponents or product center coordinates) and thus applies to fully contracted integral classes as well. A significant amount of computational labor can thereby be shifted from the κ4 stage to the κ2 and κ0 stages. Following this "earlier contraction" strategy, Head-Gordon–Pople (HGP) used the five-term variant of the OS recursion, Eq. 3.1.37, termed vertical recursion relation (VRR) that results for ERI classes with $\mathbf{j}=\mathbf{l}=\mathbf{0}$.[325] The VRR can be used to obtain the intermediates $[\mathbf{e0}\,|\,\mathbf{f0}]$, which are subsequently contracted and then transformed into integrals over CCGTOs by means of the HRR.[325] The MD algorithm benefits from the HRR as well. Only uncontracted $[\mathbf{e0}\,|\,\mathbf{f0}]$ classes have to be computed from Eq. 3.1.34, which significantly simplifies the MD transfer step in Eq. 3.1.33.

The concept of early contraction can be extended even further.[303,326,327] In this context one employs identities like

$$\overline{\mathbf{PA}}=\frac{2b}{2p}\overline{\mathbf{BA}} \qquad 3.1.40$$

and "pre-scaled" variants of the combined Hermite-Cartesian distributions from Eq. 3.1.29,

$$\tilde{P}_{\mathbf{ij}}^{\mathbf{p}u v}=\frac{(2b)^u}{(2p)^{u+v}}\tilde{P}_{\mathbf{ij}}^{\mathbf{p}} \quad . \qquad 3.1.41$$

The intermediates $\tilde{Q}_{\mathbf{kl}}^{\mathbf{q}u'v'}$ are analogously defined for the ket-side. When using Eqs. 3.1.40 and 3.1.41, the MD transfer relation can be reformulated as follows[303,326,327]

$$[\tilde{P}_{\mathbf{i}+\mathbf{1}_r,\mathbf{j}}^{\mathbf{p}uv}\,|\,\tilde{Q}_{\mathbf{kl}}^{\mathbf{q}u'v'}]=p_r\cdot[\tilde{P}_{\mathbf{ij}}^{\mathbf{p}-\mathbf{1}_r uv}\,|\,\tilde{Q}_{\mathbf{kl}}^{\mathbf{q}u'v'}]+\overline{BA}_r\cdot[\tilde{P}_{\mathbf{ij}}^{\mathbf{p},u+1,v}\,|\,\tilde{Q}_{\mathbf{kl}}^{\mathbf{q}u'v'}]+[\tilde{P}_{\mathbf{ij}}^{\mathbf{p}+\mathbf{1}_r u,v+1}\,|\,\tilde{Q}_{\mathbf{kl}}^{\mathbf{q}u'v'}]. \qquad 3.1.42$$

Apart from the integrals over the pre-scaled distributions from Eq. 3.1.41, this reformulation is free from any quantities that depend on the primitive indices.[303,326,327] Thus, Eq. 3.1.42 applies to contracted $[\tilde{P}_{\mathbf{ij}}^{\mathbf{p}uv}\,|\,\tilde{Q}_{\mathbf{kl}}^{\mathbf{q}u'v'}]$ integrals as well, just as the HRR. Indeed, the contracted variant of Eq. 3.1.42 provides efficiency gains for batches with large contraction ratios, hence the ratio between the number of CGTOs and PGTOs.[303,326,327] The identity

$$\overline{\mathbf{PQ}}=\overline{\mathbf{AC}}+\frac{2b}{2p}\overline{\mathbf{BA}}-\frac{2d}{2q}\overline{\mathbf{DC}} \qquad 3.1.43$$

allows one to apply the early contraction concept to the HGP or OS equations, Eq. 3.1.37, and even to the generation of Hermite Coulomb integrals in Eq. 3.1.27. Furthermore, the electron transfer relation[328]

$$\begin{aligned}[\mathbf{e0}\,|\,\mathbf{f}+\mathbf{1}_r,\mathbf{0}]=\Big(&e_r[\mathbf{e}-\mathbf{1}_r,\mathbf{0}\,|\,\mathbf{f0}]+f_r[\mathbf{e0}\,|\,\mathbf{f}-\mathbf{1}_r,\mathbf{0}]-2p[\mathbf{e}+\mathbf{1}_r,\mathbf{0}\,|\,\mathbf{f0}]\\&-2b\cdot\overline{AB}_r\cdot[\mathbf{e0}\,|\,\mathbf{f0}]+2d\cdot\overline{CD}_r\cdot[\mathbf{e0}\,|\,\mathbf{f0}]\Big)\Big/2q\end{aligned} \qquad 3.1.44$$

represents an additional recursion relation which, in its contracted variant, can occasionally provide further computational savings.[303] Eq. 3.1.44 allows one to shift angular momentum between bra and ket sides and emerges from Eq. 3.1.36 as well.[303,328] The algorithms resulting from Eq. 3.1.43 permit one to carry out the contraction steps already at the stage of derivatives of pre-scaled Boys functions

$$_{uv}[\mathbf{0}]^{M}_{u'v'} = \frac{(2b)^{u}(2d)^{u'}}{(2p)^{u+v}(2q)^{u'+v'}}\Gamma^{M}_{\mathbf{0}}(\gamma\overline{\mathbf{PQ}}^{2}), \qquad 3.1.45$$

which are obtained directly from Eq. 3.1.23 and defined analogously to the pre-scaled Hermite-Cartesian product distributions in Eq. 3.1.41.[327,330] However, as such early contraction strategies can significantly increase the operation count at the κ0 step for larger ℓ values, they may not always represent the optimal choice for a specific ERI class.[303] For a given ERI batch selecting the optimal sequence of transformation and contraction steps out of several different algorithmic pathways represents the key idea of the PRISM algorithm.[303,326,327,329,331,333] Alternative MD based pre-scaling methods exist.[332]

In a similar fashion, computational workload can be shifted from the κ4 to the κ0 stage by applying a rotation to the coordinates of the atomic centers, which is the key concept of the Pople–Hehre algorithm (PH).[336] The rotations are defined in such a way that many Cartesian components of the distance vectors between the centers ($\overline{\mathbf{AB}}$, $\overline{\mathbf{PA}}$, etc.) vanish, which simplifies the recursions over uncontracted intermediates.[336] The number of κ0 operations is increased though, as the corresponding inverse rotations need to be applied to the contracted integrals.[336] Therefore, the original PH approach was limited to *s* and *p*-type CGTOs.[336] Recently, more flexible combinations of PH-type rotations with the MD and PRISM algorithms were proposed as well.[333,337]

```
FOR i'_block = 0, κ_i INCREMENT i_inc
 FOR j'_block = 0, κ_j INCREMENT j_inc
  FOR k'_block = 0, κ_k INCREMENT k_inc
   FOR l'_block = 0, κ_l INCREMENT l_inc
    i'_beg = i'_block · i_inc + 1;  i'_end = i'_block · i_inc + i_inc
    j'_beg = …
    COMPUTE [e0|q](i'_beg : i'_end, j'_beg : j'_end, k'_beg : k'_end, l'_beg : l'_end)
    CONTRACT [e0|q]
  …
END
```

Scheme 3.1.1: Block reformulation of the loops in the κ4 steps. The ranges $i'_{beg}:i'_{end}$, $j'_{beg}:j'_{end}$, $k'_{beg}:k'_{end}$, and $l'_{beg}:l'_{end}$ denote the four fastest running array axes.

Apart from algorithmic reductions of the floating point operation (FLOP) counts, another essential factor has to be considered for an efficient ERI computation.[338] Modern CPU architectures are able to carry out an enormous number of FLOPs per second but exhibit only a comparatively limited bandwidth to the main memory.[338] This mismatch is partially resolved by a hierarchical structure of intermediate cache storages of successively higher

bandwidth but decreasing size.[338] To use such architectures efficiently, as many operations as possible have to be carried out on small data arrays whose sizes fit into the available cache storages.[338] In the case of the most expensive κ4 steps of ERI algorithms, this implies processing the primitive axes in blocks as shown in Scheme 3.1.1. For high angular momenta the uncontracted intermediates have rather large pre-scaling index axes, which only admit for short loops[24] over the primitive quadruples or may not even fit at all into the low-level cache storages.

This problem is less severe for Gauss-quadrature based algorithms, which represent another important approach to ERIs.[339,340] The key concept of such methods is to carry out the parameter differentiation before the one-dimensional integration in Eq. 3.1.9. To this end, Eq. 3.1.16 is reformulated as

$$\{i'j' \mid k'l'\} = Z \sum_{M=0}^{\ell_{\text{tot}}} \Omega_M F_M(\gamma \overline{\mathbf{PQ}}^2) = Z \int_0^1 \exp\left(-\gamma \overline{\mathbf{PQ}}^2 u^2\right) \left(\sum_{M=0}^{\ell_{\text{tot}}} \Omega_M u^{2M} \right) du \ . \quad 3.1.46$$

Most important is the presence of the polynomial factor in terms the variable u on the right-hand side of Eq. 3.1.46. According to the Gauss-quadrature formula, such polynomials $\Im_{2M}(u)$ up to a degree m can be exactly integrated to

$$\int_{-u'}^{u'} \Im_{2M}(u)\, \omega(u)\, du = \sum_{t}^{m} \Im_{2M}(u_t)\, w_t \ , \quad 3.1.47$$

for a specific weighting function $\omega(u)$ and over a given interval $[-u', u']$. Here, u_t and w_t are the roots and weights of the t-th member of the class of polynomials which are, for the given weighting function $\omega(u)$, orthogonal over the interval $[-u', u']$. In the case of

$$\omega(u) = \exp\left(-\gamma \overline{\mathbf{PQ}}^2 u^2\right) \quad 3.1.48$$

and $u' = 1$ this leads to the class of Rys polynomials whose roots and weights are determined by the value of $\gamma \overline{\mathbf{PQ}}^2$.[340,341]

While different Rys polynomials have to be computed for every quadruple of PGTOs, most algorithmic parts of Gauss-quadrature based ERI algorithms exhibit a very favorable scaling of operations with respect to the angular momenta.[340,341] This efficiency partially results from $m = \lfloor M/2 \rfloor + 1$, as the polynomials $\Im_{2M}(u)$ are of even order, thus need to be integrated over the interval $[0,1]$ only.[340] The techniques for the calculation of the values for u_t and w_t are significantly more involved but still resemble those used for the computation of the Boys functions.[341-345] Yet, the main advantage of Gauss-quadrature based algorithms consists in the fact that the polynomial $\Im_{2M}(u)$ in Eq. 3.1.46 factorizes into its Cartesian components

[24] Note that long loops over fast running indices are still important for modern CPU architectures because their large computing power partially results from an efficient hardware vectorization (pipelining).

$$[\mathbf{ij}\,|\,\mathbf{kl}] = Z\int_0^1 \exp\left(-\gamma\overline{\mathbf{PQ}}^2 u^2\right)\Im_x(i_x j_x k_x l_x, u)\,\Im_y(i_y j_y k_y l_y, u)\,\Im_y(i_z j_z k_z l_z, u)\,du$$
$$= Z\sum_t^m \Im_x(i_x j_x k_x l_x, u_t)\,\Im_y(i_y j_y k_y l_y, u_t)\,\Im_y(i_z j_z k_z l_z, u_t)\,w_t \quad . \qquad 3.1.49$$

The two-dimensional integrals $\Im_r(i_r j_r k_r l_r, u_t)$ can be obtained from suitably adapted variants of the MD or OS recursion relations, Eqs. 3.1.27, 3.1.34, and 3.1.37.[346] When combined with the HRR, only quantities of the size[25] $\mathcal{O}(\ell_{\text{tot}}^3)$ need to be computed before the assembly of the six-dimensional [**e0**|**f0**] integrals, hence from a correspondingly adapted variant of Eq. 3.1.49. This is to be compared with the quantities which appear in the HGP or HRR+MD approaches and whose numbers scale with $\mathcal{O}(\ell_{\text{tot}}^6)$ at least. Even the very early contraction algorithms have to deal with the pre-scaled Boys functions ${}_{uv}[\mathbf{0}]^M_{u'v'}$, which scale as $\mathcal{O}(\ell_{\text{tot}}^5)$. Due to the small number of the intermediates $\Im_r$, implementations of Gauss-quadrature based ERI algorithms[339,340,346-348] can efficiently exploit cache memory[349] and are even suitable for applications on general purpose graphic processing units.[350-352] However, it is a general drawback of such algorithms that the ERI contraction step can not be carried out prior to the assembly of the six-dimensional integrals in Eq. 3.1.49. Partial ameliorations of this disadvantage have been proposed by combining Gauss-quadrature approaches to ERIs with ideas from early contraction algorithms.[353] Nevertheless, compared to MD or OS, Gaussian-quadrature methods perform best for basis sets with high angular momenta and low contraction ratios as well as for ERI-derivatives (see Section 3.1.4).[349,354]

As their performance varies for batches with different contraction ratios, early contraction and Gaussian-quadrature based algorithms are often implemented together in DFT packages.[355] A specific algorithm is then selected according to the characteristics of the ERI batch at hand (angular momenta, contraction ratios) to achieve an optimal performance. In this context both types of algorithms complement each other with regard their performance for different classes of ERI batches. However, methods that are able to efficiently compute ERIs also in the case of highly contracted GTOs of high angular moments are still desirable. Various algorithms with such capabilities have been derived by means of computer algebra systems or implemented with metaprogramming approaches.[318,333,356-359] The most wide-spread example for an ERI algorithm formulation is the accompanying coordinate expansion (ACE), which, despite of being based on the Boys function, was originally derived from an explicit expansion of the two-dimensional $\Im_r$ integrals.[314,318,360-366] Similar to the PRISM algorithm, the ACE method exhibits different expansion paths, which exhibit very low operation counts in the limit of high angular momenta or large contraction ratios, respectively.[318] In the context of this thesis the ACE method has been extensively studied.

[25] When comparing the amount of data and operations involved in different ERI algorithms, one commonly assumes integral classes of the type $(ss\,|\,ss)$, $(pp\,|\,pp)$, $(dd\,|\,dd)$, etc., thus $\ell_i = \ell_j = \ell_k = \ell_l$. Identical considerations in terms of more general classes can be made but are more cumbersome and unlikely to provide any further insights.

However, as the definition of many relations between intermediate quantities remains unclear in the literature, this method was found to be exceptionally cumbersome to implement efficiently without the original computer algebra derivation at hand.

The rest of this section discusses the ERI implementations carried out as part of this thesis. In this context it has been found useful to implement the calculation of ERI batches separately from their subsequent treatment (see Sections 3.1.2 and 3.1.3). Thus, the modules that perform the calculation of ERIs are only supposed to deliver the final $(IJ \mid KL)$ batch of contracted ERIs. This separation allows one to employ a simpler parallelization concept (see Section 3.1.5) and enables one to switch easily between different ERI implementations.

An early reference implementation was available as an extension of existing PARAGAUSS modules. This implementation is based on the spherical harmonic tensor gradient approach, which is also used to compute the three-center integrals required for calculating the Coulomb repulsion matrix term within the DF-FF approximation, Eq. 3.1.1. However, without significant algorithmic changes, this early implementation performs most of the computational work within the κ4 steps. In consequence, this implementation imposed large memory demands and was found to be not efficient enough for routine calculations.

Thus, a complete re-implementation of the ERI calculation was carried out in the form of the newly developed integral package "ERI4C". As part of this work, also the Boys function was re-implemented with the aim to adapt it specifically to four-center integrals and modern computer architectures. This implementation is based on pre-tabulated values of the Boys function within the interval $x \in [0,46]$ and a bidirectional seven-term Taylor expansion ($M_t = 6$) of $F_M(x)$ (Eq. 3.1.19)

$$F_M(x) = \sum_{i=0}^{M_t} \frac{F_{M+i}(x_t)(x_t - x)^i}{i!} \quad . \qquad 3.1.50$$

A grid spacing of 0.05, hence $\max\{|x - x_t|\} = 0.025$, was employed for this table which includes the values of the Boys functions for up to $M = 32$. These tabulated values allow one to compute ERIs over up to *i*-type ($\ell_i = 6$) GTOs and, eventually, also the corresponding first- and second-order ERI derivatives. Thus, the tabulated Boys function values suffice for all ERI classes which are relevant for hybrid DFT calculations. While Eq. 3.1.50 is used to compute the value of the Boys function of the highest order required, the lower orders result from the "downward" recursion in Eq. 3.1.20, $F_M(x) = (2x \cdot F_{M+1}(x) + \exp(-x))/(2M+1)$. The evaluation of $\exp(-x)$ is comparatively expensive on modern CPU architectures as it needs to be computed iteratively which leads to so-called "pipeline bubbles".[338] Therefore, this function was also tabulated on the aforementioned grid and expanded as an eight-term Taylor series, which $\exp(-x)$ with a precision of 16 digits on the interval $x \in [0,46]$.[303,320] For $x > 46$, $F_0(x)$ is computed from its asymptotic form for large values of *x*, $\frac{1}{2}\sqrt{\pi/x}$ (see Eq. 3.1.21). All other $F_M(x)$ values result from the "upward" recursion formula, Eq. 3.1.22, which was found stable at these *x* values for up to $M = 28$. In this latter case the exponential

function is obtained from a standard function call. The calculation of the square roots in Eqs. 3.1.9 and 3.1.21 are expensive as well.[338] Although not addressed in the context of the present thesis, this issue could be resolved by either low-level instruction calls or the fast inverse square root technique.[338,367]

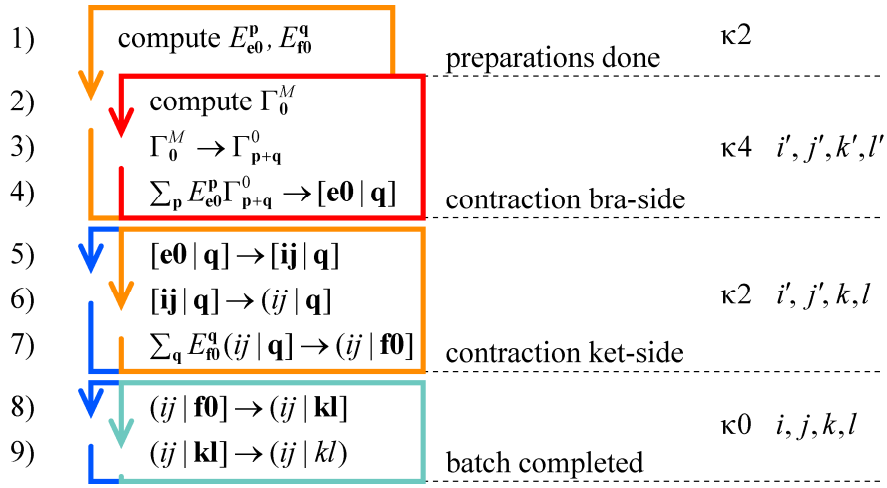

Figure 3.1.2: Individual steps of the MD+HRR algorithm as implemented in the integral package ERI4C. The loop structures comprise iterations over κ2 (orange), κ4 (red), and κ0 (blue) quantities as well as over fully contracted ERIs (light blue).

The newly developed integral package ERI4C combines the MD approach with horizontal recursion relations to expand the Boys function values $F_M(\gamma\overline{\mathbf{PQ}}^2)$ to the final ERIs. This implementation employs a matrix formulation of the MD transfer relations in Eqs. 3.1.34 to obtain the intermediate $[\mathbf{e0}\,|\,\mathbf{f0}]$ integrals. Figure 3.1.2 illustrates the various algorithmic steps of this implementation. After entering the module various auxiliary quantities are initially computed. The most crucial part of this stage is the calculation of the MD transfer matrix representations of Eqs. 3.1.34 (step 1 in Figure 3.1.2), whose Cartesian components are obtained recursively as

$$E^{\mathbf{p}}_{\mathbf{e0}} = E^{p_x}_{e_x} E^{p_y}_{e_y} E^{p_z}_{e_z} \;,\; E^{p_r}_{e_r+1} = \frac{1}{2p} E^{p_r-1}_{e_r} + \overline{PA}_r \cdot E^{p_r}_{e_r} + (p_r+1) \cdot E^{p_r+1}_{e_r}, \qquad 3.1.51$$

whereas $E^{p_r}_{e_r} = 0$ for $p_r < 0$ or $p_r > e_r$.[4] Subsequently the κ4 section is entered, which comprises the aforementioned calculation of the Boys function and its derivatives $\Gamma^{M}_{\mathbf{0}}$ according to Eqs. 3.1.19 to 3.1.23 (step 2). From the $\Gamma^{M}_{\mathbf{0}}$ values, integrals over Hermite product distributions are obtained as in Eq. 3.1.27 (step 3). Like most recursion relations in the context of ERI algorithms, Eq. 3.1.27 exhibits a certain degree of freedom with regard to the order in which the intermediates are generated.[368] One may, for example, aim to generate first the $\Gamma^{0}_{\mathbf{p+q}}$ quantities with the largest $\mathbf{p+q}$ values and then successively complete the Hermite integrals for smaller angular momenta. An alternative approach consists in a

recursion that focusses on evenly lowering the value of *M*. Both approaches were found to comprise the same number of operations.

The effort required for the Hermite-to-Cartesian transformation step is reduced if only one of the bra or ket side is transformed first (step 4). Furthermore, a three-step transformation

$$[\mathbf{e0}\,|\,\mathbf{q}] = \sum_{p_x} E_{e_x}^{p_x} [p_x, e_y, e_z, \mathbf{0}\,|\,\mathbf{q}] \;,\quad [p_x, e_y, e_z, \mathbf{0}\,|\,\mathbf{q}] = \sum_{p_y} E_{e_y}^{p_y} [p_x, p_y, e_z, \mathbf{0}\,|\,\mathbf{q}] \;,$$
$$[p_x, p_y, e_z, \mathbf{0}\,|\,\mathbf{q}] = (-1)^{q_x+q_y+q_z} \sum_{p_z} E_{e_z}^{p_z} \Gamma^0_{\mathbf{p+q}} \qquad 3.1.52$$

allows for further computational savings.[4] As none of the subsequent steps involves primitive quantities of the bra-side,[26] the first half-contraction step can be carried out on the $[\mathbf{e0}\,|\,\mathbf{q}]$ integrals. The half-contracted intermediates are converted into the $(ij\,|\,\mathbf{q}]$ integrals over bra-side SGCTOs by means of the HRR and a subsequent transformation to spherical harmonics (steps 5 and 6). Both steps are carried out as matrix multiplications to reduce the memory access.[334,349] Likewise, the ket-side is transformed by the sequence of Hermite transformation, second half-contraction, HRR, and spherical harmonics transformation (steps 7–9), yielding the final $(IJ\,|\,KL)$ SHCGTO-ERI batch.

Compared to the aforementioned early reference implementation the ERI4C modules were found be about 5–12 times more efficient in the case of small to moderately large test systems. However, a careful cache-optimization could not be carried out in the context of this thesis. Therefore, the ERI4C implementation was still found to be slower by a factor of 6–15 than the highly cache-efficient Gaussian-quadrature based ERD library of Flocke and Lotrich.[349,369] Because of this, the ERD library was employed to compute the $(IJ\,|\,KL)$ batches in most production calculations of this thesis.

3.1.2. Integral Processing and Symmetry Treatment

After being computed by means of one of the algorithms presented in Section 3.1.1, the ERI batches are ready for their subsequent processing. For the present thesis only the contraction with the density matrix to Coulomb and EXX matrices (Eqs. 2.1.10) is of interest. This algorithmic step will be discussed in the following along with the symmetry treatment of ERIs due to permutation and point group symmetries of the **g** tensor of electron-repulsion integrals, $\{\mathbf{g}\}_{ijkl} = (ij\,|\,kl)$.

Original SCF implementations of the HF method[27] computed and stored the required elements of the **g** tensor before the actual SCF iteration. These integrals were then retrieved during every SCF iteration cycle from either computer memory or hard disk storage. However, the number of ERIs and thus the required amount of data to be stored can become

[26] The same holds for the ket-side if $[\mathbf{p}\,|\,\mathbf{f0}]$ is generated first.

[27] Most of the techniques discussed in the following were developed long before the first hybrid functionals.

tremendously large.[28] In response, the direct SCF concept emerged as soon as HF calculations with more than a dozen atoms became feasible.[370] Thereby, the ERI batches are recalculated during every assembly step and immediately contracted with the corresponding blocks of the density matrix.[370] The direct SCF approach avoids the exorbitant usage of memory but in a straightforward implementation increases the computational effort proportional to the number of SCF iteration cycles as the calculation of ERIs represents by far the most expensive computational step. Thus, several measures need to be taken to reduce the computational labor of self-consistent HF and hybrid DFT calculations, which are discussed in this and the next Section.

First, the contraction of ERIs to EXX and Coulomb matrix elements can be exploited to improve the efficiency of the ERI calculation itself. Examples are the J-engine method which performs Coulomb-type density matrix contractions of ERI calculation intermediates,[371] Pople–Hehre-type rotations on Coulomb and exchange matrix elements,[328] and the storage of coordinate independent ERI intermediates.[372,373]

An almost trivial way to reduce the computational effort of the calculation of ERIs is to exploit the intrinsic permutation symmetry of the **g**-tensor,

$$(ij\,|\,kl) = (ij\,|\,lk) = (ji\,|\,kl) = (ji\,|\,lk) = (kl\,|\,ij) = (kl\,|\,ji) = (lk\,|\,ij) = (lk\,|\,ji)\ . \qquad 3.1.53$$

This reduces the number of required ERIs to pairs of pairs, $N^4/8+N^3/4+N^2 3/8+N/4$. Thus, the computational effort to compute the EXX and Coulomb matrix elements is reduced approximatively by a factor of eight.

A similar reduction is achieved for ERI batches, hence for quadruples of atomic orbital (AO) shell indices, whereas a permutation symmetry-unique batch $(IJ\,|\,KL)$ may be determined by the conditions $I \geq J$, $K \geq L$, and $(I-1)N/2+J \geq (K-1)N/2+L$. In view to restrictions due to the parallelization scheme employed in PARAGAUSS[70,374] for the ERI calculation (Section 3.1.5), the intrinsic ERI symmetries were first considered by means of a single quadruple index i_{batch} which was mapped onto the four shell indices. While this approach looks conceptually simple, the function MAP4 which maps the batch index i_{batch} back to the individual shell indices was found rather complicated. A later code restructuring allowed an explicit fourfold loop over shell indices (or ranges thereof in the case of a parallel run, see Section 3.1.5). This implementation avoids several disadvantages of the former approach, like possible data overflows of i_{batch} and the comparatively expensive mapping function. Scheme 3.1.2 shows both variants on the example of a serial run; see Section 3.1.5 for a discussion of the corresponding parallelized implementation.

---

[28] Taking as example the largest calculations that were performed as part of this thesis, systems of about 9500 CGTOs were computed which would, unless any measures like symmetry or screening treatment are taken, require about 60000 TB of memory or disk space for storing the entire **g**-tensor, $\{\mathbf{g}\}_{ijkl} = (ij\,|\,kl)$.

a)
```
FOR i_batch = 1, N_batch
  I,J,K,L = MAP4(i_batch)
  COMPUTE, PROCESS
END
```

b)
```
IJ = 0
FOR I = 1, N
  FOR J = 1, I
    IJ = IJ + 1
    KL = 0
    FOR K = 1, I
      DO WHILE(L < K AND KL < IJ)
        KL = KL + 1
        COMPUTE, PROCESS
    …
END
```

Scheme 3.1.2: Loop structures for a serial run over quadruples of AO shells in terms of a) a batch variable and b) an explicit fourfold loop over shell indices.

If the permutation symmetries of the **g** tensor in Eq. 3.1.53 are ignored, only a single contribution $\mathbf{K}_{IK}^{JL}$ to the exchange matrix block $\mathbf{K}_{IK}$ emerges from the contraction of the batch $(IJ \mid KL)$ with the density matrix block $\mathbf{P}_{JL}$. Likewise, a single contribution $\mathbf{J}_{IJ}^{KL}$ to $\mathbf{J}_{IJ}$ is obtained in this case. However, as soon as permutation symmetry is exploited, the omitted ERI batches need be compensated by a correspondingly adapted contraction scheme. In the general case, four exchange and two Coulomb contributions result from a permutation symmetry-unique batch:

$$(IJ \mid KL),\ \mathbf{P}_{JL},\ \mathbf{P}_{IL},\ \mathbf{P}_{JK},\ \mathbf{P}_{IK} \rightarrow 2\mathbf{K}_{IK}^{JL},\ 2\mathbf{K}_{JK}^{IL},\ 2\mathbf{K}_{IL}^{JK},\ 2\mathbf{K}_{JL}^{IK} \qquad 3.1.54$$

$$(IJ \mid KL),\ \mathbf{P}_{KL},\ \mathbf{P}_{IJ} \rightarrow 4\mathbf{J}_{IJ}^{KL},\ 4\mathbf{J}_{KL}^{IJ} \qquad 3.1.55$$

Furthermore, several special cases need to be considered for the **K** and **J** matrix contributions if two or more shell indices are equal:

$$(II \mid KL),\ \mathbf{P}_{IK},\ \mathbf{P}_{IL} \rightarrow 2\mathbf{K}_{IL}^{IK},\ 2\mathbf{K}_{IK}^{IL} \qquad 3.1.56a$$

$$(IJ \mid KK),\ \mathbf{P}_{IK},\ \mathbf{P}_{JK} \rightarrow 2\mathbf{K}_{JK}^{IK},\ 2\mathbf{K}_{IK}^{JK} \qquad 3.1.56b$$

$$(IJ \mid KK),\ \mathbf{P}_{IK},\ \mathbf{P}_{JK} \rightarrow 2\mathbf{K}_{JK}^{IK},\ 2\mathbf{K}_{IK}^{JK} \qquad 3.1.56c$$

$$(IJ \mid IJ),\ \mathbf{P}_{II},\ \mathbf{P}_{IJ},\ \mathbf{P}_{JJ} \rightarrow \mathbf{K}_{JJ}^{II},\ 2\mathbf{K}_{JI}^{IJ},\ \mathbf{K}_{II}^{JJ} \qquad 3.1.56d$$

$$(II \mid KK),\ \mathbf{P}_{IK} \rightarrow 2\mathbf{K}_{IK}^{IK} \qquad 3.1.56e$$

$$(II \mid II),\ \mathbf{P}_{II} \rightarrow \mathbf{K}_{II}^{II} \qquad 3.1.56f$$

$$(II \mid KL),\ \mathbf{P}_{KL},\ \mathbf{P}_{II} \rightarrow 2\mathbf{J}_{II}^{KL},\ 2\mathbf{J}_{KL}^{II} \qquad 3.1.57a$$

$$(IJ \mid KK),\ \mathbf{P}_{KK},\ \mathbf{P}_{IJ} \rightarrow 2\mathbf{J}_{IJ}^{KK},\ 2\mathbf{J}_{KK}^{IJ} \qquad 3.1.57b$$

$$(II \mid KK),\ \mathbf{P}_{II},\ \mathbf{P}_{KK} \rightarrow \mathbf{J}_{KK}^{II},\ \mathbf{J}_{II}^{KK} \qquad 3.1.57c$$

$$(IJ \mid IJ),\ \mathbf{P}_{IJ} \rightarrow 4\mathbf{J}_{IJ}^{IJ} \qquad 3.1.57d$$

$$(II \mid II),\ \mathbf{P}_{II} \rightarrow \mathbf{J}_{II}^{II} \qquad 3.1.57e$$

Note, that the prefactors in Eqs. 3.1.54 – 3.1.57 account for the (formal) coupling with transposed density matrix blocks and/or the coupling to transposed matrix blocks. In the case of the contributions to **K**, matrix blocks $\mathbf{P}_{JK}$ and $\mathbf{K}_{JK}^{IL}$ appear with $J < K$. In the PARAGAUSS[70] implementation of the exact-exchange and Coulomb matrix formation, the atomic orbital basis representations of the matrices **P**, **K**, and **J** are stored only as lower triangular matrices. In consequence, some of the matrix blocks of **P** and **K** need to be transposed before the contraction or the addition to the full matrix **K**, respectively.

Aside from the permutation symmetries of the **g**-tensor, the system under study may also exhibit spatial point group symmetries. If G denotes the order of a given point group, G operations $\hat{R}$ can be identified which map various symmetry-equivalent nuclear centers onto each other.[375,376] Likewise, the shell elements $(\varphi_1,\ldots,\varphi_n)$ centered on a nuclear center are generally mapped onto linear combinations $(\tilde{\varphi}_1,\ldots,\tilde{\varphi}_n)$ of shell members located at other, symmetry-equivalent centers.[375,376] This allows for the definition of an $N\times N$ matrix representation **R** of the point group operations $\hat{R}\varphi_i = \tilde{\varphi}_i$ in terms of the vector representations $\mathbf{b}_i$ of the shell elements; $\tilde{\mathbf{b}}_i = \mathbf{b}_i\mathbf{R}$.[375,376] The density matrix[29] **P** and the Fock matrix **f** are both representations of totally symmetric quantities and, therefore, are invariant under the following transformations[375,376]

$$\mathbf{P} = \mathbf{R}\mathbf{P}\mathbf{R}^{\dagger}, \qquad 3.1.58$$

$$\mathbf{f} = \mathbf{R}^{\dagger}\mathbf{f}\,\mathbf{R}. \qquad 3.1.59$$

Like the shell elements themselves the pairs of shell elements, hence matrix blocks $\mathbf{M}_{IJ}$, are also mapped onto linear combinations of shell pair elements. The resulting linear combinations are centered at the corresponding symmetry-equivalent pairs of nuclear positions.[377] Similar relations hold for quadruples of shell elements, thus for ERI batches $(IJ\,|\,KL)$.[377] One can now define G_{IJ} as the number of different matrix shell pair matrix blocks $\mathbf{M}_{\widetilde{IJ}}$ onto which $\mathbf{M}_{IJ}$ can be mapped by the collectivity of point group elements.[377] Likewise, G_{IJKL} is defined for quadruples of shell indices, hence batches.[377] Note, that $G_{IJ} \le G$ and $G_{IJKL} \le G$ always hold. Furthermore, a so-called skeleton matrix[377] $\bar{\mathbf{M}}$ is defined from the original matrix **M** by setting

$$\bar{\mathbf{M}}_{IJ} = G_{IJ}\mathbf{M}_{IJ} \qquad 3.1.60$$

for a single block (e.g. with the lowest pair index *IJ*) out of the G_{IJ} symmetry-equivalent matrix blocks and $\bar{\mathbf{M}}_{\widetilde{IJ}} = \mathbf{0}$ elsewhere.[377] A matrix can be symmetrized according to

$$\mathbf{M}_{\mathrm{sym}} = \frac{1}{2G}\sum_{\mathbf{R}}\mathbf{R}^{\dagger}(\mathbf{M}^{\dagger}+\mathbf{M})\mathbf{R}, \qquad 3.1.61$$

which corresponds to a transformation from an atom centered GTO basis into a basis of symmetry adapted linear combinations of atomic orbitals.[375,376] For a given shell pair, Eq. 3.1.61 represents an average over all image pairs $\widetilde{IJ}$ onto which *IJ* is mapped.[375,376] As the

[29] Note that the Hermitian adjoint in Eq. 3.1.58 appears on the right hand side of **P** because the density matrix is a projector.

Fock matrix is Hermitian and totally symmetric, applying Eq. 3.1.61 to the skeleton Fock matrix $\bar{\mathbf{f}}$ yields the original matrix $\mathbf{f}$ back, whereas the nonzero blocks $\bar{\mathbf{f}}_{IJ}$ are mapped exactly G/G_{IJ} times onto each of their corresponding image shell pair blocks $\bar{\mathbf{f}}_{\bar{I}\bar{J}}$.[377] This implies that the symmetry-unique blocks in $\bar{\mathbf{f}}$ suffice to obtain the full Fock matrix by symmetrization.[377-384] Likewise, the unique contributions $\mathbf{K}_{IK}^{JL}$, $\mathbf{J}_{IJ}^{KL}$, etc. can be shown to yield the totally symmetric contributions after application of Eq. 3.1.61.[384] The above argumentation justifies the "petit list" approach,[377] which allows one to compute and process only one out of the G_{IJKL} symmetry-equivalent ERI batches.[378-384]

This approach was implemented as symmetry treatment for the EXX matrix formation in ParaGauss.[70] Thereby, a list is generated in preparation for the direct SCF part. This list contains the shell indices that are obtained upon application of the individual point group operations to each shell. Within the loop over ERI batches, the G_{IJKL} different indices of symmetry-equivalent batches are computed from the aforementioned list that contains the mappings of the shell indices for every point group element. Whenever such an index of a symmetry-equivalent batch is found to be lower than the original batch index, the computation of the corresponding ERIs can be omitted.[377] Otherwise, the number of occurrences N_{IJKL} of the original batch index within the list of symmetry-equivalent indices is determined. From N_{IJKL} the symmetry weight G_{IJKL} is easily determined as $G_{IJKL} = G/N_{IJKL}$.[375,376] After all symmetry-unique batches are processed, the resulting skeleton matrices are symmetrized by existing PARAGAUSS procedures.[70]

The implemented symmetry treatment of the EXX term was found to provide significant efficiency gains already in the case of small systems. The speed-up values were always determined to be very close to the order G of the point group employed for the symmetry constraints; e.g., ~47.9 in the case of an O_h symmetric M_{13} cluster (see Section 4.3) where $G = 48$.

3.1.3. Integral Screening

The treatment of spatial and index symmetries can significantly reduce the number of operations involved in the calculation of EXX and Coulomb matrix elements.[30] However, these techniques do not affect the $\mathcal{O}(N^4)$ scaling of the computational requirements with respect to the size N of the basis set. Thus, several measures shall be presented in the following, which allow computing the numerically significant ERI batches only. Furthermore, corresponding implementations completed as part of this thesis are explained in detail.

The Gaussian products as in Eq. 3.1.7 include overlap factors which are exponentially decreasing in terms of the squared distance $|\mathbf{B}-\mathbf{A}|^2$. In consequence, such overlap factors will essentially vanish if the individual centers **A** and **B** are distant enough. The actual distance $|\mathbf{B}-\mathbf{A}|$ at which a product pair becomes numerically insignificant depends on the angular momentum of the basis functions and especially on their radial extent, hence the values of the exponents of the PGTOs involved. In any case, a specific orbital of a localized atomic orbitals (AO) basis set can form a numerically significant overlap only with a limited number of other orbitals located within a finite region around it. Therefore, in the limit of very large systems, the number of significant product pairs only scales as $\mathcal{O}(N)$.[385] Consequently, the tensor $\{\mathbf{g}\}_{ijkl}=(ij|kl)$ is sparse and the number of ERIs of non-negligible numerical values approaches $\mathcal{O}(N^2)$ in that limit.[385]

While the computation of individual ERI batches remains demanding, significant efficiency gains are possible if nearly vanishing batches can be identified as such and omitted when their values are found below some specific threshold. Of course the identification of the nearly vanishing batches has to be carried out by different means than the calculation of the ERI themselves. Thus, integral estimates are employed for this task, which should provide a sharp upper bound for the magnitude of the actual ERI.[385] In the case of ERIs over *s*-type GTOs, the Boys function $F_0(\gamma\overline{\mathbf{PQ}}^2)\leq 1$ can be estimated as unity so that

$$ES_{abcd}=Z\cdot\exp\left(-(ab/p)\overline{\mathbf{AB}}^2\right)\exp\left(-(cd/q)\overline{\mathbf{CD}}^2\right)\,, \qquad 3.1.62$$

represents such an upper bound for the absolute value of the integral.[370] This qualifies ES_{abcd} as a valid integral estimate for the integral screening approach discussed above.[370] On the other hand, Eq. 3.1.62 has several disadvantages as it is non-separable and thus needs to be computed inside a $\mathcal{O}(N^4)$ loop.[4,382] Furthermore, ES_{abcd} is formulated in terms of PGTO and is not well suited for CGTOs.[4,382] An additional disadvantage consists in the fact that Eq. 3.1.62 is not easily generalized to ERIs over GTOs with higher angular momenta.[4,382]

[30] The reduction can amount up to a factor of $120\times 8=960$ for large systems with icosahedral symmetry.

A better integral estimate can be obtained when considering that each ERI $(ij \mid kl)$ also qualifies as an inner product for the pair distributions *ij* and *kl* with the metric $1/|\mathbf{r}-\mathbf{r}'|$.[35,382,386,387] Thus, the Schwarz inequality

$$(ij \mid kl) \leq \sqrt{(ij \mid ij)} \cdot \sqrt{(kl \mid kl)} = ES_{ij} \cdot ES_{kl} \qquad 3.1.63$$

provides an upper integral bound.[35,382,386,387] The Schwarz estimate is not only free of the aforementioned disadvantages of Eq. 3.1.62 but also was shown to provide a considerably tighter upper bound for ERIs.[382]

The integral estimates provided by the Schwarz inequality are generally useful in integral screening approaches. However, the contributions of the ERIs to the EXX and Coulomb matrices, Eqs. 3.1.54 – 3.1.57, are far more relevant in the context of HF and hybrid DFT calculations. Thus, the computation of a batch can be omitted if all of its contributions to **K** and **J** are negligible. Also the upper bound of such contributions is estimated with the help of the Schwarz inequality as

$$\max\left\{K_{ik}^{jl}, K_{jk}^{il}, K_{il}^{jk}, K_{jl}^{ik}\right\}/2 \leq ES_{ij} \cdot ES_{kl} \cdot \max\left\{P_{jl}, P_{il}, P_{jk}, P_{ik}\right\}, \qquad 3.1.64$$

$$\max\left\{J_{ij}^{kl}, J_{kl}^{ij}\right\}/4 \leq ES_{ij} \cdot ES_{kl} \cdot \max\left\{P_{lk}, P_{ij}\right\} \qquad 3.1.65$$

in the case of exchange and Coulomb matrices, respectively.[382]

Apart from providing potentially lower estimates and a better error control for the calculation of the matrices **K** and **J**, this latter screening approach is also essential for reducing the computational requirements of the exchange term below $\mathcal{O}(N^2)$.[382] Indeed, in systems with a non-vanishing band gap, the density matrix can be shown to become sparse.[371,388-392] In such systems the sparse density matrix leads to rather localized exchange interactions.[371,388-392] The density matrix **P** couples the $\mathcal{O}(N)$ scaling bra and ket sides of the ERIs to yield exchange contributions.[385,393,394] Thus, the number of numerically significant exchange contributions also scales with $\mathcal{O}(N)$.[385,393,394]

```
FOR I = 1, N                          → O(N)
  FOR J = 1, I                        → O(1), coupled to pair partner I
    FOR K = 1, I                      → O(1), coupled to I by P_IK
      DO WHILE (L < K AND KL < IJ)    → O(1), coupled to pair partner K
        COMPUTE (IJ | KL)
        CONTRACT (IJ | KL), P_IK → K_JL^IK
    …
END
```

Scheme 3.1.3: Loop structure over ERI batches $(IJ \mid KL)$ showing the relations that lead to a number of exchange contributions that scales linearly with the number of basis functions *N*. Schematics adapted from Ref. [385].

Scheme 3.1.3 illustrates the relations between the individual, non-negligible shell pairs and between non-negligible exchange contribution from individual pairs of bra and ket-pairs.[385] Provided that the non-vanishing shell pairs are identified before entering the loop over ERI batches, the EXX matrix and energy can be obtained with a computational effort that scales linearly with the number of basis functions.[385,393,394] In practice, the density matrix often turns out to be only moderately localized due to the basis set superposition error (BSSE).[393,395] Thus, a true linear scaling is often obtained only for very large models of very sparse materials.[393]

The $\mathcal{O}(N^2)$ scaling of the number of Coulomb contributions persists though, even when one employs the estimate in Eq. 3.1.65. On the other hand, the number of contributions that correspond to non-classical Coulomb interactions was shown to scale only as $\mathcal{O}(N)$;[385] only these contributions require four-center integrals. The remaining classical Coulomb interactions between well separated charge distributions can be approximated by other strategies and thereby be computed with a linear scaling computational effort.[4,40,385,390,396]

The density-matrix-weighted Schwarz screening can be made more efficient by the so-called ΔSCF approach.[382] Instead of reconstructing the full EXX and Coulomb matrices during every SCF iteration step, the ΔSCF method works in terms of incremental matrices.[382] To this end, a difference density matrix

$$\Delta\mathbf{P}^{(t)} = \mathbf{P}^{(t)} - \mathbf{P}^{(t-1)} \qquad 3.1.66$$

is formed in each iteration step *t*. The matrix $\Delta\mathbf{P}^{(t)}$ is subsequently employed for the screening, Eqs. 3.1.64 and/or 3.1.65, as well as for the contraction with the ERI batch. This treatment yields the incremental matrices $\Delta\mathbf{K}^{(t)}$ and $\Delta\mathbf{J}^{(t)}$. From these incremental matrices the corresponding full matrices are then obtained according to

$$\mathbf{K}^{(t)} = \mathbf{K}^{(t-1)} + \Delta\mathbf{K}^{(t)} \quad \text{and} \quad \mathbf{J}^{(t)} = \mathbf{J}^{(t-1)} + \Delta\mathbf{J}^{(t)}. \qquad 3.1.67$$

The general idea behind the ΔSCF method is that $\Delta\mathbf{P}^{(t)}$ is very small if the SCF iteration approaches convergence, so that most incremental contributions are small enough to be neglected.

The density weighted Schwarz screening turns out to provide a relatively sharp upper estimate for ERIs, which in some cases even allows to store a part of the ERIs, i.e. of the computationally most demanding integrals (semi-direct SCF).[382] However, its effectiveness decreases somewhat when very sharp and diffuse GTOs are involved in the same ERI as well as in cases where the distance between the product centers becomes decisive for screening.[382,397] More elaborate alternatives exist that show a behavior regarding these issues that improves over the Schwarz screening method.[385,393,397-399] Such variants can provide an even sharper upper integral estimate than the Schwarz screening approach.[385,393,397-399]

Within the PARAGAUSS implementation of the exact-exchange term completed as part of this thesis, screening strategies are applied in a three-fold manner for both ERI libraries, ERI4C and ERD. During the first SCF iteration the diagonal batches, $(IJ \mid IJ)$, are computed

and processed separately. From these batches the subshell- and batch-wise estimates, EC_{ij} and ES_{IJ} are computed as

$$EC_{ij} = \sqrt{\max_{m_i,m_j}\{(ij\,|\,ij)\}} \quad \text{and} \tag{3.1.68}$$

$$ES_{IJ} = \sqrt{\max\{(IJ\,|\,IJ)\}} = \max_{ij}\{EC_{ij}\}, \tag{3.1.69}$$

where the maximum in Eq. 3.1.68 is to be understood over CGTOs of the same radial components, but with different magnetic quantum numbers. Both, the ES_{IJ} values and the matrix EC_{ij} are stored for later use along with the corresponding shell- and subshell-wise maxima of the density matrix which are obtained at this stage in a similar fashion. All estimates are then employed for the density-matrix-weighted Schwarz screening of the Coulomb or the exchange contributions from correspondingly adapted variants of Eqs. 3.1.64 and/or 3.1.65, depending on whether **K** and/or **J** are needed.

A batch-wise screening is carried out first, as it involves just a single estimate, but would allow one to omit most batches in the limit of large systems. Whenever a quadruple of shells passes the batch-wise screening, it undergoes the petit-list symmetry treatment described in Section 3.1.2. In the case of symmetric systems most non-negligible batches can also be excluded in this way from the ERI calculation, as long as they are symmetry-equivalent to another batch that was computed earlier (Section 3.1.2). Only the first of each group of non-negligible, symmetry-equivalent batches is then analyzed for its non-vanishing contractions. Whenever an ERI batch fulfills these conditions, Eqs. 3.1.64 and/or 3.1.65 are applied again in terms of the aforementioned subshell maxima. Only the primitive exponents and contraction coefficients $\{c_{ii'}\}$ associated with subshells that lead to non-vanishing contributions are handed over to the subroutines that calculate the ERIs. Finally, a screening of the primitive pairs is carried out.[349] In contrast to the other screening stages, this selection has to be carried out inside the ERI calculation subroutines. This approach was initially present in the ERD library[349] but was implemented in the ERI4C library later as well. During the screening of primitives the most extended bra- and ket-pairs are first identified by the smallest exponent pairs $p_{\min} = a_{\min} + b_{\min}$ and $q_{\min} = c_{\min} + d_{\min}$.[349] Subsequently, the minimum distance $PQ_{\min}$ between the two line segments $\overline{\mathbf{AB}}$ and $\overline{\mathbf{CD}}$ is determined. These quantities provide an upper bound for any pair of primitives according to

$$\begin{aligned}\{ab\,|\,cd\} &\le \{ab\,|\,c_{\min}d_{\min}\} \\ &\le Z\cdot\exp\left(-(ab/p)\overline{\mathbf{AB}}^2\right)\exp\left(-(c_{\min}d_{\min}/q_{\min})\overline{\mathbf{CD}}^2\right)F_0\left(pq_{\min}/(p+q_{\min})\,PQ_{\min}^2\right),\end{aligned} \tag{3.1.70}$$

for the pair *ab* (and analogously for *cd*). Eq. 3.1.70 also represents an upper bound for ERIs over PGTOs with higher angular momenta.[349] The indices of the non-negligible pairs are stored in a list and the κ4 steps are carried out for pairs of significant pairs of primitives only.

The hybrid DFT calculations carried out as part of this thesis were mostly performed on larger transition metal clusters (see Sections 4.3 and 4.4). Compared to typical hybrid DFT

applications on systems that mostly consist of main group atoms, screening techniques are less beneficial for transition metal clusters due to their compact structures and non-sparse density matrices (see above). Taking the O_h symmetric Pt_{55} cluster (see Section 4.3) as example, the density-matrix-weighted Schwarz screening approach allows one to omit about 46% of the symmetry-unique integral batches when a rather conservative screening threshold of 10^{-10} au. is employed. This ratio increases to about 59% for the analogous calculation of the Pt_{79} cluster. The second screening stage at the level of contractions can significantly reduce the number of quartets of primitives and/or CGTOs that need to be computed by the ERI module. In the case of the aforementioned examples this approach was observed to provide further efficiency gains by factors of about 1.5–2.5. This speedup is considerably higher when all-electron basis sets are employed. As most of the significant pairs of PGTOs are already identified at this stage, the screening of pairs of primitives provides only minor efficiency gains by factors of ~1.2–1.4 with a screening threshold of 10^{-10} au.

In the context of this thesis also the aforementioned ΔSCF method, Eqs. 3.1.66 and 3.1.67, was implemented in PARAGAUSS.[70] However, this approach was found to provide only surprisingly small efficiency gains in the calculations which were carried out as part of this thesis. This finding led to the conclusion that specialized SCF convergence acceleration approaches are essential for the ΔSCF method to take effect. Indeed, such methods have been proposed.[382] These convergence acceleration methods specifically aim to minimize the contributions $\Delta\mathbf{K}^{(t)}$ and/or $\Delta\mathbf{J}^{(t)}$ in late SCF iteration cycles.[382]

3.1.4. Gradients of the Exact-Exchange Term

The ERI derivatives with respect to the nuclear coordinates are required for computing molecular forces and vibrational frequencies. The calculation and treatment of ERI derivatives as implemented in PARAGAUSS[70] is discussed in the following.

The expressions of ERI derivatives are closely connected to the relations emerging from the parameter differentiation technique used for the calculation of the actual ERIs. Although a direct differentiation is possible,[323,324] the nuclear derivative of a single PGTO

$$\frac{\partial}{\partial A_r}(r-A_r)^{i_r}\exp\left(-a(r-A_r)^2\right)=\left(2a(r-A_r)^{i_r+1}-i_r(r-A_r)^{i_r-1}\right)\exp\left(-a(r-A_r)^2\right) \qquad 3.1.71$$

provides an often advantageous alternative in terms of uncontracted Cartesian GTOs[327]

$$\frac{\partial}{\partial A_r}[\mathbf{ij}\,|\,\mathbf{kl}]=2a[\mathbf{i}+\mathbf{1}_r,\mathbf{j}\,|\,\mathbf{kl}]-i_r[\mathbf{i}-\mathbf{1}_r,\mathbf{j}\,|\,\mathbf{kl}]\,. \qquad 3.1.72$$

Depending on the ERI class at hand, Eq. 3.1.72 can be reformulated in terms of pre-contracted intermediates, and/or combined with the MD transformation, the HRR and the OS or HGP equations (see Section 3.1.1).[327] The HRR+MD implementation in the ERI4C

library described in Section 3.1.1 was extended by routines for ERI derivatives in terms of a pre-contracted variant of Eq. 3.1.72. Similar variants of Eq. 3.1.72 exist for the two-dimensional intermediates $\Im_r(i_r j_r k_r l_r, u_t)$ as they appear in Gauss-quadrature based ERI algorithms (see Section 3.1.1, Eq. 3.1.49), which are employed in the ERD library.[349,369] As in the case of ERI batches, both of these alternative implementations were designed to deliver also the ERI derivatives in a batch-wise fashion. In the implementation carried out as part of this thesis the batch-wise calculation of ERI derivatives allowed one to process the results from both libraries in a unified way.

Both implementations provide only a single batch of integral derivatives at a time; for example, the entire batch of $\partial(ij\,|\,kl)/\partial A_r$ derivatives. This approach does not only reduce the amount of intermediate data, but also enables one to omit the calculation of several of the generally twelve distinct derivatives of each ERI. Indeed, the translational invariance of ERIs, Eq. 3.1.36, makes it possible to compute only nine of the twelve derivatives of each ERI and to express the remaining ones as

$$\frac{\partial(ij\,|\,kl)}{\partial D_r} = -\frac{\partial(ij\,|\,kl)}{\partial C_r} - \frac{\partial(ij\,|\,kl)}{\partial B_r} - \frac{\partial(ij\,|\,kl)}{\partial A_r}. \qquad 3.1.73$$

To reduce the amount of data involved, Eq. 3.1.73 can be applied also at the level of EXX and Coulomb matrix contributions.[400] This approach was implemented in PARAGAUSS in connection with both ERI libraries.[70] Although not employed in the present implementation, even more reductions would be possible when one also exploits the rotational invariance properties of ERIs.[400-402]

ERI gradients are directly contracted to the corresponding EXX and Coulomb gradient contributions

$$\partial(IJ\,|\,KL)/\partial A_r\,,\ \mathbf{P}_{IK}\mathbf{P}_{JL},\ \mathbf{P}_{IL}\mathbf{P}_{JK}\ \rightarrow 4(\partial E_{\mathrm{EXX}}/\partial A_r)^{IK,JL},\ 4(\partial E_{\mathrm{EXX}}/\partial A_r)^{IL,JK} \qquad 3.1.74$$

$$\partial(IJ\,|\,KL)/\partial A_r\,,\ \mathbf{P}_{IJ}\mathbf{P}_{KL}\ \rightarrow 8(\partial E_{\mathrm{Coul}}/\partial A_r)^{IJ,KL} \qquad 3.1.75$$

with correspondingly adapted special cases of Eqs. 3.1.56 – 3.1.57 for two or more equal shell indices (see Section 3.1.2). The estimates of gradient contributions were implemented by a correspondingly adapted variant of density-matrix-weighted Schwarz screening (see Section 3.1.3). In the case of first-order ERI derivatives the Schwarz screening method requires the calculation of additional estimate

$$EG_{ij} = \max\left(\max_r \sqrt{\partial(ij\,|\,ij)/\partial A_r}\,,\ \max_r \sqrt{\partial(ij\,|\,ij)/\partial B_r}\right) \qquad 3.1.76$$

which is then used in the following upper bounds for EXX and Coulomb contributions

$$\max\left\{(\partial E_{\mathrm{EXX}}/\partial A_r)^{ij,kl},\ldots\right\}\Big/4 \le \max\left\{ES_{ij}\cdot EG_{kl}, EG_{ij}\cdot ES_{kl}\right\}\cdot\max\left\{P_{jl}, P_{il}, P_{jk}, P_{ik}\right\}, \qquad 3.1.77$$

$$\max\left\{(\partial E_{\mathrm{Coul}}/\partial A_r)^{ij,kl},\ldots\right\}\Big/8 \le \max\left\{ES_{ij}\cdot EG_{kl}, EG_{ij}\cdot ES_{kl}\right\}\cdot\max\left\{P_{ij}, P_{kl}\right\}, \qquad 3.1.78$$

respectively. Thereby, an analogous three-fold screening strategy as described in Section 3.1.3 for the ERIs was employed for ERI gradients from both libraries. Also the treatment of

point group symmetries was implemented analogously to that of ERI batches (see Section 3.1.2). Furthermore, the fact that the molecular forces are totally symmetric allows one to further reduce the number of ERI derivatives that need to be computed. This was exploited within the PARAGAUSS implementation in terms of a list of the nuclear gradients that can contribute to the totally symmetric gradients. Within the loop over shell quadruples the calls to the ERD or ERI4C subroutines were thereby restricted to only those derivatives contained in the list. The symmetrization of the final gradients was achieved by using existing PARAGAUSS subroutines.[70]

3.1.5. Parallelization and Run Time Aspects

As the computationally most demanding step, the computation of ERIs requires a careful parallelization to ensure efficient hybrid DFT calculations on modern, highly parallel computer platforms.[403] In the following the parallelization approach implemented in PARAGAUSS[70] for the calculation of the exact-exchange matrix will be presented. The parallel efficiency of this implementation is then discussed on the example of a test case. Finally the serial and parallel efficiency of the PARAGAUSS implementation is compared with that of another well established quantum chemistry program, namely the NWChem code.[404]

Within the exact-exchange implementation (EXX) of ParaGauss,[70] a dynamic load balancing library[374,405] (DLB) is employed for an efficient parallelization. This library is based on the message passing interface (MPI) communication library (version 2.2).[406] Like most parallelization approaches, DLB subdivides the workload of a specific algorithmic step, i.e. the computation of the EXX matrix, into individual larger independent tasks.[374,405] These tasks are initially assigned to the W_{CPU} cores (workers) on which the program is executed.[374,405] The central aspect of DLB consist in eliminating the idle time (i.e. the parallel overhead) that results if one of the workers approaches the end of the list of tasks initially assigned to it.[374,405] In such a case, a worker can adopt some of the unprocessed tasks at the end of the task list of another worker (work stealing) and thereby further contribute to the completion of the algorithmic step at hand.[405] After the completion of all tasks has been detected by a special mechanism, the DLB run is concluded and the algorithmic step is finished up by collecting the results of the individual workers.[405]

When calculating the EXX matrix, the number of FLOPs and thus the runtime required to calculate individual ERI batches can vary over several orders of magnitude. As such, the parallelization scheme employed for calculation of the EXX matrix has to deal with highly inhomogeneous tasks. To achieve an efficient parallelization with the DLB approach three important prerequisites have to be met. (i) The initial distribution of the workload must be as evenly as possible to reduce the need for load balancing. (ii) A number of comparably small

tasks should be available for work stealing at the end of each workers task list. (iii) The overall number of DLB tasks should not be excessively large to reduce the overhead of assignment and distribution by the DLB library. During the development of the exact-exchange implementation in PARAGAUSS[70] the definition of DLB tasks and their assignment has been continuously refined several times to fulfill the above requirements. Only the latest approach shall be presented in the following.

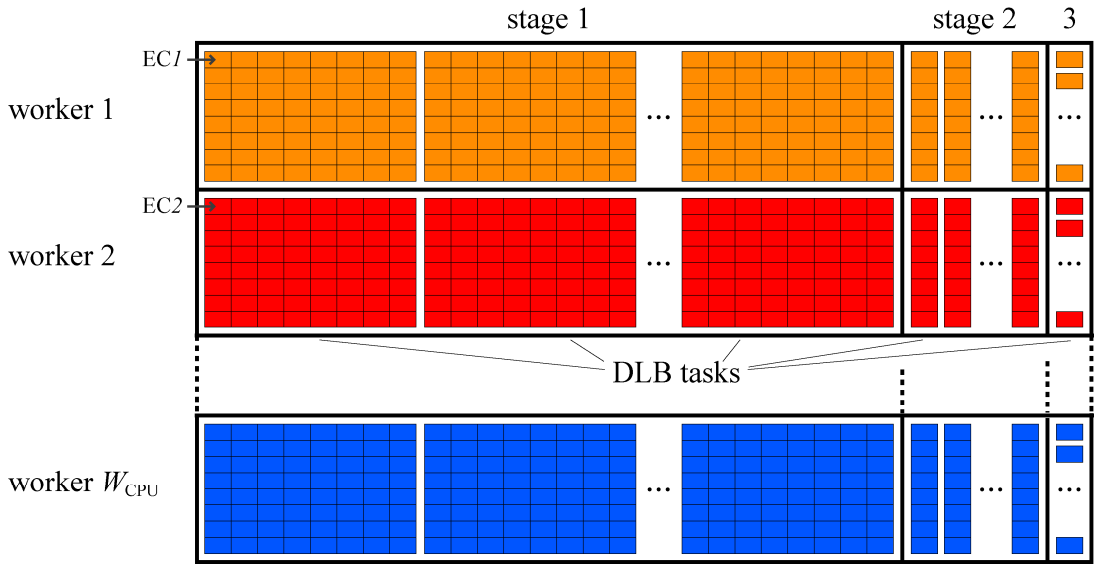

Figure 3.1.3: Staged initial assignment of ERI batches grouped in elemental chunks EC*i* which in turn comprise task chunks of varying size. The task chunks form the individual DLB tasks assigned to the workers.

During an initial preparation step the individual atomic shells are sorted according to their angular momenta. This sorting starts from the AOs with the highest ℓ-values. The ERIs over these AOs can safely be expected to be the most time consuming (see Section 3.1.2). The resulting shell indices define the sequence of shell quadruples $(IJ \mid KL)$ as $I \geq J$, $K \geq L$, and $(I-1)N/2+J \geq (K-1)N/2+L$ as described in Section 3.1.2. In the following, the (formal) list of ERI batches is subdivided equally into "elemental chunks", EC*i* (see Figure 3.1.3). Each elemental chunk contains a contiguous set of batches (within the loop structure depicted in Scheme 3.1.2b). The elemental chunks are distributed one-by-one, i.e. in a round robin fashion to the individual DLB workers to ensure an even initial distribution of the computational workload. Furthermore, the elementary chunks assigned to each worker are then combined into larger groups which correspond to the actual DLB tasks (Figure 3.1.3). This assignment primarily aims at reducing the overall number of tasks, thus the overhead of the DLB library. On the other hand, the smallest DLB tasks have to be available at the end of each workers task list for the eventual work stealing to be sufficiently fine-grained. Both of

these requirements can be fulfilled by a suitable definition of the DLB tasks, hence by varying the number of elemental chunks in each task. The largest DLB tasks which comprise the most elemental chunks are defined at the beginning of the task list of each worker. This initial stage of the largest DLB tasks is then followed by additional stages of DLB tasks, which are successively smaller, hence comprise fewer elemental chunks. The last stage includes only DLB tasks with a single elemental chunk. The number of elemental chunks per DLB task is decreased from stage to stage by the fixed factor r_{stag}. All these assignments are depicted by Figure 3.1.3. For the computing platforms employed in the context of this thesis (see below), three stages, each with 160 DLB tasks per worker, and $r_{\text{stag}} = 15$, were found to provide a good trade-off between the parallel overhead and the overhead of the DLB library itself.[31]

The run time t_W on a specific number W_{CPU} of workers relative to the execution time t_{REF} on a reference number W_{REF} of workers (whereas $W_{\text{REF}} \leq W_{\text{CPU}}$) allows for the definition of performance metrics like the parallel speedup $s(W_{\text{CPU}})$ and the parallel efficiency $eff(W_{\text{CPU}})$. These two performance metrics are defined as $s(W_{\text{CPU}}) = t_W / t_{\text{REF}}$ and

$$eff(W_{\text{CPU}}) = \frac{W_{\text{REF}} \cdot t_{\text{REF}}}{W_{\text{CPU}} \cdot t_W} = \frac{s(W_{\text{CPU}})}{W_{\text{CPU}} / W_{\text{REF}}}, \qquad 3.1.79$$

respectively. While $W_{\text{REF}} = 1$ allows to evaluate the total parallelization overhead, serial runs can often not be carried out for large test systems with a reasonable effort. Thus, parallel runs have to be taken as reference.

This is the case for TPSSh hybrid DFT calculations of the cluster $Pt_{140}(CO)_8$ (see Section 4.4), which were carried out on the computing platform SuperMUC of the Leibniz Rechenzentrum, München.[32] With 6096 CGTO basis functions this system represents a large enough computational problem for $W_{\text{REF}} = 128$ to be a reasonable reference. The individual timings t_W for the total SCF cycle and the computation of the EXX term where obtained as averages over the first 10 SCF cycles at the beginning of the SCF process. For $W_{\text{REF}} = 128$ the average run time of a single SCF cycle amounts to about 665 seconds on the SuperMUC platform.

Figure 3.1.4 depicts the parallel speedup and efficiency for up to 2048 workers.[33] For CPU counts higher than 512 the timings for the total SCF cycle and the EXX assembly step start to exhibit small, but notable deviations from the ideal speedup. Overall, the total SCF cycle exhibits a slightly less ideal scaling than the EXX assembly step, as it comprises other, computationally less demanding steps which cannot be parallelized as efficiently. The

---

[31] With 1, 15, and 15^2 elemental chunks in the DLB tasks of the third, second, and first stage, respectively, and 160 DLB tasks in each stage, this implies that the entire list of ERI batches is (formally) subdivided into $n\_\text{EC} = 160 \cdot (1 + 15 + 15^2) = 38560$ elemental chunks per worker. Whenever the elemental chunks exceed the number of ERI batches, the number of the DLB tasks in the initial stages is reduced.

[32] SuperMUC (LRZ), Intel Xeon (Sandy Bridge) CPU, Infiniband interconnect.

[33] See Sections 4.1 and 4.4 for the detailed computational parameters.

decrease of the parallel speedups is clearly noticeable at 2048 CPUs, although $s(2048)$ is still close to the ideal value for the EXX assembly. The parallel efficiency of the EXX assembly decreases by about 3% at 2048 workers while the corresponding value of the total SCF cycle differs by about 7% from the ideal scaling behavior. This behavior is most likely related to the connectivity of the individual workers.

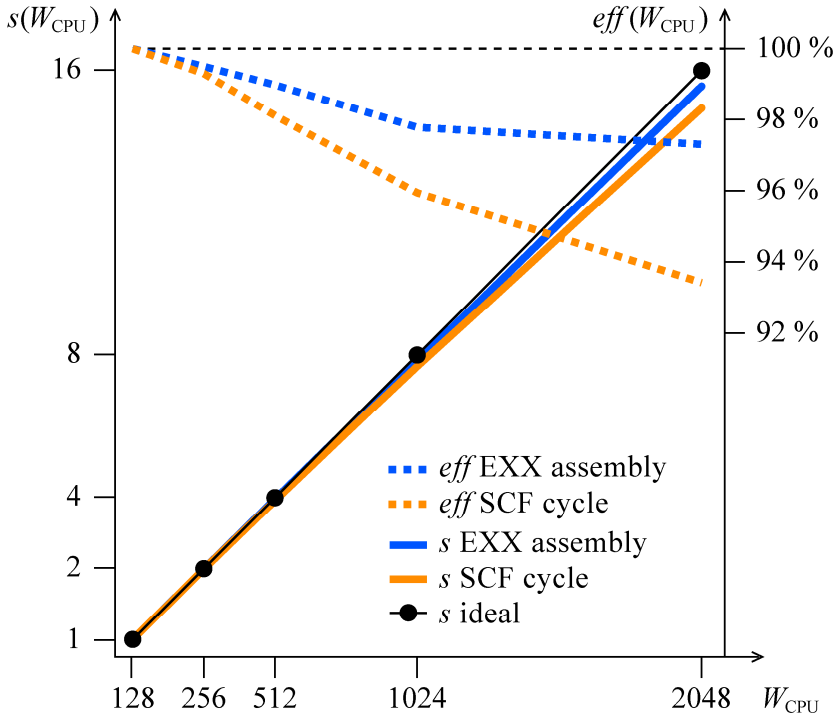

Figure 3.1.4: Parallel efficiency *eff* and speedup *s* for $W_{CPU} = 256$, 512, 1024, and 2048 workers and $W_{REF} = 128$ on the example of a TPSSh hybrid DFT calculation of the $Pt_{140}(CO)_8$ 5t cluster (see Section 4.4).

To characterize the efficiency further, the PARAGAUSS exact-exchange implementation is compared to that of the NWChem program suite[404] on the example of a PBE0 single point calculation on a small Mo-V mixed metal oxide cluster model ($Mo_4VO_{19}H_8$) using 6-31G** and Stuttgart-Dresden basis sets with the corresponding effective core potentials.[407-409] For this example the PARAGAUSS implementation exhibits lower run times than NWChem, which partially result from the different numbers of SCF cycles needed to converge the density matrix: 39 with PARAGAUSS and 47 with NWChem. To allow for a better comparison, the timings obtained with the NWChem have been multiplied by 39/47 to account for this difference. Table 3.1.1 provides the total (scaled) run times and the parallel efficiencies measured with both programs on 1 to 16 workers of the local Linux cluster.[34]

[34] Intel Xeon (Nehalem) CPU, Gigabit connection.

Table 3.1.1: Comparison of total run time and parallel efficiencies for PARAGAUSS and NWChem on the example of a single point electronic structure calculation of a $Mo_4VO_{19}H_8$ mixed metal oxide cluster model with the PBE0 hybrid DFT method. The run times obtained with NWChem were corrected by a factor of 39/47 to account for the different convergence rates of the SCF processes of both programs.

W_{CPU}		1	2	4	8	16
run time (minutes)	PARAGAUSS	189	107	54	27	30
	NWChem	205	107	55	31	27
parallel efficiency (%)	PARAGAUSS	100	88.3	88.0	87.4	39.4
	NWChem	100	95.7	93.6	81.2	46.8

The parallel efficiency obtained with PARAGAUSS is found around 88% for $W_{CPU} = 2-8$. The reason for this lies probably in the fact that the basis sets are rather small compared to the $Pt_{140}(CO)_8$-model discussed above. Because of the small basis set, the EXX assembly requires only about 60% of the total execution time (as opposed to $> 95\%$ for the $Pt_{140}(CO)_8$ example). In consequence the other algorithmic steps of the hybrid DFT calculation can significantly reduce the parallel efficiency, which agrees with the comparison of the parallel efficiency of the EXX assembly and of a whole single SCF cycle (see above). For runs on more than eight workers a sudden drop of the parallel efficiency is observed as the execution time is even slightly increased. Compared to that, the NWChem reference exhibits parallel efficiencies above 90% for $W_{CPU} = 2-4$, which drop below the corresponding value measured with PARAGAUSS on eight workers. At $W_{CPU} = 16$ a similarly dramatic efficiency drop is observed with NWChem as with PARAGAUSS. As these drops in the parallel efficiency occur with both programs at $W_{CPU} > 8$, they are most likely not related to the implementation itself. Indeed, because of the computer setup used to determine these timings, network communication becomes involved in the parallelization at $W_{CPU} > 8$. This significantly slower communication likely causes the sudden performance drops measured with both program at this CPU count.

3.2. Generalized DFT+U Method

3.2.1. Projector Generation

In Section 2.4 the DFT+U term was formulated in terms of occupation numbers of target orbitals $\{\chi_t\}$ which correspond to individual KS orbitals, to which the self-interaction correction is applied. The DFT+Umol method implemented in PARAGAUSS as part of this thesis allows one to apply the self-interaction correction in terms of projectors that consist of general linear combinations of atomic orbitals (AO). The generation of such projectors represents a crucial part of the DFT+Umol method. Thus, their treatment is discussed in the following, while the implementation of the DFT+Umol energy and gradient expressions in PARAGAUSS are presented in the two subsequent sections, respectively.

The projector orbitals are labelled by the index I and either correspond to elements of atomic subshells or to molecular orbitals of isolated fragments of the system. In any case the DFT+Umol implementation retrieves the projector coefficients $\{v_{it}\}$ as converged KS orbital coefficients from auxiliary SCF calculations on the isolated fragments or atomic systems. While allowing the self-interaction correction to become independent of the employed AO basis set, this detail represents a minor difference to the conventional DFT+U correction implemented in PARAGAUSS if the DFT+Umol projectors target atomic subshells.[70,281,283-285] However, if the MOs targeted by the DFT+U correction are very similar to single atomic basis functions, both implementations essentially provide the same results. Furthermore, the DFT+Umol implementation exactly reduces to that of the conventional DFT+U term if the contraction coefficients of the applied CGTO basis are identical to the converged KS eigenvectors of an atomic calculation.

The occupation matrix elements $\{n_{tu\sigma}\}$ represent the main variable of any DFT+U correction term. Thus, the reliability of the DFT+U approach depends on the quality of the occupation numbers and the DFT+U projectors. The most important aspect of the definition and computation of DFT+U projectors is that they remain as close as possible to the MOs they target. In consequence the target orbitals $\{\chi_t\}$ must overlap as much as possible with these MOs but exhibit essentially no overlap with any other KS orbitals. In consequence, the FLL formulations of DFT+U or DFT+Umol provide reasonable self-interaction corrections to atomic subshells only if the corrected subshell elements essentially do not interact with any other orbitals outside of the same subshell (see Section 2.4). The same holds if the correction targets molecular fragment orbitals.

However, projectors obtained from molecular fragment orbitals are linear combinations of AOs, thus exhibit additional degrees of freedom in terms of the coefficient vectors $\{v_{it}\}$ compared to atomic subshell projectors. To ensure the best possible overlap between the projector orbitals and the molecular fragment orbitals targeted by them, the former are obtained from auxiliary calculations of the molecular fragment at the geometry that the

fragment exhibits within the complete system. In the case of a geometry relaxation the auxiliary SCF calculation used to generate the DFT+Umol projectors therefore has to be repeated at every geometry optimization step. In the context of the present thesis this was enabled by conducting the DFT+Umol calculations within the suite PARATOOLS.[405,410] A special interface of PARAGAUSS to this suite allowed one to extract the required molecular fragment geometries during every step of the geometry optimization and subsequently to carry out the required auxiliary calculations on them.

The molecular fragments on which the target orbitals are located may not be symmetric while the total system is. Furthermore, the auxiliary SCF calculation of the isolated molecular fragment may also be carried out with symmetry constraints to allow for an easier identification of the projector coefficients $\{v_{it}\}$. To ensure that the coefficients $\{v_{it}\}$ are correctly imported before the main SCF iteration, the eigenvectors $\mathbf{v}$ are first unsymmetrized according to $\tilde{\mathbf{v}} = \mathbf{v}\mathbf{R}^{-1}$ (see Section 3.1.2). The resulting vectors $\tilde{\mathbf{v}}$ are then stored in a separate file for every group I of target orbitals.

3.2.2. DFT+Umol Energy and Potential

The following section discusses the implementation of the DFT+Umol energy correction

$$E^{\mathrm{U}} = \tfrac{1}{2}\sum_{I\sigma} U_I \left(\mathrm{Tr}\left\{\mathbf{n}_I^\sigma\right\} - \mathrm{Tr}\left\{\mathbf{n}_I^\sigma \mathbf{n}_I^\sigma\right\}\right) \qquad 3.2.1$$

which was established in Section 2.4 (Eq. 2.4.10) in terms of the target orbital occupation matrices (Eq. 2.4.16)

$$\mathbf{n}_I^\sigma = \mathbf{v}_I \mathbf{S}\mathbf{P}^\sigma \mathbf{S}\mathbf{v}_I^\dagger \ . \qquad 3.2.2$$

Furthermore, the implementation of the corresponding DFT+Umol potential is presented, which is required for the self-consistent application of this method.

The DFT+Umol method requires several preparation steps before commencing the SCF iteration. First, the unsymmetrized projector coefficients $\tilde{\mathbf{v}}$ from the auxiliary calculations (see Section 3.2.1) are imported from individual files for every group I of target orbitals. Subsequently, the vectors $\tilde{\mathbf{v}}$ are mapped onto the unsymmetrized AO basis set of the system. In the next step these unsymmetric projectors would have to be transformed into the symmetry adapted basis of the system. However, while Eq. 3.1.61 provides a comparatively simple way to transform matrices from the AO basis to the symmetry adapted basis, the corresponding transformation of vectors is not as easily achieved with the existing PARAGAUSS subroutines. Indeed, this approach would require significant extensions in the PARAGAUSS modules responsible for the computation of Clebsch–Gordan coefficients.

Thus, the DFT+Umol energy term was implemented in a different but equivalent formulation. After inserting Eq. 3.2.2 into Eq. 3.2.1 and expanding the traces over matrix products, the DFT+Umol energy term writes as

$$E^{\mathrm{U}} = \tfrac{1}{2}\sum_{I\sigma} U_I \left(\sum_{ij} \{\mathbf{S}\mathbf{v}_I^{\dagger}\mathbf{v}_I\mathbf{S}\}_{ji} P_{ij\sigma} - \sum_{ijkl} \{\mathbf{S}\mathbf{v}_I^{\dagger}\mathbf{v}_I\mathbf{S}\}_{li} P_{ij\sigma} \{\mathbf{S}\mathbf{v}_I^{\dagger}\mathbf{v}_I\mathbf{S}\}_{jk} P_{kl\sigma} \right). \qquad 3.2.3$$

The first term in the brackets of Eq. 3.2.3 appears as sum over the diagonal elements of the product of the symmetric matrix $\mathbf{X}_I = \mathbf{S}\mathbf{v}_I^{\dagger}\mathbf{v}_I\mathbf{S}$ and the density matrix, hence as $\mathrm{Tr}\{\mathbf{X}_I\mathbf{P}^{\sigma}\}$. Likewise, the second term is identified as $\mathrm{Tr}\{(\mathbf{X}_I\mathbf{P}^{\sigma}\mathbf{X}_I)\mathbf{P}^{\sigma}\}$. Thus, the DFT+Umol energy correction term writes as

$$E^{\mathrm{U}} = \tfrac{1}{2}\sum_{I\sigma} U_I \left(\mathrm{Tr}\{(\mathbf{X}_I - \mathbf{X}_I\mathbf{P}^{\sigma}\mathbf{X}_I)\mathbf{P}^{\sigma}\} \right), \qquad 3.2.4$$

which allows one to carry out the transformation into the symmetry adapted basis on the matrices $\mathbf{X}_I$ instead of the vectors $\mathbf{v}_I$.

As traces of matrix products with the density matrix represent expectation values, the above reformulation in Eq. 3.2.4 also provides a definition of the DFT+Umol operator

$$\hat{u} = \tfrac{1}{2}\sum_{I} U_I \left(\hat{X}_I - \hat{X}_I\hat{\rho}\hat{X}_I \right) \qquad 3.2.5$$

in terms of the projectors

$$\hat{X}_I = \sum_{t\in I} |\chi_t\rangle\langle\chi_t| \qquad 3.2.6$$

and the density matrix operator $\hat{\rho}$ from Eq. 2.4.9. The first term in brackets of Eq. 3.2.5 projects the self-interaction correction on all KS orbitals. The density matrix represents a projector onto the occupied KS orbitals. In consequence, the second term in brackets can be interpreted as a projector onto the occupied KS orbitals only. This latter term becomes dominant for fully occupied target orbitals, while both terms cancel each other in the limit of integer occupations. Thus, the operator in Eq. 3.2.5 provides a slightly different interpretation of the linear and quadratic terms of the DFT+Umol penalty functional in Eq. 3.2.1.

A self-consistent DFT+Umol calculation requires the contribution of the correction term in Eq. 3.2.4 to the matrix of the KS operator, hence the derivatives of E^{U} with respect to the elements of the density matrix. By exploiting the fact that the matrix $\mathbf{X}_I$ is symmetric the derivatives of the first term are obtained as

$$\frac{\partial}{P_{ij\sigma}} \mathrm{Tr}\{\mathbf{X}_I\mathbf{P}^{\sigma'}\} = \sum_{kl} \{\mathbf{X}_I\}_{kl} \delta_{jk}\delta_{il}\delta_{\sigma\sigma'} = \{\mathbf{X}_I\}_{ij}. \qquad 3.2.7$$

The derivatives of the second term, $\mathrm{Tr}\{(\mathbf{X}_I\mathbf{P}^{\sigma}\mathbf{X}_I)\mathbf{P}^{\sigma}\}$, result analogously. After reordering one obtains

$$\frac{\partial}{P_{ij\sigma}} \mathrm{Tr}\{(\mathbf{X}_I\mathbf{P}^{\sigma'}\mathbf{X}_I)\mathbf{P}^{\sigma'}\} = \{2\mathbf{X}_I\mathbf{P}^{\sigma}\mathbf{X}_I\}_{ij}. \qquad 3.2.8$$

By combining Eqs. 3.2.7 and 3.2.8 the total contribution of the DFT+Umol term to the KS matrix reads as

$$\mathbf{U}^{\sigma} = \tfrac{1}{2}\sum_{I} U_I \left(\mathbf{X}_I - 2\mathbf{X}_I \mathbf{P}^{\sigma} \mathbf{X}_I \right) . \qquad 3.2.9$$

During the SCF iteration the matrix $\mathbf{U}^{\sigma}$ is computed from Eq. 3.2.9 along with the DFT+Umol energy (Eq. 3.2.4) in every iteration step.

3.2.3. DFT+Umol Gradients

This section describes the implementation of the contributions of the DFT+Umol term to the gradients with respect to the nuclear positions.

These derivatives of the DFT+Umol term can be expressed in terms of the partial derivatives of the matrices involved in the DFT+Umol energy expression

$$\frac{\partial E^{\mathrm{U}}}{\partial A_r} = \sum_{ij\sigma} \frac{\partial E^{\mathrm{U}}}{\partial P_{ij\sigma}} \frac{\partial P_{ij\sigma}}{\partial A_r} + \sum_{ij} \frac{\partial E^{\mathrm{U}}}{\partial S_{ij}} \frac{\partial S_{ij}}{\partial A_r} + \sum_{it} \frac{\partial E^{\mathrm{U}}}{\partial v_{it}} \frac{\partial v_{it}}{\partial A_r} . \qquad 3.2.10$$

The first sum in Eq. 3.2.10 is the so-called Pulay term. This term comprises the partial derivatives $\partial E^{\mathrm{U}} / \partial P_{ij\sigma}$ which are nothing else than the elements of the contribution $\mathbf{U}^{\sigma}$ to the matrix of the KS operator (see Section 3.2.2). Thus, the calculation of the Pulay term is actually not required within the DFT+Umol module as this contribution is computed from the total KS operator matrix by existing modules of PARAGAUSS.[281]

The second term in Eq. 3.2.10 corresponds to the Hellmann–Feynman term and is computed analogously to the earlier DFT+U implementation in PARAGAUSS.[281] The partial derivatives with respect to the overlap matrix elements result in

$$\frac{\partial}{S_{ij}} \mathrm{Tr}\{\mathbf{X}_I \mathbf{P}^{\sigma} - (\mathbf{X}_I \mathbf{P}^{\sigma} \mathbf{X}_I)\mathbf{P}^{\sigma}\} = \{\mathbf{Y}_I \mathbf{P}^{\sigma} - 2\mathbf{Y}_I \mathbf{P}^{\sigma} \mathbf{X}_I \mathbf{P}^{\sigma} + \mathbf{P}^{\sigma} \mathbf{Y}_I^{\dagger} - 2\mathbf{P}^{\sigma} \mathbf{X}_I \mathbf{P}^{\sigma} \mathbf{Y}_I^{\dagger}\}_{ij} . \qquad 3.2.11$$

Thereby the quantity $\mathbf{Y}_I = \mathbf{v}_I^{\dagger} \mathbf{v}_I \mathbf{S}$ is readily available as it occurs as intermediate during the calculation of $\mathbf{X}_I$. The calculation of the matrices $\partial S_{ij} / A_r$ and their multiplication with the results of Eq. 3.2.11 is then carried out by existing parts of the earlier DFT+U implementation in PARAGAUSS.[281]

The third sum in Eq. 3.2.10 arises from eventual changes in the target orbitals due to altered nuclear coordinates. In cases where the target orbitals correspond to molecular fragment orbitals this term implies a calculation of derivatives of the KS eigenvectors with respect to the nuclear coordinates. In the context of this thesis this term was neglected as the implementation of the response property $\partial v_{it} / A_r$ would require significant reorganizations in many modules of PARAGAUSS. A comparison between analytical and numerical derivatives with respect to nuclear coordinates on the example of a PBE+Umol correction acting on the CO $2\pi^*$ fragment MOs of NiCO yields a maximum difference of less than 10^{-5} au. Thus, the

negligence of the third term on the right-hand side of Eq. 3.2.10 does not lead to severe consequences in the calculations carried out in the context of this thesis.

4. Applications

4.1. General Computational Details

All application calculations of this thesis were carried out with the linear combination of Gaussian-type orbital fitting-function density functional (LCGTO-FF-DF) method as implemented in the package PARAGAUSS.[39,43,70,289] More specifically, version 4.0 of the PARAGAUSS package was employed. This version includes the hybrid DFT and DFT+Umol capabilities that were implemented as part of this thesis (see Chapter 3). Further recent extensions implemented by others[405,411] address parallelization and convergence acceleration strategies.

Most of the calculations employ def2-type orbital basis sets,[412] which were chosen of triple-zeta quality (triple-zeta valence polarized, TZVP) in the case of the studies presented in Sections 4.3 and 4.4. For the elements C, O, and Ni this AO basis describes all electrons and features the contractions $(11s,6p,2d,1f) \rightarrow [5s,3p,2d,1f]$ for C and O, respectively, as well as $(17s,11p,7d,1f) \rightarrow [6s,4p,4d,1f]$ in the case of Ni.[412] In the case of the heavier elements Pd and Pt effective core potentials (ECP) of the Stuttgart-Dresden-type parametrization[413] were employed to represent the lowest 28 and 60 "small-core" spin-orbitals, respectively. The corresponding AO basis set contractions account to $(7s,7p,6d,1f) \rightarrow [6s,4p,3d,1f]$ for Pd and $(8s,7p,6d,1f) \rightarrow [6s,4p,3d,1f]$ for Pt.[412] For the calculations on the nickel carbonyl complexes presented in Section 4.2 a quadruple-zeta AO basis with additional polarization and diffuse functions (QZVPPD) was employed which exhibits the contractions $(16s,8p,4d,2f,1g) \rightarrow [8s,4p,4d,2f,1g]$ for C and $(16s,9p,4d,2f,1g) \rightarrow [8s,4p,4d,2f,1g]$ for O atoms.[412] Furthermore, the def2-QZVPPD basis features a $(24s,18p,10d,4f,2g) \rightarrow [11s,6p,5d,4f,2g]$ contraction in the case of Ni.[412]

For the representation of the density during the evaluation of the Coulomb term within the density fitting (DF-FF) approximation[35-43] Ahlrich's Coulomb fitting basis set[414,415] was employed in all cases. The density fitting approximation was also employed in the case of hybrid DFT calculations to keep its effect constant when comparing semi-local with hybrid functionals.

The local XC terms of the employed DFT methods were integrated numerically. The corresponding numerical grids were constructed according to Becke's prescription as a superposition of atom-centered grids.[162] These atom centered grids exhibit Lebedev-type angular components,[160,161] which were chosen to be locally exact for angular momenta up to $\ell = 29$ in the calculations in Sections 4.2 and 4.3 and up to $\ell = 17$ for the studies in Section

4.4. The radial grid components comprised 168, 146, 305, 315, and 305 shells for C, O, Ni, Pd, and Pt in the former two cases as well as 134, 117, and 245 shells for the elements C, O, and Pt for the calculations in Section 4.4.

The direct inversion of the iterative subspace (DIIS) method[405,416] was used to accelerate the convergence of the density matrix during the SCF iteration. After reaching a maximum change of 10^{-6} in the density matrix elements, the SCF iteration was regarded as converged. The cluster models studied in Sections 4.3 and 4.4 were calculated by using a fractional occupation number (FON) technique with a Fermi-type broadening function.[39] The corresponding broadening parameter was successively lowered during the geometry optimization to final values of 0.05 and 0.01 eV for the calculations of Sections 4.3 and 4.4, respectively.

The structures of all models were relaxed under the constraints of their respective point group symmetry by using the molecular-dynamics based "fast inertial relaxation engine" (FIRE) optimization method[417] as implemented in the utility suite PARATOOLS.[405,410] The geometry optimization was pursued until the Cartesian components of all molecular forces acting on the atomic centers dropped below 10^{-6} au.

The CO adsorption energies discussed in Section 4.4 were corrected for the basis set superposition error (BSSE)[395] using an estimate that was obtained with the counterpoise approach.[418] The nickel-CO dissociation energies presented in Section 4.2 would require the same treatment as well. However, due to the significantly larger basis set employed in this latter case study, the BSSE was estimated to be less than 0.4 kJ/mol; its correction was therefore neglected.

The occupation numbers and the projected density of states spectra discussed in Sections 4.2 and 4.4, respectively, were obtained on the basis of Mulliken population numbers.[419]

4.2. DFT+Umol Analysis of the Self-Interaction Error in $Ni(CO)_m$, $m = 1 - 4$

4.2.1. Introduction

This section presents the application of the DFT+Umol method to the nickel carbonyl complexes $Ni(CO)_m$ ($m = 1-4$). This discussion follows Ref. [287].

Because of its important applications in chemical industry the nickel tetracarbonyl complex $Ni(CO)_4$ is among the experimentally best studied transition metal carbonyl compounds.[420-427] Furthermore, as they represent very simple transition metal complexes, $Ni(CO)_4$ and its subcarbonyls $Ni(CO)_m$ ($m = 1-3$) have been characterized by means of highly accurate post-HF and multi-reference calculations as well as in various DFT studies.[57,425,428-434] The subcarbonyls $Ni(CO)_m$ ($m = 1-3$) are very difficult to isolate experimentally. Thus, corresponding experimental reference values are significantly more sparse than in the case of $Ni(CO)_4$.[423,425,426,435] For the same reason the first metal-CO dissociation energies

$$E_{\mathrm{dis}}(m) = E_{\mathrm{tot}}\left(\mathrm{Ni(CO)}_m\right) - E_{\mathrm{tot}}\left(\mathrm{Ni(CO)}_{m-1}\right) - E_{\mathrm{tot}}\left(\mathrm{CO}\right) \qquad 4.2.1$$

vary with the experimental method applied. Nevertheless, a clear trend among the $E_{\mathrm{dis}}(m)$ values can always be observed. The first CO dissociation energies are found to increase when going from $Ni(CO)_4$ over $Ni(CO)_3$ to $Ni(CO)_2$, which is rationalized by the decreasing metal-carbonyl bond competition among the CO ligands.[423-425,427,435] However, the dissociation energy of NiCO, $E_{\mathrm{dis}}(1)$, is found to be lower than $E_{\mathrm{dis}}(2)$.[423,435] This latter behavior is rationalized in terms of a formal electronic relaxation of the Ni-atom from the d^{10} closed-shell configuration in the corresponding carbonyl complexes to its atomic ground state.[57,432,433]

This peculiar trend in the CO dissociation energies is reproduced by WFT methods as well as by hybrid DFT calculations.[425,430,431] In contrast, local and semi-local DFT methods predict $E_{\mathrm{dis}}(1)$ larger than $E_{\mathrm{dis}}(2)$, hence provide a qualitatively incorrect ordering of the CO dissociation energies. Cases, where hybrid DFT yields qualitatively correct results while semi-local DFT methods fail, likely indicate an influence of the self-interaction error (see Section 2.2.5). While the nickel carbonyls represent systems certainly small enough to allow for an accurate WFT description, these entities can appear also as intermediates of much larger models.[436] In such situations an efficient and reliable DFT description of the nickel carbonyl complexes is highly desirable.

This observation is the starting ground for the following study.[287] The influence of the SIE on the $Ni(CO)_4$ compound, on the $Ni(CO)_m$ subcarbonyls, and on the nickel atom was examined by means of a DFT+Umol correction (see Sections 2.4 and 3.2) to the GGA functional PBE.[49] The DFT+Umol correction was applied to the Ni 3*d* valence subshell as well as to the $2\pi^*$ orbitals, which are the lowest unoccupied MOs (LUMO) of the CO ligand.

In the following, these two types of DFT+Umol corrections will be denoted as Umol(Ni 3*d*) and Umol(CO 2π*), respectively. To assess the effect of the DFT+Umol term on either type of orbitals, the corresponding U_I parameters were varied between $U_{3d} = 3.0\,\text{eV}$ and 6.0 eV (in steps of 0.5 eV) for the former and between $U_{2\pi^*} = 1.0$, 2.0, and 4.0 eV for the latter case. The DFT+Umol results were compared with the values obtained with the uncorrected PBE functional[49] as well as with the hybrid GGA PBE0.[87]

4.2.2. Molecular Geometries

The molecular systems were treated as symmetric structures and relaxed under the corresponding symmetry constraints. C_{8v} symmetric models were employed for CO and NiCO, while $Ni(CO)_2$, $Ni(CO)_3$, and $Ni(CO)_4$ were treated with point group symmetry constraints of C_{2v}, D_{3h}, and T_d, respectively. All models were checked for possible Jahn–Teller distortions by computing the harmonic frequencies (see Section 4.2.4) of the vibrational normal modes without symmetry constraints. The corresponding normal mode analysis was carried out with the help of the ParaTools suite,[437] which allows one to compute second-order numerical derivatives with respect to nuclear displacements.

Table 4.2.1 provides $d_{C\text{-}O}$ and $d_{Ni\text{-}C}$, the C-O distances of the gas phase CO molecule and all nickel carbonyls and the corresponding Ni-C distances as obtained with PBE0, PBE, and PBE+Umol with the DFT+Umol term applied to Ni 3*d* ($U_{3d} = 6.0$ eV), or CO 2π* ($U_{2\pi^*} = 4.0$ eV), or a combination of both ($U_{3d} = 3.0$ eV, $U_{2\pi^*} = 1.0$ eV). Note, that for the former two variants only the results at the maxima of the examined U_I parameter values are listed to assess the impact of the two DFT+Umol corrections on the geometries.

A $d_{C\text{-}O}$ value of 112 pm is obtained with PBE0 for the CO molecule in the gas phase. Within the carbonyl complexes this distance is increased to about 115 pm to 113 pm, whereas the largest bond elongation is determined in NiCO and the smallest in the nickel tetracarbonyl complex. This behavior is predicted by the Blyholder model in terms of a partial electron transfer into the antibonding CO 2π* orbitals.[438] This so-called back-bonding mechanism enhances the bond strength between the CO ligand and the metal atom, but weakens the CO bond.[438] Following this model, the back-bonding interaction is strongest in NiCO and weakest in $Ni(CO)_4$. The PBE functional yields longer $d_{C\text{-}O}$ bonds between 116 and 115 pm for the nickel carbonyls. This is rationalized by the intrinsically longer C-O bonds that are obtained with PBE compared to PBE0. Similar differences are also notable for the $d_{C\text{-}O}$ values of CO in the gas phase (113 pm for PBE). The individual DFT+Umol corrections always lead to longer C-O bonds than PBE0 but shorter ones than PBE. This is rationalized with the reduced back-bonding interaction within the carbonyl complexes due to the increased orbital localization caused by the DFT+Umol term (see Section 4.2.4).[287]

Table 4.2.1: Bond lengths C-O, $d_{C\text{-}O}$, and Ni-C, $d_{Ni\text{-}C}$, of the nickel tetracarbonyl complex and the subcarbonyls $Ni(CO)_m$ ($m = 1-3$) obtained from PBE0, PBE, and PBE+Umol calculations. Experimental and CCSD(T) references are listed as well. All values in pm.

		U_{3d} [a]	$U_{2\pi^*}$ [b]	CO	NiCO	$Ni(CO)_2$	$Ni(CO)_3$	$Ni(CO)_4$
$d_{C\text{-}O}$	PBE0			112.2	114.6	113.6	113.4	113.2
	PBE			113.5	116.4	115.4	115.0	114.8
	PBE+Umol	6.0		—	115.8	114.9	114.7	114.6
			4.0	—	114.8	114.3	114.4	114.3
		3.0	1.0	—	115.7	114.8	114.7	114.6
	Exp.[c]			—	—	—	—	114.1 ± 0.2
$d_{Ni\text{-}C}$	PBE0			—	166.2	176.0	179.7	182.0
	PBE			—	166.4	176.0	180.1	182.2
	PBE+Umol	6.0		—	167.5	176.6	180.1	182.1
			4.0	—	170.2	180.0	184.5	187.6
		3.0	1.0	—	167.6	177.6	181.1	183.2
	Exp.[c]			—	—	—	—	183.8 ± 0.2
	CCSD(T)[d]			—	167.8	177.8	—	182.6

[a] U_{3d} parameter for the Umol(Ni 3*d*) correction in eV.

[b] $U_{2\pi^*}$ parameter for the Umol(CO 2π*) correction in eV.

[c] Ref. [422]

[d] Ref. [431]

Compared to the C-O bond lengths, the $d_{Ni\text{-}C}$ values exhibit a larger spread upon application of the DFT+Umol term. PBE and PBE0 yield quite similar Ni-C distances for the compounds $Ni(CO)_m$ ($m = 1-4$), between 166 pm for NiCO and 182 pm for $Ni(CO)_4$. The $d_{Ni\text{-}C}$ results obtained with the Umol(Ni 3*d*) correction are also quite close to these values; minor bond elongations are only obtained in the case of NiCO and $Ni(CO)_2$. At variance, the DFT+Umol correction of the CO 2π* orbitals yields significantly longer bonds which increasingly differ from those of all other methods when going from NiCO to $Ni(CO)_4$. The combined projection on both types of target orbitals yields the best agreement with the corresponding CCSD(T) reference results, deviating only by fractions of a picometer. Also the $d_{Ni\text{-}C}$ values obtained with PBE, PBE0, and PBE+Umol(Ni 3*d*) agree well with the CCSD(T) results, the corresponding differences being below 2 pm.

The $Ni(CO)_2$ molecule was initially considered as linear due to artifacts of the matrix isolation technique employed in early experimental studies.[439] More recent experiments

showed this molecule to be bent.[440] For $Ni(CO)_2$ a C-Ni-C angle of 140° is obtained with the PBE method, while PBE0 and the PBE+Umol(Ni 3*d*) combination predict slightly larger values of 146° and 148°, respectively. In contrast, application of the Umol(CO 2π*) term yields a nearly linear $Ni(CO)_2$ structure. The bond angles within all other complexes are determined by their respective point group symmetries.

4.2.3. Dissociation Energies

In the following the first metal-CO dissociation energies $E_{dis}(m)$, $m = 1-4$, as obtained from PBE, PBE0, and both PBE+Umol variants according to Eq. 4.2.1 are discussed.

The $E_{dis}(1)$ result depends on the total electronic energy of the nickel atom. The atomic system was treated with C_{2v} point group symmetry constraints to allow for a localized orbital occupation within the 3*d* valence subshell.[244] Note that this broken symmetry treatment leads to an $3d^9 4s^1$ configuration for the nickel atom as opposed to the experimentally found $3d^8 4s^2$ atomic ground state, which arises from spin-orbit interaction that was not considered here.[441] Within a finite basis set the computed dissociation energies are subject to the basis set superposition error (BSSE), thus would need to be corrected by the counterpoise method.[395,418] However, due to the very flexible def2-QZVPPD basis set employed, the BSSE in the $E_{dis}(m)$ values was found to be less than 0.4 kJ/mol, thus can be safely neglected in the present discussion.

Table 4.2.2 provides the values $E_{dis}(m)$ obtained with the variants PBE+Umol(Ni 3*d*) and PBE+Umol(CO 2π*), the uncorrected PBE functional, and the hybrid GGA PBE0. For comparison the CCSD(T) reference values are shown as well. Note, that the CCSD(T) results for $E_{dis}(2)$ and $E_{dis}(3)$ were determined for a linear $Ni(CO)_2$ molecule.[431] In the case of PBE the linear and C_{2v} symmetric structures of $Ni(CO)_2$ differ by ~5 kJ/mol. Thus, compared to the variations among the disagreeing experimental results listed in Table 4.2.2, the CCSD(T) energies of the linear structure can be regarded as sufficiently accurate for the present discussion of the trends of the $E_{dis}(m)$ values.

In agreement with earlier studies,[57] the uncorrected semi-local DFT approximation PBE does not provide the correct trend $E_{dis}(1) < E_{dis}(2)$ of the first metal-CO dissociation energies. With $E_{dis}(1) = 247$ kJ/mol the strength of the Ni-C bond in NiCO is considerably overestimated and significantly larger than the corresponding dissociation energy of 208 kJ/mol obtained for $Ni(CO)_2$. In contrast, the other two $E_{dis}(m)$ values agree more with the expected trend and are successively smaller; 148 kJ/mol for *m* = 3 and 121 kJ/mol for *m* = 4. The CCSD(T) reference values amount to 144, 178, 145, and 125 kJ/mol for $m = 1-4$, respectively. The PBE0 results agree considerably better with these reference values than the PBE values. PBE0 yields a $E_{dis}(2)$ value of 178 kJ/mol, which is close to the CCSD(T)

reference and significantly larger than the dissociation energies of the other three complexes. Also $E_{dis}(3) = 132$ kJ/mol is still higher than the dissociation energy of the NiCO molecule, 126 kJ/mol. The corresponding $E_{dis}(4)$ value amounts to 101 kJ/mol. Thus, despite somewhat underestimating the Ni-CO dissociation energies, PBE0 is able to recover the trend $E_{dis}(2) > E_{dis}(3) \approx E_{dis}(1) > E_{dis}(4)$ provided by CCSD(T).

Table 4.2.2: First metal-CO dissociation energies $E_{dis}(m)$ of the $Ni(CO)_m$ complexes ($m = 1-4$) obtained with PBE0, PBE, and the two projections of the DFT+Umol correction as well as the corresponding CCSD(T) and experimental reference values. All energies in kJ/mol.

	U_{3d} [a]	$U_{2\pi^*}$ [b]	NiCO	$Ni(CO)_2$	$Ni(CO)_3$	$Ni(CO)_4$
PBE0			126	178	132	101
PBE			247	208	148	121
PBE+Umol	3.0		171	198	139	110
	4.5		135	192	135	105
	5.0		123	190	133	103
	5.5		111	188	131	101
	6.0		100	186	130	99
		1.0	218	191	126	91
		2.0	190	181	97	61
		4.0	139	164	37	1
	3.0	1.0	144	183	115	79
Exp. 1[c]			121 ± 63	226 ± 63	54 ± 8	105 ± 8
Exp. 2[d]			146 ± 13	213 ± 17	121 ± 8	—
Exp. 3[e]			169 ± 24	197 ± 24	118 ± 10	—
CCSD(T)[f]			144	178	145	125

[a] U_{3d} parameter for the Umol(Ni 3*d*) correction in eV.

[b] $U_{2\pi^*}$ parameter for the Umol(CO 2π*) correction in eV.

[c] Ref. [435]

[d] Ref. [38] in Ref. [431]

[e] Ref. [423]

[f] Ref. [431]

The Umol(Ni 3*d*) correction also provides the correct trend. With 198 kJ/mol, the metal-CO dissociation energy of $Ni(CO)_2$ is obtained higher than $E_{dis}(1)$, 171 kJ/mol, already for $U_{3d} = 3.0$ eV. At $U_{3d} = 4.5$ eV the dissociation energies $E_{dis}(3)$ and $E_{dis}(1)$ are nearly equal with 135 kJ/mol, respectively, while $E_{dis}(2)$ and $E_{dis}(4)$ amount to 192 kJ/mol and 105 kJ/mol, respectively. When comparing these results, the $E_{dis}(1)$ value is found to be much more sensitive to the value of the U_{3d} parameter than the other dissociation energies. $E_{dis}(1)$ is lowered by about 12 kJ/mol when one increases U_{3d} in steps of 0.5 eV, while the corresponding reduction of all other $E_{dis}(m)$ values is only about 2 kJ/mol. Thus, the Umol(Ni 3*d*) correction with $U_{3d} = 4.5$ eV describes the metal-CO dissociation reasonably accurate. In this case the $E_{dis}(m)$ energies show a comparable agreement with the CCSD(T) reference values as the corresponding PBE0 results. At higher values of U_{3d}, the $E_{dis}(1)$ energies are, however, underestimated, while $E_{dis}(2)$ remains higher than the corresponding coupled-cluster reference value.

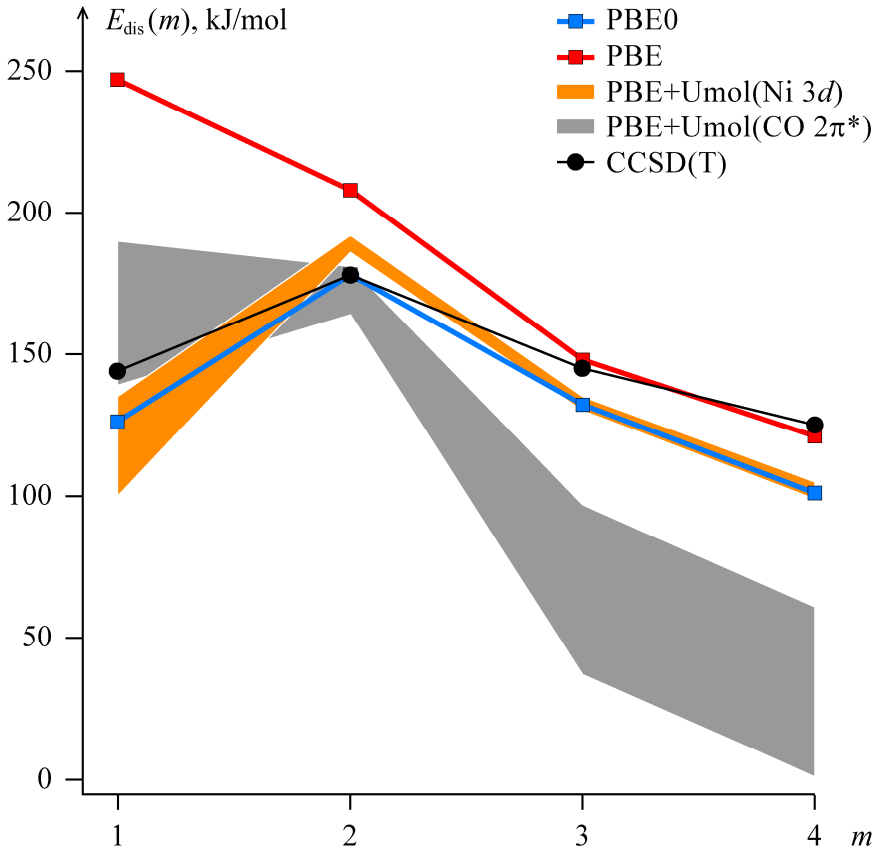

Figure 4.2.1: First metal-CO dissociation energies $E_{dis}(m)$ of the $Ni(CO)_m$ complexes ($m = 1-4$) obtained with PBE0, PBE, and the two projections of the DFT+Umol correction. For the latter the $E_{dis}(m)$ ranges obtained for the applied U_I parameter values are shown. The CCSD(T) reference results are plotted for comparison.

From a qualitative point of view, the DFT+Umol correction of the CO 2π* orbitals behaves analogously to the Umol(Ni 3*d*) term as it is able restore the trend $E_{dis}(2) > E_{dis}(1)$ as well. However, it requires $U_{2\pi^*} = 4.0$ eV to yield an $E_{dis}(1)$ value of 139 kJ/mol which is close to the CCSD(T) reference and reasonably smaller than the corresponding dissociation energy of $Ni(CO)_2$, 164 kJ/mol. While also this latter value agrees reasonably well with the CCSD(T) reference, the corresponding dissociation energies of the tri- and tetracarbonyl complexes are strongly underestimated. For $U_{2\pi^*} = 4.0$ eV the $E_{dis}(3)$ and $E_{dis}(4)$ values are calculated at 37 and 1 kJ/mol, respectively. This latter result, predicting the $Ni(CO)_4$ complex to be unstable, is a strong indication that the PBE+Umol(CO 2π*) combination provides an unphysical description of the $Ni(CO)_m$ compounds. Furthermore, while the $E_{dis}(2)$ value exhibits a similar sensitivity with respect to $U_{2\pi^*}$ as in the case of U_{3d}, the Umol(CO 2π*) approach yields lower dissociation energies for $Ni(CO)_2$ than the Umol(Ni 3*d*) term. Thus, a stronger dependency of this energy on $U_{2\pi^*}$ is to be expected for parameter values below 1 eV. The plot of the $E_{dis}(m)$ values obtained with the various computational methods (Figure 4.2.1) clearly depicts the deviations of the results obtained from the Umol(CO 2π*) correction.

The combined DFT+Umol projection on both groups of target orbitals, with $U_{3d} = 3.0$ eV and $U_{2\pi^*} = 1.0$ eV, provides accurate molecular geometries, but was found to yield reasonable dissociation energies only in the case of NiCO and $Ni(CO)_2$. With $E_{dis}(3) = 115$ kJ/mol and $E_{dis}(4) = 79$ kJ/mol, the dissociation energies of the other two carbonyls are considerably underestimated. Inspecting both DFT+Umol contributions individually, reveals again the Umol(CO 2π*) term to be mainly responsible for these deviations.

4.2.4. Electronic Structure Aspects and Vibrational Frequencies

The analysis of the electronic structure allows one to rationalize the behavior of both DFT+Umol variants with regard to the dissociation energies.[287] More specifically, the following questions are addressed; (i) Why is $E_{dis}(1)$ strongly overestimated by PBE and why is it corrected by the Umol(Ni 3*d*) term? (ii) Why do all other dissociation energies remain mostly unaffected by the Umol(Ni 3*d*) term? (iii) How can both DFT+Umol variants have a similar qualitative effect on $E_{dis}(1)$? (iv) Why does the Umol(CO 2π*) correction deteriorate the description of the $Ni(CO)_3$ and $Ni(CO)_4$ complexes to such an extent that the results cannot be regarded as physically meaningful?

As already mentioned in Section 4.2.3, all computational methods applied here yield a d^9s^1 triplet state for the nickel atom. In contrast, a formally closed shell d^{10} configurations was identified from the individual Mulliken orbital populations[419] of the nickel atom in all $Ni(CO)_m$ compounds, in agreement earlier studies.[433,434] The accumulated Mulliken

populations of the Ni 3*d* subshell provide useful insight into the electronic structure of the nickel carbonyls. These values, denoted as O_{3d}, are collected in Table 4.2.3 together with the resulting net charges q_{Ni} of the nickel atom.

The Ni 3*d* orbitals in the $Ni(CO)_m$ complexes delocalize by mixing with the ligand orbitals. Thus, the corresponding accumulated populations O_{3d} are always lower than 10 *e*. In the case of PBE0 the O_{3d} values amount to 9.16, 8.99, 8.79, and 8.34 *e* for NiCO, $Ni(CO)_2$, $Ni(CO)_3$, and $Ni(CO)_4$, respectively. In comparison, the corresponding accumulated populations obtained with the uncorrected PBE method are consistently lower, 9.08, 8.87, 8.70, and 8.34 *e*, respectively. The lower O_{3d} values obtained from PBE are a direct consequence of the larger SIE in this method. Recall that any system tends to lower its residual self-repulsion by an overly large delocalization of the affected charge distributions (see Section 2.2.5). In the present case this holds especially for the Ni 3*d* orbitals. However, without the formation of chemical bonds, the possibilities to delocalize are rather restricted for the 3*d* orbitals in the (bare) nickel atom. In this case a delocalization can only occur via a spatial expansion of the 3*d* orbitals which, however, is limited by the other, much larger terms of the KS potential. On the other hand, an overly large mixing with ligand orbitals easily admits the delocalization of the Ni 3*d* derived orbitals in the carbonyl complexes. In consequence, the destabilizing self-repulsion is not lowered as much for the d^9s^1 triplet state of the nickel atom as for the d^{10} configuration of the $Ni(CO)_m$ complexes. This explains why the uncorrected PBE functional strongly overestimates the $E_{\mathrm{dis}}(1)$ value.

Table 4.2.3: Accumulated Mulliken populations of the Ni 3*d* subshell O_{3d} and net charges q_{Ni} of the Ni atom in the $Ni(CO)_m$ systems ($m = 1-4$) obtained with PBE0, PBE, and the two projections of the DFT+Umol correction for the applied values of U_l. All values in *e*.

	U_{3d} [a]	$U_{2\pi^*}$ [b]	NiCO		$Ni(CO)_2$		$Ni(CO)_3$		$Ni(CO)_4$	
			O_{3d}	q_{Ni}	O_{3d}	q_{Ni}	O_{3d}	q_{Ni}	O_{3d}	q_{Ni}
PBE0			9.16	0.51	8.99	0.79	8.79	1.11	8.34	2.33
PBE			9.08	0.54	8.87	0.80	8.70	1.04	8.20	2.41
PBE+Umol	3.0		9.18	0.49	8.97	0.76	8.79	1.01	8.30	2.34
	4.5		9.23	0.47	9.02	0.74	8.83	0.99	8.35	2.30
	6.0		9.28	0.46	9.06	0.72	8.88	0.98	8.39	2.26
		1.0	9.10	0.50	8.93	0.75	8.74	1.01	8.29	2.32
		4.0	9.18	0.36	9.15	0.63	8.85	0.92	8.49	1.98
	3.0	1.0	9.21	0.46	9.04	0.71	8.82	0.98	8.36	2.25

[a] U_{3d} parameter for the Umol(Ni 3*d*) correction in eV.

[b] $U_{2\pi^*}$ parameter for the Umol(CO 2π*) correction in eV.

Next, the changes of the $E_{dis}(1)$ value introduced by the Umol(Ni 3*d*) term will be discussed. Recall that the effect of the DFT+Umol correction is equivalent to that of the parabolic DFT+U penalty functional (see Eq. 2.4.10 in Section 2.4)

$$E^{U} = \tfrac{1}{2}\sum_{I\sigma} U_I \left(\mathrm{Tr}\left\{\mathbf{n}_I^\sigma\right\} - \mathrm{Tr}\left\{\mathbf{n}_I^\sigma \mathbf{n}_I^\sigma\right\}\right). \qquad 4.2.2$$

The individual populations of the elements of the Ni 3*d* subshell in NiCO suggest that all of these orbitals are more than half occupied (at least by a fraction of 0.68). In consequence, the derivative of Eq. 4.2.2 is negative, which implies that in this case the Ni 3*d* orbitals are subject to an attractive potential contribution from the Umol(Ni 3*d*) term.[61] This attractive contribution increases the O_{3d} value of NiCO compared to the corresponding population resulting from the uncorrected PBE functional. Two conclusions can be drawn from the fact that the Umol(Ni 3*d*) term increases the O_{3d} values. First, the increased localization of the Ni 3*d* orbitals in NiCO by the Umol(Ni 3*d*) correction implies a reduced mixing with the orbitals of the CO ligand. According to the Blyholder model the mixing of these orbitals leads to the back-bonding interaction.[438] Thus, the application of Umol(Ni 3*d*) reduces back-bonding in NiCO. Equivalently, the Blyholder model predicts that the formation of the primary σ-interaction between the Ni 4*s* and the CO 5σ orbitals increases the net charge q_{Ni} on the nickel center.[438] In consequence, the Ni 3*d* orbitals are subject to a more repulsive potential.[438] This repulsive potential is somewhat counteracted by the aforementioned attractive potential contribution of the Umol(Ni 3*d*) term. The increased localization of the Ni 3*d* subshell by the Umol(Ni 3*d*) term also implies a higher self-repulsion in these orbitals. Note, that both of these effects, the reduced amount of back-bonding and the increased self-repulsion, have the same net influence on the NiCO system, namely the destabilization of its delocalized d^{10} configuration with respect to the localized d^9s^1 state of the nickel atom. This destabilization lowers the Ni-CO dissociation energy of NiCO, which explains why the Umol(Ni 3*d*) term is able to correct the $E_{dis}(1)$ value.

Also in the case of the other $Ni(CO)_m$ complexes, a d^{10} configuration can be deduced from the more than half occupied Ni 3*d* orbitals. The individual orbital occupations obtained from PBE amount to at least 0.71, 0.59, and 0.57 *e* in the case of $Ni(CO)_2$, $Ni(CO)_3$, and $Ni(CO)_4$, respectively. Thus, the Umol(Ni 3*d*) term has a similar effect on these systems as rationalized above for NiCO. While accurate CASSCF calculations reveal the σ-interaction to prevail in the NiCO system,[433] the amount of back-bonding is likely to increase with the number of CO ligands. Indeed, this is the case, in agreement with the Blyholder model[438] (see above), as can be deduced from the q_{Ni} values which are found to increase when going from NiCO to $Ni(CO)_4$ (Table 4.2.3). The Umol(Ni 3*d*) term localizes the Ni 3*d* orbitals and reduces back-bonding which is well in line with the traditional explanation of the bonding situation in NiCO and the other carbonyl complexes.[429-433] In consequence, the amount of back-bonding interaction in the nickel carbonyls is corrected which is overestimated by PBE due to the SIE.

Thus, also the first nickel-CO dissociation energies of $Ni(CO)_2$, $Ni(CO)_3$, and $Ni(CO)_4$ are somewhat reduced when the Umol(Ni 3*d*) correction is applied. However, in these cases the effect of the Umol(Ni 3*d*) term is not nearly as large as for the $E_{dis}(1)$ value as visible from the energetic contributions E^U of the Umol(Ni 3*d*) term which are provided in Table 4.2.4. This behavior of the E^U energy can be rationalized as follows. Within the NiCO complex three of the 3*d* derived orbitals interact with the orbitals of the CO ligand, namely z^2, *xz*, and *yz* for NiCO oriented along the *z*-axis. When going from NiCO to the di-, tri-, and tetracarbonyl complexes, the possibilities for delocalization increase due to the larger number of ligand orbitals with which the 3*d* derived orbitals can interact. However, the number of interacting orbitals of the 3*d* subshell is the same in all $Ni(CO)_m$ systems. Thus, the Ni 3*d* derived orbitals remain similarly delocalized after the removal of a single CO ligand from $Ni(CO)_2$, $Ni(CO)_3$, and $Ni(CO)_4$. This argument rationalizes the small reductions in the O_{3d} values when going from NiCO to $Ni(CO)_4$ (see Table 4.2.3). Furthermore, the above rationalization allows to understand the comparatively small growth of the energetic contributions E^U of the Umol(Ni 3*d*) term when going from NiCO to the tetracarbonyl complex (see Table 4.2.4). The energies E^U increase only slightly with the number of ligands compared to the drastic change that occurs upon addition of the first CO fragment (see Table 4.2.4). Thus, the Umol(Ni 3*d*) correction destabilizes all carbonyl complexes by roughly the same amount. This rationalizes why the dissociation energies $E_{dis}(2)$, $E_{dis}(3)$, and $E_{dis}(4)$ are significantly less affected by Umol(Ni 3*d*) than the dissociation energy of NiCO.

Table 4.2.4: DFT+Umol energy term E^U exemplarily shown for both SIE corrections. All energies in kJ/mol.

U_{3d} [a]	$U_{2\pi^*}$ [b]	Ni	NiCO	$Ni(CO)_2$	$Ni(CO)_3$	$Ni(CO)_4$
4.5		11	118	135	140	166
	4.0	0[c]	95	130	245	361

[a] U_{3d} parameter for the Umol(Ni 3*d*) correction in eV.

[b] $U_{2\pi^*}$ parameter for the Umol(CO 2π*) correction in eV.

[c] Zero by definition

Lowering the energies of the 3*d* derived orbitals is not the only way to reduce the back-bonding in the $Ni(CO)_m$ complexes. A similar reduction of the mixing between Ni 3*d* and CO 2π* orbitals is also achieved by raising the energies of the latter. This essentially describes the effect of the Umol(CO 2π*) correction. As the energy gap between the interaction partners is increased, the delocalization of the 3*d* orbitals is reduced. This in turn explains the

increased O_{3d} values that result from the Umol(CO 2π*) correction (Table 4.2.3). Thus, also the Umol(CO 2π*) term is able to reduce the delocalization within the Ni 3*d* subshell of the carbonyl complexes. This indirect localization of the Ni 3*d* subshell by the Umol(CO 2π*) correction rationalizes why both DFT+Umol variants have similar effects on the dissociation energy $E_{\mathrm{dis}}(1)$, at least from a qualitative point of view.

However, the indirect effect of the Umol(CO 2π*) correction on the O_{3d} values is rather small. In the case of NiCO, a relatively large value of $U_{2\pi^*} = 4.0$ eV is required to bring the accumulated 3*d* population close to those obtained with PBE0 or PBE+Umol(Ni 3*d*), hence, to achieve $E_{\mathrm{dis}}(2) > E_{\mathrm{dis}}(1)$ (see Table 4.2.2 in Section 4.2.3). While the O_{3d} values of the other nickel carbonyls are increased by the Umol(CO 2π*) correction, back-donation is reduced in these cases too. The energy contributions E^{U} of the Umol(CO 2π*) term are provided in Table 4.2.4 for the nickel complexes and the nickel atom. Accordingly, the reduced amount of back-bonding is accompanied by the steadily increasing E^{U} values that result from the Umol(CO 2π*) correction when going from NiCO to $Ni(CO)_4$. However, while back-donation is notable in the case of NiCO (see Section 4.2.2), this interaction also represents an important factor for the stabilization of the $Ni(CO)_3$ and $Ni(CO)_4$ complexes due to the larger number of Ni-CO bonds in these systems. Thus, the systems $Ni(CO)_3$ and $Ni(CO)_4$ are notably destabilized at $U_{2\pi^*} = 4.0$ eV. A closely related consequence of the reduced back-bonding by the Umol(CO 2π*) term are the reduced positive net charges q_{Ni} on the nickel centers (see Table 4.2.3). As the delocalization of the 3*d* derived orbitals is rather limited if the CO 2π* orbitals are too high in energy, more negative charge resides on the Ni atom. This becomes also apparent from the accumulated 3*d* population of 8.49 *e* obtained at $U_{2\pi^*} = 4.0$ eV for $Ni(CO)_4$. This value is considerably higher than those resulting from the PBE0 and PBE+Umol(Ni 3*d*) calculations. The net charge of 1.98 *e* obtained with the PBE+Umol(CO 2π*) combination is notably below the q_{Ni} values obtained with the former two methods. Note, that σ-bonding and back-bonding represent two synergetic effects. As the primary σ-bonding represents a dative interaction, it is further enhanced by the back-bonding interaction, which transfers electronic charge away from the nickel center to the CO ligands. Thus, the low charges q_{Ni} that result for $Ni(CO)_3$ and $Ni(CO)_4$ with $U_{2\pi^*} = 4.0$ eV most likely indicate that the σ-bonding is hampered by the Umol(CO 2π*) term as well. Both, the removal of back-bonding and the reduced strength of the σ-bonds, rationalize the strong destabilization of the nickel carbonyls $Ni(CO)_3$ and $Ni(CO)_4$ that results when the DFT+Umol correction is applied to the CO 2π* orbitals.

Table 4.2.5: Totally symmetric C-O and Ni-C stretching frequencies of the nickel carbonyl complexes and the CO molecule in the gas phase. All values in cm^{-1}.

	U_{3d} [a]	$U_{2\pi^*}$ [b]	CO	NiCO		$Ni(CO)_2$		$Ni(CO)_3$		$Ni(CO)_4$	
			υ_{C-O}	υ_{Ni-C}	υ_{C-O}	υ_{Ni-C}	υ_{C-O}	υ_{Ni-C}	υ_{C-O}	υ_{Ni-C}	υ_{C-O}
PBE0			2238	601	2112	471	2190	416	2205	391	2218
PBE			2128	603	2008	526	2068	415	2087	392	2100
PBE+Umol	4.5		2128	593	2033	467	2087	410	2094	387	2103
		4.0	2128	548	2068	416	2129	375	2108	360	2113
	3.0	1.0	2128	583	2034	447	2100	402	2097	381	2105
Exp.[c]			2170	—	2034[d]	—	2117[e]	—	—	380[f]	2155[f]

[a] U_{3d} parameter for the Umol(Ni 3*d*) correction in eV.

[b] $U_{2\pi^*}$ parameter for the Umol(CO 2π*) correction in eV.

[c] The measured anharmonic frequency of the free CO molecule is 2143 cm^{-1}, the experimentally derived harmonic value is larger by 27 cm^{-1}. All experimental C-O stretching frequencies are corrected by this amount to account approximately for this missing anharmonicity effect in the computational results.[442]

[d] Ref. [439]

[e] Ref. [440]

[f] Ref. [421]

Finally, the totally symmetric vibrational C-O stretching frequencies υ_{C-O} of the carbonyl complexes are discussed. These results provide a confirmation for the above rationalizations of the effects of both DFT+Umol terms on the electronic structure of the nickel carbonyls. Table 4.2.5 provides the υ_{C-O} values of these systems along with the corresponding totally symmetric frequencies υ_{Ni-C} of the Ni-C stretching modes and the frequencies of the CO molecule in the gas phase.

The Blyholder model predicts, that the charge transfer into the 2π* orbitals due to back-bonding reduces the strengths of the C-O bonds and in consequence also the υ_{C-O} frequencies of the $Ni(CO)_m$ systems.[438] Indeed, in nearly all cases the υ_{C-O} frequencies of the carbonyl complexes are lower compared to those of the CO molecule in the gas phase. The υ_{C-O} value obtained for the $Ni(CO)_2$ complex with Umol(CO 2π*) and $U_{2\pi^*} = 4.0$ eV represents the only exception. This outlier may be rationalized by the reduction of the orbital overlap in the nearly linear $Ni(CO)_2$ structure obtained in this case (see Section 4.2.2). Due to the parabolic shape of the penalty functional, the DFT+Umol term lowers the energy of more than half occupied orbitals, while less than half filled levels are raised on the energy scale.[63] Thus, the

energy gap between the Ni 3*d* and the CO 2π* orbitals of the nickel carbonyl complexes is increased by both DFT+Umol variants; either by lowering the former or by increasing the energies of the latter. In both cases, the amount of back-bonding is reduced while the $\upsilon_{C\text{-}O}$ frequencies are increased relative to those obtained with the uncorrected PBE method. The deviation of the $\upsilon_{C\text{-}O}$ values due to the DFT+Umol corrections is larger for Umol(CO 2π*) at $U_{2\pi^*} = 4.0$ eV than for Umol(Ni 3*d*) at $U_{3d} = 4.5$ eV but decreases when going from NiCO to the nickel tetracarbonyl. The PBE+Umol(Ni 3*d*) combination nearly matches the experimental reference in the case of NiCO but deviates by –30 cm^{-1} for $Ni(CO)_2$ and by –52 cm^{-1} for the tetracarbonyl complex. These deviations are in line with the slightly underestimated $E_{dis}(m)$ values for $m = 2 - 4$ and may indicate that the back-bonding interaction in the di-, tri-, and tetracarbonyls is still somewhat overestimated by PBE+Umol(Ni 3*d*). Also the description of the CO fragment by the underlying PBE functional seems to contribute to these deviations. Indeed, the Umol(CO 2π*) term essentially removes back-bonding which is reflected by the somewhat higher $\upsilon_{C\text{-}O}$ frequencies. However, in this case the deviations from the experimental reference are still comparable to those of the uncorrected PBE method. Nevertheless, the $\upsilon_{C\text{-}O}$ values obtained with the PBE method as well as with both PBE+Umol combinations agree still better with the experimental references than the frequencies that result from the PBE0 calculations.

The $\upsilon_{Ni\text{-}C}$ frequencies obtained with the functionals PBE and PBE0 as well as with the PBE+Umol(Ni 3*d*) combination mostly agree with each other, within ~10 cm^{-1}. Only the PBE result for the $\upsilon_{Ni\text{-}C}$ frequency of $Ni(CO)_2$ differs more from the corresponding results of the other methods. These deviations may be related to differences in the C-Ni-C angle. The lower $\upsilon_{Ni\text{-}C}$ frequencies that result from the Umol(CO 2π*) projection are in line with the corresponding underestimated metal-CO dissociation energies, obtained in this case.

4.2.5. Summary and Conclusions

The case study presented in this section employed the DFT+Umol correction to analyze the impact of self-interaction artifacts on various properties of nickel carbonyl complexes. To this end, the DFT+Umol correction was applied to the orbitals of the Ni 3*d* subshell as well as to the manifold of the 2π* MOs of the CO ligands.

From specific U_1 values onward both types of DFT+Umol corrections are able to restore the correct trend in the first metal-ligand dissociation energies $E_{dis}(m)$ of the $Ni(CO)_m$ complexes with $m = 1 - 4$, specifically $E_{dis}(1) < E_{dis}(2)$. The application of the DFT+Umol correction to the orbitals of the Ni 3*d* subshells provides a reasonable quantitative accuracy for the dissociation energies, bond lengths and vibrational frequencies. Opposed to that, the corresponding correction based on the CO 2π* orbitals leads to severely underestimated

$E_{\mathrm{dis}}(m)$ values for $Ni(CO)_3$ and $Ni(CO)_4$. In agreement with that, the Umol(CO 2π*) term results in overly elongated Ni-C bonds and higher $\upsilon_{C\text{-}O}$ frequencies for these systems.

The aforementioned accurate results from the Umol(Ni 3*d*) correction are obtained at values of the U_{3d} parameter which are close ~5.3 eV, a commonly employed value for this subshell.[288] This leads to the conclusion that self-interaction artifacts within the Ni 3*d* shell are the main reason for the erroneous $E_{\mathrm{dis}}(m)$ trend of GGA functionals, exemplified in the present study for the PBE functional.

The interplay between the self-repulsion energy and the delocalization of the orbitals is studied by examining some aspects of the electronic structures of the carbonyl complexes. This analysis allows one to rationalize why the Umol(CO 2π*) correction yields, from a quantitative perspective, only a poor description of the $Ni(CO)_m$ systems, while PBE+Umol(Ni 3*d*) provides a reasonable accuracy in these cases.

As the Umol(Ni 3*d*) term reduces the delocalization of the Ni 3*d* orbitals, it increases the corresponding Mulliken populations to similar values as those obtained in PBE0 calculations. In consequence, the Umol(Ni 3*d*) destabilizes all carbonyl complexes by a similar amount. Thereby the energy of the NiCO compound is adjusted relative to that of the free nickel atom while the energy differences between the various $Ni(CO)_m$ systems are much less affected. This rectifies the metal-CO dissociation energy of the NiCO system and restores the trend of the $E_{\mathrm{dis}}(m)$ values. The Umol(CO 2π*) projection can achieve a similar localization of the Ni 3*d* shell, by increasing the energy of the CO 2π* orbitals which indirectly reduces the possibility for the 3*d* orbitals to delocalize. However, due to the indirect nature of this localization, large values of the $U_{2\pi^*}$ parameter are required to achieve effects of similar size as with the Umol(Ni 3*d*) term. This in turn has a severe negative impact on the electronic structure of the carbonyl complexes, especially on the back-bonding interaction within them. Thus, the Umol(CO 2π*) term overly destabilizes especially the complexes $Ni(CO)_3$, and $Ni(CO)_4$.

The case study presented clarified many SIE related aspects in the bonding of the $Ni(CO)_m$ complexes as described by a semi-local exchange-correlation functional such as PBE. Furthermore, this study also demonstrated that the flexibility of the DFT+Umol method can be exploited for a detailed analysis of self-interaction artifacts in the electronic structure of chemical systems as obtained with semi-local DFT approximations.

4.3. Transition Metal Cluster Scaling Study with Hybrid DFT

4.3.1. Introduction

In the following, semi-local and hybrid DFT approximations are compared regarding their description of transition metals using a cluster scaling study as a vehicle. The discussion thereby follows Ref. [443].

The description of transition metals by hybrid density functional theory is a difficult problem. On the one hand, the reduced self-interaction error in hybrid DFT approximations (see Sections 2.2.5 and 2.3) should lead to a generally improved description of such materials. On the other hand, the self-interaction correction provided by the exact-exchange term also leads to a deteriorated description of static correlation effects, hence to an increased static correlation error (see Section 2.2.6). Static correlation effects can have an important influence on the electronic structure of transition metals due to the high number of nearly degenerate levels in the valence band.

The B3LYP hybrid GGA functional[47,82,84,191] is the most widely applied of all DFT approximations.[263] As such it is also well known for its failures for systems containing transition metal atoms.[245,246,444,445] These problems were often rationalized by reference to the aforementioned negative influence of the EXX term on the description of static correlation.[129] However, a recent analysis revealed the LYP correlation term to contribute notably more.[198] Indeed, this term does not reduce to an LDA correlation form in the case of the homogeneous electron gas model, which is important for slowly varying electron densities as they occur in transition metals.[198] The parametrization of the B3 part as well as the EXX term introduce errors too.[198] The contribution of these terms to the failures of the B3LYP functionals for metals were, however, found to be less dramatic than that of the LYP correlation part.[198]

As described in Section 2.3.3, various alternative hybrid DFT approximations followed the B3LYP functional, which mostly avoid the problems associated with the LYP term.[77,85,87,89,90,210,212,261] The subsequently presented study addresses the question whether some of these functionals can provide a reasonable accuracy for transition metals.[443] While comparable studies were previously conducted in terms of plane-wave studies,[198,446] the present investigation was done on series of group 10 cluster models Ni_m, Pd_m, and Pt_m of increasing size (see Section 4.3.2). [443] Following earlier assessments of density functional methods,[447,448] cluster scaling techniques were used to extrapolate the results obtained for these models to the corresponding bulk limits.[448-457] These extrapolations allow for a comparison with the respective experimental reference values as well as with results from plane-wave calculations. Thereby the performance of the hybrid DFT approximations PBE0,[87] TPSSh,[212] and M06[77,90] is examined for the extrapolated description of structural, energetic, and electronic properties of nickel, palladium, and platinum. It is worth noting that

the functionals PBE0 and M06 come with EXX mixing parameters α_1 of 0.25 and 0.27, respectively, whereas $\alpha_1 = 0.1$ for TPSSh (see Section 2.3.3). While hybrid functionals with even higher EXX mixing factors exist, the former two methods are referred to as high-EXX functionals in the following to distinguish them from TPSSh. To estimate the influence of the exact-exchange term, these three hybrid functionals are also compared with their respective semi-local counterparts PBE,[49] TPSS,[77,89,90,210] and M06L.[77] Finally, the analysis of various aspects of the electronic structure provides insight why some of the examined methods perform well while others do not.[443]

4.3.2. Cluster Scaling Procedure and Computational Models

Large transition metal clusters M_m usually represent densely packed and highly symmetric structures that consist of multiple layers of atoms (shells).[458,459] However, the environments that surround the individual atoms of such a cluster can vary significantly. In the case of the fcc metals Ni, Pd, and Pt the atoms that comprise the core moiety of a cluster are twelve-fold coordinated by neighboring atoms. In consequence, such atoms experience an environment which is close to that of the corresponding bulk material. On the other hand, the atoms forming the surface layer are coordinated by a lower number of neighboring atoms and thus, are located in an entirely different environment. This is even more the case for atoms which comprise the edges and corners of the facets that form the cluster surfaces. The properties of such clusters are influenced by all of their atoms and especially by the ratio between surface and core atoms. Indeed, cluster scaling techniques are based upon the observation that the surface to volume ratio largely governs many physical properties $X(m)$ of sufficiently large metal clusters M_m.

For very large atom counts the number of surface and core atoms scale with $m^{2/3}$ and m, respectively. Thus, the surface to volume ratio can be expressed as $m^{-1/3}$. When neglecting the influence of facet edges and corners,[453] most properties are found to scale in a linear fashion in terms of this variable

$$X(m) = X(\infty) + k_X \cdot m^{-1/3}, \qquad 4.3.1$$

with $X(\infty)$ being the corresponding bulk limit for $m \to \infty$ and k_X the slope.[448,450-457] For a property obeying Eq. 4.3.1 and a given series of corresponding results for increasingly large clusters, the bulk limit $X(\infty)$ and the k_X can be identified from a least square fit in terms of $m^{-1/3}$.[448,450-457] Eq. 4.3.1 holds from a sufficiently large atom count m_{scal} onwards, which marks the boundary between the non-scaling regime of smaller clusters dominated by quantum effects and the scaling regime of larger particles.[459] The specific value of m_{scal} depends thereby on the property and the element *M* at hand.

Larger transition metals clusters are hard to isolate for measurements and thus, experimental results for them are rare. However, the bulk limit from cluster scaling extrapolation is easily compared to the corresponding result of the bulk material. Furthermore, the extrapolation as in Eq. 4.3.1 can be considered as a physically motivated average over a series of systems. Apart from the bulk limit itself, the coefficient of determination R^2 represents a measure for the scalability of the results, while the slope k_X describes the scaling behavior. Thus, the data obtained from cluster scaling extrapolations provide more information than results from plane-wave calculations of the bulk material.

The comparably high computational costs of hybrid DFT methods impose a tradeoff between an efficient calculation of the model clusters and a good quality of the extrapolation, which is of course higher when mostly results for particles of sizes beyond m_{scal} are included. To nevertheless achieve the best possible scaling behavior, the actual cluster models were constructed as close as possible to the corresponding bulk materials. Thus, the cluster geometries were chosen as cut-outs of the corresponding fcc bulk structures. As similarity to the bulk is most important, this choice is valid even when isomers of lower energies exist.[453,460,461] To enforce an electronic structure close to that in the corresponding bulk materials, O_{h} symmetry constraints were imposed on all cluster models. Furthermore, strictly octahedral systems as well as other structures with low coordinated corner atoms were excluded to avoid electronic situations with no relevance to the bulk.

These principles lead to truncated octahedral structures which are bounded by (111) and (100) type facets but do not exhibit four- and threefold coordinated corner- or add-atoms. The cuboctahedral cluster models considered comprise up to three layers of atoms and have the nuclearities $m = 13$, 38, 55, 79, and 116. The center of the clusters M_{13}, M_{55}, and M_{79} consists thereby of a single atom, while the systems M_{38} and M_{116} exhibit an octahedral M_6 center. The cluster models employed in the present study are depicted in Figure 4.3.1.

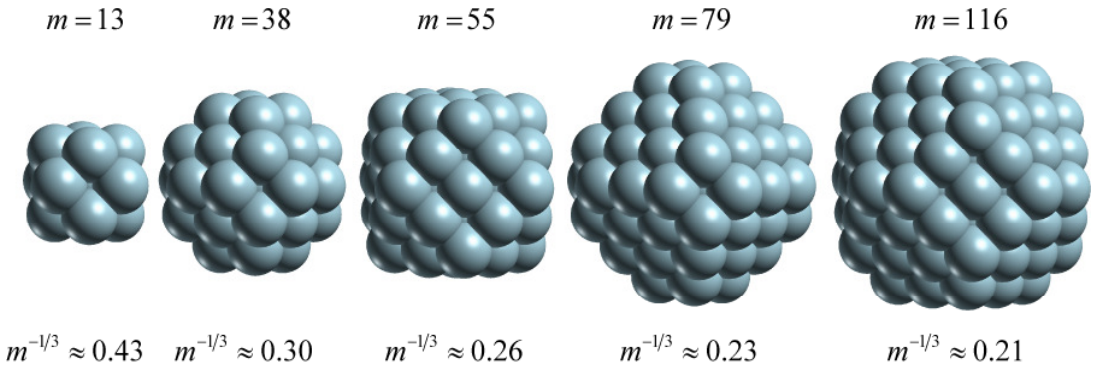

Figure 4.3.1: Series of M_m cluster models employed in the present study.

Analogously to the geometric aspects that determine the cluster models used in the extrapolation series, their electronic structure may also be unified towards that of the corresponding bulk materials. For this reason, also the effect of constraining the magnetic moments per atom μ_a of the model clusters to the corresponding value of the bulk materials, hence zero for Pd and Pt as well as 0.616 Bohr magnetons in the case of Ni, was examined. However, as the employed cluster models still tend to a notable molecular behavior (Section 4.3.3) these values are mostly discussed in comparison with the results from the spin-unrestricted treatment to examine the influence of the spin states on the cluster properties. Note, that this comparison provides only a rough indication for this influence and hybrid DFT calculations on the M_{116} clusters are quite expensive, so that the spin-restricted calculations were limited to cluster models up to M_{79}.

In the case of the cluster models Pd_m and Pt_m the high computational costs of hybrid DFT calculations also dictate the use of basis sets with effective core potentials (ECP). Although also the Stuttgart-Dresden ECP description[413] employed here affects the cluster scaling extrapolations to some extend,[456] it still allows for a meaningful comparison of the performance of the assessed functionals.

4.3.3. Structural, Energetic, and Ionization Properties

Out of the results calculated for the Ni_m, Pd_m, and Pt_m clusters, the average nearest-neighbor distances d_{av} and the corresponding extrapolations $d_{av}(\infty)$ to the bulk limit shall be discussed first. These results provide some initial hints about the quality of the structure and thus, about the quality of the electronic structure description itself. Within small to medium sized clusters the lower coordinated atoms at the cluster surface comprise a large fraction of the total atom count. Due to reduced bond competition, the interaction between these atoms and its remaining neighbors is increased, which is reflected in shorter average bond lengths for these systems.[448,451,452,454] With increasing cluster size the fraction of surface atoms is reduced so that the average coordination number grows. In consequence, increased distances d_{av} and negative fitting slopes are to be expected in this case.[448,451,452,454]

The d_{av} values as obtained from the spin-unrestricted calculations (u) of the cluster models M_m with m = 13, 38, 55, 79, and 116 are provided in Table 4.3.1 along with the results from the spin-restricted treatment (r) of the series m = 13, 38, 55, and 79. Both of these data series indeed show the increasing d_{av} values with growing cluster size. Some exceptions exist though, like the results from the unrestricted PBE calculation of Ni_{38} and Ni_{55} or from the unrestricted TPSSh treatment of Pd_{38} and Pd_{55}. However, these outliers are rare and most likely related to either the remaining molecular character of the M_{38} clusters or to the different cluster centers in M_{38} and M_{55} (single atom vs. octahedron).

Table 4.3.1: Average nearest-neighbor distances d_{av} of the model clusters M_m (M = Ni, Pd, Pt) for the series m = 13, 38, 55, 79, and 116 from the spin-unrestricted treatment (u) of the six examined functionals along with the corresponding results from the spin-restricted treatment (r) of the series with nuclearities up to $m = 79$. All values in pm.

		PBE		PBE0		TPSS		TPSSh		M06L		M06	
	m	u	r	u	r	u	r	u	r	u	r	u	r
Ni	13	246.9	246.9	248.5	248.5	245.9	245.9	246.7	246.7	247.9	247.9	248.8	248.8
	38	249.2	247.4	251.9	251.3	247.9	247.8	248.7	249.3	249.9	249.9	252.7	252.9
	55	249.0	249.0	253.1	252.3	247.7	247.7	248.5	248.5	250.0	250.0	253.1	253.1
	79	249.7	249.7	253.4	252.5	248.4	248.4	249.3	249.3	250.5	250.5	253.2	253.4
	116	249.9	—	253.2	—	248.5	—	249.4	—	250.5	—	253.9	—
Pd	13	269.6	270.2	268.2	270.3	267.4	268.1	267.1	268.7	270.6	271.6	274.1	276.5
	38	272.6	272.5	271.5	272.0	270.2	270.0	270.3	269.5	273.6	272.9	279.9	279.6
	55	273.1	273.0	272.8	272.3	270.6	270.4	270.3	270.5	273.5	273.3	279.5	279.6
	79	274.5	274.2	273.8	272.9	271.9	271.6	271.6	271.1	274.7	274.4	280.6	280.8
	116	274.8	—	274.8	—	272.2	—	272.4	—	275.1	—	281.1	—
Pt	13	269.3	269.0	267.2	266.6	268.0	267.5	267.4	266.7	271.1	270.8	274.9	278.0
	38	274.3	274.2	272.0	271.8	272.7	272.7	272.0	271.9	275.6	275.4	280.0	279.9
	55	274.9	274.8	273.2	272.2	273.2	273.1	272.4	272.2	276.2	275.8	281.1	280.8
	79	276.2	276.1	274.1	273.9	274.6	274.5	274.0	273.8	277.6	276.9	282.3	282.7
	116	276.6	—	274.3	—	275.0	—	274.1	—	277.8	—	283.0	—

Figure 4.3.2 depicts the plots of the d_{av} results for the individual model clusters along with the corresponding linear fit functions. Table 4.3.2 provides the d_{av} results from the corresponding extrapolations, $d_{av}(\infty)$ and $d_{av}^{r}(\infty)$, of spin-unrestricted and spin-restricted results, respectively, along with the coefficients of determination R^2 and the slopes from the unrestricted data series. As can be seen from the comparison between of $d_{av}(\infty)$ and $d_{av}^{r}(\infty)$ values, the d_{av} bulk limits of both series are mostly close to each other. Compared to $d_{av}(\infty)$, the $d_{av}^{r}(\infty)$ limits usually differ by about 1 to 2 pm. The extrapolations that lead to the largest differences (~3–5 pm) are uniformly lower for the spin-restricted results. These larger deviations only result for hybrid functionals and are related to the different scaling behavior as the d_{av} values obtained for the different cluster models do not differ that much. This different scaling behavior likely originates from the molecular character of the smaller cluster models, which is further amplified by the EXX term due to the increased HOMO-LUMO gap (HLG, see Section 4.3.4). Therefore, and because the unrestricted treatment provides a better description of the ionized clusters (see below), the discussion of structural results mainly focusses on the data from the latter.

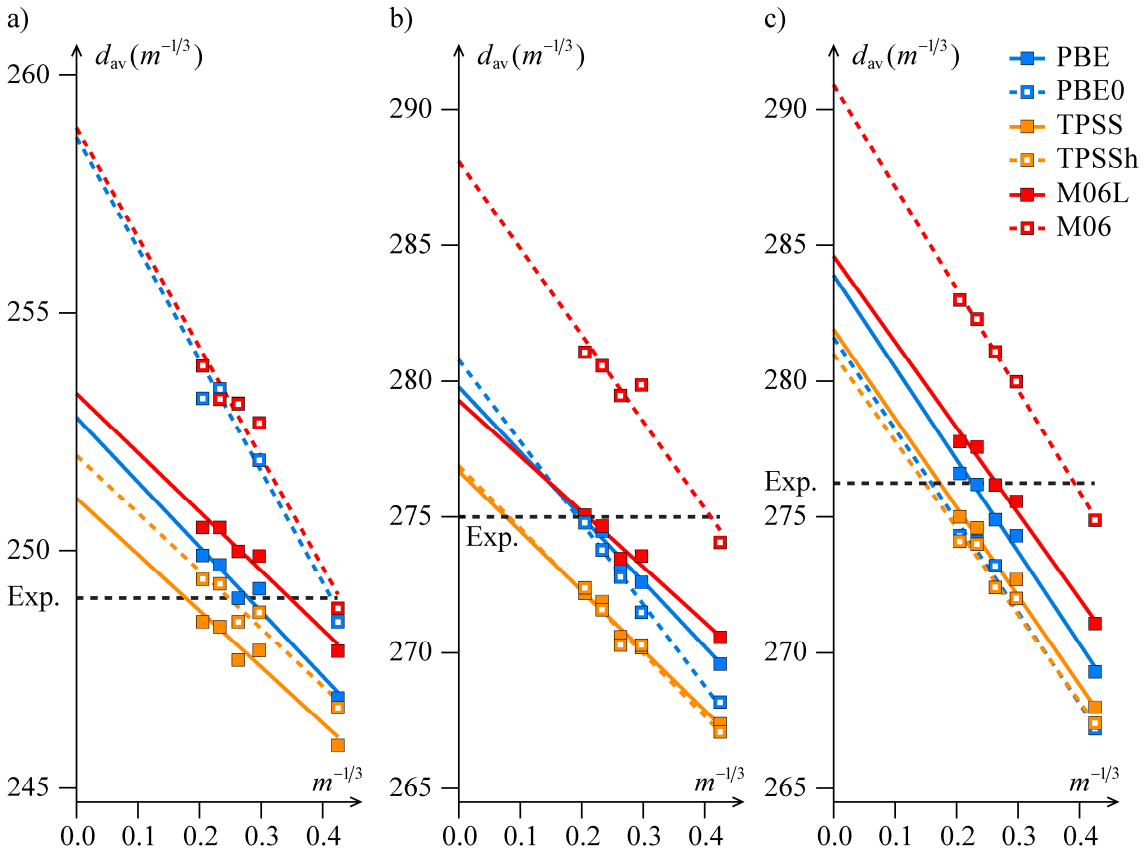

Figure 4.3.2: Average nearest-neighbor distances d_{av} in pm for the a) Ni_m, b) Pd_m, and c) Pt_m cluster models obtained from the six examined functionals (spin-unrestricted treatment) along with the corresponding trend lines linear in $m^{-1/3}$. Figure adapted from Ref. [443].

The coefficients of determination R^2 are found typically to amount to ~0.95 for Ni, around 0.98 for Pd and generally larger than that in the case of Pt. Only the value of $R^2 = 0.993$ resulting from the extrapolations of the Pd data obtained with PBE0 represents an exception to these trends. In any case these values are quite large so that the extrapolation of the d_{av} values to the bulk limit is well justified and physically meaningful.

The $d_{av}(\infty)$ values obtained with the examined functionals generally result in the order $d_{av}(\text{TPSS}) \approx d_{av}(\text{TPSSh}) < d_{av}(\text{PBE}) \approx d_{av}(\text{M06L}) < d_{av}(\text{PBE0}) \approx d_{av}(\text{M06})$. Only in the case of the Pt results for PBE0, a comparatively low bulk limit is obtained due to minor outliers in the corresponding data series.

Table 4.3.2: Extrapolated bulk limits $d_{av}(\infty)$ of the average nearest-neighbor distances d_{av} of the model clusters M_m (M = Ni, Pd, Pt) along with the corresponding R^2 values and fitting slopes k_d for the series m = 13, 38, 55, 79, and 116 as obtained from the spin-unrestricted treatment (u) of the six examined functionals. For comparison the bulk limits $d_{av}^{r}(\infty)$ resulting from the spin-restricted treatment (r) of the series with nuclearities up to $m = 79$ is shown as well as experimental reference values. R^2 dimensionless, all other values in pm.

		PBE	PBE0	TPSS	TPSSh	M06L	M06	Exp.
Ni	R^2	0.946	0.946	0.944	0.950	0.959	0.948	—
	k_d	–13.8	–23.4	–11.8	–12.1	–12.4	–23.1	—
	$d_{av}(\infty)$	252.8	258.7	251.1	252.0	253.3	258.9	249[a]
	$d_{av}^{r}(\infty)$	252.4	257.7	251.2	252.4	253.7	259.7	—
Pd	R^2	0.984	0.993	0.984	0.971	0.969	0.935	—
	k_d	–23.9	–30.0	–22.0	–23.0	–20.4	–31.9	—
	$d_{av}(\infty)$	279.8	280.8	276.7	276.9	279.3	288.1	275[b]
	$d_{av}^{r}(\infty)$	278.4	275.9	275.2	273.5	277.1	285.7	—
Pt	R^2	0.987	0.984	0.988	0.984	0.989	0.996	—
	k_d	–33.9	–33.4	–32.5	–31.8	–31.4	–37.4	—
	$d_{av}(\infty)$	283.9	281.6	281.9	281.0	284.6	290.9	277[c]
	$d_{av}^{r}(\infty)$	284.7	282.3	282.8	282.1	284.4	286.9	—

[a] Ref. [462]

[b] Ref. [463]

[c] Ref. [464]

When comparing semi-local DFT approximations and hybrid functionals, one finds that PBE0 and M06, hence the methods with a comparatively high contribution of exact-exchange, mostly overestimate the metal-metal bond lengths. The $d_{av}(\infty)$ limits of the M06 functional are by about 5–6 pm larger than those resulting from M06L. In the case of the PBE/PBE0 pair the bulk limits differ by 5.9 and 1.0 pm for Ni and Pd, respectively. Only the aforementioned low $d_{av}(\infty)$ value of Pt from PBE0 is an exception to this as it lies below the bulk estimate of PBE. A significant impact of the EXX term on the structural results is nevertheless apparent in this latter case as well. This influence is rationalized by the fact that the admixture of exact-exchange leads to a different preference for the electronic ground state (see Section 4.3.4). These altered ground states in turn can lead to different cluster structures. The slopes k_d as obtained from PBE0 and M06 for Ni and Pd are notably more negative than those resulting from the other methods. While PBE0 yields even more compact Pd_m structures than the semi-local DFT approximations PBE and M06L, the steeper slope k_d of the corresponding linear trend function leads to a larger $d_{av}(\infty)$ value for PBE0 than for the other two functionals. The situation is different for the pair TPSS/TPSSh where the EXX

mixing factor amounts to only 0.10. In this case the d_{av} bulk limits are quite similar with differences of less than 1 pm and very alike k_d values.

All six examined functionals overestimate the experimental metal-metal distances of the transition metal bulk materials. In the case of Ni, the TPSS result of 251.1 pm is closest to the reference value of 249 pm.[462] The second-most accurate estimate of 252.0 pm is only slightly larger than that and is obtained with TPSSh. The corresponding d_{av} bulk limits of Pd are even closer with 276.7 and 276.9 pm for TPSS and TPSSh, respectively. These two functionals yield also the most accurate extrapolations for Pd, where the experimental value is 275 pm.[463] For Pt, the TPSSh functional yields a bulk limit of 281.0 pm, which is even closer to the experimental reference[464] of 277 pm than its semi-local counterpart. Interestingly, also the d_{av} bulk limit of 281.6 pm resulting from the PBE0 structures is slightly closer to this experimental result than the extrapolation of the TPSS data, 281.9 pm. In the case of Pt the bulk limits of PBE and M06L, 283.9 and 284.6 pm, exhibit somewhat larger deviations than TPSSh, PBE0, and TPSS. A d_{av} limit of 290.9 pm is obtained from the M06 results which overestimates the experimental reference by far. With differences of about 0.5 pm the extrapolations from PBE and M06L are close to each other for the other metals as well. In contrast to its accurate estimate for Pt, the PBE0 functional deviates significantly more from the experiment in the case of the other two metals, by 5.8 pm and about 10 pm for Pd and Ni, respectively. With regard to these extrapolations, PBE0 behaves close to the M06 hybrid MGGA, which always overestimates the d_{av} values most.

When comparing the PBE estimate for Pd with the corresponding extrapolation of a recent all-electron cluster scaling study one finds that the results differ by only 0.1 pm.[448] From these extremely well agreeing bulk limits one can conclude that the usage of the Stuttgart-Dresden ECPs does not impose any reduction of the accuracy on structural results. Furthermore, the d_{av} extrapolations can be compared with the metal-metal distances in the bulk materials resulting from plane-wave calculations.[198,446] Despite the reasonable overall agreement between the bulk limits in Table 4.3.2 and the values obtained in this plane-wave study, the good performance of PBE0 for structural results is not confirmed by the present results.

Next, the cohesive energies, E_{coh}, of the cluster models are discussed along with the corresponding bulk limits $E_{coh}(\infty)$. In the present context, the cohesive energy is to be understood as the atomization energy of the clusters per atom,

$$E_{coh}(m) = \frac{m \cdot E_{tot}(M) - E_{tot}(M_m)}{m} = E_{tot}(M) - \frac{E_{tot}(M_m)}{m} \quad . \qquad 4.3.2$$

Thus, the calculation of E_{coh} requires also the total energies of the atomic systems. Similar to the study presented in Section 4.2, the atomic systems were treated under C_{2v} constraints. These calculations again lead to $3d^9 4s^1$ configurations in the case of nickel as spin-orbit effects were not accounted for in the present calculations.[441] For Pd and Pt $4d^{10}$ and $5d^9 6s^1$

configurations are obtained, respectively, which match the respective experimental ground states. Note, that the results from these configurations were also used for the calculation of the E_{coh} values of the spin-restricted data.

Table 4.3.3 provides the cohesive energies emerging from the spin-unrestricted (u) and restricted (r) computations of the M_m cluster models. As the fraction of lower coordinated surface atoms decreases with increasing *m*, more bonds per atom are formed on average in larger clusters. Thus, the E_{coh} values can be expected to grow with the cluster nuclearity *m*. Inspection of Table 4.3.3 shows that this is indeed the case. Furthermore, the total energies resulting from the spin-unrestricted treatment can not be higher than those from the unrestricted calculations. In consequence, the E_{coh} values are always lower for the restricted data series as shown by the results in Table 4.3.3.

Table 4.3.3: Cohesive energies E_{coh} of the model clusters M_m (*M* = Ni, Pd, Pt) for the series m = 13, 38, 55, 79, and 116 from the spin-unrestricted treatment (u) of the six examined functionals along with the corresponding results from the spin-restricted treatment (r) of the series with nuclearities up to $m = 79$. All values in kJ/mol.

		PBE		PBE0		TPSS		TPSSh		M06L		M06	
	m	u	r	u	r	u	r	u	R	u	r	u	r
Ni	13	270.8	270.8	172.9	172.9	265.6	264.9	218.4	215.2	252.2	246.5	179.7	197.3
	38	328.0	327.3	216.3	206.9	329.0	327.8	274.2	270.7	319.3	316.2	239.5	234.5
	55	335.5	335.1	222.7	222.7	337.6	336.8	284.0	281.8	331.4	327.8	246.7	249.3
	79	352.1	351.4	233.4	224.5	355.8	354.8	300.3	294.5	348.2	347.8	257.6	252.1
	116	359.1	—	239.2	—	364.5	—	307.4	—	360.4	—	263.5	—
Pd	13	232.5	228.5	153.1	162.0	242.1	236.7	213.0	207.5	235.9	233.6	157.6	163.0
	38	285.7	285.0	209.6	206.6	301.0	300.1	267.7	265.1	300.9	299.1	206.1	203.2
	55	294.6	294.3	223.6	218.4	311.2	310.7	278.1	276.0	312.6	311.9	217.0	214.2
	79	307.5	306.1	235.8	226.3	325.9	324.2	292.6	288.0	329.4	326.9	229.2	224.1
	116	316.0	—	242.4	—	336.0	—	301.7	—	341.2	—	235.7	—
Pt	13	336.3	334.6	266.0	260.5	337.5	333.8	312.3	302.7	330.6	324.7	285.2	279.8
	38	408.6	406.1	342.9	340.9	417.1	416.1	388.6	386.6	410.1	408.2	352.0	350.6
	55	416.4	415.7	355.7	349.7	429.3	427.8	400.9	397.3	424.2	421.7	364.1	421.7
	79	437.9	437.7	372.3	369.1	449.5	448.4	421.0	418.2	445.4	442.7	377.3	376.8
	116	448.1	—	380.4	—	461.3	—	431.8	—	458.5	—	387.1	—

Figure 4.3.3 depicts the plots of the cohesive energies E_{coh} for the individual model clusters and the corresponding linear trend lines from Eq. 4.3.1 from the spin-unrestricted calculations. Table 4.3.4 provides the E_{coh} bulk limits of the spin-unrestricted and spin-restricted treatments, $E_{coh}(\infty)$ and $E^{r}_{coh}(\infty)$, respectively. Also the coefficients of determination R^2 and the slopes k_E of the spin-unrestricted results are listed. When comparing bulk limits of the restricted and unrestricted data series, one notices the results to

be quite consistent. In most cases the differences are found below ~10 kJ/mol. The largest deviations of about 30 kJ/mol result from the functionals PBE0 and M06 and may again be rationalized with the preference of the EXX term for high-spin states.[198] This preference most likely renders the results of the high-EXX functionals more sensitive to the spin state compared to those from the semi-local DFT methods or TPSSh.

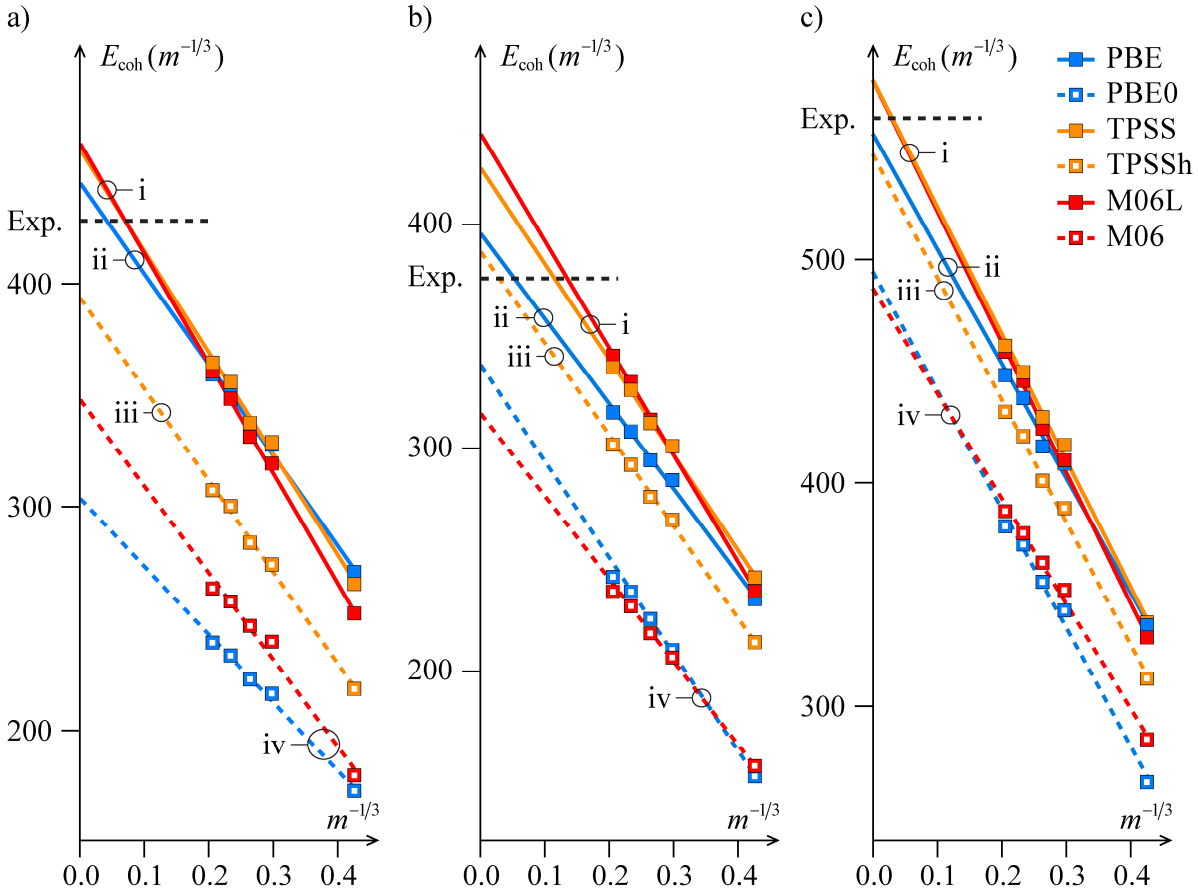

Figure 4.3.3: Cohesive energies E_{coh} in kJ/mol for the a) Ni_m, b) Pd_m, and c) Pt_m cluster models obtained from the six examined functionals (spin-unrestricted treatment) along with the corresponding trend lines linear in $m^{-1/3}$. The individual groups of functionals (see text) are marked accordingly. Figure adapted from Ref. [443].

Compared to the d_{av} values, the cohesive energies vary much more when going from the smallest to the largest cluster models. In consequence, the coefficients of determination R^2 of the E_{coh} trend lines are higher than those of the d_{av} series. Indeed, the R^2 values of the cohesive energies are always found above 0.99, with the M06 results for the Ni_m cluster model series as the only exception ($R^2 \approx 0.98$). In any case, the cohesive energy can be considered as a quantity which is accurately described by the proposed scaling law, Eq. 4.3.1.

Table 4.3.4: Extrapolated bulk limits $E_{coh}(\infty)$ of the cohesive energies E_{coh} of the model clusters M_m (M = Ni, Pd, Pt) along with the corresponding R^2 values and fitting slopes k_E for the series m = 13, 38, 55, 79, and 116 as obtained from the spin-unrestricted treatment (u) of the six examined functionals. For comparison the bulk limits $E^{r}_{coh}(\infty)$ resulting from the spin-restricted treatment (r) of the series with nuclearities up to $m = 79$ is shown as well as experimental reference values. R^2 dimensionless, all other values in kJ/mol.

		PBE	PBE0	TPSS	TPSSh	M06L	M06	Exp.[a]
Ni	R^2	0.993	0.994	0.994	0.996	0.998	0.981	—
	k_E	–405.5	–304.3	–452.6	–409.6	–491.4	–387.8	—
	$E_{coh}(\infty)$	444.6	303.6	459.4	393.5	462.2	347.8	428[b]
	$E^{r}_{coh}(\infty)$	447.0	292.3	461.3	391.4	467.8	323.7	—
Pd	R^2	0.996	1.000	0.997	0.998	0.998	0.999	—
	k_E	–381.3	–431.7	–427.5	–410.2	–478.7	–370.7	—
	$E_{coh}(\infty)$	395.9	337.1	425.0	387.8	440.3	315.4	376[c]
	$E^{r}_{coh}(\infty)$	402.1	306.8	432.3	387.5	440.9	297.6	—
Pt	R^2	0.995	0.991	0.995	0.996	0.997	0.995	—
	k_E	–512.1	–530.3	–566.0	–547.5	–583.6	–470.0	—
	$E_{coh}(\infty)$	555.9	494.5	580.1	546.8	579.9	487.1	563[c]
	$E^{r}_{coh}(\infty)$	565.4	501.5	587.2	558.4	585.2	503.6	—

[a] Zero point energy and temperature corrections (Refs. [446,465]) omitted.

[b] Ref. [466]

[c] Refs. [467,468]

Before addressing the performance of the assessed functionals for the prediction of the $E_{coh}(\infty)$ values, the present extrapolations are compared with the cohesive energies of the bulk materials as obtained in other computational studies. First, the PBE result of $E_{coh}(\infty) = 395.9$ kJ/mol is compared with the corresponding bulk limit of 375.6 kJ/mol obtained in an earlier cluster scaling study.[448] The deviation of about 20 kJ/mol results almost completely from the use of effective core potentials, as shown in another recent study, which assessed the impact of various approximate representations of the atomic core electrons on cluster scaling results.[456] Compared to the result that was obtained at the PBE/def2-TZVP level in this latter study, the corresponding $E_{coh}(\infty)$ bulk limit in Table 4.3.4 agrees within a few kJ/mol, despite of the different series of cluster models employed.[456] As the def2-TZVP basis provides an all-electron description of Ni, a similar agreement is also found between the present PBE result and that of an earlier scaling study of Ni clusters.[469] Compared to recently published plane-wave results for PBE, PBE0, TPSS, and M06L, the $E_{coh}(\infty)$ values of the present cluster scaling extrapolations are found to be somewhat lower in the case of Ni, but always larger in the case of the two other metals.[446] These differences between plane-wave and cluster scaling results are consistent with results reported earlier.[456]

The deviations between cluster scaling and plane-wave results are most likely related to methodological differences like the representation of the atomic core orbitals or the treatment of atomic systems.

When comparing the semi-local DFT approximations with their corresponding hybrid DFT counterparts one finds that the inclusion of the EXX term considerably reduces the cohesive energies. This holds especially for the $E_{\mathrm{coh}}(m)$ values of the individual cluster models. When comparing PBE0 with PBE, the slopes k_E of the former are found to be more negative in the case of Pd and Pt. Even in these cases the bulk limits of PBE are always higher than those of the hybrid functional. In the case of the other two pairs of functionals the trend lines of the semi-local DFT approximations are always steeper. For the pairs PBE/PBE0 and TPSS/TPSSh the reduction of the $E_{\mathrm{coh}}(\infty)$ bulk limit caused by the EXX term is largest for Ni as the semi-local functionals always yield much steeper trend lines. This is most likely related to the non-vanishing magnetic moment per atom μ_a found for the corresponding bulk material. In the case of the nonmagnetic bulk materials Pd and Pt the effect of the exact-exchange term on the $E_{\mathrm{coh}}(\infty)$ values is more comparable. In any case, the reduction of the $E_{\mathrm{coh}}(\infty)$ bulk limits seems to correlate roughly with the value of the EXX mixing factor as the changes are found to be more than twice as large in the case of the PBE/PBE0 pair (α_{l} = 0.25) than when going from TPSS to TPSSh (α_{l} = 0.10). Thus, the EXX term seems affect the bond strengths much more than the bond lengths in these two pairs of functionals, apart from the PBE0 description of Ni, where also the quality of structural results breaks down. The fact that a hybrid functional can yield similar metal-metal distances but much lower cohesive energies compared to its semi-local counterpart has also been reported from plane-wave calculations.[198] The situation appears to be different when the semi-local terms of a hybrid functional are parametrized in the presence of exact-exchange as in M06. In this case the slopes k_E are reduced by a similar amount for all three metals compared to those of M06L. In consequence also the reduction of the $E_{\mathrm{coh}}(\infty)$ values is always comparable when going from the M06L to M06. For this pair of functionals the bond elongations due to the EXX term are found to correlate with the resulting reductions of the bond strengths. While still being comparable for all three metals, the changes of both bulk limits, $d_{\mathrm{av}}(\infty)$ and $E_{\mathrm{coh}}(\infty)$, appear to be slightly more pronounced for Pd.

To assess the performance of the six employed DFT approximations, the results of Figure 4.3.3 and Table 4.3.4 are compared to the experimental references for the cohesive energy values. These reference values would have to be corrected for finite temperature and zero point energy effects.[446,465] However, in the present case these corrections were omitted as they are below 4 kJ/mol and thus not relevant in the present context.

The $E_{\mathrm{coh}}(\infty)$ values from Table 4.3.4 allow for a classification of the assessed functionals into four groups (see Figure 4.3.3). Group (i) includes thereby the semi-local MGGA functionals TPSS and M06L, which always yield the highest cohesive energy extrapolations

for all three metals. In the case of Pt, the $E_{coh}(\infty)$ bulk limits yield result to nearly identical values, 580.1 kJ/mol for TPSS and 579.9 kJ/mol for M06L. Thus, these two functionals overestimate the experimental reference[467,468] of 563 kJ/mol by about 17 kJ/mol. The overestimations of these functionals are somewhat more pronounced in the case of the other two metals. The $E_{coh}(\infty)$ bulk limits of nickel amount to 459.4 kJ/mol (TPSS) and 462.2 kJ/mol (M06L) and exceed the experimental reference[466] of 428 kJ/mol by about 30 kJ/mol. In the case of Pd the results of both functionals differ somewhat more from each other, 425.0 and 440.3 kJ/mol for TPSS and M06L, respectively, as well as from the experimental result[467,468] of 376 kJ/mol. Thus, with deviations of 17, 30, and 49 kJ/mol for the E_{coh} bulk limit of Pt, Ni, and Pd, respectively, the exceptional performance of TPSS previously reported[264,470] for smaller transition metal compounds cannot be confirmed by the present results for larger cluster models. In contrast, the rather larger deviation of M06L is more in line with specific deficiencies of this method that were previously noted in a study of smaller Pd clusters.[447]

The pure GGA functional PBE yields the next highest E_{coh} extrapolations for the three examined transition metals and is assigned to group (ii). Its $E_{coh}(\infty)$ bulk limits of 444.6 and 395.9 kJ/mol obtained in the case of Ni and Pd, respectively, overestimate the experimental results, while the E_{coh} extrapolation for Pt (555.9 kJ/mol) underestimates the corresponding experimental reference slightly. With deviations of about 17 and 7 kJ/mol PBE yields the best estimates for the cohesive energy of bulk Ni and Pt, respectively.

Also group (iii) includes a single functional only, namely TPSSh with its low EXX mixing factor. TPSSh yields $E_{coh}(\infty)$ extrapolations of 393.5, 387.8, and 546.8 kJ/mol for Ni, Pd, and Pt, respectively. With a deviation of 12 kJ/mol, the TPSSh estimate for Pd exhibits the best agreement with the experimental reference of all examined functionals. Also the accuracy of the other two estimates remains still comparable to that of the PBE results.

Finally, the high exact-exchange functionals PBE0 and M06 comprise group (iv) and always yield the lowest $E_{coh}(\infty)$ extrapolations. In most cases, however, this implies also the worst accuracy as the cohesive energies of the bulk materials are often strongly underestimated. In the case of Pt quite similar bulk limits are obtained with both functionals which differ by about 70 kJ/mol from the experimental reference. Compared to that, the $E_{coh}(\infty)$ values of 337.1 and 315.4 kJ/mol obtained for Pd with PBE0 and M06, respectively, deviate somewhat less from the experimental result and are thus more accurate than the corresponding M06L result. Most underestimated are the cohesive energies of bulk nickel. The corresponding error of M06 (~80 kJ/mol) is smaller than that of PBE0, ~125 kJ/mol. Thus, for the description of the bond strengths of metallic systems, the functionals with a high fraction of exact-exchange exhibit show a somewhat erratic behavior. This holds especially for the magnetic material Ni. The errors of PBE0 and M06 are likely related to the static correlation error (see Section 2.2.6), which is most pronounced in these methods.[130,217]

Table 4.3.5: Vertical ionization potentials Φ_{IP} and electron affinities Φ_{EA} of the model clusters M_m (M = Ni, Pd, Pt) for the series m = 13, 38, 55, 79, and 116 from the spin-unrestricted treatment of the six examined functionals. All values in eV.

		PBE		PBE0		TPSS		TPSSh		M06L		M06	
	m	IP	EA	IP	EA	IP	EA	IP	EA	IP	EA	IP	EA
Ni	13	5.76	2.02	5.20	0.90	5.52	1.69	5.18	1.72	5.12	2.47	5.37	2.83
	38	5.59	2.93	5.59	2.54	5.54	2.80	5.40	2.35	5.24	2.65	5.47	2.29
	55	5.48	3.08	4.75	2.70	5.21	2.83	4.97	2.64	5.05	2.73	5.65	2.95
	79	5.37	3.22	4.80	2.42	5.23	3.05	4.82	2.89	3.58	2.92	4.93	3.41
	116	5.45	3.52	4.42	2.81	5.27	3.33	4.69	2.88	4.96	3.06	5.10	3.46
Pd	13	6.39	2.89	6.48	3.43	6.24	2.69	6.23	2.39	6.26	2.58	7.10	2.97
	38	6.22	3.59	6.53	3.35	6.11	3.42	6.11	3.29	5.88	3.31	6.48	3.51
	55	5.85	3.57	5.76	3.17	5.69	3.40	5.61	3.29	5.58	3.37	6.29	3.66
	79	5.76	3.72	5.76	3.21	5.63	3.58	5.58	3.42	5.57	3.51	6.38	4.10
	116	5.78	3.97	5.81	3.91	5.65	3.83	5.53	3.78	5.53	3.74	6.43	4.11
Pt	13	7.04	3.47	5.38	3.12	6.91	3.37	6.94	3.24	6.81	3.26	7.37	3.44
	38	6.69	4.15	6.79	4.24	6.62	4.06	6.78	3.98	6.34	3.75	7.21	4.57
	55	6.42	4.13	6.31	3.75	6.34	4.02	6.53	3.90	6.07	3.97	6.90	4.24
	79	6.46	4.42	6.34	4.32	6.37	4.32	6.23	4.27	6.06	4.04	6.82	4.88
	116	6.30	4.49	6.33	4.31	6.21	4.39	6.27	4.54	6.00	4.20	6.74	4.92

Next, the vertical ionization potentials Φ_{IP} and electron affinities Φ_{EA} of the M_m cluster models shall be discussed as examples for electronic properties. These values are provided in Table 4.3.5 and were computed with the ΔSCF approximation[35]

$$\Phi_{IP}(m) = E_{tot}(M_m^+) - E_{tot}(m), \qquad 4.3.3a$$

$$\Phi_{EA}(m) = E_{tot}(m) - E_{tot}(M_m^-). \qquad 4.3.3b$$

Thus, the Φ_{IP} and Φ_{EA} values result from the energies of cationic and anionic model cluster species M_m^+ and M_m^-, respectively, which are taken to have the same structures as the corresponding neutral clusters. In contrast to the average nearest-neighbor distances and cohesive energies, the Φ_{IP} and Φ_{EA} values were obtained by means of a spin-unrestricted treatment only. In the case of larger particles, both electronic quantities are well described by a classical droplet model which previously has been discussed in great detail.[449,450,471] According to this model the excessive negative charge distribution within the anionic species minimizes its Coulomb repulsion by assuming an increasingly extended form with growing cluster size. In consequence the attractive terms of the Hamiltonian become more important so that Φ_{EA} grows with increasing cluster size.[449,471] Similarly, Φ_{IP}, the energy required to create a positive charge distribution upon removal of a single electron is reduced when going from smaller to larger clusters.[449,471] Inspection of Table 4.3.5 reveals that both quantities,

[35] Not to be confused with the ΔSCF method described in Section 3.1.3.

Φ_{IP} and Φ_{EA}, generally follow this behavior. However, various outliers can be identified which have a significant impact on the scaling behavior and thus are subsequently discussed in more detail. One further expects[13] $\Phi_{IP}(m) > \Phi_{EA}(m)$ which is fulfilled in all cases.

Table 4.3.6: Extrapolated bulk limits $\Phi_{IP}(\infty)$ and $\Phi_{EA}(\infty)$ of the vertical ionization potentials, electron affinities, and their differences $\Delta\Phi = \Phi_{IP} - \Phi_{EA}$ of the clusters M_m (M = Ni, Pd, Pt) along with the corresponding R^2 values and slopes, k_{IP} and k_{EA}, for the series m = 38, 55, 79, and 116 as obtained from the spin-unrestricted calculations with the six examined functionals as well as the experimental values of the work function. R^2 dimensionless, all other values in eV.

		PBE	PBE0	TPSS	TPSSh	M06L	M06	Exp.
Ni	R^2	0.996	0.838	0.489	0.934	0.172	0.510	—
	k_{IP}	3.23	11.49	2.71	7.46	7.98	5.96	—
	$\Phi_{IP}(\infty)$	4.63	2.02	4.46	3.10	2.72	3.80	5.04–5.35[a]
	R^2	0.944	0.141	0.876	0.899	0.961	0.919	—
	k_{EA}	–6.14	–1.66	–5.81	–6.03	–4.60	–13.16	—
	$\Phi_{EA}(\infty)$	4.72	3.03	4.45	4.20	3.99	6.31	5.04–5.35[a]
	$\Delta\Phi(\infty)$	–0.90	–1.01	0.18	–1.09	–1.28	–2.51	0.00[b]
Pd	R^2	0.756	0.589	0.722	0.759	0.752	0.017	—
	k_{IP}	4.72	7.26	4.84	5.90	3.55	0.26	—
	$\Phi_{IP}(\infty)$	4.72	4.15	4.56	4.23	4.75	6.32	5.22–5.60[a]
	R^2	0.788	0.378	0.804	0.771	0.910	0.900	—
	k_{EA}	–4.12	–5.30	–4.46	–5.11	–4.52	–7.29	—
	$\Phi_{EA}(\infty)$	4.74	4.73	4.67	4.72	4.61	5.67	5.22–5.60[a]
	$\Delta\Phi(\infty)$	–0.02	–0.58	–0.11	–0.49	0.14	0.66	0.00[b]
Pt	R^2	0.820	0.619	0.849	0.868	0.807	0.900	—
	k_{IP}	3.71	4.56	3.94	6.03	3.45	4.88	—
	$\Phi_{IP}(\infty)$	5.54	5.30	5.40	4.95	5.25	5.70	5.12–5.93[a]
	R^2	0.830	0.090	0.779	0.783	0.970	0.439	—
	k_{EA}	–4.64	–3.23	–4.13	–6.51	–4.70	–5.29	—
	$\Phi_{EA}(\infty)$	5.35	4.88	5.23	5.80	5.16	5.97	5.12–5.93[a]
	$\Delta\Phi(\infty)$	0.19	0.42	0.17	–0.58	0.09	–0.28	0.00[b]

[a] Refs. [472-474]

[b] Φ_{IP} and Φ_{EA} assume identical values of the work function in the bulk limit.

Like most electronic properties, the Φ_{IP} and Φ_{EA} values are mostly dominated by a few individual KS orbitals. Especially orbitals around the HLG can be expected to evolve quite slowly with increasing cluster size towards the corresponding levels of the bulk limit. In consequence, such properties usually exhibit a quite late onset m_{scal} of their linear scaling behavior.[475,476] Nevertheless, the extrapolation of the Φ_{IP} and Φ_{EA} results has been carried

out as well, with the corresponding bulk limits provided in Table 4.3.6. The results for the M_{13} species were not included in this extrapolation as these clusters were found to exhibit strongly molecular characteristics with regard to their electronic properties. Nevertheless, the coefficients of determination R^2 obtained from the extrapolation of the remaining Φ_{IP} and Φ_{EA} data are found to be significantly lower compared to those from the extrapolations of d_{av} and E_{coh} discussed above. In some cases, which mostly occur for the high EXX hybrid functionals PBE0 and M06, the coefficients of determination are so low, $R^2 \ll 0.75$, that the series of results obtained for the employed set of cluster models seem to scale hardly at all. Before addressing the origin of this occasional behavior the results of the smoothly extrapolating series shall be discussed first.

In the bulk limit an excessive charge distribution becomes infinitely extended and therefore its Coulomb repulsion vanishes.[449,471] Thus, for metallic materials with vanishing band gap both quantities, Φ_{IP} and Φ_{EA}, have the same bulk limit as the energy to create positive or negative charge distribution is dominated by the work function Φ in both cases.[449,471] However, this quantity is not only specific to the bulk material, but varies also with the type of the crystalline surface.[468] Therefore the ranges of experimental values[472-474] measured for different crystalline orientations are used as references.

In the case of Pt the bulk limits of the vertical ionization potentials that could be obtained with $R^2 > 0.75$ result from the functionals PBE, TPSS, TPSSh, M06L, and M06 and amount to 5.54, 5.40, 4.95, 5.25, and 5.70 eV, respectively. These values are all within the corresponding range of experimental reference values for Φ, 5.12–5.93 eV,[472-474] except for TPSSh, which slightly underestimates it. The Φ_{EA} values of PBE0 and M06 do not scale properly, while the $\Phi_{EA}(\infty)$ bulk limits of all other functionals are within the experimental range of Φ. For Pd, the functionals PBE, TPSSh, and M06L exhibit $R^2 > 0.75$ for both series, Φ_{IP} and Φ_{EA}, but always underestimate the work function by about 0.5–1.0 eV. Also the Φ_{EA} values resulting from M06 scale well, while their bulk limit is found slightly above the range of experimental Φ values. The Φ_{IP} results for Ni can be extrapolated reasonably well only in the case of PBE, PBE0, and TPSSh, whereas all functionals underestimate the work function by about 0.4, 3.0, and 1.9 eV, respectively. The corresponding Φ_{EA} values exhibit a reasonable scaling behavior for all functionals, except for PBE0. The deviations of the corresponding bulk limits from the experimental references are reduced to ~1 eV at most.

Table 4.3.6 also provides the bulk limits $\Delta\Phi(\infty)$ of the series of differences $\Delta\Phi(m) = \Phi_{IP}(m) - \Phi_{EA}(m)$. These extrapolations should yield a zero band gap and serve as indicator for the consistency of the results for Φ_{IP} and Φ_{EA}. The strongest deviations of $\Delta\Phi(\infty)$ from the expected value of zero are obtained in the case of Ni, where only the TPSS functionals yields a reasonably low estimate, $\Delta\Phi(\infty) = 0.18$ eV. All other examined functionals extrapolate the $\Delta\Phi$ series to negative values which range from about –0.9 eV in the case of PBE to the bulk limit of $\Delta\Phi(\infty) \approx -2.5\,\text{eV}$ obtained with M06. The $\Delta\Phi(\infty)$

extrapolations are closer to the theoretical limit of zero for the other two elements, whereas the semi-local DFT approximations always deviate by less than 0.2 eV. The hybrid functionals always yield larger deviations than that. Indeed, hybrid DFT methods are known to predict not necessarily a vanishing band gap for metallic systems. Therefore, one may expect $\Delta\Phi(\infty) > 0$ from hybrid functionals as opposed to some of the bulk limits for $\Delta\Phi$ listed in Table 4.3.6. These negative $\Delta\Phi(\infty)$ bulk limits are, however, mostly related to outliers in the Φ_{IP} and Φ_{EA} series and not to the electronic structure description itself.

Compared to earlier all-electron PBE results for Pd,[448] the extrapolations of the corresponding Φ_{IP} and Φ_{EA} values of the present study are lower by 0.33 and 0.15 eV, respectively. These differences most likely arise from a stronger amount of level broadening employed in the all-electron calculations as well as from a different choice of the model clusters used for the extrapolation (Pd_{147} instead of Pd_{116}). In any case, the bulk limit of $\Delta\Phi(\infty)$ obtained in the present extrapolation is significantly closer to zero.

As mentioned before, electronic properties like the vertical ionization potentials and electron affinities are often dominated by individual orbitals. The effect of the applied FON broadening technique is in some sense counteracting this aspect as it involves a potentially larger number of orbitals in the ionization process if the HOMO-LUMO gap is small. Thus, the FON broadening leads to an earlier onset of the aforementioned classical behavior of the ionic clusters according to the droplet model. However, smaller clusters still exhibit HLGs large enough to neglect these effects of the FON technique. In addition, the hybrid functionals generally tend to increase the HOMO-LUMO gap further. In these cases the Φ_{IP} and Φ_{EA} values remain mostly affected by the evolution of individual orbitals up to larger cluster sizes. This generally reduces the scalability of vertical ionization potentials and electron affinities. Furthermore, the striking outliers found in some of the series of Φ_{IP} and Φ_{EA} results seem to be related to cases where one of these orbitals involved in the ionization happens to be symmetry-degenerate (*e*- or *t*-type). In consequence, electron configurations result where individual electrons (or holes) are distributed among two or three symmetry-degenerate orbitals. This in turn leads to significant shifts in the Φ_{IP} and Φ_{EA} energies. The occurrence of symmetry-degenerate orbitals is a direct consequence of the O_h symmetry constraints that were imposed on the cluster models. Thus, the highly symmetric treatment represents a clear drawback for the calculation of electronic properties like Φ_{IP} and Φ_{EA}, at least when point group symmetries with degenerate irreducible representations are employed. Nevertheless, it has to be emphasized at this point again that high symmetries like O_h do not only reflect the electronic structure of the corresponding fcc bulk materials but are also essential for obtaining suitably converged KS orbitals of larger transition metal clusters.

4.3.4. Electronic Structure Aspects

The application of FON techniques can have a significant influence on electronic properties like ionization energies, as discussed in Section 4.3.3. This effect clearly warrants further discussion. Apart from the LDA exchange term, level broadening favors electron delocalization. Indeed, FON techniques are also known to provide an implicit description of static correlation effects (see Section 2.2.6) as well.[235,236,243] This implicit description is of course related to the employed XC approximation as well as to the system at hand. In this context one can formulate several requirements, which are necessary to achieve an implicit description of static correlation effects for transition metal clusters. These are (i) a sufficient amount of LDA exchange present in the XC term to prevent the corresponding XC hole (see Section 2.2.2) from becoming overly delocalized, (ii) a vanishing band gap in the case of larger metallic systems, (iii) a nonzero density of states (DOS) around the HOMO-LUMO gap, and (iv) the application of a FON technique with a sufficiently large broadening parameter to include as many relevant orbitals near the HLG as possible.[36]

KS-DFT represents a single-determinant formulation only, hence, does not provide any direct measure for static correlation effects. Thus, the aforementioned requirements represent a rough guideline only. In the present context they are, however, sufficient to provide a rationalization of the behavior observed for the assessed XC approximations. To this end, the number of KS orbitals located within a certain energy interval near the HOMO-LUMO gap was examined. Thereby the two intervals $[\varepsilon_F - 0.5\ \text{eV}, \varepsilon_F]$ and $[\varepsilon_F - 0.5\ \text{eV}, \varepsilon_F + 0.5\ \text{eV}]$ where studied, with ε_F being the center of the HLG, which in turn was defined as the energy difference between the lowest KS orbital with a population below $1/2$ and the highest orbital with a population of more than that. The designators $I_{\text{DOS}}^{\text{occ}}$ and $I_{\text{DOS}}^{\text{tot}}$ are used to denote the orbital counts obtained for the first and second interval, respectively. Note, that in the limit of bulk materials, $I_{\text{DOS}}^{\text{occ}}$ and $I_{\text{DOS}}^{\text{tot}}$ are to be understood as integrals of the density of states over the respective intervals. Figure 4.3.4 provides a plot of the values of both quantities on the example of the Pt_m cluster series and the functionals PBE, PBE0, and TPSSh.

Apart from minor deviations in the case of smaller systems, the number of KS orbitals around the HLG grows as expected with the cluster nuclearity. Both, $I_{\text{DOS}}^{\text{occ}}$ and $I_{\text{DOS}}^{\text{tot}}$ are found to be highest in the case of PBE as this functional yields comparatively small HOMO-LUMO gaps. A similar behavior results also from both MGGA functionals. In contrast, both I_{DOS} values obtained from PBE0 (and M06 as well) remain small even for larger cluster sizes. Especially the numbers of more than half populated KS orbitals remain very small, even for larger clusters like Pt_{116}. Thus, the behavior of high EXX hybrid functionals can be clearly distinguished from that of semi-local DFT methods. However, the I_{DOS} values resulting from

[36] The actual value of the broadening parameter is restricted, of course, because a too extensive level broadening does not lead to a realistic electronic structure description.

the low EXX hybrid functional TPSSh remain fairly large, despite of being lower than the corresponding I_{DOS}^{occ} and I_{DOS}^{tot} counts from the semi-local functionals. A similar behavior is also obtained for the other two examined transition metal elements.

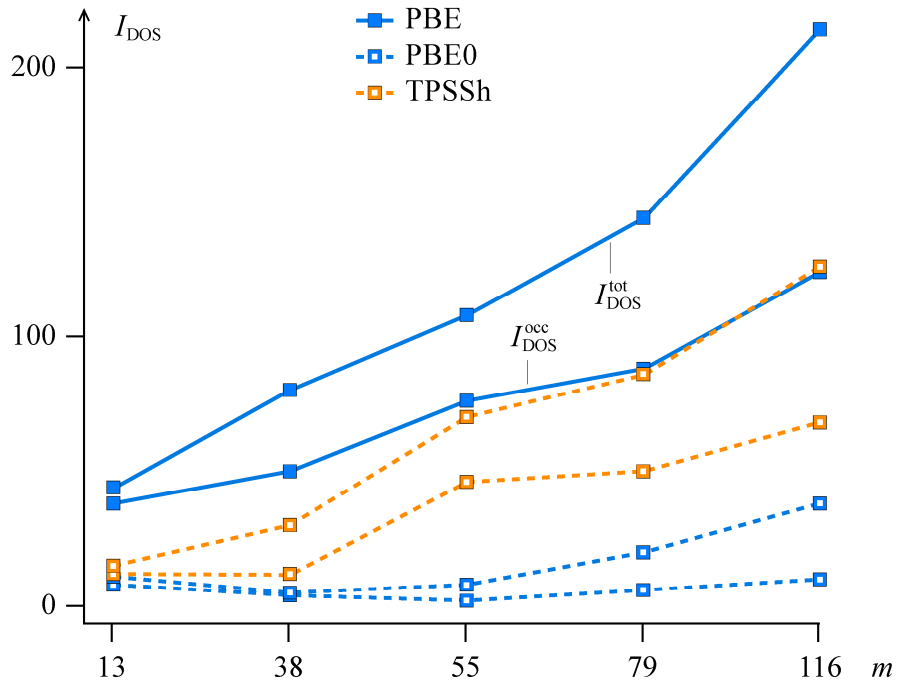

Figure 4.3.4: Orbital counts I_{DOS}^{occ} and I_{DOS}^{tot} within the intervals $[\varepsilon_F - 0.5\ \text{eV}, \varepsilon_F]$ and $[\varepsilon_F - 0.5\ \text{eV}, \varepsilon_F + 0.5\ \text{eV}]$ (see text) obtained for the Pt_m cluster models (m = 13, 38, 55, 79, and 116) with PBE, PBE0, and TPSSh. Figure adapted from Ref. [443].

Thus, the amount of exact-exchange in TPSSh can be considered as small enough to yield a reasonable narrow HOMO-LUMO gap in the case of larger clusters. In consequence, also the number of orbitals near the HLG remains significantly large. As stated at the beginning of this section, this is required for an adequate electronic structure description of metallic systems influenced by static correlation effects. On the other hand, hybrid functionals with a high EXX mixing factor such as PBE0 and M06 can be expected to behave similarly to the HF method, which severely fails for metals due to its depleted density of states around the Fermi level and its discontinuous behavior of the band dispersion.[477,478]

Table 4.3.7: Magnetic moments per atom μ_a of the series of clusters M_m (M = Ni, Pd, Pt) as obtained from the six examined functionals. All values in Bohr magnetons.

	m	PBE	PBE0	TPSS	TPSSh	M06L	M06
Ni	13	0.615	0.615	0.615	0.615	0.655	0.615
	38	0.795	0.842	0.891	0.895	0.895	0.895
	55	0.722	0.618	0.733	0.837	0.870	0.836
	79	0.682	0.785	0.730	0.760	0.778	0.658
	116	0.787	0.810	0.792	0.793	0.793	0.793
Pd	13	0.461	0.462	0.461	0.462	0.461	0.462
	38	0.214	0.211	0.216	0.474	0.473	0.316
	55	0.184	0.400	0.211	0.219	0.282	0.182
	79	0.413	0.430	0.429	0.455	0.421	0.405
	116	0.398	0.379	0.398	0.397	0.499	0.483
Pt	13	0.461	0.462	0.462	0.462	0.462	0.462
	38	0.116	0.158	0.140	0.158	0.192	0.158
	55	0.177	0.473	0.181	0.182	0.242	0.436
	79	0.192	0.278	0.208	0.405	0.602	0.228
	116	0.000	0.034	0.000	0.018	0.334	0.241

The magnetic moments per atom μ_a shall be briefly discussed as another aspect of the electronic structure computed for the examined model clusters with the assessed functionals. These values are provided in Table 4.3.7. Transition metal clusters are often magnetic even for elements which exhibit $\mu_a = 0$ in the bulk limit.[447,475,476] Furthermore, such systems feature an oscillating behavior in their μ_a values up to very large nuclearities.[447,475,476] This essentially prevents any extrapolations of μ_a results to the bulk limit from cluster sizes used in the present study. A scaling approach was therefore not attempted for this quantity. Instead, the general trends in the μ_a values of the M_m clusters were found to reflect some construction principles of the assessed functionals. The employed functionals yield mostly identical values for the M_{13} clusters due to the mostly molecular characteristics of these systems. The μ_a values from the various functionals start to differ at $m = 38$. For clusters of this size and above, the plainly added EXX term as in PBE0 and TPSSh generally causes larger magnetic moments compared to the corresponding local functionals. This propensity for larger μ_a values agrees with the previously reported preference of hybrid DFT methods for high-spin states in the case of bulk materials.[479] In contrast, the M06L functional yields mostly higher magnetic moments than its hybrid DFT counterpart M06. This agrees with the recently observed behavior[447] for the magnetic moments of Pd clusters obtained with M06L and may most likely arise from the different parametrization of the corresponding semi-local XC terms in both functionals.

4.3.5. Conclusions

The addition of exact-exchange to local DFT approximations as in hybrid density functionals leads to significant changes in the description of transition metal systems as shown in Sections 4.3.3 and 4.3.4 for the group 10 model clusters Ni_m, Pd_m, and Pt_m. In summary, hybrid DFT methods tend to underestimate the strengths of metal-metal bonds and to favor high-spin states, which both leads to significantly altered structures in some cases.

As mentioned in Section 2.3.3, the EXX mixing factor α_1 can only be chosen on empirical grounds and a specific value for α_1 may work well for systems of certain type but lead to severe failures for other species. In the present case $\alpha_1 \geq 0.25$ as in PBE0 and M06 was found to often cause an erratic behavior in the prediction of most quantities. While PBE0 is still able to provide accurate structural results in some cases, M06 always fails for this task. Furthermore, the M06 hybrid functional and its semi-local counterpart M06L, seem to suffer from the empirical aspects of its construction.

In contrast, the hybrid functional TPSSh with $\alpha_1 = 0.1$ provides an overall accurate description of the examined transition metal clusters, which is at least on a par with that of the PBE GGA functional for energetic quantities and better than that for structural results. The good accuracy of this hybrid functional is somewhat surprising as its value for the EXX mixing factor was obtained from a parametrization on properties of main group compounds only.[212] The ability of the TPSSh approximation to describe transition metals was rationalized with the density of states around the HOMO-LUMO gap which seems still sufficiently large to allow for an implicit description of static correlation effects by means of the local exchange term and level broadening. However, its actually good accuracy may be rationalized with the partial self-interaction correction provided by its EXX term. While the SIE does not cause as dramatic failures in the description of the M_m species, as in the case of nickel subcarbonyls (Section 4.2), the transition metal clusters can certainly not be considered unaffected by this artifact. Indeed in this context the TPSSh functional seems to provide a good tradeoff between the self-interaction error and the static correlation error, which may be significant in cluster scaling approaches as residual self-repulsion can scale with the system size.[215] Therefore, the TPSSh functional seems attractive for problems that simultaneously involve metallic and molecular moieties as the latter may be more prone to suffer from self-interaction artifacts.

4.4. CO Adsorption on Platinum Model Clusters

4.4.1. The CO Puzzle

The following sections discuss the results obtained with the semi-local functionals PBE, TPSS, and M06L, with the hybrid DFT approximations PBE0, TPSSh, and M06 as well as with the PBE+Umol method for the CO adsorption on the (111) facets of Pt model clusters. The presentation of the results obtained with the latter method thereby follows Ref. [286].

The correct description of the adsorption of the CO molecule on extended transition metal surfaces is a well-known challenge for semi-local DFT approximations.[480-484] Indeed, in the case of the Pt(111) surface semi-local functionals often overestimate the corresponding CO adsorption energy by more than 40 kJ/mol[482,483] compared to experimental reference values, 115±15 kJ/mol.[485-487]

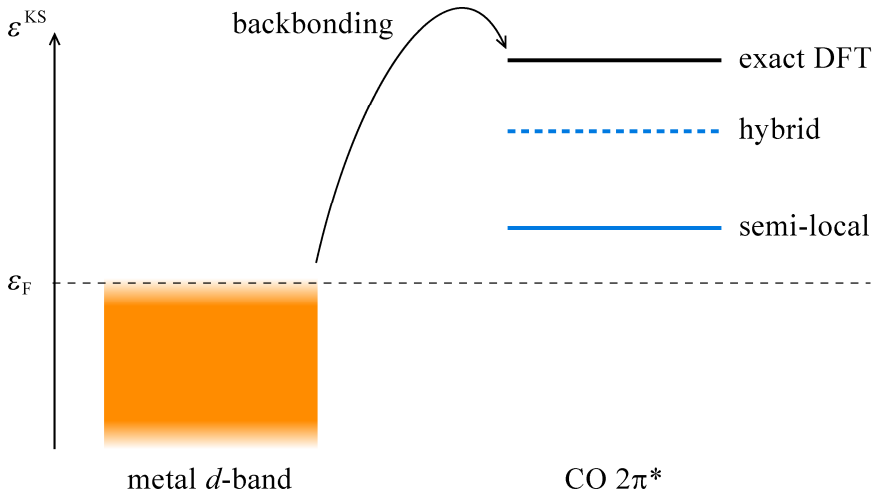

Figure 4.4.1: Schematics of the back-bonding mechanism for the adsorption of the CO molecule on extended transition metal surfaces. Due to the self-interaction error in semi-local DFT methods the energy of the 2π* orbitals of the CO molecule is too low which artificially enhances its back-bonding interaction with the metal *d*-band across the Fermi level ε_F. Figure adapted from Ref. [286].

This quantitative inaccuracy can be rationalized by referring to the back-bonding interaction within the Blyholder model (see Section 4.2).[438,488-491] In the case of the adsorption of CO on transition metal surfaces, the Blyholder model predicts a primary interaction between the CO 5σ orbital and the surface (σ-bonding) as well a partial electron transfer from the *d*-band of the extended surface back into the CO 2π* orbitals (back-bonding).[438,488-491] Back-bonding between these two interaction partners is increased when the CO 2π* orbitals are lowered in energy.[438,488-491] As a direct consequence of the missing discontinuity of the XC potential at integer occupation numbers due to the self-interaction

error (see Section 2.2.5), partially populated levels exhibit a too low energy.[480] This holds especially for the ε^{KS} energies of the CO 2π* orbitals, which is depicted in Figure 4.4.1. Thus, upon adsorption of the CO molecule on a transition metal surface, the SIE causes the band gap to be too small which in turn leads to overestimated adsorption energies.[480]

Another important issue concerns the preferred site at which the CO molecule adsorbs on the (111) surface. Figure 4.4.2 depicts the location of the four distinct, highly symmetric sites for the CO adsorption on extended (111) surfaces: the μ_1-coordinated top site (denoted by "t"), the twofold coordinated μ_2-type bridge site ("b"), and the hollow sites with a μ_3-coordination. In the case of the latter one can further distinguish between fcc-type ("f") and hcp-type ("h") hollow sites, depending on the position of the second atomic layer of the (111) surface.[481,492]

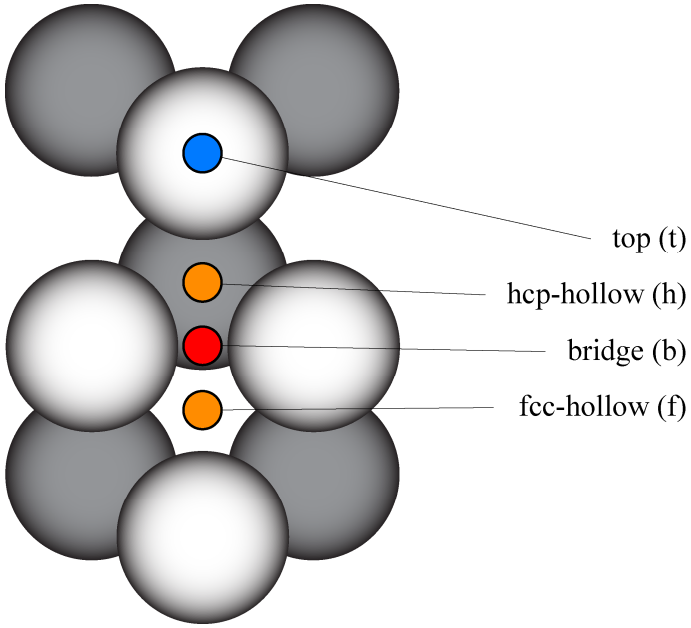

Figure 4.4.2: Positions of the top (t), bridge (b), and hcp- (h) and fcc-hollow (f) adsorption sites on the top (white) and sub-surface (dark grey) layers of an extended (111) surface.

The preference for the adsorption on a specific site depends on various properties of the surface at hand like the work function, the filling of the individual bands (especially the *d*-band), and the energetic position of the bands with respect to the Fermi level.[482,486,488-491,493] In the case of the Pt(111) surface a preference for a CO adsorption at the top site is reported by several experimental studies.[494-498] In contrast, semi-local DFT approximations yield a preference for the fcc-hollow site.[480,481,499,500] After this qualitative failure of semi-local DFT methods has been recognized, it was termed as the "CO puzzle".[480,481] Subsequently a large number of studies was dedicated to rationalize the origin of this problem. In this context, the influences of the adsorption site model,[286,492,500,501] of relativistic effects,[500,502-504] of the

representation of the core-electrons,[479,480,483,505] of empirical site-dependent corrections,[481,506] as well as of self-interaction artifacts[479,483,484,499,500,504,507] were examined.

Indeed, most of these studies identified the self-interaction error not only to cause the aforementioned overestimated CO adsorption energies of semi-local functionals but also the incorrect preference for the fcc-hollow site.[484] Like the overestimation of adsorption energies also this qualitative failure can be understood in the context of the Blyholder model.[438,489,490] Apart from the small energetic difference between the interacting Pt *d*-levels and the CO 2π* orbitals, a significant overlap between both interaction partners represents a further condition for back-bonding.[489,490] As depicted in Figure 4.3.3, the overlap between the 2π* orbitals and the levels of the Pt(111) surface is higher at a hollow site than at a top site.[489,490] Thus, back-bonding is primarily dominant at h- and f-type sites, while at top sites the primary σ-bonding between the CO 5σ orbital and the levels of the Pt surface prevails.[438,489,490,508] In combination with the aforementioned artificial enhancement of the back-bonding interaction due to the SIE, this explains why semi-local DFT approximations erroneously predict a fcc-hollow site preference for the adsorption of the CO molecule on Pt(111).[438,489,490]

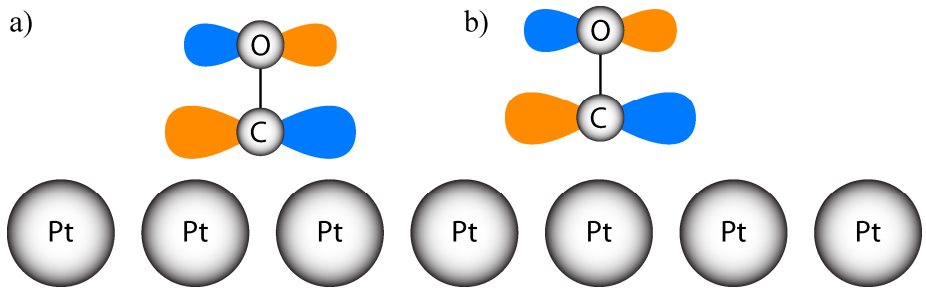

Figure 4.4.3: Position of the CO molecule at a) hollow-type and b) top sites. The overlap between the CO 2π* orbitals and the levels of the Pt surface is higher at hollow sites. Figure adapted from Ref. [286].

One is therefore confronted with the following dilemma when selecting a suitable DFT approximation for the description of the adsorption of the CO molecule on Pt(111). On the one hand, a correction of the SIE should increase the energy of the CO 2π* orbitals and thus reduce the tendency to overestimate the energetic contribution of the back-bonding at hollow sites. However, the preference for a specific adsorption site is determined by fine details of the electronic structure of the metal moiety such as the energies and the width of the bands near the Fermi level.[479,483] Thus, the correct prediction of the site preference for the CO adsorption on Pt(111) requires methods which are (nearly) free of self-interaction but are also able to provide an accurate description of the metal moiety. However, the electronic structure of the Pt(111) surface exhibits a considerable multi-reference character. As discussed in

Sections 2.2.5 and 2.2.6, any self-interaction correction automatically deteriorates the implicit description of static correlation by local exchange functionals, unless the correlation term can account for this latter effect. Thus, the rather unphysical description of the density of states from hybrid DFT methods like PBE0 (see Section 4.3) also affects the results for the CO adsorption site preference.[479,483]

The B3LYP functional was occasionally reported to predict the correct top site preference for the CO adsorption on Pt(111) or to render both, top and fcc-hollow sites, nearly degenerate.[479,500,501,507] However, given its notoriously bad description of transition metals,[198,264,266-270] B3LYP is unlikely to deliver the top site preference for the correct reason. The same is true for the vdW-DFT methods (see Section 2.2.7), which were reported to predict a CO adsorption at the top site as well, but actually do not provide any self-interaction correction at all.[509] Thus, the correct site preference obtained with vdW-DFT functionals can only result from an altered description of the electronic structure of the metal moiety compared to semi-local functionals, but not from the energy of the CO 2π* orbitals.

According to the results of the case study presented in Section 4.3 the hybrid functional TPSSh provides an accurate description of late transition metals.[443] One may thus hope that its comparatively small exact-exchange term ($\alpha_1 = 0.1$) reduces the self-interaction sufficiently enough to correct the energy of the CO 2π* orbitals. This motivated the subsequently presented study where the performance of six DFT approximations, namely PBE,[49] PBE0,[87] TPSS,[75] TPSSh,[212] M06L,[77] and M06[77,90] was assessed on the example of the CO adsorption at various sites on the (111) facets of different cluster models (see Section 4.4.2). Furthermore, the influence of scalar relativistic effects was briefly examined.

Furthermore, these models were also studied with the PBE+Umol method, whose SIE correction was projected onto the CO 2π* orbitals.[286] To assess the influence of this correction the value of the parameter $U_{2\pi^*}$ (see Sections 2.4 and 4.2) was varied between 1.0, 1.5, and 2.0 eV.[286] At this point it is worth emphasizing that, while the Umol(CO 2π*) term led to unphysical results for the nickel carbonyl complexes (see Section 4.2), the situation is quite different in the case of larger Pt clusters. First, the Pt 5*d* subshell is rather delocalized in larger transition metal particles so that the prerequisites for an application of the DFT+Umol correction to the Pt 5*d* orbitals are not really met. While the correct localization of the Ni 3*d* subshell in the nickel carbonyl complexes is important, its orbitals are significantly more compact than those of the Pt 5*d* subshell. Thus, in the 5*d* orbitals, self-repulsion is much lower and so is the tendency to minimize it through delocalization. Furthermore, the HOMO-LUMO gap is smaller in larger transition metal clusters compared to the carbonyl complexes. In consequence, the correct energy of the CO 2π* orbitals is, according to the above well-established rationalization, most important for the correct prediction of the CO adsorption site preference. Therefore, the application of the Umol(CO 2π*) correction term is well justified in the case of the CO adsorption on Pt model clusters.

4.4.2. Adsorption Site Models

In the following the adsorption site models on the (111) facets of the Pt model clusters employed in the present case study are presented. These sites are subject to two main effects resulting from the finite size of the cluster models;[454,455,510-513] the influence of under-coordinated atoms of the facet border and of elongated metal-metal distances between surface atoms that are induced by the clusters core atoms. Especially the former effect can lead to significantly higher adsorption energies, which demands a careful analysis. The effect of the average metal-metal distances on the CO adsorption energies is briefly addressed at the end of this section.

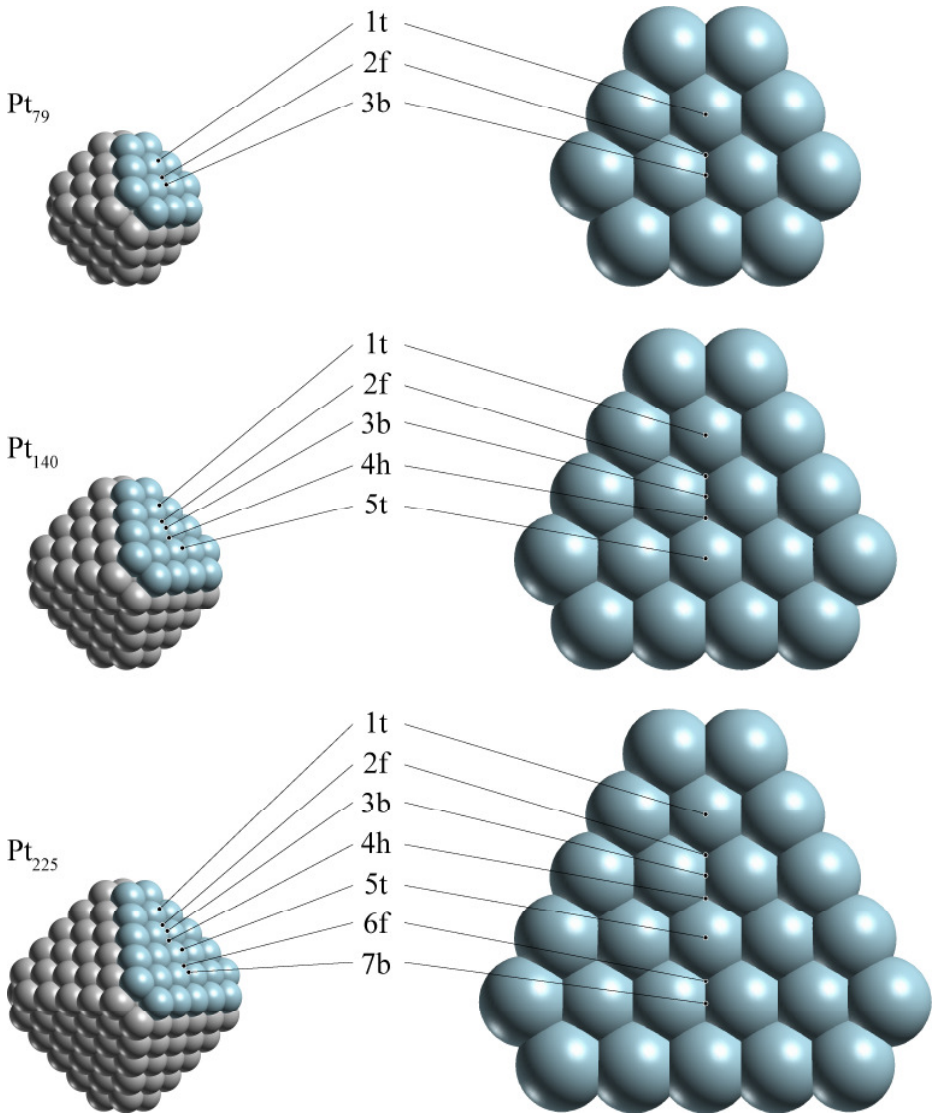

Figure 4.4.4: Position of the CO adsorption sites on the (111) facets of the model clusters Pt_{79}, Pt_{140}, and Pt_{225} employed in the present case study.

Figure 4.4.4 depicts the (111) facets of the model clusters Pt_{79}, Pt_{140}, and Pt_{225} as well as the positions of the examined CO adsorption sites on them. The Pt_{79} cluster corresponds to the same atom-centered model used in the cluster scaling study of Section 4.3. The Pt_{140} model derives from the Pt_{116} cluster (see Figure 4.3.1, Section 4.3) upon addition of 4 atoms per (100) facet and thus exhibits an octahedral center. The Pt_{225} model originates from the larger cuboctahedral cluster Pt_{147} and is atom-centered. Despite the different origins of these cluster models, the "upper" corners of their (111) facets feature the same local topologies (see Figure 4.4.4). In consequence one notices a repeating pattern in the types of adsorption sites, i.e. 1t, 2f, 3b, etc., when going from the upper corner to the lower border. Due to the employed D_{4h} symmetry constraints one CO molecule is adsorbed on each of the eight (111) facets, which leads to the adsorption complexes $Pt_{79}(CO)_8$, $Pt_{140}(CO)_8$, and $Pt_{225}(CO)_8$.

In the present application of the six examined XC functionals and the DFT+Umol method CO adsorption is studied on adsorption sites of these model clusters. The E_{ads} values are to be understood as adsorption energies per CO molecule

$$E_{ads} = \frac{E_{tot}\left(Pt_m(CO)_8\right) - E_{tot}\left(Pt_m\right) - 8 \cdot E_{tot}\left(CO\right)}{8}. \qquad 4.4.1$$

All subsequently discussed adsorption energies were obtained by using the def2-TZVP basis set,[412] which implies a Stuttgart-Dresden effective core potential (ECP) representation of the atomic core orbitals of Pt (see Section 4.1 for the detailed computational parameters). As shown by comparison with a scalar-relativistic[514,515] using a SARC-type all-electron basis set[516] (see Section 4.4.4), the influence of the ECP approximation on the E_{ads} values is generally smaller than the corresponding effect on the cohesive energies (see Section 4.3.3). All E_{ads} values were corrected for the basis set superposition error (BSSE)[395] which was estimated in terms of the counterpoise approach.[418] The resulting BSSE estimates amount mostly to ~10 kJ/mol per CO molecule (~16 kJ/mol at most) and are lowest at the top sites.[37]

Also the model character of the studied sites on the cluster models for the CO adsorption on the extended Pt(111) surface has to be addressed to admit a methodological assessment by comparing the results to available experimental references.[486,487] From earlier adsorption studies two main effects of the employed cluster model on the CO adsorption energies are known.[454,455,510-513] The first one arises from the under-coordinated atoms at the borders and edges of the cluster facets.[511,513] The influence of these facet borders significantly affects the adsorption behavior on small clusters[511,513] and, to a certain extent, remains present near the edges of larger facets as well.[517,518] The borders of such (111) facets are known to have an attractive effect in the case of CO adsorbates.[512,513] Thus, the CO adsorption energies on (111) facets generally decrease when going from smaller to larger cluster models as well as when going from sites close to facet borders to those near the center of a facet.[512,513]

[37] The larger BSSE estimates at hollow and bridge sites are again rationalized by the higher overlap between the interacting orbitals there.

To put the influence of the under-coordinated atoms on the (111) facets of the employed cluster models in a more general context, the average coordination numbers of the surface atoms associated with the individual adsorption sites are examined.[286] On (111) surfaces the 1, 2, and 3 atoms that form top, bridge, and hollow-type adsorption sites are surrounded by 6, 8, and 9 nearest-neighbor surface atoms, respectively. In this context a total of $n_{\mathrm{site}} = 7,\ 10,$ and 12 surface atoms are associated with the individual top, bridge, and hollow sites, respectively. For each adsorption site the average nearest-neighbor coordination numbers

$$CN_{\mathrm{av}} = \frac{1}{n_{\mathrm{site}}} \sum_{i}^{n_{\mathrm{site}}} CN_i \qquad 4.4.2$$

are computed as average of the nearest-neighbor coordination numbers CN_i (including surface and sub-surface atoms) of those n_{site} atoms associated with the site.[286] The resulting average nearest-neighbor coordination numbers of the groups of 7, 10, and 12 surface atoms always amount to $CN_{\mathrm{av}} = 9$ in the case of the extended (111) surface. For the sites on the (111) facets of the three employed cluster models the CN_{av} values are mostly lower and range between ~7 and 9.[286]

Figure 4.4.5 provides a plot of the individual CO adsorption energies E_{ads} (see Section 4.4.4) obtained with the PBE functional for all studied adsorption sites as a function of CN_{av}. The overall linear regression function, based on the results of all sites and cluster models,

$$E_{\mathrm{ads}}(CN_{\mathrm{av}}) = (282 - 16.3 \cdot CN_{\mathrm{av}}) \text{ kJ/mol} \qquad 4.4.3$$

reflects a rough trend only ($R^2 = 0.64$) due to the different behavior of the various types of adsorption sites. Much better correlations ($R^2 \approx 0.9$) are obtained when one eliminates the effect of the different types of sites by calculating the linear regression functions $E^{\mathrm{t}}_{\mathrm{ads}}(CN_{\mathrm{av}})$, $E^{\mathrm{b}}_{\mathrm{ads}}(CN_{\mathrm{av}})$, and $E^{\mathrm{f}}_{\mathrm{ads}}(CN_{\mathrm{av}})$ for the individual series of adsorption energies at t, b, and f sites, respectively (see Figure 4.4.5).[286] The linear trends of the CO adsorption energies have a certain empirical flavor and are not as well physically justified as the cluster scaling relations (see Section 4.3.2). Nevertheless, they allow for several observations about the general behavior of the employed CO adsorption site models.

When comparing these three linear functions one notices the much steeper slope of the $E^{\mathrm{b}}_{\mathrm{ads}}(CN_{\mathrm{av}})$ values obtained at bride sites. At the 3b site of the Pt_{79} cluster the overall highest CO adsorption energy is obtained (see Section 4.4.4). This large adsorption energy most likely results from the influence of the adjacent facet edge (see Figure 4.4.4).[286] However, on the (111) facets of the two larger cluster models this effect vanishes and the corresponding adsorption energies are significantly smaller. Furthermore, one notices the slightly steeper slope of $E^{\mathrm{t}}_{\mathrm{ads}}(CN_{\mathrm{av}})$ compared to that of $E^{\mathrm{f}}_{\mathrm{ads}}(CN_{\mathrm{av}})$, which probably indicates that the 1t sites of all cluster models are subject to a somewhat stronger influence of facet border than the corresponding adjacent 2f sites.

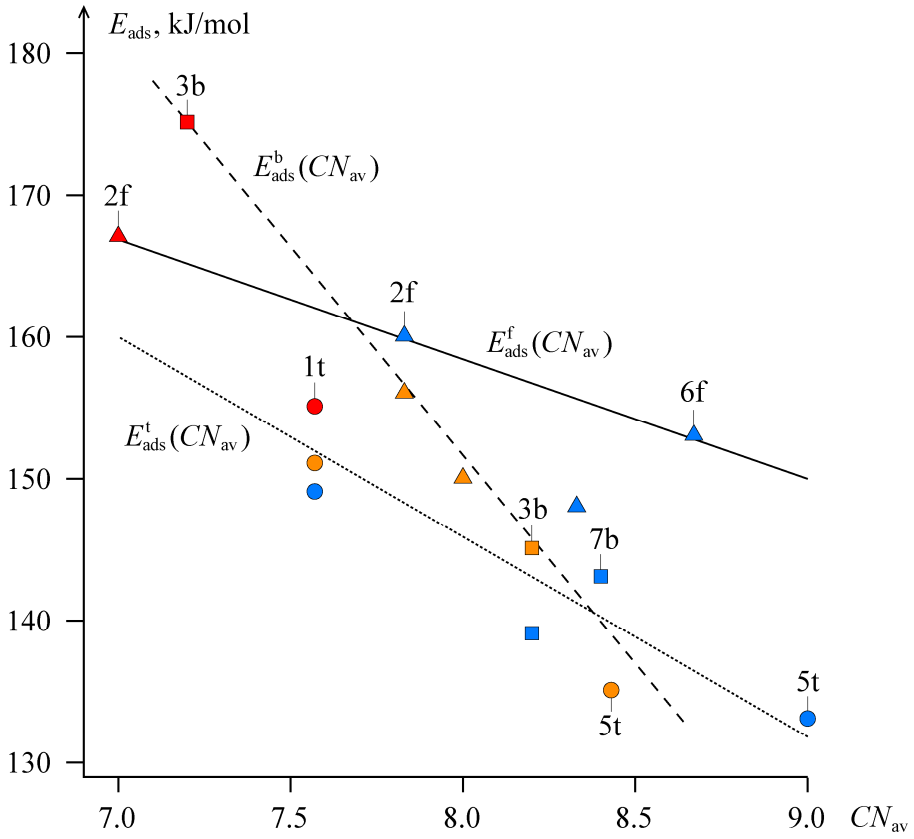

Figure 4.4.5: PBE adsorption energies in kJ/mol at top (circles), hollow (triangles), and bridge sites (squares) of the (111) facets of the cluster models Pt_{79} (red), Pt_{140} (orange), Pt_{225} (blue) in terms of the average coordination number CN_{av} (see text) as well as the linear regression functions for the series of E_{ads} values at t, f, and b sites as dotted, solid, and dashed lines, respectively. Figure adapted from Ref. [286].

The sites 5t and 6f of the Pt_{225} cluster feature the largest CN_{av} values, 9.00 and 8.67, respectively, as they are located at the center of the largest facet studied. These sites can be expected to be closest to the corresponding top and fcc-hollow sites on Pt(111) and thus qualify best as models for the CO adsorption on this extended surface.

The influence of the facet borders certainly represents the most significant finite cluster size effect on the adsorption energies.[510,517,518] However, it is not the only effect resulting from limited cluster sizes. Another important influence arises from the slightly increased metal-metal nearest-neighbor distances within the clusters due to the reduced fraction of under-coordinated atoms when approaching the bulk limit (see Section 4.3.3).[454,455,512,513] While this structural pattern originates from the core part of a cluster, it translates also to the surface layer.[454,455,512,513] In consequence, the elongated metal-metal distances between under-coordinated surface atoms give rise to a bonding competition.[454,455,512,513] Thus, as the metal-metal interaction decreases, the CO adsorption energies increase again for large clusters at sites which are mostly unaffected by facet borders.[454,455,512,513]

In a previous CO adsorption study on Pd clusters the aforementioned effect of elongated metal-metal distances was discussed in detail.[454] This study also showed that the effect of elongated metal-metal distances can be mimicked by cluster models in which only the surface layer was allowed to relax while the nearest-neighbor distances between all subsurface atoms were fixed to the corresponding bulk limit.[454] The resulting CO adsorption behavior on such cluster models is similar to that on much larger particles close to the bulk limit.[454]

This type of a cluster model was also employed during the assessment of the DFT+Umol method.[286] Thereby the octahedral Pt_{44} core of the $Pt_{140}(CO)_8$ cluster model was fixed at the bulk limit (281.3 pm) of the d_{av} distances, which were obtained from a cluster scaling extrapolation (see Section 4.3) of the series Pt_{79}, Pt_{116}, Pt_{140}, Pt_{201}, and Pt_{225}.[286] However, compared to the fully relaxed cluster model, only changes of about 4 kJ/mol or less were observed in the corresponding CO adsorption energies.[286] Thus, this comparison leads to the conclusion that influence of elongated metal-metal distances is only of a lesser importance for the present methodological assessment.

4.4.3. Structural Aspects

Out of the different structural parameters of the various adsorption complexes and cluster models, only the C-O distances $d_{C\text{-}O}$ are essential for the discussion of the description of the CO adsorption in terms of the Blyholder model.[438,489,490] Furthermore, the present discussion is restricted to some selected sites on the cluster models Pt_{79} and Pt_{225}, namely 1t, 2f, and 3b on Pt_{79} as well as 5t and 6f on Pt_{225}. Table 4.4.1 provides the corresponding C-O bond lengths for the methods PBE, PBE0, TPSS, TPSSh, M06L, and M06 as well as for the PBE+Umol(CO 2π*) combination with the parameter value $U_{2\pi^*} = 2.0\,\text{eV}$.

Upon adsorption of a CO molecule on the Pt cluster models, the C-O bond is weakened as the anti-bonding CO 2π* orbitals are partially populated due to back-bonding.[438,488-491] The elongation of the C-O bond roughly correlates with the amount of back-bonding at the individual adsorption sites (see also Section 4.2.2).[438,488-491] The $d_{C\text{-}O}$ values found at the three sites of the Pt_{79} model are ordered according to 1t < 3b < 2f, which reflects the expected relative amount of back-bonding. The variants PBE0 and M06 always yield the shortest $d_{C\text{-}O}$ values which partially results from the description of the CO molecule itself as these methods yield the shortest C-O bonds already for CO in the gas-phase.

Relative to the respective gas-phase $d_{C\text{-}O}$ values, the examined hybrid DFT methods yield less elongated C-O bonds than their semi-local counterparts. Thus, back-bonding is indeed reduced by the EXX term. Compared to the sites on the Pt_{79} model, the $d_{C\text{-}O}$ values found in the $Pt_{225}(CO)_8$ adsorption complexes are reduced further by a small amount (< 0.3 pm) as finite cluster size effects are reduced in this case.

Table 4.4.1: C-O bond lengths, $d_{C\text{-}O}$, obtained with the six examined functionals and the PBE+Umol(CO 2π*) combination ($U_{2\pi^*} = 2.0$ eV) for some of adsorption complexes of $Pt_{79}(CO)_8$ and $Pt_{225}(CO)_8$ as well as for a CO molecule in the gas-phase. All values in pm.

		PBE	PBE0	TPSS	TPSSh	M06L	M06	PBE+Umol
Pt_{79}	1t	115.2	113.5	114.9	114.2	114.2	113.4	113.4
	2f	119.3	117.4	118.6	117.9	117.9	116.9	118.9
	3b	117.7	—[a]	117.4	—[a]	—[a]	—[a]	117.2
Pt_{225}	5t	115.0	—	114.8	—	—	—	114.2
	6f	119.0	—	118.6	—	—	—	118.5
CO_{gas} [b]		113.7	112.4	113.5	113.0	112.8	112.3	113.7

[a] Relaxation converges to CO adsorption complex at an adjacent hollow-site.

[b] Experimental reference for CO in the gas phase $d_{C\text{-}O} = 112.8$ pm, Ref. [519].

4.4.4. CO Adsorption Energies

This section discusses the CO adsorption energies E_{ads} obtained from the DFT approximations PBE,[49] PBE0,[87] TPSS,[75] TPSSh,[212] M06L,[77] and M06[77,90] and from the PBE+Umol(CO 2π*) method using $U_{2\pi^*} = 1.0$, 1.5, and 2.0 eV (see Section 4.2).

Table 4.4.2 provides the CO adsorption energies calculated with the hybrid DFT methods PBE0,[87] TPSSh,[212] and M06[77,90] as well as their semi-local counterparts PBE,[49] TPSS,[75] and M06L.[77] The discussion begins with the E_{ads} values obtained with the PBE GGA functional to extend the general observations of the behavior at the different adsorption sites, stated in Section 4.4.2. On the (111) facet of Pt_{79} PBE yields the lowest E_{ads} value of 156 kJ/mol at the 1t top site. While the adsorption energy of $E_{ads} = 168$ kJ/mol at the 2f site is higher than that, the 3b site ($E_{ads} = 176$ kJ/mol) is clearly most preferred on this cluster model (see Table 4.4.2). As expected from the effect of under-coordinated atoms on cluster surfaces (see Section 4.4.2) and the SIE (see Section 4.4.1), all these results are significantly higher than the experimental reference value of 115±15 kJ/mol.[485-487] However, neither these experiments nor plane-wave calculations of the extended Pt(111) surface yield a bridge-site preference for the CO adsorption as it results from the present calculations of the model cluster Pt_{79}.[484]

Table 4.4.2: CO adsorption energies[a] E_{ads} obtained at several sites on the (111) facets of the model clusters Pt_{79}, Pt_{140}, and Pt_{225} with the six examined functionals including the correction for the BSSE. All values in kJ/mol.

		1t	2f	3b	4h	5t	6f	7f
PBE	Pt_{79}	156	168	176				
	Pt_{140}	152	157	146	151	136		
	Pt_{225}	150	161	140	149	134	154	144
PBE0	Pt_{79}	180	196	—[b]				
TPSS	Pt_{79}	151	160	174				
	Pt_{225}	—	—	—	—	127	146	—
TPSSh	Pt_{79}	156	164	—[b]				
	Pt_{225}	—	—	—	—	128[c]	153[c]	—
M06L	Pt_{79}	145	153	—[b]				
M06	Pt_{79}	159	176	—[b]				

[a] Experimental result for top site on Pt(111): 115±15 kJ/mol; Refs. [485-487].

[b] Relaxation converges to CO adsorption complex at adjacent hollow-site.

[c] Single-point result at corresponding TPSS geometry.

Indeed, the preference for the 3b site on the (111) facet of the Pt_{79} cluster seems to be related to the adjacent "lower" facet border (see Figure 4.4.4). On the Pt_{140} model this facet edge is more distant from the corresponding 3b site. An E_{ads} value of 146 kJ/mol is obtained at the 3b site of this cluster, which is lower than most other CO adsorption energies calculated on this cluster. With $E_{ads} = 157$ kJ/mol the neighboring 2f site is most preferred on the Pt_{140} cluster. A slightly lower adsorption energy of 151 kJ/mol is obtained at the 4h site, which results from its hcp-hollow topology as well as from its reduced interaction with the facet border.[492] When comparing the E_{ads} results of 152 and 136 kJ/mol obtained at the two top sites 1t and 5t, respectively, one notices even more clearly the considerable effect of the nearby facet borders at the former.

Furthermore, the difference in the adsorption energies at the sites 1t and 5t also implies that the effects of facet corners and edges are of a similar magnitude as the differences arising for different types of adsorption sites. Thus, only adjacent top and fcc-hollow sites, hence the pairs 1t/2f and 5t/6f, are to be compared with each other when discussing site preferences on the employed model clusters. However, a slightly different influence of facet borders remains notable even at such pairs of neighboring sites. When comparing the E_{ads} values obtained at the 1t and 2f sites on the different cluster models one notices that their difference decreases from 12 to 5 kJ/mol when going from Pt_{79} to Pt_{140} but increases again to 11 kJ/mol on the

Pt_{225} model. This trend may be caused by the effect of elongated Pt-Pt distances in larger clusters (see Section 4.4.2) which seems to affect the 2f site more than the 1t site.

On the other hand, the adsorption energies at the sites 4h and 5t appear quite converged with respect to the size of the cluster model as both E_{ads} values only change by ~2 kJ/mol, respectively, when going from Pt_{140} to Pt_{225}. The site 6f was not examined on the Pt_{140} cluster due to its location near the facet border. However, a similar convergence with respect to the cluster size can be expected also for this site on Pt_{225} ($E_{ads} = 154$). This becomes even more apparent when considering that the site 6f on Pt_{225} features a CN_{av} value (see Section 4.4.2) which is even higher than that of the corresponding 4h site.

In the case of the 7b site on Pt_{225} a similar behavior may be expected as for the 3b site on the Pt_{79} cluster. However, 7b exhibits a significantly larger CN_{av} value than the latter so that no dramatic effect of under-coordinated edge atoms on the adsorption energy is observed there. In contrast to the strongly increased adsorption energy found at the 3b site on Pt_{79}, the potential energy surface at 7b seems to exhibit only a rather shallow minimum as the CO adsorbate tends to converge easily to the adjacent 6f site upon relaxation.

While in the case of PBE and PBE+Umol (see below) all adsorption sites presented in Section 4.4.2 were thoroughly examined,[286] the assessment of PBE0,[87] TPSS,[75] TPSSh,[212] M06L,[77] and M06[77,90] mainly focusses on the pair 1t/2f of adsorption sites on Pt_{79}. According to the PBE results discussed above one can safely assume that the influence of the facet edges on both of these sites is sufficiently similar for the present discussion.

The E_{ads} values of 180 kJ/mol and 196 kJ/mol obtained with the PBE0 functional on the 1t and 2f sites of Pt_{79}, respectively, are significantly larger than the corresponding PBE results. On the other hand, PBE0 reduces the C-O distances in the adsorbate fragments by ~1 pm more than PBE, which, according to the Blyholder model, suggests a reduced amount of back-bonding (see Section 4.4.3).[438,488-491] Given the fact that the back-bonding interaction is reduced by the EXX term, it seems counterintuitive that this term leads to higher adsorption energy at the same time. However, similarly increased CO adsorption energies are reported in plane-wave calculations of slab models of the extended Pt(111) surface.[479,483] This behavior was rationalized with an increased broadening of the Pt 5*d* band (see Section 4.4.5), caused by the EXX term as well.[479,483] The broadening of the Pt 5*d* band was found to essentially counteract the effect of the higher energies of the $2\pi^*$ orbitals.[479,483] The E_{ads} values obtained with PBE0 at the 1t and 2f sites of Pt_{79} are in line with the corresponding plane-wave results of 187 and 193 kJ/mol for top and fcc-hollow sites, respectively.[483] However, in the case of the cluster model the hollow-site preference is higher by 10 kJ/mol, which is similar to the corresponding differences obtained with PBE results.[286] Furthermore, these agreements have to be considered with some caution as the E_{ads} values on the cluster models are known to be subject to attractive finite cluster size effects (see Section 4.4.2), while the plane-wave results are not. With PBE0 (and most other examined functionals) no stable

adsorption geometry could be obtained at the site 3b on the cluster Pt_{79}. The CO adsorbate rather relaxes to the neighboring hcp-hollow site at the facet border, similarly to the behavior observed with PBE and PBE+Umol (see below) at the 7b site on the Pt_{225} model.

The M06 functional yields CO adsorption energies of 159 kJ/mol and 176 kJ/mol for 1t and 2f, respectively, which are considerably lower than the corresponding PBE0 results. Indeed, the E_{ads} values from M06 are closer to those from the PBE functional. When considering that M06 features an even slightly larger EXX mixing factor of $\alpha_1 = 0.27$ than PBE0 ($\alpha_1 = 0.25$) this result is somewhat surprising. However, the low adsorption energies from M06 may be related to its questionable description of the metal moiety (see Section 4.3) as well as to the parametrization of its semi-local terms.[443] The E_{ads} values resulting from the M06L functional are even lower than those from M06 and with $E_{ads} = 145$ kJ/mol and 153 kJ/mol for the sites 1t and 2f the overall lowest adsorption energies calculated on the Pt_{79} cluster with the six examined functionals.

Also the TPSS functional yields lower CO adsorption energies than PBE: 151 kJ/mol and 160 kJ/mol for 1t and 2f, respectively. When comparing the adsorption energies of these two sites, the slightly reduced preference of about 9 kJ/mol for the fcc-hollow site is noteworthy. Furthermore, TPSS also yields a stable adsorption structure at the 3b site. The adsorption energy of 174 kJ/mol computed at this site is very similar to the corresponding PBE result. Due to its small EXX mixing factor ($\alpha_1 = 0.10$) the TPSSh functional yields only slightly increased adsorption energies compared to TPSS. With 156 and 164 kJ/mol for 1t and 2f, respectively, TPSSh yields even a slightly lower preference for the fcc-hollow site than its semi-local counterpart.

Motivated by these comparatively low preferences for the 2f site as well as by the surprisingly good description of metal-metal bonds provided by TPSSh (see Section 4.3), the 5t/6f pair of adsorption sites on the Pt_{225} cluster was studied with TPSS and TPSSh as well. Compared to the E_{ads} values obtained with PBE, the TPSS functional yields consistently lower adsorption energies, whereas the differences of 7–8 kJ/mol are comparable to those of the Pt_{79} cluster. The TPSS adsorption energies decrease when going from the sites 1t and 2f on Pt_{79} to the sites 5t and 6f on Pt_{225}. However, due to the aforementioned stronger influence of the facet borders at 1t this decrease is not the same for both types of sites. In the case of the top-sites the difference in the adsorption energies when going from Pt_{79} to Pt_{225} amounts to 24 kJ/mol but only to 14 kJ/mol for the fcc-hollow sites. Thus, the site preference between the 5t/6f pair is increased to 19 kJ/mol in favor of the 6f site, similarly to the increased preference of 20 kJ/mol found with PBE.

Given the substantial computational effort required to carry out hybrid DFT calculations for the $Pt_{225}(CO)_8$ models, the application of TPSSh was restricted in that case to single-point calculations at the corresponding TPSS geometries. To evaluate the effect of this strategy the TPSSh functional was first applied to the TPSS geometries of the Pt_{79} cluster. The adsorption

energies from the single-point calculations differ by only 1 kJ/mol from the E_{ads} values obtained at the relaxed TPSSh structures. At the two examined sites of the Pt_{225} cluster, the single-point TPSSh adsorption energies were computed as 128 kJ/mol (5t) and 153 kJ/mol (6f). Thus, the site preference of TPSSh in favor of the 6f site is estimated to 25 kJ/mol.

Aside from DFT methods with reduced self-interaction, scalar-relativistic electronic structure descriptions have been reported to restore the top-site preference on Pt(111) as well.[503,504] This has been rationalized with a different energy of the Pt 6*s* levels which increases their interaction with the 5σ orbital of the CO molecule, hence the σ-bonding which dominates at top-sites.[489,490,503,504] In the context of the present cluster study this aspect was briefly examined as well. To this end, scalar-relativistic all-electron calculations were carried out with the second-order Douglas-Kroll-Hess approach.[514,515] Thereby a SARC-type all-electron basis set[516] was employed for Pt in combination with a well-established prescription for the generation of the auxiliary density fitting basis set.[39] The corresponding adsorption energies were again calculated in a single-point fashion at the geometries obtained at the TPSS/def2-TZVP level. The resulting E_{ads} values of 150 kJ/mol (1t) and 160 kJ/mol (2f) confirm the adsorption energies obtained with the def2-TZVP basis. These results are consistent with the E_{ads} values of an earlier cluster model study.[500] However, they do not support the claims that a scalar-relativistic electronic structure treatment solves the CO puzzle as the 1t/2f pair exhibits a smaller preference for the fcc-hollow site than the 5t/6f pair.

The sites 5t and 6f on the cluster Pt_{225} can be considered as reliable models for the corresponding top and fcc-hollow sites on Pt(111), respectively. Furthermore, the adsorption energies of the pair 1t/2f on Pt_{79} suggest that the 2f site is slightly less preferred over 1t than the 6f site on Pt_{225} over the corresponding site 5t. In consequence, any method that does not predict a top-site preference on the cluster Pt_{79} is unlikely to yield this preference on the Pt_{225} model or the extended Pt(111) surface. Thus, the results discussed above allow the conclusion that neither one of the six examined DFT approximation nor a scalar-relativistic treatment represent a viable solution of the CO puzzle. Indeed, the failure of hybrid DFT methods to reproduce the CO adsorption site preference on the Pt(111) surface represents a perfect example where improvements on one aspects of a system (i.e. the reduced SIE) deteriorates some other aspects (i.e. the description of the metal moiety).

In this context the very localized self-interaction correction provided by the PBE+Umol(CO 2π*) combination becomes interesting. The E_{ads} values obtained at the individual sites of the Pt_{79}, Pt_{140}, and Pt_{225} clusters for values of 1.0, 1.5, and 2.0 eV for the parameter $U_{2\pi^*}$ are provided by Table 4.4.3 and shall be discussed in the following.

Table 4.4.3: CO adsorption energies[a] E_{ads} obtained at several sites on the (111) facets of the model clusters Pt_{79}, Pt_{140}, and Pt_{225} with PBE+Umol(CO 2π*) method at several values of the parameter $U_{2\pi^*}$ including the correction for the BSSE. All values in kJ/mol.

	$U_{2\pi^*}$[b]		1t	2f	3b	4h	5t	6f	7f
PBE		Pt_{79}	156	168	176				
		Pt_{140}	152	157	146	151	136		
		Pt_{225}	150	161	140	149	134	154	144
PBE+Umol	1.0	Pt_{79}	119	120	132				
		Pt_{140}	110	110	102	104	99		
		Pt_{225}	113	114	95	102	97	107	—[c]
	1.5	Pt_{79}	101	97	110				
		Pt_{140}	92	86	80	80	81		
		Pt_{225}	95	90	72	79	79	83	—[c]
	2.0	Pt_{79}	83	73	88				
		Pt_{140}	75	63	58	57	63		
		Pt_{225}	77	67	51	55	62	60	—[c]

[a] Experimental result for top site on Pt(111): 115±15 kJ/mol; Refs. [485-487].

[b] $U_{2\pi^*}$ parameter for the Umol(CO 2π*) correction in eV.

[c] Relaxation converges to CO adsorption complex at adjacent hollow-site.

When comparing the PBE+Umol results with those from the uncorrected PBE functional the Umol(CO 2π*) correction is found to generally reduce the E_{ads} values. This is to be expected as the DFT+U energy correction in the fully localized limit, Eqs. 2.4.6 and 2.4.10, is a strictly positive function of the occupation matrix elements $n_{mu\sigma}$. The same holds for the DFT+Umol reformulation in terms of projectors, Eq. 3.2.4. Thus, the Umol(CO 2π*) correction either directly destabilizes the $Pt_m(CO)_8$ adsorption complexes or leads to destabilizing changes in their electronic structure (see Section 4.2).

However, this destabilization is different for the individual types of adsorption sites. When going from PBE to PBE+Umol with $U_{2\pi^*} = 1.0$ eV the E_{ads} value at the 1t site of the Pt_{79} cluster is reduced by 37 kJ/mol while the corresponding adsorption energy at 2f is decreased by 48 kJ/mol down to 120 kJ/mol. With $E_{ads} = 119$ kJ/mol the 1t site is almost degenerate to 2f in this case and becomes preferred at higher values of the parameter $U_{2\pi^*}$. For $U_{2\pi^*} = 1.5$ and 2.0 eV the adsorption energy at the 1t site of Pt_{79} is reduced to 101 and 83 kJ/mol, respectively, while the corresponding E_{ads} values at the 2f site amount to 97 and 73 kJ/mol. The effect of the Umol(CO 2π*) correction on the adsorption energies of the 3b site on Pt_{79} is

only slightly weaker than for the 2f site as E_{ads} is reduced by 44 kJ/mol when going from PBE to PBE+Umol with $U_{2\pi^*} = 1.0$ eV. However, the effect of the Umol(CO 2π*) term is not strong enough to overcome the influence of the adjacent facet border, so that the 3b site remains favored on Pt_{79} even at $U_{2\pi^*} = 2.0$ eV.

On the larger cluster models the changes in the E_{ads} values induced by the Umol(CO 2π*) correction are remarkably similar to those observed for the corresponding top, hollow, and bridge adsorption sites on Pt_{79}, respectively. Compared to the results from the uncorrected PBE method, the Umol(CO 2π*) term (with $U_{2\pi^*} = 1.0$ eV) again reduces the CO adsorption energies; by ~37 kJ/mol at top sites, ~48 kJ/mol at hollow-type sites, and ~48 kJ/mol at bridge sites. Only in the case of the 1t site on Pt_{140} the E_{ads} value decreases by 42 kJ/mol, down to 110 kJ/mol, when going from PBE to PBE+Umol(CO 2π*) with $U_{2\pi^*} = 1.0$ eV. However, as the uncorrected PBE functional yields a comparatively small site preference of only 5 kJ/mol for 2f over 1t on Pt_{140}, both sites are also degenerate at $U_{2\pi^*} = 1.0$ eV. At $U_{2\pi^*} = 2.0$ eV the 1t site on Pt_{140} is preferred by 12 kJ/mol over the adjacent 2f site. For $U_{2\pi^*} = 1.0$ eV, the adsorption energies at the three remaining sites on the (111) facet of Pt_{140} are 102 kJ/mol at 3b, 104 kJ/mol at 4h, and 99 kJ/mol at 5t. At $U_{2\pi^*} = 1.5$ eV all three sites are nearly degenerate with $E_{ads} \approx 80$ kJ/mol, while at $U_{2\pi^*} = 2.0$ eV the expected ordering 5t > 4h > 3b is reached (see Table 4.4.3).

Like on the Pt_{79} and Pt_{140} models, the 1t and 2f sites on the Pt_{225} cluster are found almost isoenergetic ($E_{ads} \approx 113$ kJ/mol) at $U_{2\pi^*} = 1.0$ eV. The DFT+Umol method renders 3b the least preferred site on the Pt_{225} cluster. While the shallow energetic minimum of the 7b site has already been noticed with PBE, no minimum was found at this site with the PBE+Umol combination. When comparing the pair 5t/6f at the center of the (111) facet of Pt_{225}, the Umol(CO 2π*) correction is found to reduce the initial preference for the fcc-hollow site of 20 kJ/mol to 10 kJ/mol at $U_{2\pi^*} = 1.0$ eV. The corresponding adsorption energies amount to 97 kJ/mol and 107 kJ/mol for 5t and 6f, respectively. When increasing the value of the $U_{2\pi^*}$ parameter to 1.5 eV the site preference is further reduced to 4 kJ/mol. Finally, at $U_{2\pi^*} = 2.0$ eV the 5t site becomes preferred over 6f.

Thus, the PBE+Umol method is able to correct the site preference on the employed cluster model of the Pt(111) surface. However, while these results certainly represent an improvement from a qualitative point of view, the corresponding CO adsorption energy of 62 kJ/mol computed at the 5t site with $U_{2\pi^*} = 2.0$ eV considerably underestimates the experimental reference for the E_{ads} value of 115±15 kJ/mol.[485-487]

The adsorption energy obtained at the 5t site of Pt_{255} is also lower than the E_{ads} value reported in an earlier application of the DFT+U method[499] to the CO 2π* fragment molecular orbitals in a plane-wave study of CO/Pt(111). However, the fcc-hollow site preference obtained with the uncorrected PBE functional in these plane-wave calculations is already lower than in the present case (only ~12 kJ/mol compared to 20 kJ/mol here).[499] The

lower preference for the fcc-hollow site obtained in such plane-wave calculations likely results from the details of the employed representation of the core electrons, hence the atomic parameters employed in the projector-augmented wave (PAW) approach.[499] Indeed, the difference in the CO adsorption energies obtained at fcc-hollow and top sites was found to be quite sensitive to certain PAW parameters like the PAW cutoff-radius.[499] Furthermore, the aforementioned better agreement of the plane-wave results with the experimental reference was based on PAW parameter values that strongly reduce the preference of the PBE functional for the fcc-hollow site.[499] Thus, the better quantitative agreement of the plane-wave E_{ads} results is likely an indirect consequence of the parametrization of the approximate treatment of the core electrons of Pt. Second, the CO adsorption energies obtained with PBE plane-wave calculations are already notably higher than the present PBE estimates for E_{ads}. Thus, the better quantitative agreement of the aforementioned top-site adsorption energy from the DFT+U plane-wave calculation at least partially seems to result from a favorable error compensation.

4.4.5. Electronic Structure Aspects

The subsequent section analyzes the electronic structure descriptions provided by PBE, TPSS, TPSSh, and PBE0 on the example of the CO molecule in the gas phase, the bare Pt_{79} cluster, and its adsorption complexes formed with CO at the sites 1t and 2f. Furthermore, the effect of the Umol(CO 2π*) term on the electronic structure of the aforementioned adsorption complexes is examined as well.

On the case of the bare CO molecule one always obtains the expected energetic ordering of the orbitals $4\sigma^* < 1\pi < 5\sigma < 2\pi^*$.[520] The energies of the occupied orbitals 4σ*, 1π, and 5σ are successively lowered when going from TPSS to TPSSh and to PBE0, while the 2π* LUMO is shifted up in energy. As expected, the increasing EXX mixing factor in these three functionals yields a widened HOMO-LUMO gap (HLG) $\Delta\varepsilon_{HLG}$, which amounts to 7.4, 8.6, and 10.1 eV for TPSS, TPSSh, and PBE0, respectively.

Figure 4.4.6 provides the projected densities of states (PDOS) which were obtained on the basis of Mulliken population numbers[419] with TPSS, TPSSh, PBE0, PBE, and PBE+Umol(CO 2π*) with $U_{2\pi^*} = 2.0$ eV for the Pt_{79} cluster and the 1t and 2f $Pt_{79}(CO)_8$ adsorption complexes, respectively. To this end, the density of states was projected onto the 6*s* and 5*d* of the three Pt atoms at the center of the (111) facet of Pt_{79} (see Figure 4.4.4) as well as onto the 2*s* and 2*p* orbitals of the C and O atoms.

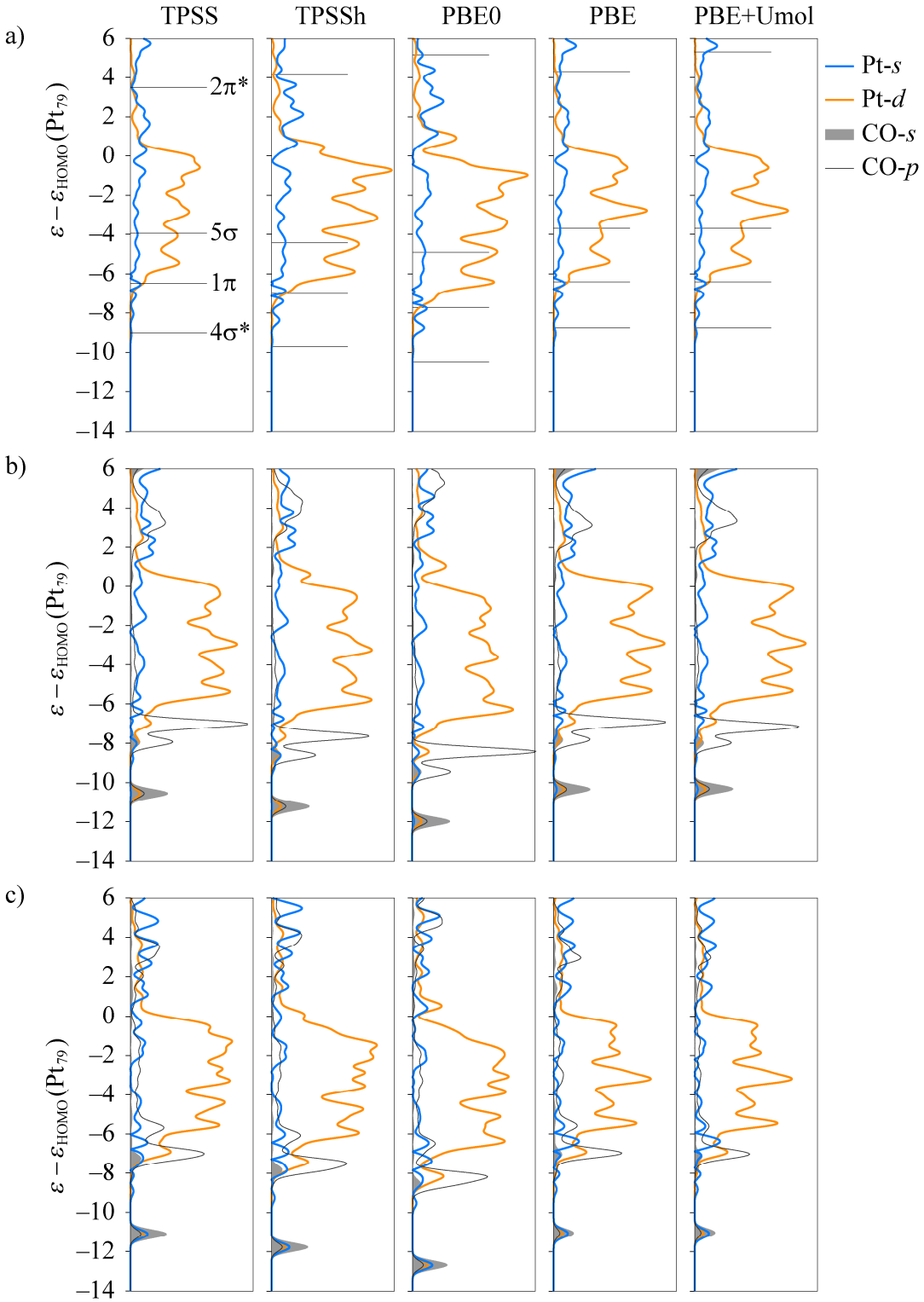

Figure 4.4.6: Projected density of states (arbitrary units, Mulliken population numbers, 0.3 eV orbital energy broadening) from TPSS, TPSSh, PBE0, PBE, and PBE+Umol(CO 2π*) of a) Pt_{79} (and free CO), and $Pt_{79}(CO)_8$ at b) 1t and c) 2f: *s* (blue lines) and *d* orbitals (orange lines) of Pt surface atoms in the center of the (111) facet; *s* (grey areas) and *p* orbitals (black lines) of C and O atoms. For comparison the orbital energies of free CO are marked in a). Vertical axis in eV.

The TPSS functional describes the Pt_{79} cluster and both adsorption complexes as essentially metallic, hence yields $\Delta\varepsilon_{HLG} \approx 0.0$. In contrast, the hybrid DFT methods TPSSh and PBE0 yield $\Delta\varepsilon_{HLG} = 0.2$ and 0.5 eV for Pt_{79}, respectively, which is also notable in Figure 4.4.6 by the increasingly large dent at the upper edge of the Pt *d*-PDOS (with increasing amount of EXX). Likewise, the Pt *s*-PDOS splits into two parts by the increased HLG as well. TPSSh and PBE0 yield slightly increased $\Delta\varepsilon_{HLG}$ values for the 2f adsorption complex compared to the bare Pt_{79} cluster (0.3 and 0.6 eV, respectively) as adsorbates may reduce the metallic properties of finite clusters further.[521] Furthermore, the corresponding HOMO-levels are found somewhat lower in energy. In contrast, slightly decreased $\Delta\varepsilon_{HLG}$ values and upshifted HOMO levels result for the 1t adsorption complex with PBE and TPSSh. These latter findings are rationalized by the net increase of negative charge at the adsorption site due to the σ-bonding which prevails at top sites. The increased electronic charge raises the electrostatic potential which in turn reduces the HOMO-LUMO gap. This is supported by the Mulliken populations[419] obtained for the three Pt surface-atoms in the center of the (111) facet of Pt_{79}. Upon adsorption of the CO molecule at the 1t site the population is increased by 1.2 *e*, while the corresponding increase at 2f amounts to ~0.3 *e* only. In agreement with recent plane-wave studies on slab-models,[479,522] one notices the increased width of the Pt 5*d* manifold when going from TPSS over TPSSh to PBE0.

The DOS projections on the *p* orbitals of the C and O atoms exhibit two distinct peaks near the lower edge of the Pt *d*-band. Out of these, the lower lying corresponds to the CO 5σ-derived orbitals as it always coincides with a peak in the PDOS of the *s*-orbitals of the C and O atoms. Thus, the higher of these two peaks corresponds to the CO 1π orbitals. Note, that upon adsorption of the CO molecule the 5σ orbital is shifted below the 1π levels, which agrees with spectroscopic results and other theoretical studies.[483,500,523,524]

The 5σ orbital of the CO molecule in the gas-phase always coincides with a local maximum of the *d*-band of the bare Pt_{79} cluster (see Figure 4.4.6, panel a). The same holds for the 5σ peak in the PDOS of both $Pt_{79}(CO)_8$ systems. However, in the 1t adsorption complex the corresponding peak in the Pt *d*-PDOS is well-separated from the rest of the *d*-manifold, while it is still part of the main *d*-band extension when CO adsorbs on the 2f site. Furthermore, a significantly stronger Pt *s*-PDOS maximum can be found at the 5σ peak in the case of the 2f adsorption complex. This indicates a mixing at this site between *sd*-hybridized Pt levels and the CO 5σ orbital. With increasing amount of EXX the resulting σ-*sd* levels are moved towards more negative energies. The downshift of these σ-*sd* levels with increasing EXX mixing factor is stronger than the corresponding downshift of the HOMO-levels, which indicates that the EXX term increases the σ-bonding interaction at the 2f site.

The energetically lowest peak in each of the PDOS spectra obtained with the various methods corresponds to the CO 4σ∗ orbital. The presence of peaks in the Pt *s*- and *d*-PDOS of the 2f adsorption complex indicates that the CO 4σ∗ orbital also contributes to the σ-*sd*

interaction. Indeed, such a participation of the 4σ∗ orbital has previously been noticed in theoretical and experimental studies of the CO adsorption on Ni and Cu surfaces.[489,490] While both, the Pt *s*- and *d*-manifolds, seem to interact with the 4σ∗ orbital at the 2f site, the PDOS spectra of the 1t adsorption complex only show an interaction with the Pt *d*-levels.

In the 1t adsorption complex the CO 1π orbitals always form a rather distinct peak in the PDOS spectra obtained from the various methods. This is different when the CO molecule adsorbs at the 2f site of Pt_{79}. In this latter case all examined methods yield a broader 1π peak in the PDOS which always coincides with a local maximum of the Pt *s*-PDOS at –5.8, –6.0, and –6.3 eV for TPSS, TPSSh, and PBE0, respectively. Both of these observations indicate a mixing of the 1π orbitals at the 2f site. Indeed, due to the presence of the Pt-moiety linear combinations between the 1π and 2π* orbitals become feasible. As in the case of the 4σ∗ orbital, such a contribution of the 1π levels to the back-bonding interaction has already been reported in earlier theoretical and experimental studies.[483,489,490] The EXX term appears to broaden the 1π peak slightly more and to increase the corresponding local Pt *s*-PDOS maximum. Thus, the EXX term seems to affect also the contribution of the 1π orbitals to the back-bonding.

From the C and O *p*-DOS projections the CO 2π* derived orbitals are identified as broadened peak which extends from 2 eV to 5 eV in the case of PBE and is, as expected, shifted upward in energy when going over TPSSh to PBE0. The Umol(CO 2π*) correction has a similar effect. Indeed the 2π* peak in the *p*-PDOS of the C and O atoms appears upshifted by a comparable amount as the energies of the 2π* orbitals in the gas-phase CO molecule. Apart from that, the PDOS spectra obtained from the PBE+Umol(CO 2π*) combination are remarkably similar to those from the uncorrected PBE functional. This indicates that the Umol(CO 2π*) term acts on the 2π* level of the $Pt_{79}(CO)_8$ adsorption complex only and has no notable effect on the remaining electronic structure of the system. This effect clearly differs from the influence of the Umol(CO 2π*) correction on the Ni 3*d* orbitals of the nickel carbonyls studied in Section 4.2.

In the following the effect of the Umol(CO 2π*) term shall be examined further. To this end, the elements of the occupation matrices $\mathbf{n}_I^\sigma$ are studied (see Section 2.4). As described in Section 3.2.2, the DFT+Umol implementation in PARAGAUSS completely bypasses calculation of occupation matrices $\mathbf{n}_I^\sigma$.[286] Yet, under the assumption that the CO adsorbates are sufficiently separated, the 2×2 occupation matrix block corresponding to the 2π* orbitals of a single CO fragment can still be computed as $\mathbf{n}^\sigma = \mathbf{vSP}^\sigma\mathbf{Sv}^\dagger$ from the fragment MO coefficients $\mathbf{v}$. In the present case these matrix blocks are always found diagonal due to the orientation of the CO fragment in the $Pt_{79}(CO)_8$ adsorption complexes. In any case only the diagonal elements $n_{tt\sigma}$ need to be discussed as the occupation matrices can always be diagonalized. Figure 4.4.7 shows a plot of the individual contributions to the DFT+U penalty function in the fully localized limit for the employed values of $U_{2\pi^*}$ as a function of the

individual diagonal elements of the occupation matrix block. The two $n_{tt\sigma}$ values obtained for the CO molecule adsorbed on each of the sites 1t, 2f, and 3b and for the employed $U_{2\pi^*}$ parameter values, respectively, are marked on the corresponding parabolic DFT+Umol penalty functions (which result for each value of $U_{2\pi^*}$, see Section 2.4),

$$E^{\mathrm{U}} = \tfrac{1}{2}\sum_{I\sigma} U_I \sum_{t,u\in I}\left(n_{tt\sigma} - n_{tu\sigma}n_{ut\sigma}\right). \qquad 4.4.4$$

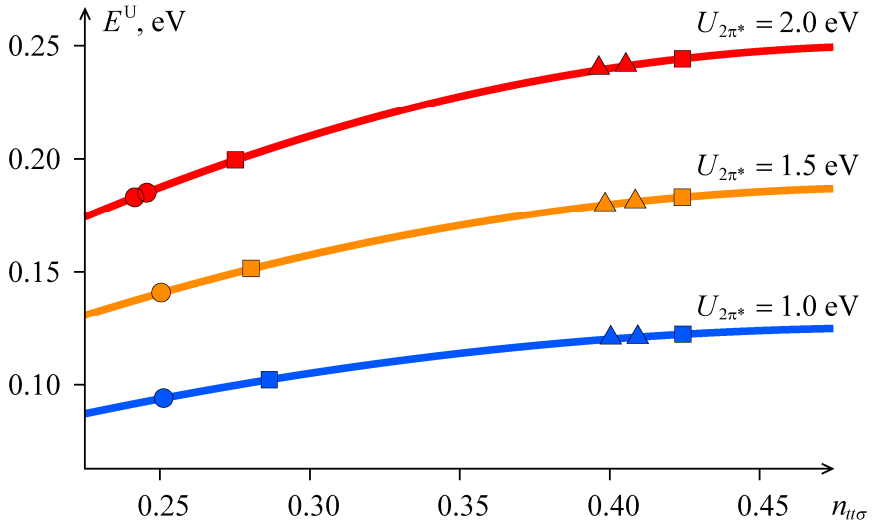

Figure 4.4.7: FLL penalty function E^{U} in eV in terms of the diagonal elements of the occupation matrices $\mathbf{n}_I^\sigma$ evaluated for the 2π* orbitals of the CO molecule at the 1t (circles), 2f (triangles), and 3b (squares) sites for the values 1.0, 1.5, and 2.0 eV of the parameter $U_{2\pi^*}$. Figure adapted from Ref. [286].

As back-bonding is less dominant at top sites, the 1t adsorption complex always features the lowest occupation numbers. The corresponding $n_{tt\sigma}$ values range from 0.255 for $U_{2\pi^*} = 1.0$ eV and 0.242 for $U_{2\pi^*} = 2.0$ eV and are nearly identical due to the approximatively C_{3v}-symmetric local environment of the 1t site. The same holds for the occupation matrix elements obtained at the 2f site, which are, however, found between 0.397 and 0.410, thus significantly larger than the $n_{tt\sigma}$ values at 1t. These larger $n_{tt\sigma}$ values can be expected due to the larger amount of back-bonding interaction at hollow-type sites.[489,490] The local environment of the 3b site exhibits only an approximate C_{2v} symmetry which leads to two very distinct $n_{tt\sigma}$ values. The lower one ranges from 0.276 to 0.287 and thus is only slightly higher than the $n_{tt\sigma}$ values obtained for the 1t adsorption complex. In contrast, the larger $n_{tt\sigma}$ value amounts to 0.425 and is close to the corresponding values at the 2f site. In this context the situation at the bridge site can be considered as intermediate between top and hollow sites as back-bonding is dominant for one of the two CO 2π* orbitals while the other one behaves more like the 2π* orbitals of a CO fragment adsorbed at a top site.

The most important observation that can be made from Figure 4.4.7 is the fact that the specific $n_{tt\sigma}$ values hardly change with increasing value of the parameter $U_{2\pi^*}$. Only the smaller occupation matrix elements, obtained at the 1t site and for one of the 2π* orbitals at the 3b adsorption complex, seem to be slightly more affected. This is most likely a consequence of the larger derivative of the parabolic penalty function at smaller $n_{tt\sigma}$ values which is proportional to the DFT+Umol potential. As the $n_{tt\sigma}$ values remain essentially unaffected by the value of the $U_{2\pi^*}$ parameter, the Umol(CO 2π*) correction appears to have only a very limited effect on the electronic structure. This also agrees with its very localized influence on the PDOS in Figure 4.4.6. Thus, in the case of the examined $Pt_n(CO)_8$ models, the Umol(CO 2π*) term purely acts as a energetic correction. The top-site adsorption preference obtained with the PBE+Umol(CO 2π*) combination is therefore a direct consequence of the larger $n_{tt\sigma}$ values which result in the corresponding adsorption complexes. The finding, that the electronic structure of the $Pt_n(CO)_8$ models does not relax upon application of the Umol(CO 2π*) correction, also rationalizes the significant destabilization of the adsorption complexes caused by this term and the resulting low CO adsorption energies.

4.4.6. Conclusions

The adsorption of the CO molecule was studied on various top, bridge, fcc- and hcp-hollow sites of the (111) facets of the model clusters Pt_{79}, Pt_{140}, and Pt_{225}. First, the behavior of the adsorption energy at these sites was examined on the basis of the corresponding results obtained with the PBE method. Thereby the average coordination number CN_{av} of the cluster surface-atoms associated with the individual adsorption sites was employed to examine the influence of the facet borders on the individual adsorption energies. This analysis revealed that the sites 1t and 2f sites on the Pt_{79} cluster are significantly, but comparably affected by the facet borders. Thus, these two sites qualify for the qualitative assessment of the functionals PBE, PBE0, TPSS, TPSSh, M06L, and M06 regarding the relative top- vs. hollow-site preference. Finally, the sites 5t and 6f on the much larger Pt_{225} model can be considered as reliable qualitative and quantitative models for the CO adsorption on the extended Pt(111) surface.

However, neither one of the semi-local approximations PBE, TPSS, and M06L nor any of the assessed hybrid DFT methods PBE0, TPSSh, and M06 are able to provide the experimentally characterized top-site preference. This finding is well in line with the results from corresponding plane-wave studies on slab-models for the extended Pt(111) surface.[479,483,484]

The rationalization that self-interaction effects prevent semi-local functionals from predicting the correct site preference is widely accepted.[479,483,484,499,500] On the other hand, the origin of the failure of hybrid DFT methods for the CO puzzle has been less well explored in the past.[479,483] Indeed, the failure of hybrid functionals to describe properly the site preference for CO on Pt(111) was rationalized in a rather unspecific way by the increased broadening of the Pt 5*d*-manifold. While this latter effect is confirmed in the plots of the projected density of states in Figure 4.4.6, the conclusions that can be made from the results of the present study may provide a more detailed picture of the artifacts introduced by the EXX term in the description of adsorption complexes.

As expected, hybrid DFT methods yield less elongated C-O bonds in the $Pt_{79}(CO)_8$ adsorption complexes, which suggests that back-bonding is reduced by the EXX term. Furthermore, the reduction is slightly more pronounced at fcc-hollow sites as back-bonding is more dominant there. From this reduction of the back-bonding interaction one might expect lower adsorption energies. However, in agreement with the results from plane-wave studies of slab-models for the Pt(111) surface,[479,483] the hybrid DFT methods were always found to increase the E_{ads} values compared to the results of the corresponding semi-local functionals. These findings represent a strong indication for the EXX term to increase the σ-bonding while reducing the back-bonding interaction at the same time. Furthermore, the increase of the σ-bonding should be higher at fcc-hollow sites as the preference for these sites is even slightly enhanced by the EXX term.

The analysis of the projected DOS plots confirms this assumption. In agreement with earlier plane-wave studies,[479,483] the Pt-*d* band is found to be overly broadened by the EXX term. Furthermore, the levels at the fcc-hollow sites are always somewhat downshifted compared to those at top sites. This downshift is rationalized by the reduced electrostatic potential due to the charge redistribution via the back-bonding. In combination with the broadened Pt-*d* band, this brings the PDOS peak of the CO 5σ-derived levels inside the Pt-*d* band at fcc-hollow sites. In consequence, an increased mixing of these levels with the Pt-*d* band, hence σ-bonding, becomes feasible at fcc-hollow sites. Thus, the EXX term reduces back-bonding at hollow-sites while simultaneously increasing the amount of σ-bonding there. This conclusion provides a more precise picture about how the improved hybrid DFT description of CO 2π* orbitals is abrogated by the deteriorated description of the metallic moiety delivered by such methods.

The application of a DFT+Umol correction to the CO 2π* orbitals is found to restore the experimentally determined top-site preference for the adsorption of the CO molecule on the employed cluster models of the extended Pt(111) surface. At the sites on the Pt_{225} cluster which were previously determined as the best models for the CO adsorption at the top and fcc-hollow sites on the extended surface, this top-site preference is reached at DFT+U parameter values of $U_{2\pi^*} \approx 2.0$ eV. However, at these $U_{2\pi^*}$ values the experimental reference

for E_{ads} is considerably underestimated. The PDOS plots and the DFT+Umol occupation numbers show that this qualitative inaccuracy derives from the fact that the DFT+Umol terms essentially acts as a destabilizing energy term which does not induce any relaxation in the electronic structure of the $Pt_m(CO)_8$ adsorption complexes.

5. Summary

The present thesis addresses self-interaction and delocalization artifacts in semi-local approximations to Kohn–Sham density functional theory (DFT) as well as the closely related static correlation error in hybrid DFT methods. In this context also the methodological and implementation aspects of hybrid density functionals and the DFT+Umol method are discussed, which represent different approaches for correcting self-interaction and delocalization errors. Both method variants have been implemented in the DFT program PARAGAUSS as part of this thesis. Furthermore, these methods are applied in several case studies to examine their performance for systems which are known to be strongly affected by the aforementioned errors.

Hybrid DFT methods add a nonlocal exact-exchange (EXX) term to semi-local DFT approximations. The EXX term in turn is computed from four-center electron-repulsion integrals (ERI). As the number of ERIs scales with the fourth-order with respect to the number of basis functions, the computation of the EXX term is very demanding. Thus, the evaluation of ERIs has to be implemented by using an efficient algorithm as well as by taking into account the structure of modern computer architectures. Most ERI algorithms are based on the Boys function which represents a starting point for the ERI implementation made in the context of this thesis. The Boys function and its derivatives are expanded to the final integrals. Most ERI algorithms employ recursion relations for this expansion. A variant of the McMurchie–Davidson expansion has been implemented for this task, which employs so-called horizontal recursion relations to reduce the amount of intermediate quantities. In the case of strongly contracted Gaussian-type orbitals, early contraction strategies may allow for a more efficient expansion of the Boys function. While all of these aforementioned approaches become inefficient for basis functions of high angular momentum, Gauss-quadrature based ERI algorithms, which are formulated in terms of roots and weights of Rys polynomials instead of the Boys function, perform better in such cases. This holds especially on modern computer architectures which allow for very rapid computations, provided that the employed implementation features only a comparatively limited number of intermediates. Thus, an existing, highly optimized implementation of a Gauss-quadrature based algorithm was interfaced to the EXX calculation modules of PARAGAUSS as well and used in most hybrid DFT production calculations.

The final ERIs are contracted with the density matrix to the EXX matrix and the EXX energy term. Several measures need to be taken also at this stage to make hybrid DFT calculations on larger systems feasible. Such measures rely on accounting for the internal index symmetries of the tensor formed by all ERIs, as well as for spatial point group

symmetries. The EXX implementation carried out in this thesis takes into account both of these symmetries. Thereby the so-called petit-list approach is employed to omit all but one of the ERIs that are equivalent by point group symmetry. Integral screening approaches allow to reduce further the effort when calculating the EXX term. Thereby one skips the computation of ERIs that do not provide a numerically significant contribution to the EXX term. Integral screening approaches can lower the formal forth-order scaling of the computational requirements of the EXX term to a linear scaling in the limit of very large systems with a notable HOMO-LUMO gap. The most important ERI-screening approach, namely the density-weighted Schwarz screening ΔSCF method was implemented as part of this thesis for the EXX term. Similar symmetry and screening treatments are used also in the implementation of the gradients of the EXX term with respect to nuclear coordinates.

Finally, the application of hybrid DFT methods to larger systems requires an efficiently parallelized implementation. The parallel implementation done in this thesis is based on an existing dynamic load balancing (DLB) library which employs a work-stealing strategy to achieve an efficient parallelization. In this implementation, a special algorithm assigns groups of ERIs to the actual DLB tasks which are then dynamically allocated by the DLB library to the individual CPU cores. On the example of a large transition metal cluster with ligands, a parallel efficiency of ~93 % of the hybrid DFT SCF iteration was achieved for up to 2048 cores. Opposed to that, the parallelization of smaller unsymmetric systems still seems to suffer from the comparatively slow exchange of data between computing nodes.

The DFT+Umol method as developed and implemented as part of this thesis represents an extension of the conventional DFT+U method. Compared to hybrid DFT method, this approach provides a more efficient, very localized correction for self-interaction and delocalization errors. The DFT+Umol method is based on molecular fragment orbital occupation numbers of those orbitals which are targeted by the self-interaction correction. To avoid a complicated symmetrization of these fragment orbitals, the DFT+Umol energy and potential terms have been implemented in terms of projectors. The DFT+Umol gradients are computed largely with parts of an earlier implementation of the traditional DFT+U method.

Three case studies have been carried out as part of this thesis in which hybrid DFT functionals and/or the DFT+Umol method are applied. The first application examined the trend of the first metal-CO dissociation energies $E_{\mathrm{dis}}(m)$ of the nickel carbonyl complexes $\mathrm{Ni(CO)}_m$ with $m = 1-4$. From experimental and accurate post-HF results these dissociation energies are known to increase when going from $\mathrm{Ni(CO)}_4$ to $\mathrm{Ni(CO)}_2$ due to a reduced bonding competition. This trend is broken by $E_{\mathrm{dis}}(2) > E_{\mathrm{dis}}(1)$ as the electronic configuration of the nickel atom formally relaxes from the d^{10} configuration which appears in the nickel carbonyl complexes. The overall trend of the $E_{\mathrm{dis}}(m)$ values is predicted correctly by hybrid DFT methods, but not by semi-local functionals. This situation in turn suggests that the dissociation energies obtained with semi-local DFT approximations are affected by the self-

interaction error. To further examine these self-interaction artifacts, the DFT+Umol correction was projected onto the Ni 3*d* subshell as well as onto the CO 2π* orbitals. Several values of the DFT+Umol parameters U_{3d} and $U_{2\pi^*}$ were applied, which control the strength of both self-interaction corrections. In the case of the DFT+Umol correction applied to the Ni 3*d* orbitals one finds that the correct trend in the dissociation energies is restored already at U_{3d} values below 3.0 eV. Around the parameter value of 5.3 eV, which is commonly employed in the literature for this subshell, the DFT+Umol results agree well with CCSD(T) reference values. Surprisingly, the correction of the 2π* orbitals yields the correct trend in the $E_{\mathrm{dis}}(m)$ values as well, but only at a comparatively large value of $U_{2\pi^*} = 4.0$ eV. However, at this parameter value the $Ni(CO)_3$ and $Ni(CO)_4$ complexes become unphysically destabilized. A detailed analysis of the electronic structure reveals that the proper localization of the Ni 3*d* subshell is essential to achieve $E_{\mathrm{dis}}(2) > E_{\mathrm{dis}}(1)$. Semi-local DFT methods overly delocalize these orbitals within the carbonyl complexes, which lowers the energy of these systems with respect to the nickel atom and yields the incorrect trend. The DFT+Umol correction of the Ni 3*d* subshell directly localizes these orbitals. Also the DFT+Umol correction of the CO 2π* orbitals can achieve the same effect by essentially removing the back-bonding interaction, which leads to the aforementioned destabilization of $Ni(CO)_3$ and $Ni(CO)_4$.

The second study addressed the description of transition metals provided by hybrid DFT methods. To this end, the newly implemented hybrid functionals PBE0, TPSSh, and M06 were compared with their semi-local counterparts PBE, TPSS, and M06L for their performance in a cluster scaling study of the cluster models Ni_m, Pd_m, and Pt_m (m = 13, 38, 55, 79, 116). The extrapolations of average nearest-neighbor distances, cohesive energies, as well as vertical ionization energies and electron affinities to their respective bulk limits allow a comparison with experimental references for the bulk systems. While PBE0 and M06 often exhibit a quite erratic behavior, the hybrid DFT method TPSSh provided surprisingly accurate results for most of these quantities. Inspection of the number of orbitals around the HOMO-LUMO gap showed that TPSSh yields significantly large values for the examined clusters. A large number of orbitals around the HOMO-LUMO gap is a prerequisite for mimicking static correlation effects by a level broadening technique.

Finally, CO adsorption on the (111) facets of the cluster models Pt_{79}, Pt_{140}, and Pt_{225} was studied with the aforementioned hybrid and semi-local functionals as well as with the DFT+Umol correction of the CO 2π* orbitals. In the case of the extended Pt(111) surface semi-local functionals are known to predict the fcc-hollow site to be preferred for the adsorption of the CO molecule as opposed to the experimentally determined top-site preference. Furthermore, the corresponding CO adsorption energies are significantly overestimated. This failure of semi-local DFT methods, known as the “CO puzzle”, originates from the self-interaction error which cases a too low energy of the CO 2π* orbitals. Thus, the correct description of the CO adsorption on Pt(111) requires an electronic structure

description which is nearly free of self-interaction while simultaneously accounting for static correlation effects in the metal moiety. As expected, the examined semi-local functionals predict CO adsorption on the fcc-hollow site as preferred for the employed cluster models. Furthermore, the three applied hybrid DFT methods yield a top-site preference while overestimating the CO adsorption energy even slightly more. However, the smaller elongation of the C-O bond in the adsorbed CO fragments indicates, as expected, that back-bonding is reduced by the EXX term in hybrid functionals. As hybrid functionals yield higher adsorption energies, the reduced amount of back-bonding has to be compensated by an enhanced σ-bonding interaction. The analysis of the projected densities of states supports this conclusion. The EXX term increases σ-bonding more at fcc-hollow sites due to a combination of the overly broadened Pt *d*-band and the energetic lowering of all levels at this site caused by the electrostatic effect of the remaining back-bonding charge transfer. On the other hand, the DFT+Umol projection onto the CO $2\pi^*$ orbitals restores the correct top-site preference on the examined model clusters at a moderately large value of $U_{2\pi^*} \approx 2.0$ eV. However, the corresponding CO adsorption energies obtained in this case are found to underestimate the experimental reference value. Inspection of the projected density of states as well as of the DFT+Umol orbital occupation matrix elements reveals that the DFT+Umol correction affects only the energy of the $2\pi^*$ orbitals, while the residual electronic structure of the $Pt_m(CO)_8$ systems remains essentially unchanged. Thus, the DFT+Umol term purely acts as energetic penalty function as opposed to its behavior found in the nickel carbonyls.

The case studies made in this thesis provided new insight and rationalizations about the behavior of self-interaction, delocalization, and static correlation errors in several types of systems. However, the results of these studies also illustrated the limitations of the employed methods. While the TPSSh hybrid functional can certainly be suggested for the study of transition metal compounds, it fails to describe the adsorption of the CO molecule on Pt surfaces. For this problem, local hybrid functionals which can adapt the amount of exact-exchange to the local electronic situation or novel DFT approximations that feature explicit static correlation terms may provide a better accuracy. The DFT+Umol method represents an efficient method which provided qualitatively correct answers in the applications studied in this thesis. This approach may be refined further, especially with regard to a non-empirical determination of its parameters and by introducing variants that allow for a better reorganization of the electronic structure.

The implementation work made in the context of this thesis can be refined as well. The parallelization of the EXX term (and other parts of PARAGAUSS) may be improved by a distributed memory strategy. Its serial efficiency should be increased by more advanced screening strategies, a semi-direct SCF approach in which the computationally most expensive ERI batches are stored in memory instead of being recalculated as well as by a cache-efficient implementation of modern ERI algorithms.

References

1. McWeeny, R. *Methods of Molecular Quantum Mechanics*. second edition; Academic Press: London, **1989**.
2. Szabo, A.; Ostlund, N.S. *Modern Quantum Chemistry: Introduction to Advanced Electronic Structure Theory*. revised edition; McGraw-Hill: New York, **1989**.
3. Yarkony, D.R. *Modern Electronic Structure Theory*. World Scientific: Singapore, **1995**.
4. Helgaker, T.; Jørgensen, P.; Olsen, J. *Molecular Electronic-Structure Theory*. Wiley: Chichester, **2000**.
5. Martin, R.M. *Electronic Structure. Basic Theory and Practical Methods*. Cambridge University Press: Cambridge, **2004**.
6. Jensen, F. *Introduction to Computational Chemistry*. Wiley: Chichester, **2007**.
7. Piela, L. *Ideas of Quantum Chemistry*. second edition; Elsevier: Amsterdam, **2013**.
8. Cramer, C.J. *Essentials of Computational Chemistry. Theories and Models*. second edition; Wiley: Chichester, **2004**.
9. Heine, T.; Joswig, J.O.; Gelessus, A. *Computational Chemistry Workbook*. Wiley-VCH: Weinheim, **2009**.
10. Lewars, E.G. *Computational Chemistry: Introduction to the Theory and Applications of Molecular and Quantum Mechanics*. second edition; Springer: Dordrecht, **2011**.
11. Schrödinger, E. An Undulatory Theory of the Mechanics of Atoms and Molecules. *Phys. Rev.* **1926**, *28*, 1049-1070.
12. Burrau, Ø. Berechnung des Energiewertes des Wasserstoffmolekel-Ions (H_2^+) im Normalzustand. *Naturwissenschaften* **1927**, *15*, 16-17.
13. Levine, I.N. *Quantum Chemistry, 7th editiion*. Prentice Hall: Upper Saddle River, **2013**.
14. Hartree, D.R. The Wave Mechanics of an Atom with a Non-Coulomb Central Field. Part I. Theory and Methods. *Proc. Camb. Phil. Soc.* **1928**, *24*, 89-312.
15. Hartree, D.R. The Wave Mechanics of an Atom with a Non-Coulomb Central Field. Part II. Some Results and Discussion. *Proc. Cambridge Phil. Soc.* **1928**, *24*, 111-132.
16. Fock, V. Näherungsmethode zur Lösung des quantenmechanischen Mehrkörperproblems. *Z. Phys.* **1930**, *61*, 126-148.
17. Hylleraas, E.A. Über den Grundzustand des Heliumatoms. *Z. Phys.* **1928**, *48*, 469-494.
18. Parr, R.G.; Craig, D.P.; Roos, I.G. Molecular Orbital Calculations of the Lower Excited Electronic Levels of Benzene, Configuration Interaction Included. *J. Chem. Phys.* **1950**, *18*, 1561-1563.
19. Boys, S.F. Electronic Wave Functions. IX. Calculations for the Three Lowest States of the Beryllium Atom. *Proc. R. Soc.* **1953**, *A217*, 136-150.
20. Boys, S.F. Electronic Wave Functions. X. A Calculation of Eight Variational Poly-Detor Wave Functions for Boron and Carbon. *Proc. R. Soc.* **1953**, *A217*, 235-251.
21. Møller, C.; Plesset, M.S. Note on an Approximation Treatment for Many-Electron Systems. *Phys. Rev.* **1934**, *46*, 618-622.
22. Paldus, J.; Čížek, J.; Shavitt, I. Correlation Problems in Atomic and Molecular Systems. IV. Extended Coupled-Pair Many-Electron Theory and Its Application to the BH_3 Molecule. *Phys. Rev. A* **1972**, *5*, 50-67.
23. Purvis, G.D.; Bartlett, R.J. A Full Coupled-Cluster Singles and Doubles Model: The Inclusion of Disconnected Triples. *J. Chem. Phys.* **1982**, *76*, 1910-1918.
24. Pople, J.A.; Head-Gordon, M.; Raghavachari, K. Quadratic Configuration Interaction. A General Technique for Determining Electron Correlation Energies. *J. Chem. Phys.* **1987**, *87*, 5968-5975.
25. Sherrill, C.D.; Schaefer III, H.F. In *Advances in Quantum Chemistry*, Löwdin, P.-O.; Sabin, J.R.; Zerner, M.C.; Brändas, E., Eds. Academic Press: San Diego, **1999**; Vol. 34.
26. Shavitt, I.; Bartlett, R.J. *Many-Body Methods in Chemistry and Physics*. Cambridge University Press: Cambridge, **2009**.
27. Hohenberg, P.; Kohn, W. Inhomogeneous Electron Gas. *Phys. Rev.* **1964**, *136*, B864-B871.
28. Kohn, W.; Sham, L.J. Self-Consistent Equations Including Exchange and Correlation Effects. *Phys. Rev.* **1965**, *140*, A1133-A1138.
29. Yang, W.; Parr, R.G. *Density-Functional Theory of Atoms and Molecules*. Oxford University Press: Oxford, **1989**.
30. Joubert, D. *Density Functionals: Theory and Applications*. Springer: Berlin, **1998**.
31. Koch, W.; Holthausen, M.C. *A Chemist's Guide to Density Functional Theory*. second edition; VCH: Weinheim, **2001**.
32. Eschrig, H. *The Fundamentals of Density Functional Theory*. second edition; Edition am Gutenbergplatz: Leibzig, **2003**.
33. Fiolhais, C.; Nogueira, F.; Marques, M.A.L. *A Primer in Density Functional Theory*. Springer: Berlin, **2003**.
34. Ziegler, T. Approximate Density Functional Theory as a Practical Tool in Molecular Energetics and Dynamics. *Chem. Rev.* **1991**, *91*, 651-667.

35. Whitten, J.L. Coulombic Potential Energy Integrals and Approximations *J. Chem. Phys.* **1973**, *58*, 4496-4501.
36. Baerends, E.J.; Ellis, D.E.; Ros, P. Self-Consistent Molecular Hartree-Fock-Slater Calculations I. The Computational Procedure. *Chem. Phys.* **1973**, *2*, 41-51.
37. Dunlap, B.I.; Connolly, J.W.D.; Sabin, J.R. On the Applicability of LCAO-Xα Methods to Molecules Containing Transition Metal Atoms: The Nickel Atom and Nickel Hydride. *Int. J. Quantum Chem.* **1977**, *12*, 81-87.
38. Dunlap, B.I.; Connolly, J.W.D.; Sabin, J.R. On Some Approximations in Applications of Xα Theory. *J. Chem. Phys.* **1979**, *71*, 3396-3402.
39. Dunlap, B.I.; Rösch, N. The Gaussian-Type Orbitals Density-Functional Approach to Finite Systems. *Adv. Quantum Chem.* **1990**, *21*, 317-339.
40. Vahtras, O.; Almlöf, J.; Feyereisen, M.W. Integral Approximations for LCAO-SCF Calculations. *Chem. Phys. Lett.* **1993**, *213*, 514-518.
41. Skylaris, C.-K.; Gagliardi, L.; Handy, N.C.; Ioannou, A.G.; Spencer, S.; Willetts, A. On the Resolution of Identity Coulomb Energy Approximation in Density Functional Theory. *J. Mol. Struct. Theochem* **2000**, *501*, 229-239.
42. Domínguez-Soria, V.D.; Geudtner, G.; Morales, J.L.; Calaminici, P.; Köster, A.M. Robust and Efficient Density Fitting. *J. Chem. Phys.* **2009**, *131*, 124102-9.
43. Dunlap, B.I.; Rösch, N.; Trickey, S.B. Variational Fitting Methods for Electronic Structure Calculations. *Mol. Phys.* **2010**, *108*, 3167-3180.
44. Ma, S.-K.; Brueckner, K.A. Correlation Energy of an Electron Gas with a Slowly Varying High Density. *Phys. Rev.* **1968**, *165*, 18-31.
45. Langreth, D.C.; Mehl, M.J. Beyond the Local-Density Approximation in Calculations of Ground-State Electronic Properties. *Phys. Rev. B* **1983**, *28*, 1809-1834.
46. Becke, A. Density-Functional Exchange-Energy Approximation with Correct Asymptotic Behavior. *Phys. Rev. A* **1988**, *38*, 3098-3100.
47. Lee, C.; Yang, W.; Parr, R.G. Development of the Colle-Salvetti Correlation-Energy Formula into a Functional of the Electron Density. *Phys. Rev. B* **1988**, *37*, 785-789.
48. Perdew, J.P. In *Electronic Structure of Solids '91*, Ziesche, P.; Eschrig, H., Eds. Akademie Verlag: Berlin, **1991**.
49. Perdew, J.P.; Burke, K.; Ernzerhof, M. Generalized Gradient Approximation Made Simple. *Phys. Rev. Lett.* **1996**, *77*, 3865-3868.
50. Hamprecht, F.A.; Cohen, A.J.; Tozer, D.J.; Handy, N.C. Development and Assessment of New Exchange-Correlation Functionals. *J. Chem. Phys.* **1998**, *109*, 6264-6271.
51. Kutzler, F.W.; Painter, G.S. Energies of Atoms with Nonspherical Charge Densities Calculated with Nonlocal Density-Functional Theory. *Phys. Rev. Lett.* **1987**, *59*, 1285-1288.
52. Mlynarski, P.; Salahub, D.R. Self-Consistent Implementation of Nonlocal Exchange and Correlation in a Gaussian Density-Functional Method. *Phys. Rev. B* **1991**, *43*, 1399-1410.
53. Becke, A. Density-Functional Thermochemistry. I. The Effect of the Exchange-Only Gradient Correction. *J. Chem. Phys.* **1992**, *96*, 2155-2160.
54. Becke, A. Density-Functional Thermochemistry. II. The Effect of the Perdew–Wang Generalized-Gradient Correlation Correction. *J. Chem. Phys.* **1992**, *97*, 9173-9177.
55. Perdew, J.P.; Chevary, J.A.; Vosko, S.H.; Jackson, K.A.; Pederson, M.R.; Singh, D.J.; Fiolhais, C. Atoms, Molecules, Solids, and Surfaces: Applications of the Generalized Gradient Approximation for Exchange and Correlation. *Phys. Rev. B* **1992**, *46*, 6671-6687.
56. Johnson, B.G.; Gill, P.M.W.; Pople, J.A. The Performance of a Family of Density Functional Methods. *J. Chem. Phys.* **1993**, *98*, 5612-5626.
57. Matveev, A.; Staufer, M.; Mayer, M.; Rösch, N. Density Functional Calculations on Small Molecules and Transition Metal Carbonyls using Revised PBE Functionals. *Int. J. Quantum Chem.* **1999**, *75*, 863-873.
58. Tsuneda, T.; Hirao, K. Self-Interaction Corrections in Density Functional Theory. *J. Chem. Phys.* **2014**, *140*, 18A513-13.
59. Perdew, J.P.; Zunger, A. Self-Interaction Correction to Density-Functional Approximations for Many-Electron Systems. *Phys. Rev. B* **1981**, *23*, 5048-5079.
60. Anisimov, V.I.; Zaanen, J.; Andersen, O.K. Band Theory and Mott Insulators: Hubbard *U* instead of Stoner *I*. *Phys. Rev. B* **1991**, *44*, 943-953.
61. Anisimov, V.I.; Solovyev, I.V.; Korotin, M.A.; Czyzyk, M.T.; Sawatzky, G.A. Density-Functional Theory and NiO Photoemission Spectra *Phys. Rev. B* **1993**, *48*, 16929-16934.
62. Czyżyk, M.T.; Sawatzky, G.A. Local-Density Functional and on-Site Correlations: The Electronic Structure of La_2CuO_4 and $LaCuO_3$. *Phys. Rev. B* **1994**, *49*, 14211-14228.
63. Dudarev, S.L.; Botton, G.A.; Savrasov, S.Y.; Humphreys, C.J.; Sutton, A.P. Electron-Energy-Loss Spectra and the Structural Stability of Nickel Oxide: An LSDA+U Study. *Phys. Rev. B* **1998**, *57*, 1505-1509.
64. Picket, W.E.; Erwin, S.C.; Ethridge, E.C. Reformulation of the *LDA+U* Method for a Local-Orbital Basis. *Phys. Rev. B* **1998**, *58*, 1201-1209.
65. Cococcioni, M.; de Gironcoli, S. Linear Response Approach to the Calculation of the

Effective Interaction Parameters in the *LDA+U* Method. *Phys. Rev. B* **2005**, *71*, 035105-16.

66. Han, M.J.; Ozaki, T.; Yu, J. O(N) LDA+U Electronic Structure Calculation Method based on the Nonorthogonal Pseudoatomic Orbital Basis. *Phys. Rev. B* **2006**, *73*, 045110-11.
67. Kulik, H.J.; Cococcioni, M.; Scherlis, D.A.; Marzari, N. Density Functional Theory in Transition-Metal Chemistry: A Self-Consistent Hubbard U Approach. *Phys. Rev. Lett.* **2006**, *97*, 103001-4.
68. Ylvisaker, E.R.; Picket, W.E.; Koepernik, K. Anisotropy and Magnetism in the LSDA+U Method. *Phys. Rev. B* **2009**, *79*, 035103-12.
69. O'Regan, D.D.; Payne, M.C.; Mostofi, A.A. Subspace Representations in Ab Initio Methods for Strongly Correlated Systems. *Phys. Rev. B* **2011**, *83*, 245124-14.
70. Belling, T.; Grauschopf, T.; Krüger, S.; Nörtemann, F.; Staufer, M.; Mayer, M.; Nasluzov, V.A.; Birkenheuer, U.; Hu, A.; Matveev, A.V.; Shor, A.V.; Fuchs-Rohr, M.S.K.; Neyman, K.M.; Ganyushin, D.I.; Kerdcharoen, T.; Woiterski, A.; Majumder, S.; Gordienko, A.B.; Huix i Rotllant, M.; Ramakrishnan, R.; Dixit, G.; Nikodem, A.; Soini, T.M.; Roderus, M.; Rösch, N. *ParaGauss, Version 4.0, Technische Universität München*, **2012**.
71. Becke, A. Density-Functional Thermochemistry. IV. A New Dynamical Correlation Functional and Implications for Exact-Exchange Mixing. *J. Chem. Phys.* **1996**, *104*, 1040-1046.
72. Becke, A. A New Inhomogeneity Parameter in Density-Functional Theory. *J. Chem. Phys.* **1998**, *109*, 2092-2098.
73. Van Voorhis, T.; Scuseria, G.E. A Novel Form of the Exchange-Correlation Energy Functional. *J. Chem. Phys.* **1998**, *109*, 400-410.
74. Perdew, J.P.; Kurth, S.; Zupan, A.; Blaha, P. Accurate Density Functional with Correct Formal Properties: A Step Beyond the Generalized Gradient Approximation. *Phys. Rev. Lett.* **1999**, *82*, 2544-2547.
75. Tao, J.; Perdew, J.P.; Staroverov, V.N.; Scuseria, G.E. Climbing the Density Functional Ladder: Nonempirical Meta-Generalized Gradient Approximation Designed for Molecules and Solids. *Phys. Rev. Lett.* **2003**, *91*, 146401-4.
76. Perdew, J.P.; Tao, J.; Staroverov, V.N.; Scuseria, G.E. Meta-Generalized Gradient Approximation: Explanation of a Realistic Nonempirical Density Functional. *J. Chem. Phys.* **2004**, *120*, 6898-6911.
77. Zhao, Y.; Truhlar, D.G. A New Local Density Functional for Main Group Thermochemistry, Transition Metal Bonding, Thermochemical Kinetics, and Noncovalent Interactions *J. Chem. Phys.* **2006**, *125*, 194101-18.
78. Becke, A.; Johnson, E.R. A Simple Effective Potential for Exchange. *J. Chem. Phys.* **2006**, *124*, 221101-4.
79. Becke, A.; Edgecombe, K.E. A Simple Measure of Electron Localization in Atomic and Molecular Systems. *J. Chem. Phys.* **1990**, *92*, 5397-5403.
80. Becke, A. Hartree-Fock Exchange Energy of an Inhomogeneous Electron Gas. *Int. J. Quantum Chem.* **1983**, *23*, 1915-1922.
81. Becke, A. A New Mixing of Hartree-Fock and Local Density Functional Theories. *J. Chem. Phys.* **1993**, *98*, 1372-1377.
82. Becke, A. Density Functional Thermochemistry. III. The Role of Exact Exchange. *J. Chem. Phys.* **1993**, *98*, 5648-5652.
83. Perdew, J.P.; Ernzerhof, M.; Burke, K. Rationale for Mixing Exact Exchange with Density Functional Approximations. *J. Chem. Phys.* **1996**, *105*, 9982-9985.
84. Stephens, P.J.; Devlin, F.J.; Chabalowski, C.F.; Frisch, M.J. Ab Initio Calculation of Vibrational Absorption and Circular Dichroism Spectra Using Density Functional Force Fields. *J. Phys. Chem.* **1994**, *98*, 11623-11627.
85. Becke, A. Density-Functional Thermochemistry. V. Systematic Optimization of Exchange-Correlation Functionals. *J. Chem. Phys.* **1997**, *107*, 8554-8560.
86. Schmider, H.L.; Becke, A. Optimized Density Functionals from the Extended G2 Test Set. *J. Chem. Phys.* **1998**, *108*, 9624-9631.
87. Adamo, C.; Barone, V. Toward Reliable Density Functional Methods without Adjustable Parameters: The PBE0 Model. *J. Chem. Phys.* **1999**, *110*, 6158-6170.
88. Boese, A.D.; Martin, J.M.L. Development of Density Functionals for Thermochemical Kinetics. *J. Chem. Phys.* **2004**, *121*, 3405-3416.
89. Zhao, Y.; Schultz, N.E.; Truhlar, D.G. Exchange-Correlation Functionals with Broad Accuracy for Metallic and Nonmetallic Compounds, Kinetics, and Noncovalent Interactions. *J. Chem. Phys.* **2005**, *123*, 161103-4.
90. Zhao, Y.; Truhlar, D.G. The M06 Suite of Density Functionals for Main Group Thermochemistry, Thermochemical Kinetics, Noncovalent interactions, Excited States, and Transition Elements: Two New Functionals and Systematic Testing of Four M06 Functionals and Twelve Other Functionals. *Theor. Chem. Acc.* **2008**, *120*, 215-241.
91. Iikura, H.; Tsuneda, T.; Yanai, T.; Hirao, K. Long-Range Correction Scheme for Generalized-Gradient-Approximation Exchange Functionals. *J. Chem. Phys.* **2001**, *115*, 3540-3544.
92. Tawada, Y.; Tsuneda, T.; Yanagisawa, S.; Yanai, T.; Hirao, K. A Long-Range-Corrected

Time-Dependent Density Functional Theory. *J. Chem. Phys.* **2004**, *120*, 8425-8433.
93. Vydrov, O.A.; Scuseria, G.E. Assessment of a Long-Range Corrected Hybrid Functional. *J. Chem. Phys.* **2006**, *125*, 234109-9.
94. Chai, J.-D.; Head-Gordon, M. Systematic Optimization of Long-Range Corrected Hybrid Density Functionals. *J. Chem. Phys.* **2008**, *128*, 084106-15.
95. Chai, J.-D.; Head-Gordon, M. Long-Range Corrected Hybrid Density Functionals with Damped Atom-Atom Dispersion Corrections. *Phys. Chem. Chem. Phys.* **2008**, *10*, 6615-6620.
96. Baer, R.; Livshits, E.; Salzner, U. Tuned Range-Separated Hybrids in Density Functional Theory. *Annu. Rev. Phys. Chem.* **2010**, *61*, 85-109.
97. Peverati, R.; Truhlar, D.G. Screened-Exchange Density Functionals with Broad Accuracy for Chemistry and Solid-State Physics. *Phys. Chem. Chem. Phys.* **2012**, *14*, 16187-16191.
98. Heyd, J.; Scuseria, G.E.; Ernzerhof, M. Hybrid Functionals based on a Screened Coulomb Potential. *J. Chem. Phys.* **2004**, *118*, 8207-8215.
99. Heyd, J.; Scuseria, G.E.; Ernzerhof, M. Erratum: Hybrid Functionals based on a Screened Coulomb Potential. *J. Chem. Phys.* **2006**, *124*, 219906-1.
100. Jaramillo, J.; Scuseria, G.E.; Ernzerhof, M. Local Hybrid Functionals. *J. Chem. Phys.* **2003**, *118*, 1068-1073.
101. Cohen, A.J.; Mori-Sánchez, P.; Yang, W. Fractional Charge Perspective on the Band-Gap in Density-Functional Theory. *Phys. Rev. B* **2008**, *77*, 115123-6.
102. Becke, A. Density Functionals for Static, Dynamical, and Strong Correlation. *J. Chem. Phys.* **2013**, *138*, 074109-10.
103. Staroverov, V.N. In *Matter of Density: Exploring the Electron Density Concept in the Chemical, Biological, and Materials Sciences*, Sukumar, N., Ed. Wiley: Hoboken, NJ, **2013**.
104. Sándor, K.; Pulay, P. Can (Semi)Local Density Functional Theory Account for the London Dispersion Forces? *Chem. Phys. Lett.* **1994**, *229*, 175-180.
105. Wu, Q.; Yang, W. Empirical Correction to Density Functional Theory for Van Der Waals Interactions. *J. Chem. Phys.* **2002**, *116*, 515-524.
106. Grimme, S. Semiempirical GGA-Type Density Functional Constructed with a Long-Range Dispersion Correction. *J. Comput. Chem.* **2006**, *27*, 1787-1799.
107. Tkatchenko, A.; Scheffler, M. Accurate Molecular Van Der Waals Interactions from Ground-State Electron Density and Free-Atom Reference Data. *Phys. Rev. Lett.* **2009**, *102*, 073005-4.
108. Bohm, D.; Pines, D. A Collective Description of Electron Interactions. I. Magnetic Interactions. *Phys. Rev.* **1951**, *82*, 625-634.
109. Görling, A.; Levy, M. Exact Kohn-Sham Scheme Based on Perturbation Theory. *Phys. Rev. A* **1994**, *50*, 196-204.
110. Furche, F. Molecular Tests of the Random Phase Approximation to the Exchange-Correlation Energy Functional. *Phys. Rev. B* **2001**, *64*, 195120-8.
111. Zhao, Y.; Lynch, B.J.; Truhlar, D.G. Doubly Hybrid Meta DFT: New Multi-Coefficient Correlation and Density Functional Methods for Thermochemistry and Thermochemical Kinetics. *J. Phys. Chem. A* **2004**, *108*, 4786-4791.
112. Grimme, S. Semiempirical Hybrid Density Functional with Perturbative Second-Order Correlation. *J. Chem. Phys.* **2006**, *124*, 034108-16.
113. Chai, J.-D.; Mao, S.-P. Seeking for Reliable Double-Hybrid Density Functionals without Fitting Parameters: The PBE0-2 Functional. *Chem. Phys. Lett.* **2008**, *538*, 121-125.
114. Goerigk, L.; Grimme, S. Efficient and Accurate Double-Hybrid-Meta-GGA Density Functionals - Evaluation with the Extended GMTKN30 Database for General Main Group Thermochemistry, Kinetics, and Noncovalent Interactions. *J. Chem. Theory Comput.* **2011**, *7*, 291-309.
115. Andersson, Y.; Langreth, D.C.; Lundqvist, B.I. Van Der Waals Interactions in Density-Functional Theory. *Phys. Rev. Lett.* **1996**, *76*, 102-105.
116. Dion, M.; Rydberg, H.; Schröder, E.; Langreth, D.C.; Lundqvist, B.I. Van der Waals Density Functional for General Geometries. *Phys. Rev. Lett.* **2004**, *92*, 246401-4.
117. Vydrov, O.A.; Van Voorhis, T. Nonlocal Van Der Waals Density Functional Made Simple. *Phys. Rev. Lett.* **2009**, *103*, 063004-4.
118. Lee, K.; Murray, É.D.; Kong, L.; Lundqvist, B.I.; Langreth, D.C. Higher-accuracy van der Waals density functional. *Phys. Rev. B* **2010**, *82*, 081101-4.
119. Tkatchenko, A.; Scheffler, M. Accurate and Efficient Method for Many-Body van der Waals Interactions. *Phys. Rev. Lett.* **2012**, *108*, 236402-5.
120. Cohen, A.J.; Mori-Sánchez, P.; Yang, W. Development of Exchange-Correlation Functionals with Minimal Many-Electron Self-Interaction Error. *J. Chem. Phys.* **2007**, *126*, 191109-5.
121. Born, M.; Oppenheimer, J.R. Zur Quantentheorie der Molekeln. *Ann. Phys.* **1927**, *389*, 457-484.
122. Slater, J.C. The Theory of Complex Spectra *Phys. Rev.* **1929**, *34*, 1293-1322.

123. Slater, J.C. Note on Hartree's Method. *Phys. Rev.* **1930**, *35*, 210-211.
124. Roothaan, C.C.J. New Developments in Molecular Orbital Theory. *Rev. Mod. Phys.* **1951**, *23*, 69-89.
125. Pople, J.A.; Nesbet, R.K. Self-Consistent Orbitals for Radicals. *J. Chem. Phys.* **1954**, *22*, 571-572.
126. Davidson, E.R. *Reduced Density Matrices in Quantum Chemistry*. Academic Press: New York, **1976**.
127. Löwdin, P.-O. Quantum Theory of Many-Particle Systems. III. Extension of the Hartree-Fock Scheme to Include Degenerate Systems and Correlation Effects. *Phys. Rev.* **1955**, *97*, 1509-1520.
128. Handy, N.C.; Cohen, A.J. Dynamic Correlation. *Mol. Phys.* **2001**, *99*, 607-615.
129. Handy, N.C.; Cohen, A.J. Left-Right Correlation Energy. *Mol. Phys.* **2001**, *99*, 403-412.
130. Perdew, J.P.; Ruzsinszky, A.; Constantin, L.A.; Sun, J.; Csonka, G.I. Some Fundamental Issues in Ground-State Density Functional Theory: A Guide for the Perplexed. *J. Chem. Theory Comput.* **2009**, *5*, 902-908.
131. Becke, A. Perspective: Fifty Years of Density-Functional Theory in Chemical Physics. *J. Chem. Phys.* **2014**, *140*, 18A301-18.
132. Lee, T.J.; Taylor, P.R. A Diagnostic for Determining the Quality of Single-Reference Electron Correlation Methods. *Int. J. Quantum Chem. Symp.* **1989**, *36*, 199-207.
133. Lyakh, D.I.; Musiał, M.; Lotrich, V.F.; Bartlett, R.J. Multireference Nature of Chemistry: The Coupled-Cluster View. *Chem. Rev.* **2012**, *112*, 182-243.
134. Yaeger, D.L.; Jørgensen, P. Convergency Studies of Second and Approximate Second Order Multiconfigurational Hartree-Fock Procedures. *J. Chem. Phys.* **1979**, *71*, 755-760.
135. Dalgaard, E.; Jørgensen, P. Optimization of Orbitals for Multiconfigurational Reference States. *J. Chem. Phys.* **1978**, *69*, 3833-3844.
136. Roos, B.O.; Taylor, P.R.; Siegbahn, P. A Complete Active Space SCF Method (CASSCF) Using a Density-matrix Formulated Super-CI Approach. *Chem. Phys.* **1980**, *48*, 157-173.
137. Froese Fischer, C.; Lagowski, J.B.; Vosko, S.H. Ground States of Ca^- and Sc^- from Two Theoretical Points of View. *Phys. Rev. Lett.* **1987**, *59*, 2263-2266.
138. Bright-Wilson, E. In *Structural Chemistry and Molecular Biology*, Rich, A.; Davidson, N., Eds. W. H. Freeman: San Francisco, **1968**.
139. Theophilou, A.K. The Energy Density Functional Formalism for Excited States *J. Phys. C: Solid State Phys.* **1979**, *12*, 5419-5430.
140. Gritsenko, O.; Baerends, E.J. The Spin-Unrestricted Molecular Kohn-Sham Solution and the Analogue of Koopmans's Theorem for Open-Shell Molecules *J. Chem. Phys.* **2004**, *120*, 8364-8372.
141. Strange, P. *Relativistic Quantum Mechanics With Applications in Condensed Matter and Atomic Physics*. Cambridge University Press: Cambridge, **1998**.
142. Levy, M. Universal Variational Functionals of Electron Densities, First-Order Density Matrices, and Natural Spin-Orbitals and Solution of the V-Representability Problem *Proc. Natl. Acad. Sci. U.S.A.* **1979**, *76*, 6062-6065.
143. Levy, M. Electron Densities in Search of Hamiltonians. *Phys. Rev. A* **1982**, *26*, 1200-1208.
144. Lieb, E.H. Density Functionals for Coulomb Systems. *Int. J. Quantum Chem.* **1983**, *24*, 243-277.
145. Lieb, E.H. In *Density Functional Methods In Physics*, Dreizler, R.M.d.P., J., Ed. Plenum: New York, **1985**.
146. Gilbert, T.L. Hohenberg-Kohn Theorem for Nonlocal External Potentials. *Phys. Rev. B* **1975**, *12*, 2111-2120.
147. Harriman, J.E. Orthonormal Orbitals for the Representation of an Arbitrary Density. *Phys. Rev. A* **1981**, *24*, 680-682.
148. Thomas, L.H. The Calculation of Atomic Fields. *Math. Proc. Cambridge Philos. Soc.* **1927**, *23*, 542-548.
149. Fermi, E. Un Metodo Statistico per la Determinazione di alcune Prioprietà dell'Atomo. *Rend. Accad. Naz. Lincei* **1927**, *6*, 602-607.
150. Dirac, P.A.M. Note on Exchange Phenomena in the Thomas-Fermi Atom. *Math. Proc. Camb.Philos. Soc.* **1930**, *26*, 376-385.
151. Teller, E. On the Stability of Molecules in the Thomas-Fermi Theory. *Rev. Mod. Phys.* **1962**, *34*, 627-631.
152. Slater, J.C. A Simplification of the Hartree-Fock Method. *Phys. Rev.* **1951**, *81*, 385-390.
153. Becke, A. Numerical Hartree-Fock-Slater Calculations on Diatomic Molecules *J. Chem. Phys.* **1982**, *76*, 6037-6045.
154. Becke, A. Numerical Hartree-Fock-Slater Calculations on Diatomic Molecules: Addendum. *J. Chem. Phys.* **1983**, *78*, 4787-4788.
155. Slater, J.C. Statistical Exchange-Correlation in the Self-Consistent Field. *Adv. Quantum Chem.* **1972**, *6*, 1-92.
156. Perdew, J.P.; Yue, W. Accurate and Simple Density Functional for the Electronic Exchange Energy: Generalized Gradient Approximation. *Phys. Rev. B* **1986**, *33*, 8800-8802.
157. Levy, M.; Perdew, J.P. Hellmann-Feynman, Virial, and Scaling Requisites for the Exact Universal Density Functionals. Shape of the Correlation Potential and Diamagnetic

Susceptibility for Atoms. *Phys. Rev. A* **1985**, *32*, 2010-2021.
158. Perdew, J.P.; Parr, G.R.; Levy, M.; Balduz, J.L.J. Density-Functional Theory for Fractional Particle Number: Derivative Discontinuities of the Energy. *Phys. Rev. Lett.* **1982**, *49*, 1691-1694.
159. Levy, M.; Perdew, J.P. Comment on ''Significance of the Highest Occupied Kohn-Sham Eigenvalue''. *Phys. Rev. B* **1997**, *56*, 16021-16028.
160. Lebedev, V.I. Values of the Nodes and Weights of Ninth to Seventeenth Order Gauss-Markov Quadrature Formulae Invariant Under the Octahedron Group with Inversion. *Zh. vychisl. Mat. mat. Fiz.* **1975**, *15*, 48-54.
161. Lebedev, V.I. Quadratures on a Sphere. *Zh. vychisl. Mat. mat. Fiz.* **1976**, *16*, 293-306.
162. Becke, A. A Multicenter Numerical Integration Scheme for Polyatomic Molecules. *J. Chem. Phys.* **1988**, *88*, 2547-2553.
163. Murray, C.W.; Handy, N.C.; Laming, G.J. Quadrature Schemes for Integrals of Density Functional Theory. *Mol. Phys.* **1993**, *78*, 997-1014.
164. Treutler, O.; Ahlrichs, R. Efficient Molecular Numerical Integration Schemes. *J. Chem. Phys.* **1995**, *102*, 346-354.
165. Mura, M.E.; Knowles, P.J. Improved Radial Grids for Quadrature in Molecular Density-Functional Calculations. *J. Chem. Phys.* **1996**, *104*, 9848-9858.
166. Stratmann, R.E.; Scuseria, G.E.; Frisch, M.J. Achieving Linear Scaling in Exchange-Correlation Density Functional Quadratures. *Chem. Phys. Lett.* **1996**, *257*, 213-223.
167. Von Barth, U.; Hedin, L. A Local Exchange-Correlation Potential for the Spin Polarized Case. I. *J. Phys. C: Solid State Phys.* **1972**, *5*, 1629-1642.
168. Runge, E.; Gross, E.K.U. Density-Functional Theory for Time-Dependent Systems. *Phys. Rev. Lett.* **1984**, *52*, 997-1000.
169. Vignale, G.; Rasolt, M. Density-Functional Theory in Strong Magnetic Fields. *Phys. Rev. Lett.* **1987**, *59*, 2360-2363.
170. Gunnarsson, O.; Lundqvist, B.I.; Wilkins, J.W. Contribution to the Cohesive Energy of Simple Metals: Spin-Dependent Effect. *Phys. Rev. B* **1974**, *10*, 1319-1327.
171. Oliver, G.L.; Perdew, J.P. Spin-Density Gradient Expansion for the Kinetic Energy. *Phys. Rev. A* **1979**, *20*, 397-403.
172. Hedin, L.; Lundqvist, S. In *Solid State Physics*, Ehrenreich, H.; Seitz, F.; Turnbull, D., Eds. Academic Press: New York, **1969**; Vol. 23.
173. Ceperley, D.M.; Alder, B.J. Ground State of the Electron Gas by a Stochastic Method. *Phys. Rev. Lett.* **1980**, *45*, 566-569.
174. Ortiz, G.; Ballone, P. Correlation Energy, Structure Factor, Radial Distribution Function, and Momentum Distribution of the Spin-Polarized Uniform Electron Gas. *Phys. Rev. B* **1994**, *50*, 1391-1405.
175. Kwon, Y.; Ceperley, D.M.; Martin, R.M. Effects of Backflow Correlation in the Three-Dimensional Electron Gas: Quantum Monte Carlo Study. *Phys. Rev. B* **1998**, *58*, 6800-6806.
176. Peverati, R.; Truhlar, D.G. Exchange-Correlation Functional with Good Accuracy for Both Structural and Energetic Properties while Depending Only on the Density and its Gradient. *J. Chem. Theory Comput.* **2012**, *8*, 2310-2319.
177. Cremer, D.; Filatov, M.; Polo, V.; Kraka, E.; Shaik, S. Implicit and Explicit Coverage of Multi-Reference Effects by Density Functional Theory. *Int. J. Mol. Sci.* **2002**, *3*, 604-638.
178. Polo, V.; Gräfenstein, J.; Kraka, E.; Cremer, D. Long-Range and Short-Range Coulomb Correlation Effects as Simulated by Hartree-Fock, Local Density Approximation, and Generalized Gradient Approximation Exchange Functionals. *Theor. Chem. Acc.* **2003**, *109*, 22-35.
179. Harris, J.; Jones, R.O. Surface-Energy of a Bounded Electron-Gas. *J. Phys. F: Met. Phys.* **1974**, *4*, 1170-1186.
180. Langreth, D.C.; Perdew, J.P. Exchange-Correlation Energy of a Metal Surface. *J. Solid State Commun.* **1975**, *17*, 1425-1429.
181. Gunnarsson, O.; Lundqvist, B.I. Exchange and Correlation in Atoms, Molecules, and Solids by the Spin-Density-Functional Formalism. *Phys. Rev. B* **1976**, *13*, 4274-4298.
182. Gáspár, R. Über eine Approximation des Hartree-Fockschen Potentials durch eine Universelle Potentialfunktion. *Acta Phys. Acad. Scien. Hung.* **1954**, *3*, 263-286.
183. Johnson, K.H.; Jr. Smith, F.C. Chemical Bonding of a Molecular Transition-Metal Ion in a Crystalline Environment. *Phys. Rev. B* **1972**, *5*, 831-843.
184. Salahub, D.R. From Xα-Scattered Wave to End-of-the-Century Applications of Density Functional Theory in Chemistry. Perspective on "Chemical Bonding of a Molecular Transition-Metal Ion in a Crystalline Environment". *Theor. Chem. Acc.* **2000**, *103*, 311-312.
185. Hoe, W.-M.; Cohen, A.J.; Handy, N.C. Assessment of a New Local Exchange Functional OPTX. *Chem. Phys. Lett.* **2001**, *341*, 319-328.
186. Wigner, E.P. On the Interaction of Electrons in Metals. *Phys. Rev.* **1934**, *46*, 1002-1011.
187. Wigner, E.P. Effects of the Electron Interaction on the Energy Levels of Electrons in Metals. *Trans. Faraday Soc.* **1938**, *34*, 678-685.

188. Gell-Mann, M.; Brueckner, K.A. Correlation Energy of an Electron Gas at High-Density. *Phys. Rev.* **1957**, *106*, 364-368.
189. Carr, W.J. Energy, Specific Heat, and Magnetic Properties of the Low-Density Electron Gas. *Phys. Rev.* **1961**, *122*, 1437-1446.
190. Carr, W.J.; Maradudin, A.A. Ground-State Energy of a High-Density Electron Gas. *Phys. Rev.* **1964**, *133*, A371-A374.
191. Vosko, S.H.; Wilk, L.; Nusair, M. Accurate Spin-Dependent Electron Liquid Correlation Energies for Local Spin Density Calculations: A Critical Analysis. *Can. J. Phys.* **1983**, *58*, 1200-1211.
192. Perdew, J.P.; Wang, Y. Accurate and Simple Analytic Representation of the Electron-Gas Correlation Energy. *Phys. Rev. B* **1992**, *45*, 13244-13249.
193. Gunnarsson, O.; Jonson, M.; Lundqvist, B.I. Description of Exchange and Correlation Effects in Inhomogeneous Electron Systems. *Phys. Rev. B* **1979**, *20*, 3136-3164.
194. Kim, Y.-H.; Lee, I.-H.; Nagaraja, S.; Leburton, J.-P.; Hood, R.Q.; Martin, R.M. Two-Dimensional Limit of Exchange-Correlation Energy Functional Approximations. *Phys. Rev. B* **2000**, *61*, 5202-5211.
195. Herman, F.; Van Dyke, J.P.; Ortenburger, I.B. Improved Statistical Exchange Approximation for Inhomogeneous Many-Electron Systems. *Phys. Rev. Lett.* **1969**, *22*, 807-811.
196. Perdew, J.P.; Burke, K. Comparison Shopping for Gradient-Corrected Density Functionals. *Int. J. Quantum Chem.* **1996**, *57*, 309-319.
197. Svedsen, P.S.; Von Barth, U. Gradient Expansion of the Exchange from Second-Order Density Response Theory. *Phys. Rev. B* **1996**, *54*, 17402-17413.
198. Paier, J.; Marsman, M.; Kresse, G. Why Does the B3LYP Hybrid Functional Fail for Metals? *J. Chem. Phys.* **2007**, *127*, 024103-10.
199. Slamet, M.; Sahni, V. The Gradient Expansion Approximation for Exchange: A Physical Perspective. *Int. J. Quantum Chem.* **1992**, *44*, 333-345.
200. Jemmer, P.; Knowles, P.J. Exchange Energy in Kohn-Sham Density-Functional Theory. *Phys. Rev. A* **1995**, *51*, 3571-3575.
201. Neumann, R.; Handy, N.C. Higher-Order Gradient Corrections for Exchange-Correlation Functionals. *Chem. Phys. Lett.* **1997**, *266*, 16-22.
202. Boese, A.D.; Handy, N.C. New Exchange-Correlation Density Functionals: The Role of the Kinetic-Energy Density. *J. Chem. Phys.* **2002**, *116*, 9559-9569.
203. Perdew, J.P.; Constantin, L.A. Laplacian-Level Density Functionals for the Kinetic Energy Density and Exchange-Correlation Energy. *Phys. Rev. B* **2007**, *75*, 155109-9.
204. Sharp, R.T.; Horton, G.K. A Variational Approach to the Unipotential Many-Electron Problem. *Phys. Rev.* **1953**, *90*, 317-317.
205. Talman, J.D.; Shadwick, W.F. Optimized Effective Atomic Central Potential. *Phys. Rev. A* **1976**, *14*, 36-40.
206. Krieger, J.B.; Li, Y.; Iafrate, G.J. Construction and Application of an Accurate Local Spin-Polarized Kohn-Sham Potential with Integer Discontinuity: Exchange-Only Theory. *Phys. Rev. A* **1992**, *45*, 101-126.
207. Arbuznikov, A.V.; Kaupp, M. The Self-Consistent Implementation of Exchange-Correlation Functionals Depending on the Local Kinetic Energy Density. *Chem. Phys. Lett.* **2003**, *381*, 495-504.
208. Seidl, A.; Görling, A.; Vogl, P.; Majewski, J.A.; Levy, M. Generalized Kohn-Sham Schemes and the Band-Gap Problem. *Phys. Rev. B* **1996**, *53*, 3764-3774.
209. Perdew, J.P.; Ruzsinszky, A.; Tao, J.; Staroverov, V.N.; Scuseria, G.E.; Csonka, G.I. Prescription for the Design and Selection of Density Functional Approximations: More Constraint Satisfaction with Fewer Fits. *J. Chem. Phys.* **2005**, *123*, 062201-9.
210. Zhao, Y.; Schultz, N.E.; Truhlar, D.G. Design of Density Functionals by Combining the Method of Constraint Satisfaction with Parametrization for Thermochemistry, Thermochemical Kinetics, and Noncovalent Interactions. *J. Chem. Theory Comput.* **2006**, *2*, 364-382.
211. Perdew, J.P.; Schmidt, K. In *Density Functional Theory and Its Application to Materials*, Van Doren, V.; Van Alsenoy, C.; Geerlings, P., Eds. American Institute of Physics: New York, **2001**.
212. Staroverov, V.N.; Scuseria, G.E.; Tao, J.; Perdew, J.P. Comparative Assessment of a New Nonempirical Density Functional: Molecules and Hydrogen-Bonded Complexes. *J. Chem. Phys.* **2003**, *119*, 12129-12137.
213. Wilson, E.K. Battle of the 'Functionals'. *Chem. Eng. News* **2008**, *86*, 34-37.
214. Mori-Sánchez, P.; Cohen, A.J.; Yang, W. Many-Electron Self-Interaction Error in Approximate Density Functionals. *J. Chem. Phys.* **2006**, *125*, 201102-4.
215. Cohen, A.J.; Mori-Sánchez, P.; Yang, W. Insights into Current Limitations of Density Functional Theory. *Science* **2008**, *321*, 792-794.
216. Johnson, E.R.; Mori-Sánchez, P.; Cohen, A.J.; Yang, W. Delocalization Errors in Density Functionals and Implications for Main-Group Thermochemistry. *J. Chem. Phys.* **2008**, *129*, 204112-6.
217. Cohen, A.J.; Mori-Sánchez, P.; Yang, W. Challenges for Density Functional Theory. *Chem. Rev.* **2012**, *112*, 289-320.
218. Ruzsinszky, A.; Perdew, J.P.; Csonka, G.I.; Vydrov, O.A.; Scuseria, G.E. Spurious

Fractional Charge on Dissociated Atoms: Pervasive and Resilient Selfinteraction Error of Common Density Functionals. *J. Chem. Phys.* **2006**, *125*, 194112-8.

219. Perdew, J.P.; Ruzsinszky, A.; Csonka, G.I.; Vydrov, O.A.; Scuseria, G.E.; Staroverov, V.N.; Tao, J. Exchange and Correlation in Open Systems of Fluctuating Electron Number. *Phys. Rev. A* **2007**, *76*, 040501-4.
220. Ruzsinszky, A.; Perdew, J.P.; Csonka, G.I.; Vydrov, O.A.; Scuseria, G.E. Density Functionals that are One- and Two- are not Always Many-Electron Selfinteraction-Free, as Shown for H_2^+ , He_2^+, LiH^+ , and Ne_2^+. *J. Chem. Phys.* **2007**, *126*, 104102-8.
221. Pederson, M.R.; Ruzsinszky, A.; Perdew, J.P. Self-Interaction Correction with Unitary Invariance in Density Functional Theory. *J. Chem. Phys.* **2014**, *140*, 121103-4.
222. Gritsenko, O.; van Leeuwen, R.; Baerends, E.J. Analysis of Electron Interaction and Atomic Shell Structure in Terms of Local Potentials. *J. Chem. Phys.* **1994**, *101*, 8955-8963.
223. Perdew, J.P.; Levy, M. Physical Content of the Exact Kohn-Sham Orbital Energies: Band Gaps and Derivative Discontinuities. *Phys. Rev. Lett.* **1983**, *51*, 1884-1887.
224. Sham, L.J.; Schlüter, M. Density-Functional Theory of the Energy Gap. *Phys. Rev. Lett.* **1983**, *51*, 1888-1891.
225. Almbladh, C.-O.; von Barth, U. Exact Results for the Charge and Spin Densities, Exchange-Correlation Potentials, and Density-Functional Eigenvalues. *Phys. Rev. B* **1985**, *31*, 3231-3244.
226. Gill, P.M.W.; Johnson, B.G.; Gonzales, C.A.; Pople, J.A. A Density Functional Study of the Simplest Hydrogen Abstraction Reaction. Effect of Self-Interaction Correction. *Chem. Phys. Lett.* **1994**, *221*, 100-108.
227. Körzdörfer, T.; Parrish, R.M.; Sears, J.S.; Sherrill, C.D.; Brédas, J.-L. On the Relationship between Bond-Length Alternation and Many-Electron Self-Interaction Error. *J. Chem. Phys.* **2012**, *137*, 124305-8.
228. Haunschild, R.; Henderson, T.M.; Jiménez-Hoyos, C.A.; Scuseria, G.E. Many-Electron Self-Interaction and Spin Polarization Errors in Local Hybrid Density Functionals. *J. Chem. Phys.* **2010**, *133*, 134116-10.
229. Becke, A. Real-Space Post-Hartree-Fock Correlation Models. *J. Chem. Phys.* **2005**, *122*, 064101-6.
230. Mori-Sánchez, P.; Cohen, A.J.; Yang, W. Self-Interaction-Free Exchange-Correlation Functional for Thermochemistry and Kinetics. *J. Chem. Phys.* **2006**, *124*, 091102-4.
231. Mermin, N.D. Thermal Properties of the Inhomogeneous Electron Gas. *Phys. Rev.* **1965**, *137*, A1441-A1443.
232. Nesbet, R.K. Fractional Occupation Numbers in Density-Functional Theory. *Phys. Rev. A* **1997**, *56*, 2665-2669.
233. Janak, J.F. Proof that $\partial E/\partial n_i=\varepsilon_i$ in Density-Functional Theory. *Phys. Rev. B* **1978**, *18*, 7165-7168.
234. Slater, J.C.; Mann, J.B.; Wilson, T.M.; Wood, J.H. Nonintegral Occupation Numbers in Transition Atoms in Crystals. *Phys. Rev.* **1969**, *184*, 672-694.
235. Dunlap, B.I.; Mei, W.N. Basis Set Effects on Spectroscopic Constants for C_2 and Si_2 and the Symmetry Dilemma in the Xα Model. *J. Chem. Phys.* **1983**, *78*, 4997-5003.
236. Averill, F.W.; Painter, G.S. Steepest-Descent Determination of Occupation Numbers and Energy Minimization in the Local-Density Approximation. *Phys. Rev. B* **1992**, 2498-2502.
237. Wang, S.G.; Schwarz, W.H.E. Simulation of Nondynamical Correlation in Density Functional Calculations by the Optimized Fractional Orbital Occupation Approach: Application to the Potential Energy Surfaces of O_3 and SO_2. *J. Chem. Phys.* **1996**, *105*, 4641-4648.
238. Stein, T.; Autschbach, J.; Govind, N.; Kronik, L.; Bear, R. Curvature and Frontier Orbital Energies in Density Functional Theory. *J. Phys. Chem. Lett.* **2012**, *3*, 3740-3744.
239. Dreizler, R.M.; da Providência, J. *Density Functional Methods in Physics*. Plenum: **1985**.
240. Schipper, P.R.T.; Gritsenko, O.; Baerends, E.J. One-Determinantal Pure State Versus Ensemble Kohn-Sham Solutions in the Case of Strong Electron Correlation: CH_2 and C_2. *Theor. Chem. Acc.* **1998**, *99*, 329-343.
241. Morrison, R.C. Electron Correlation and Noninteracting V-Representability in Density Functional Theory: The Be Isoelectronic Series. *J. Chem. Phys.* **2002**, *117*, 10506-6.
242. Katriel, J.; Roy, S.; Springborg, M. A Study of the Adiabatic Connection for Two-Electron Systems. *J. Chem. Phys.* **2004**, *121*, 12179-12.
243. Chai, J.-D. Density Functional Theory with Fractional Orbital Occupations. *J. Chem. Phys.* **2012**, *136*, 154104-17.
244. Savin, A. In *Recent Developments and Applications of Modern Density Functional Theory*, Seminario, J.M., Ed. Elsevier: Amsterdam, **1996**; Vol. 4.
245. Harvey, J.N. On the Accuracy of Density Functional Theory in Transition Metal Chemistry. *Annu. Rep. Prog. Chem. Sect. C* **2006**, *102*, 203-226.
246. Reiher, M.; Salomon, O.; Hess, B.A. Reparameterization of hybrid functionals based on energy differences of states of different multiplicity. *Theor. Chem. Acc.* **2001**, *107*, 48-55.

247. Becke, A.; Johnson, E.R. A Density-Functional Model of the Dispersion Interaction. *J. Chem. Phys.* **2005**, *123*, 154101-9.
248. London, F. Zur Theorie und Systematik der Molekularkräfte. *Z. Phys.* **1930**, *63*, 245-279.
249. Grimme, S.; Antony, J.; Ehrlich, S.; Krieg, S. A Consistent and Accurate ab Initio Parametrization of Density Functional Dispersion Correction (DFT-D) for the 94 Elements H-Pu. **2010**.
250. Zaremba, E.; Kohn, W. Van der Waals Interaction Between an Atom and A Solid Surface. *Phys. Rev. B* **1976**, *13*, 2270-2285.
251. Nordlander, P.; Harris, J. The Interaction of Helium with Smooth Metal Surfaces. *J. Phys. C: Solid State Phys.* **1984**, *17*, 1141-1152.
252. Mercurio, G.; McNellis, E.R.; Martin, I.; Hagen, S.; Leyssner, F.; Soubatch, S.; Meyer, J.; Wolf, M.; Tegeder, P.; Tautz, F.S.; Reuter, K. Structure and Energetics of Azobenzene on Ag(111): Benchmarking Semiempirical Dispersion Correction Approaches. *Phys. Rev. Lett.* **2010**, *104*, 036102-4.
253. Risthaus, T.; Grimme, S. Benchmarking of London Dispersion-Accounting Density Functional Theory Methods on Very Large Molecular Complexes. *J. Chem. Comput. Theory* **2013**, *9*, 1580-1591.
254. Román-Pérez, G.; Soler, J.M. Efficient Implementation of a Van Der Waals Density Functional: Application to Double-Wall Carbon Nanotubes. *Phys. Rev. Lett.* **2009**, *103*, 096102-4.
255. Langreth, D.C.; Lundqvist, B.I.; Chakarova-Käck, S.D.; Cooper, V.R.; Dion, M.; Hyldgaard, P.; Kelkkanen, A.; Kleis, J.; Kong, L.; Li, S.; Moses, P.G.; Murray, E.; Rydberg, H.; Schröder, E.; Thonhauser, T. A Density Functional for Sparse Matter. *J. Phys.: Condens. Matter.* **2009**, *21*, 084203-15.
256. Stoll, H.; Pavlidou, C.M.E.; Preuß, H. On the Calculation of Correlation Energies in the Spin-Density Functional Formalism. *Theor. Chim. Acta* **1978**, *49*, 143-149.
257. Stoll, H.; Golka, E.; Preuß, H. Correlation Energies in the Spin-Density Functional Formalism. *Theor. Chim. Acta* **1980**, *55*, 29-41.
258. Clementi, E.; Chakravorty, S.J. A Comparative Study of Density Functional Models to Estimate Molecular Atomization Energies. *J. Chem. Phys.* **1990**, *93*, 2591-2602.
259. Burke, K.; Ernzerhof, M.; Perdew, J.P. The Adiabatic Connection Method: A Non-Empirical Hybrid. *Chem. Phys. Lett.* **1997**, *265*, 115-120.
260. Grüning, M.; Marini, A.; Rubio, A. Density Functionals from Many-Body Perturbation Theory: The Band Gap for Semiconductors and Insulators. *J. Chem. Phys.* **2006**, *124*, 154108-9.
261. Csonka, G.I.; Perdew, J.P.; Ruzsinszky, A. Global Hybrid Functionals: A Look at the Engine under the Hood. *J. Chem. Theory Comput.* **2010**, *6*, 3688-3703.
262. Görling, A.; Levy, M. Correlation-Energy Functional and its High-Density Limit Obtained from a Coupling-Constant Perturbation Expansion. *Phys. Rev. B* **1993**, *47*, 13105-13113.
263. Sousa, S.F.; Fernandes, P.A.; Ramos, M.J. General Performance of Density Functionals. *J. Phys. Chem. A* **2007**, *111*, 10439-10452.
264. Furche, F.; Perdew, J.P. The Performance of Semi-Local and Hybrid Density Functionals in 3d Transition Metal Chemistry. *J. Chem. Phys.* **2006**, *124*, 044103-27.
265. Staroverov, V.N.; Scuseria, G.E.; Tao, J.; Perdew, J.P. Erratum: "Comparative Assessment of a New Nonempirical Density Functional: Molecules and Hydrogen-Bonded Complexes" [J. Chem. Phys. 119, 12129 (2003)] *J. Chem. Phys.* **2003**, *121*, 11507-11507.
266. Redfern, P.C.; Zapol, P.; Curtiss, L.A. Assessment of Gaussian-3 and Density Functional Theories for Enthalpies of Formation of C_1–C_{16} Alkanes. *J. Phys. Chem. A* **2000**, *104*, 5850-5854.
267. Csonka, G.I.; Ruzsinszky, A.; Tao, J.; Perdew, J.P. Energies of Organic Molecules and Atoms in Density Functional Theory. *Int. J. Quantum Chem.* **2005**, *101*, 506-511.
268. Check, C.E.; Gilbert, T.M. Progressive Systematic Underestimation of Reaction Energies by the B3LYP Model as the Number of C–C Bonds Increases: Why Organic Chemists Should Use Multiple DFT Models for Calculations Involving Polycarbon Hydrocarbons. *J. Org. Chem.* **2005**, *70*, 9828-9834.
269. Grimme, S. Seemingly Simple Stereoelectronic Effects in Alkane Isomers and the Implications for Kohn-Sham Density Functional Theory. *Angew. Chem., Int. Ed.* **2006**, *45*, 4460-4464.
270. Wodrich, M.D.; Corminboeuf, C.; von Ragué Schleyer, P. Systematic Errors in Computed Alkane Energies Using B3LYP and Other Popular DFT Functionals. *Org. Lett.* **2006**, *8*, 3631-3634.
271. Perdew, J.P.; Staroverov, V.N.; Tao, J.; Scuseria, G.E. Density Functional with Full Exact Exchange, Balanced Nonlocality of Correlation, and Constraint Satisfaction. *Phys. Rev. A* **2008**, *78*, 052513-13.
272. Della Sala, F.; Görling, A. Efficient Localized Hartree-Fock Methods as Effective Exact-Exchange Kohn-Sham Methods for Molecules. *J. Chem. Phys.* **2001**, *115*, 5718-5732.
273. Krukau, A.V.; Scuseria, G.E.; Perdew, J.P.; Savin, A. Hybrid Functionals with Local Range

Separation. *J. Chem. Phys.* **2008**, *129*, 124103-7.
274. Janesko, B.G.; Krukau, A.V.; Scuseria, G.E. Self-Constistent Generalized Kohn-Sham Local Hybrid Functionals of Screened Exchange: Combining Local and Range-Separated Hybridization. *J. Chem. Phys.* **2008**, *129*, 124110-9.
275. Himmetoglu, B.; Floris, A.; de Gironcoli, S.; Cococcioni, M. Hubbard-corrected DFT energy functionals: The LDA+U description of correlated systems. *Int. J. Quantum Chem.* **2014**, *114*, 14-49.
276. Wang, L.; Maxisch, T.; Ceder, G. Oxidation Energies of Transition Metal Oxides Within the GGA+U Framework. *Phys. Rev. B* **2006**, *73*, 195107-6.
277. Anisimov, V.I.; Izyumov, Y. *Electronic Structure of Strongly Correlated Materials*. Springer: Heidelberg, **2010**.
278. Hubbard, J. Electron Correlations in Narrow Energy Bands. *Proc. R. Soc. Lond. A* **1963**, *276*, 238-257.
279. Kotliar, G.; Vollhardt, D. Strongly Correlated Materials: Insights from Dynamic Mean-Field Theory. *Phys. Today* **2004**, *57*, 53-59.
280. Kotliar, G.; Savrasov, S.Y.; Haule, K.; Oudovenko, V.S.; Parcollet, O.; Marianetti, C.A. Electronic Structure Calculations with Dynamical Mean-Field Theory. *Rev. Mod. Phys.* **2006**, *78*, 865-951.
281. Ramakrishnan, R. The DFT+U Method in the Framework of the Parallel Density Functional Code ParaGauss. Doctoral dissertation, Technische Universität München, München, **2011**.
282. Cococcioni, M. A LDA+U Study of Selected Iron Compounds. Doctoral dissertation, Trieste, **2002**.
283. Ramakrishnan, R.; Matveev, A.; Rösch, N. The DFT+U Method in the Linear Combination of Gaussian-Type Orbitals Framework: Role of 4*f* Orbitals in the Bonding of LuF_3. *Chem. Phys. Lett.* **2009**, *468*, 158-161.
284. Ramakrishnan, R.; Matveev, A.V.; Krüger, S.; Rösch, N. Self-Interaction Artifacts on Structural Features of Uranyl Monohydroxide from Kohn-Sham Calculations. *Theor. Chem. Acc.* **2011**, *130*, 361-369.
285. Ramakrishnan, R.; Matveev, A.V.; Rösch, N. Effects of the Self-Interaction Error in Kohn–Sham Calculations: A DFT+U Case Study on Penta-Aqua Uranyl(VI). *Computational and Theoretical Chemistry* **2011**, *963*, 337-343.
286. Soini, T.M.; Krüger, S.; Rösch, N. The DFT+Umol Method and its Application to the Adsorption of CO on Platinum Model Clusters. *J. Chem. Phys.* **2014**, *140*, 174709-9.
287. Soini, T.M.; Rösch, N. A DFT + Umol Model Study of the Self-Interaction Error in Standard Density Functional Calculations of $Ni(CO)_m$ (m = 1-4). *Theor. Chem. Acc.* **2014**, *133*, 1561-9.
288. Rohrbach, A.; Hafner, J.; Kresse, G. Molecular Adsorption on the Surface of Strongly Correlated Transition-Metal Oxides: A Case Study for CO/NiO(100) *Phys. Rev. B* **2004**, *69*, 075413-13.
289. Belling, T.; Grauschopf, T.; Krüger, S.; Nörtemann, F.; Staufer, M.; Mayer, M.; Nasluzov, V.A.; Birkenheuer, U.; Rösch, N. In *Scientific Computing in Chemical Engineering II*, Keil, F.; Mackens, M.; Voß, H.; Werthe, J., Eds. Springer: Heidelberg, **1999**; Vol. 1.
290. Weigend, F. A Fully Direct RI-HF Algorithm: Implementation, Optimised Auxiliary Basis Sets, Demonstration of Accuracy and Efficiency. *Phys. Chem. Chem. Phys.* **2002**, *4*, 4285-4291.
291. Boys, S.F. Electronic Wave Functions. I. A General Method of Calculation for the Stationary States of Any Molecular System. *Proc. R. Soc. Lond. A* **1950**, *200*, 542-554.
292. Clementi, E. Ab Initio Computations in Atoms and Molecules. *IBM J. Res. and Dev.* **1965**, *9*, 2-19.
293. Hehre, W.J.; Stewart, R.F.; Pople, J.A. Self-Consistent Molecular-Orbital Methods. I. Use of Gaussian Expansions of Slater-Type Atomic Orbitals. *J. Chem. Phys.* **1969**, *51*, 2657-2664.
294. Shavitt, I. The History and Evolution of Gaussian Basis Sets. *Isr. J. Chem.* **1993**, *33*, 357-367.
295. Preuß, H. Bemerkung zum Self-Consistent-Field-Verfahren und zur Methode der Konfigurationswechselwirkung in der Quantenchemie. *Z. Naturforsch.* **1956**, *11a*, 823-831.
296. Shavitt, I.; Karplus, M. Multicenter Integrals in Molecular Quantum Mechanics. *J. Chem. Phys.* **1962**, *36*, 550-551.
297. Shavitt, I. In *Methods in Computational Physics*, Alder, B.J.; Fernbach, S.; Rotenberg, M., Eds. Academic Press: New York, **1963**; Vol. 2.
298. Davidson, E.R.; Feller, D. Basis Set Selection for Molecular Calculations. *Chem. Rev.* **1988**, *86*, 681-696.
299. Steinborn, E.O.; Ruedenberg, K. In *Advances in Quantum Chemistry*, Löwdin, P.-O., Ed. Academic: New York, **1973**.
300. Fieck, G. The Multi-Centre Integrals of Derivative, Spherical GTOs. *Theor. Chim. Acta* **1980**, *54*, 323-332.
301. Dunlap, B.I. Three-Center Gaussian-Type-Orbital Integral Evaluation Using Spherical Harmonics. *Phys. Rev. A* **1990**, *42*, 1127-1137.
302. Görling, A. Zur Verwendung von Dipolmomenten in der LCGTO-LDF-Methode. Doctoral dissertation, Technische Universität München, München, **1990**.

303. Gill, P.M.W. Molecular Integrals Over Gaussian Basis Functions. *Adv. Quantum Chem.* **1994**, *25*, 141-205.
304. Lindh, R. In *Encyclopedia of Computational Chemistry*, Von Ragué Schleyer, P., Ed. Wiley: Hoboken, New Jersey, **1998**; Vol. 2.
305. Reine, S.; Helgaker, T.; Lindh, R. Multi-Electron Integrals. *WIREs Comput. Mol. Sci.* **2012**, *2*, 290-303.
306. Abramowitz, M.; Stegun, I.A. *Handbook of Mathematical Functions*. Dover: New York, **1965**.
307. Taketa, H.; Huzinaga, S.; O-ohata, K. Gaussian-Expansion Methods for Molecular Integrals. *J. Phys. Soc. Jpn.* **1966**, *21*, 2313-2324.
308. Dunlap, B.I. Direct Quantum Chemical Integral Evaluation. *Int. J. Quantum Chem.* **2001**, *81*, 373-383.
309. Dunlap, B.I. Generalized Gaunt Coefficients. *Phys. Rev. A* **2002**, *66*, 032502-7.
310. Dunlap, B.I. Angular Momentum in Molecular Quantum Mechanical Integral Evaluation. *Comput. Phys. Commun.* **2005**, *165*, 18-36.
311. Weniger, E.J. The Spherical Tensor Gradient Operator. *Collect. Czech. Chem. Commun.* **2005**, *70*, 1225-1271.
312. Kuang, J.; Lin, C.D. Molecular Integrals Over Spherical Gaussian-Type Orbitals: I. *J. Phys. B: At. Mol. Opt. Phys.* **1997**, *30*, 2529-2548.
313. Matsuoka, O. Molecular Integrals Over Real Solid Spherical Gaussian-Type Functions. *J. Chem. Phys.* **1998**, *108*, 1063-1067.
314. Ishida, K. Accompanying Coordinate Expansion Formulas Derived with the Solid Harmonic Gradient. *J. Comput. Chem.* **2002**, *23*, 378-393.
315. Schlegel, H.B.; Frisch, M.J. Transformation Between Cartesian and Pure Spherical Harmonic Gaussians. *Int. J. Quantum Chem* **1990**, *54*, 83-87.
316. Reine, S.; Tellgren, E.; Helgaker, T. A Unified Scheme for the Calculation of Differentiated and Undifferentiated Molecular Integrals Over Solid-Harmonic Gaussians. *Phys. Chem. Chem. Phys.* **2007**, *9*, 4771-4779.
317. Fortunelli, A.; Salvetti, O. Recurrence Relations for the Evaluation of Electron Repulsion Integrals Over Spherical Gaussian Functions. *Int. J. Quantum Chem.* **1993**, *48*, 257-265.
318. Ishida, K. ACE Algorithm for the Rapid Evaluation of the Electron-Repulsion Integral over Gaussian-Type Orbitals. *Int. J. Quantum Chem.* **1996**, *59*, 209-218.
319. McMurchie, L.E.; Davidson, E.R. One- and Two-Electron Integrals Over Cartesian Gaussian Functions. *J. Comp. Phys.* **1978**, *26*, 218-231.
320. Gill, P.M.W.; Johnson, B.G.; Pople, J.A. Two-Electron Repulsion Integrals Over Gaussian s Functions. *Int. J. Quantum Chem.* **1991**, *40*, 745-752.
321. Obara, S.; Saika, A. Efficient Recursive Computation of Molecular Integrals over Cartesian Gaussian Functions. *J. Chem. Phys.* **1986**, *84*, 3963-3974.
322. Obara, S.; Saika, A. General Recurrence Formulas for Molecular Integrals Over Cartesian Gaussian Functions. *J. Chem. Phys.* **1988**, *89*, 1540-1559.
323. Schlegel, H.B. An Efficient Algorithm for Calculating Ab Initio Energy Gradients Using s, p Cartesian Gaussians. *J. Chem. Phys.* **1982**, *77*, 3676-3681.
324. Schlegel, H.B. Analytical Second Derivatives of Two Electron Integrals Over s and p Cartesian Gaussians *J. Chem. Phys.* **1989**, *90*, 5630-5634.
325. Head-Gordon, M.; Pople, J.A. A Method for Two-Electron Gaussian Integral and Integral Derivative Evaluation Using Recurrence Relations. *J. Chem. Phys.* **1988**, *89*, 5777-5786.
326. Gill, P.M.W.; Head-Gordon, M.; Pople, J.A. An Efficient Algorithm for the Generation of Two-Electron Repulsion Integrals Over Gaussian Basis Functions. *Int. J. Quantum Chem. Symp.* **1989**, *23*, 269-280.
327. Gill, P.M.W.; Head-Gordon, M.; Pople, J.A. Efficient Computation of Two-Electron-Repulsion Integrals and Their *n*th-Order Derivatives Using Contracted Gaussian Basis Sets. *J. Chem. Phys.* **1990**, *94*, 5564-5572.
328. Hamilton, T.; Schaefer III, H.F. New Variations in Two-Electron Integral Evaluation in the Context of Direct SCF Procedures. *Chem. Phys.* **1991**, *150*, 163-171.
329. Gill, P.M.W.; Pople, J.A. The Prism Algorithm for Two-Electron Integrals. *Int. J. Quantum Chem.* **1991**, *40*, 753-772.
330. Ten-no, S. An Efficient Algorithm for Electron Repulsion Integrals Over Contracted Gaussian-Type Functions. *Chem. Phys. Lett.* **1993**, *211*, 259-264.
331. Adams, T.R.; Adamson, R.D.; Gill, P.M.W. A Tensor Approach to Two-Electron Matrix Elements. *J. Chem. Phys.* **1997**, *107*, 124-131.
332. Fletcher, G.D. Recursion Formula for Electron Repulsion Integrals Over Hermite Polynomials. *Int. J. Quantum Chem.* **2006**, *106*, 355-360.
333. Sandberg, J.A.R.; Rinkevicius, Z. An Algorithm for the Efficient Evaluation of Two-Electron Repulsion Integrals Over Contracted Gaussian-Type Basis Functions. *J. Chem. Phys.* **2012**, *137*, 234105-10.
334. Johnson, B.G.; Gill, P.M.W.; Pople, J.A. The Efficient Transformation of (m0|n0) to (ab|cd) Two-Electron Repulsion Integrals. *Chem. Phys. Lett.* **1993**, *206*, 229-238.
335. Makowski, M. Simple Yet Powerful Techniques for Optimization of Horizontal Recursion Steps in Gaussian-Type Two-Electron Integral Evaluation Algorithms. *Int. J. Quantum Chem.* **2007**, *107*, 30-36.

336. Pople, J.A.; Hehre, W.J. Computation of Electron Repulsion Integrals Involving Contracted Gaussian Basis Functions. *J. Comp. Phys.* **1978**, *27*, 161-168.
337. Ishimura, K.; Nagase, S. A New Algorithm of Two-Electron Repulsion Integral Calculations: A Combination of Pople-Hehre and McMurchie-Davidson Methods. *Theor. Chem. Acc.* **2008**, *120*, 185-189.
338. Hager, G.; Wellein, G. *Introduction to High Performance Computing for Scientists and Engineers*. CRC Press: Boca Raton, **2010**.
339. Saunders, V.R. In *Computational Techniques in Quantum Chemistry and Molecular Physics*, Diercksen, G.H.F.; Sutcliffe, B.T.; Veillard, A., Eds. Reidel: Dordrecht, **1975**.
340. Dupuis, M.; Rys, J.; King, H.F. Evaluation of Molecular Integrals Over Gaussian Basis Functions. *J. Chem. Phys.* **1976**, *65*, 111-116.
341. King, H.F.; Dupuis, M. Numerical Integration Using Rys Polynomials. *J. Comput. Phys.* **1976**, *21*, 144-165.
342. Chin, R.C.Y. A Domain Decomposition Method for Generating Orthogonal Polynomials for a Gaussian Weight on a Finite Interval. *J. Comput. Phys.* **1992**, *99*, 321-336.
343. Sagar, R.P.; Smith, V.H.J. On the Calculation of Rys Polynomials and Quadratures. *Int. J. Quantum Chem.* **1992**, *42*, 827-836.
344. Schneider, B.I.; Nygaard, N. Orthogonal Functions, Discrete Variable Representation, and Generalized Gauss Quadratures. *J. Phys. Chem. A* **2002**, *106*, 10773-10776.
345. Flocke, N. On the Use of Shifted Jacobi Polynomials in Accurate Evaluation of Roots and Weights of Rys Polynomials *J. Chem. Phys.* **2009**, *131*, 064107-15.
346. Lindh, R.; Ryu, U.; Liu, B. The Reduced Multiplication Scheme of the Rys Quadrature and New Recurrence Relations for Auxiliary Function Based Two-Electron Integral Evaluation. *J. Chem. Phys.* **1991**, *95*, 5889-5897.
347. Rys, J.; Dupuis, M.; King, H.F. Computation of Electron Repulsion Integrals Using the Rys Quadrature Method. *J. Comput. Chem.* **1983**, *4*, 154-157.
348. Saunders, V.R. In *Methods in Computational Molecular Physics*, Diercksen, G.H.F.; Wilson, S., Eds. Reidel: Dordrecht, **1983**.
349. Flocke, N.; Lotrich, V.F. Efficient Electronic Integrals and Their Generalized Derivatives for Object Oriented Implementations of Electronic Structure Calculations. *J. Comput. Chem.* **2008**, *29*, 2722-2736.
350. Yasuda, K. Two-Electron Integral Evaluation on the Graphics Processor Unit. *J. Comput. Chem.* **2008**, *29*, 334-342.
351. Asadchev, A.; Allada, V.; Felder, J.; Bode, B.M.; Gordon, M.S.; Windus, T.L. Uncontracted Rys Quadrature Implementation of up to G Functions on Graphical Processing Units. *J. Chem. Theory Comput.* **2010**, *6*, 696-704.
352. Wilkinson, K.A.; Sherwood, P.; Guest, M.F.; Naidoo, K.J. Acceleration of the GAMESS-UK Electronic Structure Package on Graphical Processing Units. *J. Comput. Chem.* **2011**, *32*, 2313-2318.
353. Dupius, M.; Marques, A. The Rys Quadrature Revisited: A Novel Formulation for the Efficient Computation of Electron Repulsion Integrals over Gaussian Functions. *J. Chem. Phys.* **2001**, *114*, 2067-2078.
354. Lindh, R. The Reduced Multiplication Scheme of the Rys-Gauss Quadrature for 1st Order Integral Derivatives. *Theor. Chem. Acc.* **1993**, *85*, 423-440.
355. Kong, J.; White, C.A.; Krylov, A.I.; Sherrill, D.; Adamson, R.D.; Furlani, T.R.; Lee, M.S.; Lee, A.M.; Gwaltney, S.R.; Adams, T.R.; Ochsenfeld, C.; Gilbert, A.T.B.; Kedziora, G.S.; Rassolov, V.A.; Maurice, D.R.; Nair, N.; Shao, Y.; Besley, N.A.; Maslen, P.E.; Dombroski, J.P.; Daschel, H.; Zhang, W.; Korambath, P.P.; Baker, J.; Byrd, E.F.C.; Van Voorhis, T.; Oumi, M.; Hirata, S.; Hsu, C.-P.; Ishikawa, N.; Florian, J.; Warshel, A.; Johnson, B.G.; Gill, P.M.W.; Head-Gordon, M.; Pople, J.A. Q-Chem 2.0: A High-Performance Ab Initio Electronic Structure Program Package. *J. Comp. Chem.* **2000**, *21*, 1532-1548.
356. Bracken, P.; Bartlett, R.J. Calculation of Gaussian Integrals Using Symbolic Manipulation. *Int. J. Quantum Chem.* **1997**, *62*, 557-570.
357. Ufimtsev, I.S.; Martínez, T.J. Quantum Chemistry on Graphical Processing Units. 1. Strategies for Two-Electron Integral Evaluation. *J. Chem. Theory Comput.* **2008**, *4*, 222-231.
358. Ufimtsev, I.S.; Martínez, T.J. Quantum Chemistry on Graphical Processing Units. 2. Direct Self-Consistent-Field Implementation. *J. Chem. Theory Comput.* **2009**, *4*, 1004-1015.
359. Ufimtsev, I.S.; Martínez, T.J. Quantum Chemistry on Graphical Processing Units. 3. Analytical Energy Gradients, Geometry Optimization, and First Principles Molecular Dynamics. *J. Chem. Theory Comput.* **2009**, *5*, 2619-2628.
360. Ishida, K. Rigorous Formula for the Fast Calculation of the Electron Repulsion Integral Over the Solid Harmonic Gaussian-Type Orbitals. *J. Chem. Phys.* **1998**, *109*, 881-890.
361. Ishida, K. Rapid Algorithm for Computing the Electron Repulsion Integral Over Higher Order Gaussian-Type Orbitals: Accompanying Coordinate Expansion Method. *J. Comput. Chem.* **1998**, *19*, 923-934.

362. Ishida, K. Rigorous and Rapid Calculation of the Electron Repulsion Integral Over the Uncontracted Solid Harmonic Gaussian-Type Orbitals. *J. Chem. Phys.* **1999**, *111*, 4913-4922.
363. Ishida, K. Rigorous Algorithm for the Electron Repulsion Integral over the Generally Contracted Solid Harmonic Gaussian-Type Orbitals. *J. Chem. Phys.* **2000**, *113*, 7818-7829.
364. Kobayashi, M.; Nakai, H. New Recurrence Relations for the Rapid Evaluation of Electron Repulsion Integrals Based on the Accompanying Coordinate Expansion Formula. *J. Chem. Phys.* **2004**, *121*, 4050-4058.
365. Katouda, M.; Kobayashi, M.; Nakai, H.; Nagase, S. Practical Performance Assessment of Accompanying Coordinate Expansion Recurrence Relation Algorithm for Computation of Electron Repulsion Integrals. *J. Theor. Comput. Chem.* **2005**, *4*, 139-149.
366. Hayami, M.; Seino, J.; Nakai, H. Extension of Accompanying Coordinate Expansion and Recurrence Relation Method for General-Contraction Basis Sets. *J. Comput. Chem.* **2014**, *35*, 1517-1527.
367. Kushner, D. The Wizardry of id. *IEEE Spectrum* **2002**, *39*, 42-47.
368. Johnson, B.G.; Gill, P.M.W.; Pople, J.A. Exact and Approximate Solutions to the One-Center McMurchie-Davidson Tree-Search Problem. *Int. J. Quantum Chem.* **1991**, *40*, 809-827.
369. Lotrich, V.F.; Flocke, N.; Ponton, M.; Yau, A.; Perera, A.; Deumens, E.; Bartlett, R.J. Parallel Implementation of Electronic Structure Energy, Gradient and Hessian Calculation. *J. Chem. Phys.* **2008**, *128*, 194104-15.
370. Almlöf, J.; Faegri Jr., K.; Korsell, K. Principles for a Direct SCF Approach to LCAO-MO Ab-Initio Calculations. *J. Comput. Chem.* **1982**, *3*, 385-399.
371. White, C.A.; Head-Gordon, M. A J Matrix Engine for Density Functional Theory Calculations. *J. Chem. Phys.* **1996**, *104*, 2620-2629.
372. Takashima, H.; Kitamura, K. Rapid Computation of All Sets of Electron-Repulsion Integrals for Large-Scale Molecules. *Chem. Phys. Lett.* **2003**, *377*, 43-48.
373. Nakai, H.; Kobayashi, M. New Algorithm for the Rapid Evaluation of Electron Repulsion Integrals: Elementary Basis Algorithm. *Chem. Phys. Lett.* **2004**, *388*, 50-54.
374. Nikodem, A.; Matveev, A.V.; Soini, T.M.; Rösch, N. Load Balancing by Work-Stealing in Quantum Chemistry Calculations: Application to Hybrid Density Functional Methods. *Int. J. Quantum Chem.* **2014**, *114*, 813-822.
375. Hamermesh, M. *Group Theory and its Application to Physical Problems, Reprint Edition*. Dover: New York, **1989**.
376. Bishop, D.M. *Group Theory and Chemistry, Una Rev Edition*. Dover: New York, **1993**.
377. Dupuis, M.; King, H.F. Molecular Symmetry and Closed-Shell SCF Calculations. I. *Int. J. Quantum Chem.* **1977**, *11*, 613-625.
378. Dacre, P.D. On the Use of Symmetry in SCF Calculations. *Chem. Phys. Lett.* **1970**, *7*, 47-48.
379. Brailsford, D.F.; Hylton, J. Fast Assembly of Fock Matrices Utilising Symmetry Properties of the Basis Set. *Chem. Phys. Lett.* **1973**, *18*, 595-597.
380. Pitzer, R.M. Contribution of Atomic Orbital Integrals to Symmetry Orbital Integrals. *J. Chem. Phys.* **1973**, *58*, 3111-3112.
381. Elder, M. Use of Molecular Symmetry in SCF Calculations. *Int. J. Quantum Chem.* **1973**, *7*, 75-85.
382. Häser, M.; Ahlrichs, R. Improvements on the Direct SCF Method. *J. Comput. Chem.* **1989**, *10*, 104-111.
383. Häser, M.; Almlöf, J.; Feyereisen, M.W. Exploiting Non-Abelian Point Group Symmetry in Direct Two-Electron Integral Transformations. *Theor. Chem. Acc.* **1991**, *79*, 115-122.
384. Häser, M. Molecular Point-Group Symmetry in Electronic Structure Calculations. *J. Chem. Phys.* **1991**, *95*, 8259-8265.
385. Ochsenfeld, C.; Kussmann, J.; Lambrecht, D.S. In *Reviews in Computational Chemistry*, Lipkowitz, K.B.; Cundari, T.R., Eds. **2007**; Vol. 23.
386. Power, J.D.; Pitzer, R.M. Inequalities For Electron Repulsion Integrals. *Chem. Phys. Lett.* **1974**, *24*, 478-483.
387. Ahlrichs, R. Methods for Efficient Evaluation of Integrals for Gaussian Type Basis Sets. *Theor. Chem. Acc.* **1974**, *33*, 157-167.
388. Böhm, H.J.; Ahlrichs, R. A Study of Short-Range Repulsions. *J. Chem. Phys.* **1982**, *77*, 2028-2034.
389. Maeder, F.; Claverie, P. The Exact Multicenter Multipolar Part of a Molecular Charge Distribution and its Simplified Representations. *J. Chem. Phys.* **1988**, *88*, 4934-4948.
390. Panas, I.; Almlöf, J.; Feyereisen, M.W. Ab Initio Methods for Large Systems. *Int. J. Quantum Chem.* **1991**, *40*, 797-807.
391. Termath, V.; Handy, N.C. A Kohn-Sham Method Involving the Direct Determination of the Coulomb Potential on a Numerical Grid. *Chem. Phys. Lett.* **1994**, *230*, 17-24.
392. Ahmadi, G.R.; Almlöf, J. The Coulomb Operator in a Gaussian Product Basis. *Chem. Phys. Lett.* **1995**, *246*, 364-370.
393. Schwegler, E.; Challacombe, M. Linear Scaling Computation of the Hartree–Fock Exchange Matrix. *J. Phys. Chem.* **1996**, *105*, 2726-2734.
394. Ochsenfeld, C.; White, C.A.; Head-Gordon, M. Linear and Sublinear Scaling Formation of

Hartree-Fock-type Exchange Matrices. *J. Chem. Phys.* **1998**, *109*, 1663-1669.
395. Jansen, H.B.; Ros, P. Non-Empirical Molecular Orbital Calculations on the Protonation of Carbon Monoxide. *Chem. Phys. Lett.* **1969**, *3*, 140-143.
396. Shao, Y.; White, C.A.; Head-Gordon, M. Efficient Evaluation of the Coulomb Force in Density Functional Theory Calculations. *J. Chem. Phys.* **2001**, *114*, 6572-6577.
397. Gill, P.M.W.; Johnson, B.G.; Pople, J.A. A Simple Yet Powerful Upper Bound for Coulomb Integrals. *Chem. Phys. Lett.* **1994**, *217*, 65-68.
398. Lambrecht, D.S.; Ochsenfeld, C. Multipole-Based Integral Estimates for the Eigorous Description of Distance Dependence in Two-Electron Integrals. *J. Chem. Phys.* **2005**, *123*, 184101-14.
399. Maurer, S.A.; Lambrecht, D.S.; Flaig, D.; Ochsenfeld, C. Distance-Dependent Schwarz-Based Integral Estimates for Two-Electron Integrals: Reliable Tightness vs. Rigorous Upper Bounds. *J. Chem. Phys.* **2012**, *136*, 144107-15.
400. Kahn, L.R. Relationships Among Derivatives of the Integrals in the Calculation of the Gradient of the Electronic Energy with Respect to the Nuclear Coordinates. *J. Chem. Phys.* **1981**, *75*, 3962-3966.
401. Banerjee, A.; Jensen, J.O.; Simons, J. Translational and Rotational Symmetries in Integral Derivatives. *J. Chem. Phys.* **1985**, *82*, 4566-4576.
402. Banerjee, A.; Jensen, J.O.; Simons, J. Translational and Rotational Symmetries in Integral Derivatives of Arbitrary Order. *Chem. Phys.* **1986**, *102*, 45-54.
403. Jansen, C.L.; Nielsen, I.M.B. *Parallel Computing in Quantum Chemistry*. CRC Press: Boca Raton, **2008**.
404. Valiev, M.; Bylaska, E.J.; Govind, N.; Kowalski, K.; Straatsma, T.P.; Van Dam, H.J.J.; Wang, D.; Nieplocha, J.; Apra, E.; Windus, T.L.; de Jong, W.A. NWChem: A Comprehensive and Scalable Open-Source Solution for Large Scale Molecular Simulations. *Comput. Phys. Commun.* **2010**, *181*, 1477-1489.
405. Nikodem, A. ParaGauss and ParaTools – Transition State Search and Efficient Parallelization for Density Functional Calculations. Doctoral dissertation, Technische Universität München, München, **2013**.
406. *MPI: A Message-Passing Interface Standard, Version 2.2. Specification*, Message Passing Interface Forum: **2009**.
407. Hariharan, P.C.; Pople, J.A. The Influence of Polarization Functions on Molecular Orbital Hydrogenation Energies. *Theor. Chem. Acc.* **1973**, *28*, 213-222.
408. Kaupp, M.; Von Ragué Schleyer, P.; Stoll, H.; Preuß, H. Pseudopotential Approaches to Ca, Sr, and Ba Hydrides. Why Are Some Alkaline Earth MX_2 Compounds Bent? *J. Chem. Phys.* **1991**, *94*, 1360-1366.
409. Rassolov, V.A.; Pople, J.A.; Ratner, M.A.; Windus, T.L. 6-31G* Basis Set for Atoms K Through Zn *J. Chem. Phys.* **1998**, *109*, 1223-1229.
410. Nikodem, A.; Matveev, A.V.; Chaffey-Millar, H.; Soini, T.M.; Rösch, N. *ParaTools, Version 2.0, Technische Universität München*, **2012**.
411. Roderus, M. Parallelization Strategies for Density Functional Software. Doctoral dissertation, Technische Universität München, München, **2012**.
412. Weigend, F.; Ahlrichs, R. Balanced Basis Sets of Split Valence, Triple Zeta Valence and Quadruple Zeta Valence Quality for H to Rn: Design and Assessment of Accuracy. *Phys. Chem. Chem. Phys.* **2005**, *7*, 3297-3305.
413. Andrae, D.; Häußermann, U.; Dolg, M.; Stoll, H.; Preuß, H. Energy-Adjusted Ab-Initio Pseudopotentials for the Second and Third Row Transition Elements. *Theor. Chem. Acc.* **1990**, *77*, 123-141.
414. Eichkorn, K.; Treutler, O.; Öhm, H.; Häser, M.; Ahlrichs, R. Auxiliary Basis Sets to Approximate Coulomb Potentials. *Chem. Phys. Lett.* **1995**, *240*, 283-290.
415. Eichkorn, K.; Weigend, F.; Treutler, O.; Ahlrichs, R. Auxiliary Basis Sets for Main Row Atoms and Transition Metals and their use to Approximate Coulomb Potentials. *Theor. Chem. Acc.* **1997**, *97*, 119-124.
416. Pulay, P. Convergence Acceleration of Iterative Sequences. The Case of SCF Iteration. *Chem. Phys. Lett.* **1980**, *73*, 393-398.
417. Bitzek, E.; Koskinen, P.; Gähler, F.; Moseler, M.; Gumbsch, P. Structural Relaxation Made Simple. *Phys. Rev. Lett.* **2006**, *97*, 170201-4.
418. Boys, S.F.; Bernardi, F. The Calculation of Small Molecular Interactions by the Differences of Separate Total Energies. Some Procedures with Reduced Errors. *Mol. Phys.* **1970**, *19*, 553-566.
419. Mulliken, R.S. Electronic Population Analysis on LCAO-MO Molecular Wave Functions. I. *J. Chem. Phys.* **1955**, *23*, 1833-1849.
420. Mond, L.; Langer, C.; Quincke, F. Action of Carbon Monoxide on Nickel. *J. Chem. Soc. Trans.* **1890**, *57*, 749-753.
421. Stammreich, H.; Kawai, K.; Sala, O.; Krumholz, P. Raman Spectra of Metal Carbonyl Compounds. III. Raman Spectrum, Vibrational Analysis, and Bond Structure of Nickel Tetracarbonyl. *J. Chem. Phys.* **1961**, *35*, 2168-2174.
422. Hedberg, L.; Ijima, T.; Hedberg, K. Nickel Tetracarbonyl, $Ni(CO)_4$. I. Molecular Structure by Gaseous Electron Diffraction. II. Refinement

of Quadratic Force Field. *J. Chem. Phys.* **1979**, *70*, 3224-3229.
423. Sunderlin, L.S.; Wang, D.; Squires, R.R. Metal (Iron and Nickel) Carbonyl Bond Strengths in $Fe(CO)_n^-$ and $Ni(CO)_n^-$. *J. Am. Chem. Soc.* **1992**, *114*, 2788-2796.
424. Dyson, P.J.; McIndoe, J.S. *Transition Metal Carbonyl Cluster Chemistry*. OPA: Amsterdam, **2000**; Vol. 2.
425. Liang, B.; Zhou, M.; Andrews, L. Reactions of Laser-Ablated Ni, Pd, and Pt Atoms with Carbon Monoxide: Matrix Infrared Spectra and Density Functional Calculations on $M(CO)_n$ (n = 1-4), $M(CO)_n^-$ (n = 1-3), and M(CO)n+ (n = 1-2), (M = Ni, Pd, Pt). *J. Phys. Chem. A* **2000**, *104*, 3905-3914.
426. Macchia, P.; Sironi, A. Chemical Bonding in Transition Metal Carbonyl Clusters: Complementary Analysis of Theoretical and Experimental Electron Densities. *Coord. Chem. Rev.* **2003**, *238-239*, 383-412.
427. Elschenbroich, C. *Organometallics*. Wiley VCH: Weinheim, **2006**.
428. Jörg, H.; Rösch, N. On the Bonding in Transition-Metal Compounds: A Comparison of LDF and HF Results for $Ni(CO)_4$. *Chem. Phys. Lett.* **1985**, *120*, 359-362.
429. Rösch, N.; Jörg, H.; Kotzian, M. Photofragments of $Ni(CO)_4$: A Linear Combination of Gaussian-Type Orbitals (LCGTO) Xα Study. *J. Chem. Phys.* **1987**, *86*, 4038-4045.
430. Blomberg, M.; Brandemark, U.; Siegbahn, P.; Wennerberg, J.; Bauschlicher, C.W., Jr. The Ni-CO Binding Energy in $Ni(CO)_x$ (x = 1 - 4). A Theoretical Investigation. *J. Am. Chem. Soc.* **1988**, *110*, 6650-6655.
431. Blomberg, M.; Siegbahn, P.; Lee, T.J.; Rendell, A.P.; Rice, J.E. Binding Energies and Bond Distances of $Ni(CO)_x$, x=1–4: An Application of Coupled-Cluster Theory. . *J. Chem. Phys.* **1991**, *95*, 5898-5905.
432. Chung, S.-C.; Krüger, S.; Pacchioni, G.; Rösch, N. Relativistic Effects in the Electronic Structure of the Monoxides and Monocarbonyls of Ni, Pd, and Pt: Local and Gradient-Corrected Density Functional Calculations. *J. Chem. Phys.* **1995**, *102*, 3695-3702.
433. Xu, X.; Lü, X.; Wang, N.; Zhang, Q.; Ehara, M.; Nakatsuji, H. CASSCF Study of Bonding in NiCO and FeCO. *Int. J. Quantum Chem.* **1999**, *72*, 221-231.
434. Wolters, L.P.; Bickelhaupt, F.M. Nonlinear d^{10}-ML_2 Transition-Metal Complexes. *ChemistryOpen* **2013**, *2*, 106-114.
435. Stevens, A.E.; Feigerle, C.S.; Lineberger, W.C. Laser Photoelectron Spectrometry of $Ni(CO)_n^-$, n = 1-3. *J. Am. Chem. Soc.* **1982**, *104*, 5026-5031.
436. Chang, C.-R.; Zhao, Z.-J.; Köhler, K.; Genest, A.; Rösch, N. Theoretical Study on the Leaching of Palladium in a CO Atmosphere. *Catal. Sci. Tech.* **2012**, *2*, 2238-2248.
437. Nikodem, A.; Matveev, A.V.; Chaffey-Millar, H.; Soini, T.M.; Rösch, N. **2012**, *ParaTools, Version 2*.
438. Blyholder, G. Molecular Orbital View of Chemisorbed Carbon Monoxide. *J. Phys. Chem.* **1964**, *68*, 2772-2777.
439. DeKock, R.L. Preparation and Identification of Intermediate Carbonyls of Nickel and Tantalum by Matrix Isolation. *Inorg. Chem.* **1971**, *10*, 1205-1211.
440. Manceron, L.; Alikhani, M.E. Infrared Spectrum and Structure of $Ni(CO)_2$: A Matrix Isolation and DFT Study. *Chem. Phys.* **1999**, *244*, 215-226.
441. Warren, K.D. Ligand Field Theory of Metal Sandwich Complexes. Axial Field Spin-Orbit Perturbation Calculations for $d^1(d^9)$, $d^2(d^8)$, and $d^3(d^7)$ Configurations. *J. Phys. Chem.* **1973**, *77*, 1681-1686.
442. Huber, K.P.; Herzberg, G. *Constants of Diatomic Molecules*. Van Nostrand-Reinhold: New York, **1979**.
443. Soini, T.M.; Genest, A.; Nikodem, A.; Rösch, N. Hybrid Density Functionals for Clusters of Late Transition Metals: Assessing Energetic and Structural Properties. *J. Chem. Theory Comput.* **2014**, *10*, 4408-4416.
444. Schultz, N.E.; Zhao, Y.; Truhlar, D.G. Databases for Transition Element Bonding: Metal-Metal Bond Energies and Bond Lengths and Their Use To Test Hybrid, Hybrid Meta, and Meta Density Functionals and Generalized Gradient Approximations. *J. Phys. Chem. A* **2005**, *109*, 4388-4403.
445. Schultz, N.E.; Zhao, Y.; Truhlar, D.G. Density Functionals for Inorganometallic and Organometallic Chemistry. *J. Phys. Chem. A* **2005**, *109*, 11127-11143.
446. Janthon, P.; Luo, S.; Kozlov, S.M.; Viñes, F.; Limtrakul, J.; Truhlar, D.G.; Illas, F. Bulk Properties of Transition Metals: A Challenge for the Design of Universal Density Functionals. *J. Chem. Theory Comput.* **2014**, *10*, 3832-3839.
447. Koitz, R.; Soini, T.M.; Genest, A.; Trickey, S.B.; Rösch, N. Structure-Dependence of the Magnetic Moment in Small Palladium Clusters: Surprising Results from the M06-L Meta-GGA Functional. *Int. J. Quantum Chem.* **2012**, *112*, 113-120.
448. Koitz, R.; Soini, T.M.; Genest, A.; Trickey, S.B.; Rösch, N. Scalable Properties of Metal Clusters: A Comparative Study of Modern Exchange-Correlation Functionals. *J. Chem. Phys.* **2012**, *137*, 034102-9.
449. Pacchioni, G.; Chung, S.-C.; Krüger, S.; Rösch, R. On the Evolution of Cluster to Bulk

Properties: A Theoretical LCGTO-LDF Study of Free and Coordinated Ni_n Clusters (n=6-147). *Chem. Phys.* **1994**, *184*, 125-137.

450. Häberlen, O.D.; Chung, S.-C.; Stener, M.; Rösch, N. From Clusters to the Bulk. A Relativistic Density Functional Investigation on a Series of Gold Clusters Au_n, n = 6,...,147. *J. Chem. Phys.* **1997**, *106*, 5189-5201.
451. Krüger, S.; Nörtemann, F.; Staufer, M.; Vent, S.; Rösch, N. The Average Bond Length in Pd Clusters Pd_n, n = 4-309: A Density-Functional Case Study on the Scaling of Cluster Properties. *J. Chem. Phys.* **2001**, *115*, 2082-2087.
452. Krüger, S.; Vent, S.; Rösch, N. Size Dependence of Bond Length and Binding Energy in Palladium and Gold Clusters. *Ber. Bunsenges. Phys. Chemie* **1997**, *101*, 1640-1643.
453. Nava, P.; Sierka, M.; Ahlrichs, R. Density Functional Study of Palladium Clusters. *Phys. Chem. Chem. Phys.* **2003**, *5*, 3372-3381.
454. Yudanov, I.V.; Metzner, M.; Genest, A.; Rösch, N. Size-Dependence of Adsorption Properties of Metal Nanoparticles: A Density Functional Study on Palladium Nanoclusters. *J. Phys. Chem. C* **2008**, *112*, 20269-20275.
455. Yudanov, I.V.; Genest, A.; Rösch, N. DFT Studies of Palladium Model Catalysts: Structure and Size Effects. *J. Clust. Sci.* **2011**, *22*, 433-448.
456. Marchal, R.; Yudanov, I.V.; Matveev, A.V.; Rösch, N. Scalable Properties of Metal Clusters: A Comparative DFT Study of Ionic-Core Treatments. *Chem. Phys. Lett.* **2013**, *578*, 92-96.
457. Peng, D.; Middendorf, N.; Weigend, F.; Reiher, M. An Efficient Implementation of Two-Component Relativistic Exact-Decoupling Methods for Large Molecules. *J. Chem. Phys.* **2013**, *138*, 184105-14.
458. Braunstein, P.; Oro, L.A.; Raithby, P.R. *Metal Clusters in Chemistry*. Wiley: Weinheim, **1999**.
459. Heiz, U.; Landman, U. *Nanocatalysis*. Springer: Berlin, Heidelberg, **2007**.
460. Wang, L.-L.; Johnson, D.D. Density Functional Study of Structural Trends for Late-Transition-Metal 13-Atom Clusters. *Phys. Rev. B* **2007**, *75*, 235405-10.
461. Zhang, M.; Fournier, R. Density-Functional-Theory Study of 13-Atom Metal Clusters M_{13}, M = Ta-Pt. *Phys. Rev. A* **2009**, *79*, 043203-10.
462. Taylor, A. *J. Inst. Metals* **1950**, *77*, 585.
463. Rao, C.N.; Rao, K.K. Effect of Temperature on Lattice Parameters of Some Silver-Palladium Alloys. *Can. J. Phys.* **1964**, *42*, 1336-1342.
464. Waseda, Y.; Hirata, K.; Ohtani, M. *High Temp. High Pressures* **1975**, *7*, 221-226.
465. Lejaeghere, K.; Van Speybroeck, V.; Van Oost, G.; Cottenier, S. Error Estimates for Solid-State Density-Functional Theory Predictions: An Overview by Means of the Ground-State Elemental Crystals. *Crit. Rev. Solid State Mater. Sci* **2014**, *39*, 1-24.
466. Chase, M.W.; Davies, C.A.; Downey, J.R.; Frurip, D.J.; McDonald, R.A.; Syverud, A.N. JANAF Thermochemical Tables, Third Edition. *J. Phys. Chem. Ref. Data* **1985**, *14, Suppl. 1*.
467. Schumm, R.H.; Wagman, D.D.; Bailey, S.; Evans, W.H.; Parker, V.B. National Bureau of Standards (USA), Technical Notes 270-1 to 270-8: **1973**.
468. Kittel, C. *Introduction to Solid State Physics, 8th. edition*. Wiley: New York, **2005**.
469. Seemüller, T.J. Density Functional Studies on Properties of Nickel Clusters and their Scaling with Cluster Size. Diploma Thesis, Technische Universität München, München, **2000**.
470. Zhao, Y.; Truhlar, D.G. Comparative Assessment of Density Functional Methods for 3d Transition-Metal Chemistry. *J. Chem. Phys.* **2006**, *124*, 224105-6.
471. Häberlen, O.D.; Chung, S.-C.; Rösch, N. On the Metallic Droplet Model for Successive Ionization Potentials of Metal Clusters-Relativistic Electronic Structure Investigations of the Icosahedral Gold Cluster Au_{55}. *Ber. Bunsenges. Phys. Chemie* **1994**, *98*, 882-885.
472. Riviere, J.C. Work Function: Measurements and Results. In *Solid State Surface Science*, Green, M., Ed. Decker: New York, **1969**.
473. Michaelson, H.B. The Work Function of the Elements and its Periodicity. *J. Appl. Phys.* **1977**, *48*, 4729-4733.
474. Hölzl, J.; Schulte, F.K. Work Functions of Metals. In *Solid Surface Physics*, Höhler, G., Ed. Springer: Berlin, **1979**.
475. Apsel, S.E.; Emmert, J.W.; Deng, J.; Bloomfield, A. Surface-Enhanced Magnetism in Nickel Clusters. *Phys. Rev. Lett.* **1996**, *76*, 1441-1444.
476. Alonso, J.A. Electronic and Atomic Structure, and Magnetism of Transition-Metal Clusters. *Chem. Rev.* **2000**, *100*, 637-677.
477. Bardeen, J. Theory of the Work Function. II. The Surface Double Layer. *Phys. Rev.* **1936**, *49*, 653-663.
478. Monkhorst, H.J. Hartree-Fock Density of States for Extended Systems. *Phys. Rev. B* **1979**, *20*, 1504-1513.
479. Stroppa, A.; Kresse, G. The shortcomings of semi-local and hybrid functionals: what we can learn from surface science studies. *New J. Phys.* **2008**, *10*, 063020-17.
480. Feibelman, P.J.; Hammer, B.; Nørskov, J.K.; Wagner, F.; Scheffler, M.; Stumpf, R.; Watwe, R.; Dumesic, J. The CO/Pt(111) Puzzle. *J. Phys. Chem. B* **2001**, *105*, 4018-4025.
481. Grinberg, I.; Yourdshahyan, Y.; Rappe, A.M. CO on Pt(111) Puzzle: A Possible Solution. *J. Chem. Phys.* **2002**, *117*, 2264-2270.

482. Gajdoš, M.; Eichler, A.; Hafner, J. CO Adsorption on Close-Packed Transition and Noble Metal Surfaces: Trends from Ab Initio Calculations. *J. Phys.: Condens. Matter.* **2004**, *16*, 1141-1164.
483. Stroppa, A.; Termentzidis, K.; Paier, J.; Kresse, G.; Hafner, J. CO Adsorption on Metal Surfaces: A Hybrid Functional Study with Plane-Wave Basis Set. *Phys. Rev. B* **2007**, *76*, 195440-12.
484. Schimka, L.; Harl, J.; Stroppa, A.; Grüneis, A.; Marsman, M.; Mittendorfer, F.; Kresse, G. Accurate Surface and Adsorption Energies from Many-Body Perturbation Theory. *Nat. Mater.* **2010**, *9*, 741-744.
485. Yeo, Y.Y.; Vattuone, L.; King, D.A. Calorimetric Heats for CO and Oxygen Adsorption and for the Catalytic Oxidation Reaction on Pt(111). *J. Chem. Phys.* **1997**, *106*, 392-401.
486. Lu, C.; Lee, I.C.; Masel, R.I.; Wieckowski, A.; Rice, C. Correlations between the Heat of Adsorption and the Position of the Center of the D-Band: Differences between Computation and Experiment. *J. Phys. Chem. A* **2002**, *106*, 3084-3091.
487. Westerberg, S.; Wang, C.; Somorjai, G.A. Heat of Adsorption of CO on Pt(111) Obtained by Sum Frequency Generation Vibrational Spectroscopy - A New Technique to Measure Adsorption Isotherms. *Surf. Sci.* **2005**, *582*, 137-144.
488. Sung, S.S.; Hoffmann, R. How Carbon Monoxide Bonds to Metal Surfaces. *J. Am. Chem. Soc.* **1985**, *107*, 578-584.
489. Föhlisch, A.; Nyberg, M.; Bennich, P.; Triguero, L.; Hasselström, J.; Karis, O.; Pettersson, L.G.M.; Nilsson, A. The Bonding of CO to Metal Surfaces. *J. Chem. Phys.* **2000**, *112*, 1946-1958.
490. Föhlisch, A.; Nyberg, M.; Hasselström, J.; Karis, O.; Pettersson, L.G.M.; Nilsson, A. How Carbon Monoxide Adsorbs in Different Sites. *Phys. Rev. Lett.* **2000**, *85*, 3309-3312.
491. Groß, A. *Theoretical Surface Science: A Microscopic Perspective*. Springer: Heidelberg, **2009**.
492. Yang, H.; Sanz, J.F.; Wang, Y.; Whitten, J.L. Adsorption Energetics of NO and CO on Pt(111). *J. Clust. Sci.* **1999**, *10*, 581-590.
493. Hammer, B.; Nørskov, J.K. Theoretical Surface Science and Catalysis - Calculations and Concepts. *Adv. Catal.* **2000**, *45*, 71-129.
494. Steininger, H.; Lehwald, S.; Ibach, H. On the Adsorption of CO on Pt(111). *Surf. Sci.* **1982**, *123*, 264-282.
495. Ogletree, D.F.; Van Hove, M.A.; Somorjai, G.A. LEED Intensity Analysis of the Structures of Clean Pt(111) and of CO Adsorbed on Pt(111) in the c(4 × 2) Arrangement. *Surf. Sci.* **1986**, *173*, 351-365.
496. Blackman, G.S.; Xu, M.L.; Ogletree, D.F.; Van Hove, M.A.; Somorjai, G.A. Mix of Molecular Adsorption Sites Detected for Disordered CO on Pt(111) by Diffuse Low-Energy Electron Diffraction. *Phys. Rev. Lett.* **1988**, *61*, 2352-2355.
497. Bocquet, M.L.; Sautet, P. STM and Chemistry: A Qualitative Molecular Orbital Understanding of the Image of CO on a Pt Surface. *Surf. Sci.* **1996**, *360*, 128-136.
498. Pedersen, M.Ø.; Bocquet, M.L.; Sautet, P.; Lægsgaard, E.; Stensgaard, I.; Besenbacher, F. CO on Pt(111): Binding Site Assignment from the Interplay Between Measured and Calculated STM Images. *Chem. Phys. Lett.* **1999**, *299*, 403-409.
499. Kresse, G.; Gil, A.; Sautet, P. Significance of Single-Electron Energies for the Description of CO on Pt (111). *Phys. Rev. B* **2003**, *68*, 073401-4.
500. Gil, A.; Clotet, A.; Ricart, J.M.; Kresse, G.; Garcia-Hernandez, M.; Rösch, N.; Sautet, P. Site Preference of CO Chemisorbed on Pt(111) from Density Functional Calculations. *Surf. Sci.* **2003**, *530*, 71-87.
501. Huang, Y.-W.; Lee, S.-L. Hybrid DFT and Hyper-GGA DFT Studies of the CO Adsorption on Pt Nanoclusters: Effects of the Cluster Size and Better CO LUMO Description. *Chem. Phys. Lett.* **2010**, *492*, 98-102.
502. Geschke, D.; Bastug, T.; Jacob, T.; Fritzsche, S.; Sepp, W.-D.; Fricke, B.; Varga, S.; Anton, J. Adsorption of CO on Cluster Models of Platinum (111): A Four-Component Relativistic Density-Functional Approach. *Phys. Rev. B* **2001**, *64*, 235411-9.
503. Olsen, R.A.; Philipsen, P.H.T.; Baerends, E.J. CO on Pt(111): A Puzzle Revisited. *J. Chem. Phys.* **2003**, *119*, 4522-4528.
504. Orita, H.; Itoh, N.; Inada, Y. All Electron Scalar Relativistic Calculations on Adsorption of CO on Pt(111) with Full-Geometry Optimization: A Correct Estimation for CO Site-Preference. *Chem. Phys. Lett.* **2004**, *384*, 271-276.
505. Grönbeck, H. CO Bonded to Platinum: Effects of Semi-Core Polarization. *Surf. Sci.* **2004**, *559*, 214-222.
506. Abild-Pedersen, F.; Andersson, M.P. CO Adsorption Energies on Metals with Correction for High Coordination Adsorption Sites - A Density Functional Study. *Surf. Sci.* **2007**, *601*, 1747-1753.
507. Doll, K. CO Adsorption on the Pt(111) Surface: a Comparison of a Gradient Corrected Functional and a Hybrid Functional. *Surf. Sci.* **2004**, *573*, 464-473.
508. Ganduglia-Pirovano, M.V.; Natoli, V.; Cohen, M.H.; Kudrnovský, J.; Turek, I. Potential, Core-

Level, and d Band Shifts at Transition-Metal Surfaces. *Phys. Rev. B* **1996**, *54*, 8892-8898.
509. Lazić, P.; Alaei, M.; Atodiresei, N.; Caciuc, V.; Brako, R.; Blügel, S. Density Functional Theory with Nonlocal Correlation: A Key to the Solution of the CO Adsorption Puzzle. *Phys. Rev. B* **2010**, *81*, 045401-6.
510. Yudanov, I.V.; Sahnoun, R.; Neyman, K.; Rösch, R. Metal Nanoparticles as Models of Single Crystal Surfaces and Supported Catalysts: Density Functional Study of Size Effects for CO/Pd(111). *J. Chem. Phys.* **2002**, *117*, 9887-9896.
511. Yudanov, I.V.; Sahnoun, R.; Neyman, K.; Rösch, N.; Hoffmann, J.; Schauermann, S.; Johanek, V.; Unterhalt, H.; Rupprechter, G.; Libuda, J.; Freund, H.-J. CO Adsorption on Pd Nanoparticles: Density Functional and Vibrational Spectroscopy Studies. *J. Phys. Chem. B* **2003**, *107*, 255-264.
512. Fischer-Wolfarth, J.-H.; Farmer, J.A.; Flores-Camacho, J.M.; Genest, A.; Yudanov, I.V.; Rösch, N.; Campell, C.T.; Schauermann, S.; Freund, H.-J. Particle-Size Dependent Heats of Adsorption of CO on Supported Pd Nanoparticles as Measured with a Single-Crystal Microcalorimeter. *Phys. Rev. B.* **2010**, *81*, 241416-4.
513. Yudanov, I.V.; Genest, A.; Schauermann, S.; Freund, H.-J.; Rösch, N. Size-Dependence of the Adsorption Energy of CO on Metal Nanoparticles: A DFT Search for the Minimum Value. *Nano Lett.* **2012**, *12*, 2134-2149.
514. Buenker, R.J.; Chandra, P.; Hess, B.A. Matrix Representation of the Relativistic Kinetic Energy Operator: Two-Component Variational Procedure for the Treatment of Many-Electron Atoms and Molecules. *Chem. Phys.* **1984**, *84*, 1-9.
515. Rösch, N.; Matveev, A.V.; Nasluzov, V.A.; Neyman, K.M.; Moskaleva, L.V.; Krüger, S. In *Relativistic Electronic Structure Theory - Applications*, Schwerdtfeger, P., Ed. Elsevier: Amsterdam, **2004**.
516. Pantazis, D.A.; Chen, X.-Y.; Landis, C.R.; Neese, F. All-Electron Scalar Relativistic Basis Sets for Third-Row Transition Metal Atoms. *J. Chem. Theory Comput.* **2008**, *4*, 908-919.
517. Neyman, K.; Vayssilov, G.N.; Rösch, N. Transition Metal Clusters and Supported Species with Metal-Carbon Bonds from First-Principles Quantum Chemistry. *J. Organomet. Chem.* **2004**, *689*, 4384-4394.
518. Neyman, K.; Inntam, C.; Gordienko, A.; Yudanov, I.V.; Rösch, N. Adsorption of Carbon on Pd Clusters of Nanometer Size: A First-Principles Theoretical Study. *J. Chem. Phys.* **2005**, *122*, 174705-9.
519. Gilliam, O.R.; Johnson, C.M.; Gordy, W. Microwave Spectroscopy in the Region from Two to Three Millimeters. *Phys. Rev.* **1950**, *78*, 140-144.
520. Hollas, M.J. *Modern Spectroscopy, 4th edition*. Wiley: Chichester, **2004**.
521. Ackermann, L.; Rösch, N.; Dunlap, B.I.; Pacchioni, G. Electronic and Magnetic Properties of Organometallic Clusters: from the Molecular to the Metallic State. *Int. J. Quantum Chem: Quantum Chem. Symp.* **1992**, *26*, 605-619.
522. Stroppa, A.; Termentzidis, K.; Paier, J.; Kresse, G.; Hafner, J. CO adsorption on metal surfaces: A hybrid functional study with plane-wave basis set. *Phys. Rev. B* **2007**, *76*, 195440.
523. Bare, S.R.; Griffiths, K.; Hofmann, P.; King, D.A.; Nyberg, G.L.; Richardson, N.V. A Synchrotron Radiation Study of the Electronic and Geometric Structure of CO on Pt{110}. *Surf. Sci.* **1982**, *120*, 367-375.
524. Tsimilis, G.; Kutzner, J.; Zacharias, H. Photoemission Study of Clean and c(4×2)-2CO-Covered Pt(111) Using High-Harmonic Radiation *Appl. Phys. A* **2003**, *76*, 743-749.